Local magnetic detection and stimulation of neuronal activity

Vincent Trauchessec

To cite this version:

Vincent Trauchessec. Local magnetic detection and stimulation of neuronal activity. Biological Physics [physics.bio-ph]. Université Paris Saclay (COmUE), 2017. English. NNT : 2017SACLS301 . tel-01629395

université
PARIS-SACLAY

NNT : 2017SACLS301

Local magnetic detection and stimulation of neuronal activity

Thèse de doctorat de l'Université Paris-Saclay
préparée au Service de Physique de l’Etat Condensé, CEA

École doctorale n°564 Physique de l’Ile de France
Spécialité de doctorat: Physique

Thèse présentée et soutenue à Gif-sur-Yvette, le 4 Octobre 2017, par

Vincent Trauchessec

Composition du Jury :

André Thiaville Directeur de recherche CNRS Laboratoire de Physique des Solides, Orsay	Président
Nora Dempsey Directrice de recherche CNRS Institut Néel, Grenoble	Rapporteur
Lauri Parkkonen Professeur Aalto University, Helsinki	Rapporteur
Claire Baraduc Directrice de recherche CEA Spintech, Grenoble	Examinatrice
Bruno Le Pioufle Professeur Ecole Normale Supérieure Paris-Saclay	Examinateur
Myriam Pannetier-Lecoeur Directrice de recherche CEA Service de Physique de l’Etat Condensé, Gif-sur-Yvette	Directrice de thèse

Thèse de doctorat

Remerciements

Ce manuscrit vient conclure mes trois années de thèse au Service de Physique de l'Etat Condensé du CEA. Si elles furent aussi enrichissantes, à la fois sur le plan scientifique et personnel, c'est grâce à toutes les personnes que j'ai pu cotoyer et que je tiens à remercier ici.

Je tiens à remercier en premier lieu ma directrice de thèse, Myriam Pannetier-Lecoeur. Grâce à sa confiance, j'ai pu intégrer ce grand projet *Magnetrode* qu'elle a dirigé durant trois ans. Elle m'a permis d'avoir d'excellentes conditions de travail tout en me laissant une liberté très appréciable au quotidien. Je lui suis également très reconnaissant d'avoir pu profiter de la dimension internationale qu'elle a donnée à ma thèse, à travers plusieurs missions qui rendraient jaloux plus d'un thésard (Helsinki, Lisbonne, Francfort, Marseille, Séoul, Dublin, etc...)!

Je remercie également le directeur du groupe LNO, Claude Fermon, dont les compétences scientifiques remarquables couvrent un spectre aussi large que celui reliant la physique fondamentale à l'ingénierie. Ses conseils et ses idées novatrices ont été un atout considérable pour l'avancement de cette thèse.

J'ai aussi eu la chance de travailler avec d'autres étudiants qui ont participé à faire avancer ce projet. Tout d'abord, Laure Caruso, première thésarde à se lancer courageusement dans la fabrication de *magnetrodes* et avec qui j'ai eu le plaisir d'interagir pendant un peu plus d'un an. Puis Josué Trejo-Rosillo, post-doc durant un an, dont les compétences en instrumentation furent très précieuses. Deux stagiaires de master ont également participé au projet, Jocelyn Boutzen sur la "délicate" découpe laser, et Chloé Chopin, récemment promue thésarde, grâce à qui ce travail ira j'en suis sûr bien plus loin.

Je tiens à remercier Elodie Paul, spécialiste microfabrication, dont l'aide m'a permis de gagner beaucoup de temps, que ce soit durant les process ou avec KLayout.

De même, l'efficacité de Grégory Cannies et Gérald Le Goff pour fabriquer tout type de pièces mécaniques sur mesure fut très appréciable. Un grand merci également à Aurélie Solignac pour tous nos échanges et tout le temps qu'elle m'a consacré, en particulier durant la phase de rédaction puis de préparation de la soutenance. Merci à Jean-Yves Chauleau, nouvelle recrue du LNO, toujours prêt à discuter physique ou autre, autour d'un café ou plutôt d'une bière. J'ai aussi une pensée pour Corinne Kopec-Coelho pour sa disponibilité et parce qu'elle m'a largement facilité les tâches administratives pour chaque mission. Je remercie également le directeur du SPEC, François Daviaud, pour avoir pris le temps de faire avec moi des points réguliers sur ma thèse et ma situation personnelle.

Tous les résultats présentés dans cette thèse n'auraient pas vu le jour sans le travail de nos collaborateurs neuroscientifiques. Interagir avec eux fut très enrichissant et m'a permis d'aborder la compléxité d'un système biologique avec un recul et une humilité indispensables. Tout d'abord, les dizaines de tentatives et le nombre d'heures incalculables passées à essayer de mesurer ce signal biomagnétique furent récompensées grâce à la persévérance et à la rigueur de l'équipe composée de Gilles Ouanounou, Francesca Barbieri, Apostolis Mikroulis, Thierry Bal et Alain Destexhe. Je remercie également l'équipe du Professeur Pascal Fries pour leur professionnalisme et leur enthousiasme durant ces mémorables expériences *in vivo*: Thomas Wunderle, Chris Lewis, Jianguan Ni, et en particulier Patrick Jendritza pour avoir eu, au milieu de la seconde nuit, cette idée lumineuse du montage qui a finalement permis la toute première mesure magnétique intracorticale de spikes.

Enfin je remercie les membres du jury qui ont accepté d'examiner ce travail de thèse: André Thiaville, Nora Dempsey, Claire Baraduc, Bruno Le Pioufle, et en particulier Lauri Parkkonen, dont l'impressionnante culture et rigueur scientifique m'ont permis de peaufiner ce manuscrit dans les moindres détails.

Je pense également à tous mes collègues qui ont rendus ces trois années de thèse très agréables. Que ce soit les grands anciens du laboratoire: Camille, Pierre-André, Christian, Sylvio; l'équipe du midi avec qui chaque repas se passe dans la bonne humeur: mon parrain Yannick, les incollables du classement ATP Grégoire, Michel et Jean-Baptiste, les GMT; les membres de Crivasense: Amal, Paolo, Yann, Raphaël, Florian, Maxime; et tout ceux avec qui j'ai pu partagé de bons moments au SPEC ou sur un terrain de foot: Sebastian, Matthieu, Maëlle, Chloé, Marc, Reina, Fawaz, Julien, Andrin, Théophile, Stefan, Nathanaël, Li, Xavier, Anaëlle, Bastien, Romain, Daniela, Bartolo, Fernanda, Manon, François-Damien, Alizée, Thomas, Kristinn, Philippe, Patrick, Patrice, Gwen, Vincent, Ramiro, Minky, Vishal, etc...

Néanmoins, je ne serais pas arrivé jusqu'ici sans avoir croisé la route de quelques brillants professeurs. Je me dois de citer l'excellente équipe de prépa ATS du lycée La Fayette de Clermont-Ferrand, à qui je dois la large majorité de mes quelques connaissances scientifiques, et sans qui je n'aurais jamais atteint l'ENS: Bruno Abadie, Emmanuel Hehunstre, Christophe Pierre, Jean-François Planeix, Philippe Josselin, et Marie-Christine Lesprit. A Cachan, les cours de Arnaud Bournel, Sylvie Retailleau, Jean-Pierre Barbot, furent également passionnants, et j'ai eu la chance d'intégrer mon premier laboratoire sous la direction de Damien Querlioz, avec qui j'ai pris beaucoup de plaisir à faire de la recherche pour la première fois, et dont les qualités scientifiques lui assureront une carrière déjà brillante.

Enfin, je remercie tous mes amis pour m'avoir fait penser à autre chose que cette thèse durant ces trois ans, ma famille, ma soeur Valérie, grâce à qui j'étais dans les meilleures conditions pour réussir l'année déterminante de classe prépa, mes parents, qui m'ont depuis toujours encouragé à poursuivre dans la voie scientifique, ma belle-famille, grâce à qui j'ai pu notamment peaufiner ce manuscrit à l'ombre d'oliviers gardois, et enfin Valentine, pour tout son soutien quotidien sans faille. Merci à tous!

Résumé

L'activité cérébrale se traduit par des courants ioniques circulant dans le réseau neuronal. La compréhension des mécanismes cérébraux implique de sonder ces courants, via des mesures électriques ou magnétiques. Pour cela, différents outils de mesure ont été développés, couvrant une échelle spatiale qui s'étend sur plusieurs ordres de grandeurs, de la dizaine de nanomètres à la taille d'une aire cérébrale. Le comportement d'un neurone est bien identifié grâce aux techniques d'électrophysiologie traditionnelles, du type micro-électrodes ou patch-clamp. A l'échelle du cerveau, les techniques d'imagerie non-invasives permettent de cartographier les différentes régions et leurs fonctions associées. La méthode la plus simple est l'électroencéphalographie (EEG), qui consiste à placer des électrodes directement sur le cuir chevelu du patient afin d'enregistrer les variations de potentiel électrique. Sa facilité de mise en oeuvre fait de l'EEG une technique largement répandue dans les hôpitaux et les centres de recherche. Cependant, la résolution spatiale est particulièrement faible: le nombre de neurones corticaux présents dans la zone couverte par la surface d'une électrode de 1 cm^2 est d'environ 10^7. De plus, si cette technique présente l'avantage d'être non-invasif, les ions déplacés par l'activité neuronale doivent se propager à travers plusieurs tissus (méninges, crâne, cuir chevelu) présentant des propriétés différentes avant d'atteindre l'électrode, ce qui rend le signal EEG sensible à la distorsion et au filtrage. A cette activité électrique est associé un champ magnétique, détectable de façon non-invasive par des capteurs ultra-sensibles. L'activation synchrone d'une population de neurones génère un champ magnétique de quelques 10^{-13}T à une distance de l'ordre de 3 cm. Cette technique, la magnétoencéphalographie (MEG), est basée sur l'utilisation de SQUIDs (Superconducting QUantum Interference Devices). Ces capteurs, constitués d'une boucle supraconductrice et de deux jonctions Josephson, atteignent des sensibilités de l'ordre de 10^{-15} $\text{T}/\sqrt{\text{H}z}$. Les systèmes MEG possèdent jusqu'à 306 SQUIDs qui permettent une localisation des sources plus précise que l'EEG. En effet, la perméabilité des tissus étant égale à celle du vide, le champ magnétique se propage des neurones jusqu'aux capteurs sans le moindre effet de filtrage ou de distorsion. Le signal MEG est simplement

attenué par la distance source-capteur. Néanmoins, le refroidissement à l'Hélium liquide (4,2 K) des SQUIDs requiert une isolation thermique qui implique une distance source-capteur comprise entre 3 et 5 cm. Des études récentes ont montré la faisabilité de mesures MEG basées sur des magnétomètres atomiques. Ne nécessitant pas de système cryogénique, ces magnétomètres peuvent être positionnés directement sur le cuir-chevelu. Les champs magnétiques enregistrés atteignent alors 10^{-12} T. Cependant, il n'existe pas d'outils permettant de mesurer localement le champ magnétique à l'intérieur du cortex, de la même manière qu'une micro-électrode insérée au sein du réseau neuronal donne accès aux variations locales du potentiel électrique. Un tel outil de magnétophysiologie présenterait plusieurs avantages. Tout d'abord, une électrode conventionnelle traduit une quantité scalaire, le potentiel électrique, dû aux variations du nombre de charges présentes autour de son extrémité, indépendamment de leurs directions de propagation. Un capteur de champ magnétique fournit une quantité vectorielle, contenant deux informations: l'intensité des courants ioniques ainsi que leurs directions de propagation. Cette information simplifierait grandement la reconstruction de la configuration géométrique de la zone sondée. De plus, tout comme le signal MEG, le champ magnétique mesuré localement traverse les tissus et le milieu conducteur environnant sans subir de distorsion. La mesure locale permettrait également de faciliter l'interprétation du signal MEG enregistré à l'échelle cérébrale. Enfin, le champ magnétique émit par un neurone lors de l'émission d'un potentiel d'action permettrait de remonter au courant axial le long de l'axone sans être en contact direct avec la cellule. Toute ces perspectives nécessitent le développement de capteurs magnétiques à la fois suffisamment sensibles pour être capable de détecter le champ magnétique généré par les courants neuronaux (de l'ordre de 10^{-9} T), dont la géométrie est miniaturisable aux dimensions des cellules, et fonctionnant à température ambiante. C'est l'objet de cette thèse, organisée de la façon suivante.

Le premier chapitre présente l'état de l'art des mesures de l'activité neuronale, en mettant l'accent sur les mesures magnétiques. A l'échelle cérébrale, les techniques d'imagerie dites structurelles (Imagerie par Résonance Magnétique) et fonctionnelles (IRM fonctionnelle, Tomographie par Emission de Positons (TEP), EEG, MEG) permettent d'obtenir des cartographies de l'activité cérébrale avec différentes résolutions spatiales et temporelles. Les techniques d'IRMf et TEP sont dites hémodynamiques: l'activité des cellules augmente la consommation d'oxygène, entrainant localement un flux de sang plus important. Les propriétés magnétiques de l'hémoglobine dépendant de la quantité d'oxygène transportée, ce flux génère un signal dit BOLD (Blood-Oxygen-Level Dependent) détectable par IRMf. Cependant, la résolution temporelle de la mesure de la réponse hémodynamique neuronale est intrinsèquement limitée par la propagation du flux sanguin, c'est-à-dire à quelques centaines de millisecondes. Par ailleurs, détecter le champ électromagnétique émis par les neurones donne une vision directe et quasi-instantanée de l'activité cérébrale, avec une résolution temporelle de l'ordre de la milliseconde. Afin d'interpréter les signaux enregistrés par les techniques d'EEG et MEG décrites précédemment, les mécanismes de génération et de transmission du signal électrique entre neurones sont décrits. Deux principales sources de champ magnétique peuvent être identifiées: les courants dus à la propagation du potentiel d'action et les courants post-synaptiques. Ces courants post-synaptiques représentent la contribution la plus forte sur les signaux EEG/MEG, du fait notamment de leur plus grande extension temporelle, quelques dizaines de millisecondes, augmentant ainsi l'effet global de sommation. La détection de potentiel d'action n'est possible que via des outils d'électrophysiologie, dont la partie sensible est positionnée soit à l'intérieur du neurone actif (enregistrement intra-cellulaire) soit dans le milieu extérieur, afin de mesurer les potentiels d'actions de la population de neurones proches de l'électrode (enregistrement extra-cellulaire). La signature magnétique d'un potentiel d'action n'a été mesurée que dans des systèmes biologiques simples (axone géant de calmar ou d'écrevisse, muscle squelettique, ver), via l'utilisation de SQUIDs, de bobine d'induction, ou plus récemment de magnétomètre à centres NV. Les capteurs développés dans cette thèse sont basés sur un effet quantique dit de magnétorésistance géante. Leur principe de fonctionnement, leur fabrication et leurs performances sont décrits dans le second chapitre.

L'effet de magnétorésistance géante fut découvert expérimentalement par A. Fert et P. Grünberg en 1988. L'expérience pionnière montre que la résistance électrique de multi-couches Fer/Chrome varie de 80% entre les états d'aimantation parallèles et anti-parallèle de deux couches adjacentes. A partir de cette découverte, B. Dieny et S. Parkin développèrent un nouveau type de capteur magnétique, la vanne de spin. Ces vannes de spin, ou capteurs GMR, sont constituées d'une couche d'un matériau magnétique à haute coercivité (couche dure) et d'une couche d'un matériau magnétique à faible coercivité (couche libre) séparées par un espaceur non-magnétique. En présence d'un champ magnétique extérieur, la couche libre alignera son aimantation avec celui-ci, alors que la couche dure conserva la même direction d'aimantation, ce qui entrainera une variation de la résistance globale du dispositif. Afin d'obtenir une variation linéaire de la résistance en fonction du champ magnétique appliqué, le design de la vanne de spin est choisi de façon à ce que les aimantations de la couche libre et la couche dure soient perpendiculaires à champ nul. Pour les structure de l'ordre du micromètre, un fort rapport d'aspect permet de créer une anisotropie de forme qui satisfait cette condition. Pour les structures de taille plus importante, un aimant dit de bias permet d'orienter la couche libre dans la direction souhaitée. Dans les deux cas, la forme de la vanne de spin est obtenue par gravure sèche à l'Argon après une étape de lithographie UV. La vanne de spin est ensuite contactée électriquement via des lignes de Titane/Or déposées par évaporation (150 nm), puis le capteur est passivé par pulvérisation d'une bicouche d'alumine et de nitrure de silicium (300 nm). Les capteurs sont ensuite découpés par gravure ionique réactive profonde, afin de les libérer du substrat de silicium de 200 micromètres d'épaisseur. Chaque capteur est ensuite collé sur un circuit PCB et testé afin de déterminer sa sensibilité et son niveau de bruit. Les sensibilités typiques sont comprises entre 2 %/mT et 20 %/mT selon la taille de la vanne de spin, tandis que les niveaux de bruit sont de l'ordre de 1 nT/$\sqrt{Hz}$ à 1 kHz. Dans la bande de fréquence inférieure [1 Hz - 1 kHz], la composante de bruit dominante est celle du bruit dit en 1/f. Une technique de modulation fut développée durant cette thèse afin de réduire ce bruit basse fréquence et ainsi augmenter la détectivité des capteurs dans cette bande de fréquence d'intérêt central en neuroscience.

Le troisième chapitre présente une expérience *in vitro* de mesure du champ magnétique généré par un potentiel d'action basée sur des capteurs GMR. Ces mesures ont été réalisées en collaboration avec l'équipe UNIC (Unité de Neurosciences, Information et Compléxité) du CNRS. Le système biologique choisi est le muscle soléaire de souris, qui présente beaucoup de caractéristiques favorables à une première validation de ce genre de mesure. Il est constitué d'environ 800 fibres musculaires alignées parallèlement, innervées chacune en leur centre par une seule synapse excitatrice. Le potentiel d'action est déclenché dans le nerf par une impulsion électrique puis se propage jusqu'à la jonction neuromusculaire au centre du muscle et génère deux potentiels d'action se propageant symétriquement vers les deux extrémités. Les courants axiaux générés par la propagation de ces potentiels d'action génèrent un champ magnétique détectable en positionnant le muscle sur des capteurs GMR dont le design est adapté à la taille du système (1 mm * 10 mm). Les signaux magnétiques enregistrés représentent une variation biphasique de 2,5 nT d'amplitude sur une durée d'environ 4 ms. Ces courbes ont été obtenues après un moyennage sur 500 stimulations et présentent un rapport signal sur bruit de l'ordre de 10. Trois mesures de contrôles ont permis de vérifier la véracité de ces enregistrements. Tout d'abord, la même mesure fut réalisée en coupant le courant d'alimentation de la vanne de spin. Ainsi, toute variation de résistance dûe à un champ magnétique est supposée disparaître, contrairement à un artefact dû au couplage capacitif à travers la solution conductrice dans laquelle le muscle est immergé. Une nouvelle mesure fut enregistrée en positionnant le muscle à 90 degrés par rapport au capteur, afin que les lignes de champ magnétique ne soient plus orientée selon la direction de sensibilité de la vanne de spin. Enfin, une dernière vérification fut mise en oeuvre en mesurant le signal après avoir injecté une dose de curare dans le bain afin de bloquer la propagation du potentiel d'action au niveau de la jonction neuromusculaire. Dans les trois cas, ces expériences furent concluantes, permettant d'affirmer respectivement que le signal mesuré est bien dû à un champ magnétique, créé par des courants axiaux le long des fibres musculaires, eux-mêmes dûs à la propagation du potentiel d'action. Par ailleurs les modèles théoriques développés sont en accord avec les mesures expérimentales, suggérant notamment que près de 75% du champ magnétique généré par les courants axiaux est écranté par les courants de retour dans le milieu extra-cellulaire. Toute cette étude valide l'utilisation de capteurs GMR pour la mesure de signaux biomagnétiques et fut publiée dans *Scientific Reports*.

Le quatrième chapitre est consacré aux mesures *in vivo* réalisées dans le cortex visuel de chats et présente les premières signatures magnétiques intra-corticales de potentiels d'action. Ces mesures ont été réalisées en collaboration avec le groupe du Professeur Pascal Fries de l'Ernst Strüngmann Institute de Francfort. Pour cela, des capteurs GMR de (3µm*50µm) ont été déposés à l'extrémité de pointes d'une finesse et d'une épaisseur de 200 µm, afin d'obtenir l'équivalent magnétique des électrodes traditionnelles. Ces *magnetrodes* doivent être suffisamment robustes pour résister à l'insertion dans le cortex, et suffisamment fines pour créer le moins de dommage possible au niveau des neurones corticaux. Une électrode de tungstène est placée sur la *magnetrode* de façon à mesurer le potentiel local au plus près du capteur GMR. La pointe est insérée dans le cortex visuel, dont la profondeur est de l'ordre de 1,6 mm, puis une stimulation visuelle est appliquée durant 1 seconde via un écran placé face au chat. La stimulation génère une augmentation de l'activité neuronale dans le cortex visuel, facilement mesurable électriquement par l'électrode placée dans le milieu extra-cellulaire. Le nombre de potentiels d'action enregistrés passent de 30 spikes/sec à environ 200 spikes/sec. Un enregistrement typique correspond à 1000 stimuli de 1 seconde, séparés par un délai de 2 secondes et d'un délai aléatoire pour éviter l'adaptation neuronale. Le traitement des données enregistrées permet ensuite d'extraire le signal magnétique de la façon suivante. Chaque spike enregistré par l'électrode est assez facilement extractible grâce à un bon rapport signal sur bruit. Environ 40 000 spikes sont ainsi extraits selon leur polarité positive ou négative, centrés sur une fenêtre de 10 ms, puis moyennés. Le spike moyen présente une amplitude de 40 μV. Pour chaque spike électrique, le signal magnétique mesuré par le capteur GMR est enregistré sur la même fenêtre de 10 ms. Le fait de moyenner 40 000 fois ces acquisitions permet de diminuer le bruit d'un facteur 200, pour atteindre environ 0,4 nT. Un signal magnétique de 1,2 nT d'amplitude, durant 0.4, msapparaît alors clairement hors du bruit. Ce signal magnétique change également de polarité lorsque la polarité des spikes électriques s'inverse. Son origine magnétique est confirmée par le même contrôle que lors des expériences *in vitro*: lorsque le courant dans le capteur est nul, le signal magnétique disparait. Ce résultat représente la première mesure magnétique *in vivo* intra-corticale de potentiels d'action. Cependant, ce résultat pose plusieurs questions et ouvre beaucoup de perspectives: sachant que la modélisation est beaucoup plus complexe que le modèle du muscle squelettique présenté précédemment, il est difficile de prévoir l'amplitude et la durée du signal. Le nombre de neurones participant à ce signal est également difficile à estimer, étant donné la distribution continue de l'amplitude des spikes mesurés. Néanmoins, des avancées peuvent être réalisées à plusieurs niveaux: la sensibilité des capteurs peut être augmentée en utilisant le phénomène de magnétorésistance tunnel (TMR) et en réduisant leur bruit basse fréquence par la technique de modulation présentée au chapitre 2. Des *magnetrodes* comportant plusieurs vannes de spin (ou TMR) et plusieurs électrodes intégrées le long de la pointe permettront de faire des mesures laminaires dans la profondeur du cortex et d'avoir une cartographie des potentiels et des courants bien plus précise. Par ailleurs, une mesure simultanée du signal magnétique local via des *magnetrodes* et du signal magnétique mesuré en MEG via un SQUID permettrait d'affiner la résolution du problème inverse. Enfin, une micro-bobine pourrait être intégrée sur la pointe de la *magnetrode* et ainsi stimuler localement une population de neurones via des impulsions de champ magnétique. Ce projet a été abordé au début de cette thèse et fait l'objet du dernier chapitre.

Ce cinquième et dernier chapitre de cette thèse présente les travaux dont l'objectif était de stimuler localement une population de neurones via une impulsion de champ magnétique. Si la stimulation électrique est aujourd'hui largement utilisée pour le traitement de maladies neurodégénératives, elle présente plusieurs inconvénients (faible contrôle des champs électriques, inflammation des tissus, rejet de l'électrode par la cellule). La stimulation magnétique s'affranchit de ces effets mais cette solution n'a été mise en œuvre qu'à l'échelle cérébrale, par la stimulation transcrânienne (TMS). L'objectif est de développer des micro-inducteurs capables de générer un champ électromagnétique suffisamment important pour induire une réponse des quelques neurones ciblés. Les travaux présentés jusqu'à présent dans ce domaine mettent en œuvre des bobines de dimensions de l'ordre du centimètre qui génèrent des champs magnétiques et électriques beaucoup plus intenses (environ 2 Tesla et 100 V/m). Un seul groupe a fait état, en 2012, de stimulation magnétique à une échelle micrométrique, en utilisant des inducteurs de 500 µm de diamètre. Un code de simulation numérique pour étudier l'influence des différents paramètres (rayon, longueur, nombre de spires), ainsi que pour calculer les champs créés dans tout l'espace en s'adaptant à la géométrie des inducteurs fabriqués a été développé. En collaboration avec le groupe UNIC du CNRS, une première expérience de stimulation *in vitro* sur une tranche d'hippocampe a été mise en place. Cette expérience consiste à placer la bobine, de 5 mm de rayon, au plus près des neurones, tout en enregistrant électriquement leurs réponses via une électrode plongée dans le milieu extra-cellulaire. Les neurones étant sensibles uniquement au champ électrique, il est nécessaire de fournir des impulsions de courant générant un champ magnétique variable pour engendrer des courants induits dans le milieu cellulaire. Pour cela un condensateur de grande capacité est déchargé directement dans la micro-bobine. Ces impulsions génèrent à la fois un artefact de stimulation mesuré par les électrodes ainsi qu'un artéfact dû aux vibrations de la bobine durant la décharge. Les dernières expériences donnent plusieurs pistes d'amélioration du système, afin notamment de s'affranchir des artéfacts et de mesurer en temps réel l'évolution du potentiel de membrane d'un neurone soumis à la stimulation magnétique locale.

Contents

Introduction

> *La culture, c'est ce qui répond à*
> *l'homme quand il se demande ce*
> *qu'il fait sur terre.*
>
> André Malraux

Understanding the genesis of our intellectual faculties and of our emotions is one of the most challenging tasks for scientists to take up. This ambitious goal can only be achieved by bridging gaps between different areas of science. The various backgrounds of neuroscientists, clinicians, physicists, and engineers span a diversity of approaches, and connecting them efficiently is of key importance to achieve major breakthroughs.

Research in electroencephalography (EEG) and magnetoencephalography (MEG) illustrates very well this point. There is a need to overcome the barriers that stand in the way of a fruitful communication between a physicist and a prospective physiologist. However, both have to deal with a very complex inhomogeneous system, where non-linear processes unfold. While the first is used to describe physical phenomena with concise equations, the latter takes advantage of a large amount of data output to develop models in the light of experiments. Even if physics is in essence an experimental science, the theoretical framework leading to perform an experiment often needs to be clearly defined. Fortunately, EEG and MEG specialists have not always followed this path. They have been able to carry out groundbreaking experiments without a prior complete modeling exercise. A relevant example is the observation of spontaneous activity, such as alpha rhythm (8 - 13 Hz) present in a subject with eyes closed, or the detection of epileptic seizures. Anyway, scientists are striving more than ever for improved tools to measure brain activity. This great enthusiasm will certainly persist, until light is shed through what Paul Nunez [9] calls the *window on the mind*.

This thesis aims at providing one of these tools. A wide range of techniques to record electrical activity are successful, spanning from the micro-scale (single ion channel), to the meso-scale (Local Field Potential), up to the brain macro-scale (EEG). Current sensors used in MEG are very sensitive but cannot be miniaturized. Moreover, they operate at a very low temperature, which is prohibitive for any contact with living tissue. These are the main reasons why biological magnetic fields have not been measured at the neuronal scale so far. Yet, having a magnetic counterpart of the traditional micro-electrode would represent a step forward towards the investigation of local sources of neuronal magnetic activity.

Before embarking on such a project, it is definitely essential to analyze the path that was taken by scientists since the very early times. To build this technology up, we benefited from a deep understanding of the principles of electromagnetism, developed during the XIX century, and also from the more recent discoveries in quantum physics. If the brain is still fascinating people nowadays, it is worth noting that the attraction between two magnets was also considered as a mysterious phenomenon for centuries. The major steps taken over two thousand years are described below. Assessing how far we have come, from considering magnetism as a divine power to the rigor of Maxwell's equations, might be an example for other areas of science.

The discovery of magnetism is lost in the past of Ancient Greece, but the earliest known mention is attributed to Thales of Miletus (-625 BC ; -546 BC). The attraction between naturally magnetized pieces of magnetite, called lodestone, and small pieces of iron has fascinated Thales and many philosophers like Plato (-428 ; -348), Aristotle (-384 ; -322) and Lucretius (-99 ; -54). Magnetite is a ferrimagnetic mineral that forms during volcanic eruption when liquid iron gets oxidized in contact with air. Its remanent magnetization is caused by the Earth's magnetic field that polarizes the stone throughout its cooling. Lucretius, in *De Natura Rerum*, confirmed that the name "magnetite" was attributed in reference to Magnesia, a city that owes its name to *Magnes*, son of Zeus and Thyia.

Following this golden Hellenic era, it took several centuries until a renewed scientific interest. The french Pierre de Maricourt wrote in 1269 the first treaty describing the laws of magnetic attraction and repulsion, *Epistola de magnete*. As a military engineer, he was obviously interested in the issues of compass, a strategic tool of key importance for the navy. The work of de Maricourt was acknowledged by the one who stands as one of the pioneer of experimental science, William Gilbert. He published *De Magnete* in 1600, after twenty years of various experiments. He set himself the objective to remove any doubts concerning magnetic phenomena, especially chasing all the superstitions which prevailed at the time. Plenty of experiments on a sphere-shaped magnet led him to conclude that the Earth was itself a magnet, and deduced why the compass needle points directly at the north pole. He was also able to separate the electrostatic attraction of amber from the magnetic attraction of lodestones, laying out the very first electricity basics.

Despite the success of Gilbert's work, the main obstacle in the development of a complete electromagnetic theory was the lack of a continuous source of electricity. The triggering event that led the physicist Alessandro Volta to the discovery of the voltaic pile was a lively debate with a... biologist! Luigi Galvani, anatomist at the university of Bologna, published *De viribus electricitatis in moto musculari* in 1791. He had observed that the contact between his scalpel and the crural nerve of a dead frog induced a contraction, at the exact moment when an electric spark was generated in close vicinity. Amazed by this fortuitous event, Galvani shifted the experiment on the roof of his house to check the twitch response of the muscle being struck by lightning. The experiment met his expectations, but, more importantly, he discovered that the mere contact between the copper hook, connected to the spinal cord, and the iron balustrade induced the same response without any lightning bolt. After this finding, Galvani coined the term "animal electricity". However, Volta was convinced that the electric source was not the muscle, but was generated by the contact between the two different metals. His will to rule out the theory of Galvany led him to produce, in 1800, a stack of copper and zinc discs, on top of each other, separated by a layer of cardboard soaked in saline water. This invention, still known as the voltaic pile, provided scientists a continuous stable current source, giving rise to the upcoming electromagnetic revolution.

The starting gun was fired in 1820 in Copenhagen. Hans Christian Oersted, a Danish physicist, was giving a lecture on electricity at the University. Switching on a battery to supply a circuit, he noticed that the compass needle deflected from the North pole when current was flowing through the wire. The providential circumstances of this discovery has been disputed; anyhow, the intimate relation between electricity and magnetism was demonstrated for the very first time. Beyond the tremendous impact of this discovery, it was the first ever example of the conversion of electrical energy to mechanical energy, which is still largely present in our daily life. Oersted's experiment spread over Europe, especially in France, after being presented to the Academy of Sciences by Francois Arago. One of his colleague, André Marie Ampère, a brilliant mathematician, promptly took charge of this issue that just begged to be formalized. Besides, Ampère demonstrated the equivalence between a magnet and a solenoid supplied by an electric current. Inspired by the work of his French peers, Michael Faraday, made an essential contribution despite his unusual academic trajectory. Born into a poor family, he started working at the age of 14 in a bookstore, and he first began doing science at 22. As a gifted experimentalist, he observed the opposite phenomenon to Oersted, the electromagnetic induction. By moving a magnet inside a coil, he measured an induced current in the coil, creating the first dynamo, the starting point of a thriving industrial sector. Through his remarkable work, Faraday highlighted the fact that electromagnetic field lines are curved. This concept of field was in contrast with the acknowledged point of view of Newton, whose gravitation theory implies that forces act through straight lines. At that time, such a discovery could certainly not have been possible by a university-trained scientist confined to the traditional system of thought.

The mathematical synthesis that was going to conclude this successful XIX century was achieved by James Clerk Maxwell [6]. Elegant and concise, his set of equations embodied the novel idea that electric and magnetic fields travel through space as waves, moving at the speed of light. Henceforth, these equations form the complete basis of classical electromagnetism, giving masterly the final touch to this scientific adventure. At the beginning of the XX^{th} century, Max Planck, a German theoretical physicist, proposed, as a solution to the black-body radiation problem, that energy exchanges between electromagnetic radiation and matter were quantized. This conceptual upheaval led to the development of quantum mechanics, whose success has not been denied so far. Its story is punctuated by numerous great ideas, ingenious experiments, and philosophical debates, that makes it much too long to be discussed here.

As stated above, the magnetic sensors developed in this work are based on a quantum effect, discovered in 1988 and detailed later in the text. However, although quantum mechanics is needed to describe the behavior of atomic-scale devices, biological systems of the dimensions of neurons must be analyzed with classical electromagnetism due to their complexity. Fortunately, in the realm of electro-magneto-physiology, quantum effects such as superpositions of states, wave-particle duality, and the uncertainty principle, are negligible. These approximations offer welcome determinism when one wants to measure current or cellular potential. Nevertheless, the question about the role of quantum mechanics in biological processes is still open. A few recent studies showed the occurrence of quantum process in organisms that undergo photosynthesis, so that they harvest light-energy efficiently [4, 10]. The current controversy on the mechanisms underlying magnetoreception is another obvious example. It is well known that the Earth's magnetic field guides millions of birds and many other species during their seasonal migration. Several models with different biochemical magnetoreceptor candidates have been proposed, notably magnetite-based [8], which were quickly ruled out [12], and proteins being magnetically sensitive to photochemical reactions [5, 11], also contradicted recently [7]. More generally, even if we are still far from a molecular compass, studying the effects of a magnetic field on neuronal activity is of great interest, and that is what the last chapter of this thesis is dedicated to. Indeed, when one tries to detect a magnetic field of biological source, one of the first questions that arise is how the neurons themselves are influenced, or even triggered, by an external magnetic field. In order to try to clarify these points, here is how this manuscript is organized.

The first chapter is dedicated to the state of the art in magnetophysiology. The first thing is to presents the basics of the earliest technique, magnetoencephalography (MEG). The invention of the Superconducting QUantum Interference Device (SQUID) in the 1960s, led to extensive development of MEG. The essentials aspects of MEG instrumentation, modeling and clinical applications will be presented, along with the latest advances, such as "on-scalp MEG", a new measurement technique based on optically-pumped magnetometers. As the purpose of this work is to measure the magnetic signature of brain activity at the neuronal scale, the theoretical framework will be set to specify the differences between MEG and a local recording. In this sense, a few attempts have been made recently, using other technologies such as sensors based on nitrogen-vacancy (NV) quantum defects in diamond. A description of the state of the art concerning this local magnetic recording field will be provided.

The second chapter presents the technologies used and developed in this thesis. As stated above, one of the sensor that offers sufficient sensitivity for the detection of the very weak magnetic fields emitted by currents flowing into neurons is the SQUID. Placed outside the skull and cooled down at liquid Helium temperature, this kind of a magnetometer is able to detect MEG signals, typically in the range of 10^{-14} to 10^{-12} Tesla. However, the distance between the source of the magnetic field, the cortical neurons, and the sensor, is about 3-5 cm, because of the required thermal insulation layer of the Helium Dewar, and the thickness of both the skull and the scalp. Assuming that a magnetic sensor could be inserted in the very vicinity of neurons, the expected measured amplitude would be a few orders of magnitude higher. This claim requires to have a micron-sized, non-cooled and needle-shaped magnetic sensor. The only technology that meets all these requirements at once is based on the magnetoresistance effect. This term refers to a structure whose resistance varies according to the external magnetic field. The fundamental physical principles underlying this effect will be presented, without delving deeply into quantum processes, as well as several milestones achieved in different fields of science since the discovery of this effect. This effect would not have been highlighted without significant advances in micro-fabrication techniques. A paragraph will be dedicated to the manufacturing process that was conducted to obtain a functional tool. The sensitivity of the sensor was tested, and, finally, an original method to reduce the low-frequency intrinsic noise of this kind of a sensor is proposed.

The third chapter reports the first *in vitro* experiments conducted with these magneto-resistive sensors. A complete study of the magnetic signature generated by an action potential (AP) propagating along the soleus muscle of a mouse is provided. Among many other advantages, this simple nerve-muscle biological structure allows for reliable modeling. The great agreement between theoretical expectations and measured magnetic signals led to the validation of the proposed technology. All these experiments were performed as a cooperation with the "Unité de Neurosciences, Information et Complexité" (UNIC) of the CNRS, within the group of Professor Alain Destexhe.

The fourth chapter is dedicated to the very first *in vivo* magnetic recording of neuronal activity. Experiments with *magnetrodes*, the magnetic counterpart of usual electrodes, in visual cortex of a cat are reported. *Magnetrodes* are custom-made needle-shaped devices, so that they can be inserted into the cortex without substantially damaging the neuropil. The applied visual stimuli elicited event-related magnetic fields which have been measured, making this experiment the first proof of concept for *in vivo* recording of neuronal activity inside the cortical layers. A total of three sessions of *in vivo* experiments were performed, at the "Ernst Strüngmann Institute" (ESI) in Frankfurt, within the group of Professor Pascal Fries.

The fifth and final chapter of this thesis investigates a new kind of magnetic stimulation technology. Through the first four chapters, the common thread was to produce miniaturized sensors to detect the magnetic field emitted by neurons. However, it is a great deal of interest to explore how a magnetic field could influence the behavior of a neuron. The current technology, called transcranial magnetic stimulation (TMS), has become an important routine tool since the first successful attempt on brain tissue in 1985 [1]. When combined with a measurement technique, such as EEG, TMS can provide information about connectivity between brain regions, and can also indicate cortical excitability of a specific brain area. Based on the Faraday's law of induction, TMS requires magnetic field pulses of up to 2 to 3 tesla [3], which implies huge current discharges in centimeter-sized coils. In line with the perspective pursued through the development of micron-sized sensors, the possibilities of scaling down a magnetic stimulation system were investigated. A first attempt, published in 2012 [2], guided this part of the thesis, although it has led to disparate results. A local magnetic stimulation (LMS) system could be encapsulated with biocompatible materials, ruling out the need of an electric contact with the tissue, and allowing an implant in the vicinity of the targeted cells. In the long run, this technology could result in advances in the treatment of a wide range of neurological diseases.

Throughout this manuscript, several physical and biological concepts will be addressed, with a viewing angle that should allow people from both communities to appreciate every detail. Wishing you a pleasant reading.

Bibliography

[1] Barker, A. T., R. Jalinous et I. L. Freeston. 1985, «Non-invasive magnetic stimulation of human motor cortex», *The Lancet*, vol. 325, no. 8437, p. 1106–1107. 6

[2] Bonmassar, G., S. W. Lee, D. K. Freeman, M. Polasek, S. I. Fried et J. T. Gale. 2012, «Microscopic magnetic stimulation of neural tissue», *Nature communications*, vol. 3, p. 921. 7

[3] Ilmoniemi, F. J., J. Fuohonen et J. Karhu. 1999, «Transcranial magnetic stimulation–a new tool for functional imaging», *Critical Reviews" in Biomedical Engineering*, vol. 27, no. 3-5, p. 241–284. 7

[4] Lambert, N., Y.-N. Chen, Y.-C. Cheng, C.-M. Li, G.-Y. Chen et F. Nori. 2013, «Quantum biology», *Nature Physics*, vol. 9, no. 1, p. 10–18. 4

[5] Maeda, K., K. B. Henbest, F. Cintolesi, I. Kuprov, C. T. Rodgers, P. A. Liddell, D. Gust, C. R. Timmel et P. Hore. 2008, «Chemical compass model of avian magnetoreception», *Nature*, vol. 453, no. 7193, p. 387–390. 5

[6] Maxwell, J. C. 1865, «A dynamical theory of the electromagnetic field», *Philosophical transactions of the Royal Society of London*, vol. 155, p. 459–512. 4

[7] Meister, M. 2016, «Physical limits to magnetogenetics», *Elife*, vol. 5, p. e17 210. 5

[8] Mora, C. V., M. Davison, J. M. Wild et M. M. Walker. 2004, «Magnetoreception and its trigeminal mediation in the homing pigeon», *Nature*, vol. 432, no. 7016, p. 508–511. 5

[9] Nunez, P. L. et R. Srinivasan. 2006, *Electric fields of the brain: the neurophysics of EEG*, Oxford University Press, USA. 1

[10] O'Reilly, E. J. et A. Olaya-Castro. 2014, «Non-classicality of the molecular vibrations assisting exciton energy transfer at room temperature», *Nature communications*, vol. 5. 4

[11] Qin, S., H. Yin, C. Yang, Y. Dou, Z. Liu, P. Zhang, H. Yu, Y. Huang, J. Feng, J. Hao et collab.. 2016, «A magnetic protein biocompass», *Nature materials*, vol. 15, no. 2, p. 217–226. 5

[12] Treiber, C. D., M. C. Salzer, J. Riegler, N. Edelman, C. Sugar, M. Breuss, P. Pichler, H. Cadiou, M. Saunders, M. Lythgoe et collab.. 2012, «Clusters of iron-rich cells in the upper beak of pigeons are macrophages not magnetosensitive neurons», *Nature*, vol. 484, no. 7394, p. 367–370. 5

Chapter 1

Brain Imaging and Magnetophysiology

> *It is one of the most exciting times to be a neuroscientist, only because the techniques have finally caught up with the complexity of the problem*
>
> Pr. Arthur Toga

Contents

1.1 Large-scale brain imaging

1.1.1 Basics of brain imaging

1.1.1.1 Structural imaging

Until the end of the XIX century, the only source of information about the brain structure was to perform post-mortem examination. A French anatomist, Paul Broca, provided the very first evidence of localization of a brain function in 1861 [9]. After having performed an autopsy of a patient who had suffered from a progressive loss of the ability to speak, he observed a lesion in the frontal lobe of the left cerebral hemisphere. This experiment supported the involvement of this brain area with language capacity, and, therefore, this region was named after him. Broca's experiment led the way to *structural* imaging, the field that encompasses every technique aiming at localizing the different parts of the central nervous system.

Nowadays, the main technique for structural imaging is based on nuclear magnetic resonance (NMR). The high concentration of hydrogen atoms in biological tissues, enables a precise 2D or 3D mapping during a magnetic resonance imaging (MRI) scan. When exposed to a strong static magnetic field, the magnetic moments of these hydrogen nuclei line up in a parallel formation. Then, this equilibrium is disturbed by sending pulses of radio waves. Magnetic moments return to alignment while emitting a measurable electromagnetic signal, whose decay rate depends on the type of tissue. From a given disorder and the observation of a MRI image of a brain injury, a physiologist can deduce the function of the damaged area. However, the strength of the static magnetic field (from 1,5 T to 7 T) and its uniformity (10-100 ppm homogeneity) imply the use of onerous equipments. The unit price of a MRI system hovers around 1 million euros per Tesla. Thus, several attempts to perform low-field or ultra-low field MRI have been reported [36, 45]. Despite the reduction of amplitude of the signal of interest, performing low-field MRI or ultra-low-field MRI could provide many advantages: an open system ideal for claustrophobic patients, allowing babies and even patients who have metallic implants to be scanned.

The continuous improvement of MRI systems allows to distinguish precise differences between patients. For example, a recent study focused on the evolution of the size of the hippocampus - a part of the brain involved in spatial memory - between London taxi drivers and control subjects. The results showed that the posterior hippocampus volume correlates with the time spent as a taxi driver [35]. This illustrates

Figure 1.1: MRI system (source : Philips Healthcare) and sagittal section of a human brain via magnetic resonance imaging

very well the phenomenon of neuroplasticity, the capacity of the brain to adapt itself in response to environmental constraints and needs. Despite the efficiency of structural imaging, the possibility to measure directly which parts of the brain process given information is also of great interest. This is referred to as *functional* imaging, on which a particular emphasis will be placed here.

1.1.1.2 Functional imaging

In 1875, Richard Caton proved the existence of electric currents in the brain of monkeys by positioning one electrode on the gray matter and the other one on the surface of the skull [15]. Caton's experiments laid the foundation for *functional* measurements, which consist of the instantaneous identification of the activity of a brain area associated with a given function that can be activated by a specific stimulus. Since then, many imaging techniques have been developed to be able to extract clean signals, and to understand the correlations between them and the underlying brain processes. Among all of the functional imaging techniques, we can differentiate between hemodynamic and electromagnetic ones.

Hemodynamic techniques

Hemodynamic techniques are based on the fact that an increase of neuronal activity will generate a larger demand for oxygen and glucose, inducing more cerebral blood flow to the active region. Recording these changes associated with blood flow can be made by functional magnetic resonance imaging (fMRI) or by positron emission tomography (PET). The large amount of oxygen, brought to firing neurons of a specific area, creates a relative change of the concentration between oxygenated blood cell (oxyhemoglobin) and deoxygenated blood cell (deoxyhemoglobin). Since the magnetic properties of a blood cell depend on whether it carries an oxygen molecule, this relative change creates a blood-oxygen-level dependent (BOLD) signal that can be detected by MRI. This technique achieves a good spatial resolution of 1 mm, but the temporal resolution, around 1 second, does not allow to reconstruct the chronology between different activation patterns associated with different stages of stimulus processing. Positron emission tomography consists in measuring blood flow variations by means of the injection of a radioactive tracer, injected into the bloodstream before scanning the patient. Usually, fluorine-18 (^{18}F) is chosen because of its short half-life (109 min) and its high rate of positron emission during decay, yielding stable oxygen-18 [16]. This radioisotope is synthesized into fluorodeoxyglucose that binds to tissues which have a high glucose consumption; tumors, cardiac muscle, and active parts of the brain. Once administrated to the patient, the radioisotope emits positrons that will collide with electrons after a traveling distance shorter than 1 mm. During the collision, the two particles annihilate each other, and produce two photons traveling in opposite directions. These electromagnetic radiation are detected externally by a scintillator and are used to measure both the quantity and the location of the positron emitter. As a functional imaging tool, PET is particularly efficient for the diagnoses of dementia due to progressive neurodegenerative diseases, such as Alzheimer disease [41, 47]. Compared to fMRI, despite the invasiveness of the injection of radioisotopes, PET imaging benefits from a wide range of tracers that allow to target specific tissues, especially in cancer research.

Electromagnetic techniques

The temporal resolution of hemodynamic techniques are intrinsically limited by the slow flow of blood through the brain. Furthermore, they do not measure directly neuronal activity but a relative variation of the metabolic response due to this activity. Since neurons communicate by sending each other tiny electric pulses, detecting the electromagnetic field induced by these movements of charges would give a direct and quasi-instantaneous information on the ongoing neuronal process.

After Caton's first experiments, a German psychiatrist, Hans Berger, published in 1929 the first article about recording of the electric potential oscillations of human brain [5]. He coined the term *electroencephalogram* (EEG), and observed the first rhythmic activity, the *alpha* waves, in a specific frequency range (**8 - 13**) Hz. Being able to record dynamic brain behavior, with a non-invasive and painless technique has constituted an important step forward in neural science.

During an EEG measurement, the scalp is covered with about twenty to two hundred electrodes, whose size range from 0.5 to 1 cm. However, one electrode collects information coming from millions of neurons firing in synchrony. It is generally assumed that most of the EEG signal comes from the activity of cortical neurons that are packed up to 10^5 per mm^3 [51]. This high density, compared to the surface area of the electrodes, illustrates the difficulty to achieve a good spatial resolution. Moreover, even if one could imagine a set of infinitely small electrodes, the current would still be strongly distorted and filtered when spreading through the several layers of the head volume conductor, such as the cerebrospinal fluid, the meninges, the skull and the scalp. The positive counterpart is that EEG signals do not depend strongly on the size of the electrodes, unlike other micro-scale electrophysiology experiments. In addition, the study of cognitive processes is based on large-scale recordings, when thousands of neurons of a given area generate a coherent response. It seems intuitive that an intracranial microelectrode will be only sensitive to local fluctuations of a small group of neurons and will not give a global realistic picture of the dynamic behavior of the brain.

Magnetoencephalography (MEG) refers to in recording the magnetic counterpart of the EEG signals. The theory of electromagnetism indicates that EEG and MEG signals are closely connected, as they are generated by the same synchronized neuronal processes. Each method described so far has its own strengths and weaknesses; this is why multimodal imaging, the combination of several techniques for solving the source localization problem, is being investigated more and more. Existing EEG and MEG systems enable measurement of both electric potential and magnetic field at the brain scale. However, at the cellular level, there is no such "magnetic electrode" that could complement the set of tools developed so far by electrophysiologists. As this work aims at providing a new kind of sensor, in order to detect the magnetic field at the neuronal scale, the following section will emphasize the theoretical framework and the instrumentation of MEG. Making the link between these brain-scale recordings and intracranial information will not be a trivial issue, but getting access to local magnetic recordings would be of key interest to propose further signal correlations.

1.1.2 Magnetoencephalography

1.1.2.1 Magnetic fields of the brain

Before depicting the sensors used for MEG experiments, it is worth trying to understand how the location and time-varying strength of the sources is deduced from a typical

MEG measurement. Reconstructing the current distribution underlying a given recording is called the *inverse problem*. Generally, in the field of physics, inverse problems are not what the French mathematician Jacques Hadamard called "well-posed problems" [23]. A mathematical model of a physical phenomenon should have the three following properties: a solution exists, the solution is unique, and the solution doesn't change dramatically with a slight modification of initial conditions. Concerning MEG, it was shown by Helmholtz, as early as in 1853, that an infinite number of current distributions could generate a given magnetic field outside a conductive body. Theoretically, assuming a spherical conducting volume, any radial current source can be added to a given solution of the inverse problem without consequence. Therefore, the MEG inverse problem is an "ill-posed" problem. There is no unique solution, and it has to be confined to a restricted range of configurations.

On the other hand, the *forward problem* consists of computing the magnetic field that would be created by the electric activity of certain area of the cortex. Forward problem has a unique solution which is needed to solve the inverse problem. Many mathematical models have been developed to solve both forward and inverse problem [29, 43], but they won't be described here. However, it is worth introducing the basic assumptions that are usually made to simplify the modeling.

Quasi-static approximation

As stated earlier, Maxwell unified electric and magnetic phenomena in a set of equations (1.1). It is considered that electric field **E** is produced by stationary charges (charge density ρ), while magnetic field **B** is due to moving charges (current density **J**). Nevertheless, stationarity and movement depend on the chosen frame of reference. This is what is highlighted by Maxwell's equations: both electric and magnetic fields are linked, one being the time-derivative of the other. A variation of electric field induces a magnetic field and vice versa. In these equations, ε_0 is the permittivity of free-space, μ_0 the magnetic permeability of free-space. Bold letters are used to represent vectorial quantities.

$$\left\{\begin{array}{rcl} \nabla\cdot\mathbf{E} & = & \frac{\rho}{\varepsilon_0} \\ \nabla\times\mathbf{E} & = & -\frac{\partial\mathbf{B}}{\partial t} \\ \nabla\cdot\mathbf{B} & = & 0 \\ \nabla\times\mathbf{B} & = & \mu_0\mathbf{J}+\varepsilon_0\mu_0\frac{\partial\mathbf{E}}{\partial t} \end{array}\right. \tag{1.1}$$

Neuronal processes generate electromagnetic fields whose frequency can reach about 1 kHz. These processes will be described in more details, at the cellular level, in the next section. Adopting the quasi-static approximation means that, for this range of frequencies, electric fields and magnetic fields are considered uncoupled. The two source terms varying as $\partial/\partial t$ are neglected, just like it was considered before Maxwell's breakthrough. This approximation greatly simplifies the modeling, so it has to be justified, by putting numbers [25], to estimate its validity.

Let's consider an electric field $\mathbf{E}$ in the brain, varying at a given frequency $f = 1$ kHz:

$$\mathbf{E} = \mathbf{E_0} \exp\left(j 2\pi f t\right) \tag{1.2}$$

The current density $\mathbf{J}$ is deduced both from the Ohm's law by taking a typical value for the macroscopic tissue conductivity $\sigma = 0.3$ S/m, and by adding the contribution due to the variation of the polarization $\mathbf{P}$ in the material. The polarization is assumed to be proportional to the electric field; hence $\mathbf{P} = (\varepsilon - \varepsilon_0)\mathbf{E}$. ε_0 is the permittivity of vacuum and ε the one of brain tissues, around 10^5 times greater :

$$\mathbf{J} = \sigma \mathbf{E} + \frac{\partial \mathbf{P}}{\partial t} = \sigma \mathbf{E} + (\varepsilon - \varepsilon_0)\frac{\partial \mathbf{E}}{\partial t} \tag{1.3}$$

The combination of the Maxwell-Ampere equation 1.1 and 1.3 gives :

$$\nabla \times \mathbf{B} = \mu_0 \sigma \mathbf{E} + \mu_0 \varepsilon \frac{\partial \mathbf{E}}{\partial t} \tag{1.4}$$

It needs to be emphasized that the permeability of the tissues in the brain is the same as the vacuum permeability μ_0 [53]. This is why the magnetic field doesn't undergo distortions when propagating between the sources and the sensor. Equation 1.4 gives the boundary condition for the quasi-static approximation:

$$\sigma \mathbf{E} \gg \varepsilon \frac{\partial \mathbf{E}}{\partial t} \Longrightarrow \sigma \gg \varepsilon 2\pi f \tag{1.5}$$

The values chosen above lead to $\varepsilon 2\pi f/\sigma = 0.02 \ll 1$. Similar reasoning proves that the source term in the Maxwell-Faraday equation of induction is also negligible in our case. Let's take the curl of both sides :

$$\nabla \times \nabla \times \mathbf{E} = -\frac{\partial}{\partial t}(\nabla \times \mathbf{B}) = -\mu_0 \frac{\partial}{\partial t}(\sigma \mathbf{E} + \varepsilon \frac{\partial \mathbf{E}}{\partial t}) \simeq -\mu_0 \frac{\partial}{\partial t}(\sigma \mathbf{E}) \tag{1.6}$$

This equation is similar to the one describing an undamped harmonic oscillator. The analog of the angular frequency of the oscillator, *i.e* the length scale of the system, is calculated via: $\lambda = (\mu_0 \sigma 2\pi f)^{-1/2} = 21$ meters. This result is three orders of magnitude larger than the distance between neurons and the sensors. That is why the use of the quasi-static version of Maxwell's equations is appropriate for handling the forward problem. Therefore, it is considered that the source term for the magnetic field generated on the scalp can be directly linked to the current inside the brain, without taking into account the consequences of high-frequency fields.

MEG sources

Each neuron communicates by sending electrical impulses to each other. Here is a simplified version of how neurotransmission occurs :

1. These pulses, called action potentials, propagate from the cell body along an axon towards its ends, the synaptic terminal.
2. When an action potential reaches a synapse, it triggers the release of neurotransmitter, that bind to the receptors of the target neuron.
3. These transmitter molecules activate specific ionic channels of the cell membrane, creating a flow of current inside and outside the post-synaptic neuron.
4. Depending on whether sodium channels or potassium and calcium channels are triggered, it generates positive or negative voltage variations of the membrane potential, called excitatory or inhibitory post-synaptic potentials (EPSP/IPSP).
5. When the sum of EPSPs and IPSPs coming from surrounding neurons reaches a certain threshold, the neuron fires an action potential that will travel along its axon.

Based on this description, one can discriminate between two categories of current sources in the brain (see Figure 1.2).

The first one, due to the post-synaptic potentials, is an intracellular longitudinal current within the dendrites, that may last tens of milliseconds. It is referred to as synaptic current or *primary current* $\mathbf{J_p}$. As synaptic currents are flowing through neighboring aligned cells, they can be modeled as an equivalent current dipole. A current dipole is a mathematical model that approximates a current density within a volume as a point source. This assumption is widely used in MEG, and is quite effective since the typical measurement distance is much larger than the characteristic size of the system.

The second category includes the two intracellular oppositely oriented currents due to the propagation of an action potential. Indeed, the leading edge of depolarization and the trailing edge of repolarization generate local opposite currents during the propagation of an action potential, which can be described as a quadrupolar source of magnetic field, decreasing quickly as $1/r^3$. It is also considered that transmembrane currents do not induce a significant magnetic field because of the cylindrical symmetry of an axon. Moreover, considering the short duration, around 1 ms, of an action potential, it is very unlikely to obtain a perfect synchrony of thousands of events that would make their global contribution close to a detectable level.

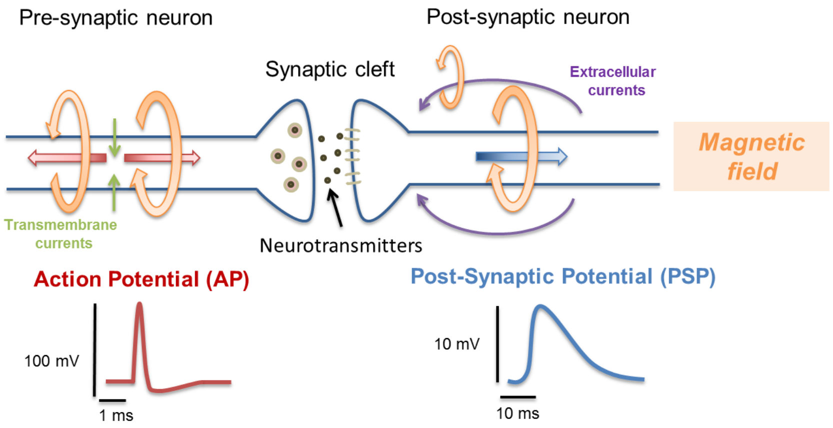

Figure 1.2: **Sources of magnetic field.** The propagation of an action potential induces two opposite intracellular currents (red arrows) and transmembrane currents (green arrows). Due to the cylindrical symmetry of the axon, the magnetic field produced by transmembrane currents cancels out. The magnetic field generated by intracellular currents can be seen as a quadrupole at large distance. Post-synaptic currents (blue arrow), are approximated by a dipole, and are considered as the main source of the signal measured in MEG. Purple arrows illustrate the return currents flowing back in the extracellular medium. They create a magnetic field that partially screens the field of interest. Adapted from [13].

This description would not be complete without applying the continuity equation for electric charges:

$$\nabla \cdot \mathbf{J} + \frac{\partial \rho}{\partial t} = 0 \tag{1.7}$$

This equation states that the amount of electric charges displaced by primary currents has to be compensated by charges flowing back through the extracellular medium. This loop of ionic flow is usually called return or volume currents. These currents cause voltage differences at the scalp surface that can be picked up by EEG electrodes. If one considers that neurons are embedded in an infinite, uniformly conductive medium, then the symmetric distribution of these return currents should results in no net magnetic field. Actually, the finite size of the brain implies to consider the distortions due to the boundary effects.

An important feature of the cortex to consider in MEG is its folded configuration. The cortical surface is made of ridges and furrows, respectively called gyri and sulci. Activation of neurons of a gyrus is modeled by a radial dipole, locally perpendicular to the scalp surface. In contrast, the current dipole associated to neuronal cells of a sulcus is oriented parallel to the said surface (see Figure 1.3).

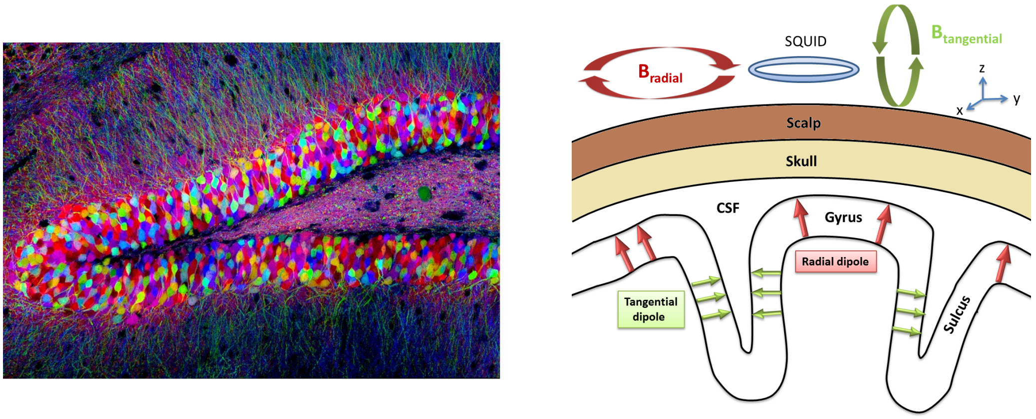

Figure 1.3: **Left:** Gyrus of a mice hippocampus imaged after labelling by fluorescent proteins, one can notice the precise alignment of the neurons (scale: 220 µm × 160 µm), from [52]. **Right:** Schematic of the folded cortical surface that induces radial (red arrows) and tangential (green arrows) equivalent current dipoles.

All the points raised so far aim at simplifying the source localization techniques. However, from a technological point of view, being able to detect a magnetic field intensity of around 100 femtoTesla is also a challenging task. For now, the great majority of MEG measurements have been made with superconducting sensors, named SQUIDs. Recently, there have been a few attempts to use optically-pumped magnetometers, which allow measuring closer to the sources, to do what is called "on-scalp MEG". Both of this techniques are presented below.

1.1.2.2 MEG with SQUIDs

The emergence of MEG happened in the early 1970's. Preliminary magnetic recordings of cardiac activity were published by Baule and McFee in 1963, using a 2 million-turn, hand-wound (!), induction coil [4]. Armed with his 1 million-turn coil, David Cohen, physicist at the Massachusetts Institute of Technology, demonstrated the first magnetic signature of alpha rhythm [19]. Four years later, he improved those results by taking advantage of both a strongly shielded room, and of the development by James Zimmerman [58] of a new kind of magnetometer : the Superconducting QUantum Interference

Device (SQUID) [18]. This was the very first step of MEG, followed by many contributions that always relied on Cohen's building blocks.

The SQUID is one of the most sensitive magnetic sensors. With a typical pick-up coil, it can achieve a sensitivity of 1 $fT/\sqrt{Hz}$. Most of contemporary MEG devices are based on array of up to 306 SQUIDs. For the interested reader, many papers propose a full physical approach of the effects underlying a SQUID [17]. Here, a simplified model is presented in order to understand how this device converts a magnetic flux to a measurable voltage.

DC-SQUID is made of a superconducting loop with a Josephson junction incorporated in both arms. A superconducting material shows both a complete loss of electric resistance when cooled below a critical temperature T_c, and perfect diamagnetism, *i.e* any external magnetic field is ejected from the material due to the circulation of a screening supercurrent. A Josephson junction consists of two superconductors coupled by a thin layer of an insulating material (S-I-S junction). When an external magnetic field flux passes through a superconducting loop, a screening current J flows into it without dissipation, so that the flux enclosed by the superconducting loop will be an integer number of magnetic flux quantum $\phi_0 = h/2e$, where h is Planck's constant and e the electronic charge. The two Josephson junctions impose a higher limit for the supercurrent that can be sustained without losing superconductivity: as soon as it becomes larger than a critical value I_c in either branch, the resistance is no longer zero and a voltage appears across the junction. The SQUID is supplied by a bias current just above I_c, so that any flux variation will lead to a voltage variation. The relation between the applied flux and the output voltage is non-linear and ϕ_0-periodic. However, for a standard design of SQUID, a typical MEG magnetic field intensity of 100 fT corresponds to a flux transfer of about $2.10^{-4}\phi_0$. In practice, a negative feedback is applied to obtain a linear response of the sensor.

The majority of SQUIDs used in MEG are made of Niobium (*Nb*), whose superconducting transition temperature is around 9.2 K. This property implies to keep the SQUIDs in a cryogenic storage system filled with liquid helium, whose boiling temperature is 4.2 K. The cryostat, usually called a Dewar, has to meet several criteria :

- Being made of non-magnetic materials
- Providing an efficient thermal insulation to reduce the boiling rate of the content
- Being made of very thin material to minimize the source-sensor distance

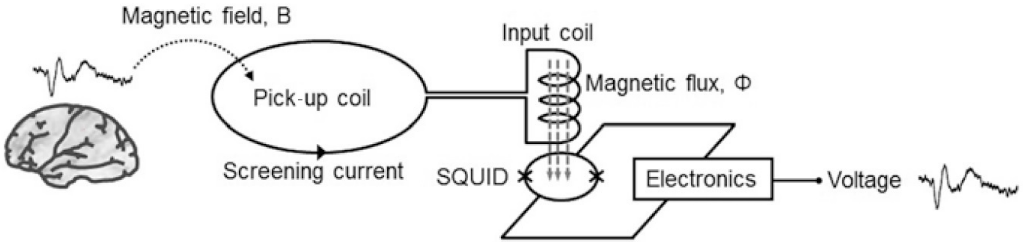

Figure 1.4: MEG measurement principle, from [34]. The pick-up coil and the SQUID loop sizes are respectively around 10 mm and 0.1 mm.

- Allowing helmet-shaping to adapt to the head form

Considering the extreme sensitivity of these devices, it is of key importance to reduce the ambient magnetic disturbances, which can be 6 orders of magnitude higher than the signals of interest. Power lines of the laboratory are radiating fields at 50/60 Hz and many of the harmonics. Moving metallic objects, such as elevators, or even cars and buses across the street can also distort the Earth's magnetic field and create perturbations. An efficient MEG experiment can be achieved by means of two technological developments: operating in a magnetically-shielded room, and using gradiometric coil configurations.

Different kinds of material are used to build a magnetically-shielded room, depending on the targeted frequency range of the shielding. Very low frequencies (< 10 Hz) are attenuated by a few layers of a material which exhibits an extremely high permeability, called mu-metal. Composed of 79% of nickel and 21% of iron, its permeability is around 80000 times the one of air, that is why any external magnetic field outside the room will take this path of largest permeability and will not disturb the measurement. These mu-metal layers are mounted on aluminum plates that ensure an efficient shielding against higher frequencies (> 10 Hz). This passive technique can be improved by adding an active compensation: a controlled current feed Helmholtz coils to cancel the residual field. Other strategies that are based on sophisticated processing methods can also be used to reduce the noise [49].

Despite these efforts, the level of the background noise may remain often too high to conduct a MEG experiment. The second strategy is then to modify the configuration of the detection circuit, from a simple magnetometer to a gradiometer. Most of gradiometers are made of two oppositely-wound coils separated by a few centimeters. It is based on the assumption that the residual magnetic noise in the shielded room will be quite uniform, whereas the two coils of the gradiometer will see a very different field from nearby neuronal sources. For example, a coil, positioned at 4 cm from a dipolar magnetic source, will measure a field 75% smaller than a coil located at 2 cm. The steepness of the gradient close to the source make this gradiometric configuration efficient to discriminate between the signal of interest and a noise coming from far away. Different geometries of gradiometers have been developed, such as planar configuration, which is easier to develop using thin-film technology. Concerning the local magnetic detection, at the neuronal scale, presented in this work, a gradiometer could be used with magneto-resistive sensors, but it will be shown that its relevance is more limited.

Considering the required equipment in terms of shielding of the laboratory and the set up of an array of SQUIDs, a MEG device is about 10 to 100 times more expensive than an EEG system. Moreover, a continuous helium-cooling imposes considerable running costs. That is why researchers are always striving for improved tools, especially non-cooled devices, such as optically-pumped magnetometers. A quick overview of the possible future developments of MEG systems is given below.

1.1.2.3 Future developments

The current helium shortage has led to an increase of interest in other technologies for MEG systems. In the late 1980s, a superconducting material, Yttrium Barium Copper Oxide (YBCO), exhibiting a critical temperature of 90 K was discovered [54]. It was the first material found to remain superconductive above 77 K, the boiling point of liquid nitrogen. A few MEG recordings based on high-T_c SQUIDs have been published [22, 39, 50, 57]. However high-T_c SQUIDs exhibit a higher noise level compared to their low-T_c equivalents [12], and a full-head high-T_c SQUIDs system has not been demonstrated yet. Current research is strongly focused on the development of another type of magnetometer, to perform so-called "on-scalp" MEG [56].

Optically-Pumped Magnetometers (OPM)

One of the best candidate as a magnetic sensor to perform helium-free MEG, is the optically-pumped magnetometer (OPM). A few groups have already demonstrated detection of MEG signals [1, 42, 55]. OPMs are made of a glass cell containing a vapor of an alkali metal (*Cesium, Rubidium, Potassium*). The main characteristic of alkali metals is that their atoms have only one electron in their outer-most electron shell. A circularly polarized light is used to "optically pump" the atoms [20]: the spin from incident photons is transferred to the atoms during absorption, which induces an alignment of the atomic spins along this beam optical axis (see Figure 1.5). Every atom has a magnetic moment μ, which arises from the electronic orbital motion and from its intrinsic spins (see Chapter 2). In the presence of a magnetic field **B**, a torque acts on the atoms such as: $\tau = \mu \times \mathbf{B}$. This torque, induced by **B**, will make these magnetic moments precess at the Larmor frequency, given by $\omega_0 = \gamma B$, γ being the gyromagnetic ratio of the atomic species. This change in the atomic spins direction induces a modification of the absorptive and dispersive properties of the medium. Then, a probing laser beam, generally oriented orthogonally to the pumping light, is sent through the vapor cell. Two modes of detection can be set up: either by measuring the variations of intensity of the transmitted signal (modification of absorption), or by measuring its polarization rotation, called the Faraday effect (modification of dispersion). The probe light is linearly polarized, so it can be decomposed into two circularly polarized waves, one rotating clockwise, the other anti-clockwise, which are propagating at a slightly different speed. The phase shift induces a relative rotation of the polarization that is directly linked to the magnetic field. This method provides a reduced sensitivity to the laser intensity noise compared to the direct measurement of the transmission signal. Moreover, the sensitivity of OPM increases with the square root of the number of atoms in the vapor cell, and the square root of the spin-coherence time. In order to get the best signal-to-noise ratio, the main options are to maximize the density of atoms by heating the cell, usually around 150°C, and by coating the walls of the cells with specific material that help reducing relaxation.

The sensitive volume of OPM is around a few mm^3. When operating in the Spin Exchange Relaxation-Free (SERF) regime, OPM can achieve similar sensitivity as low-T_c SQUIDs, or even outperform them: (0,54 $fT/\sqrt(Hz)$) for a cell volume of 0.3 cm^3 [32], and even 0.16 $fT/\sqrt(Hz)$ for a cell volume of 0.45 cm^3 [21]. One of the main drawback is the small operation bandwidth, limited to a few hundred Hertz, but it allows resolving typical evoked responses of the brain. Another drawback is the very limited range of operation of the OPM, below 100 nT [31]. Recent experiments relate the development of a specially designed 3D-printed head-cast to house up to 13 OPM sensors [7]: this technique allows to locate and orient accurately the sensors. The placement of the OPMs directly on the scalp surface leads to a 4 times larger amplitude than typical SQUID measurement (see Figure 1.5). This type of experiment has to be performed in a magnetically shielded room (MSR). In this case, the head-cast was fixed to the subject head but also to the MSR, to avoid any relative motion of the sensors. Recent theoretical study also confirms the capacity of OPM to outperform traditional SQUIDs magnetometers [28].

Aside from MEG recordings, the very high sensitivity at room temperature of OPMs could also be useful to detect the activity of other biological objects. A recent study, [30], reported the development of miniaturized OPM, for the detection of the magnetic signature of an action potential propagating along a frog sciatic nerve. The amplitude of the signal was about 24 pT at a distance of a few millimeters from the nerve. The axial ionic current was estimated to be 23 nA and the conduction velocity around 34 m/s. This kind of local measurements could make OPM a useful medical tool, but the massive experimental setup (pump beam, probe beam, polarization detector, etc...) turns out to be prohibitive in the case of *in vivo* recording at neuronal scale. Yet, the current development of multichannel devices foretells a promising future for the use of low-cost, maintenance-free, OPM-based MEG systems.

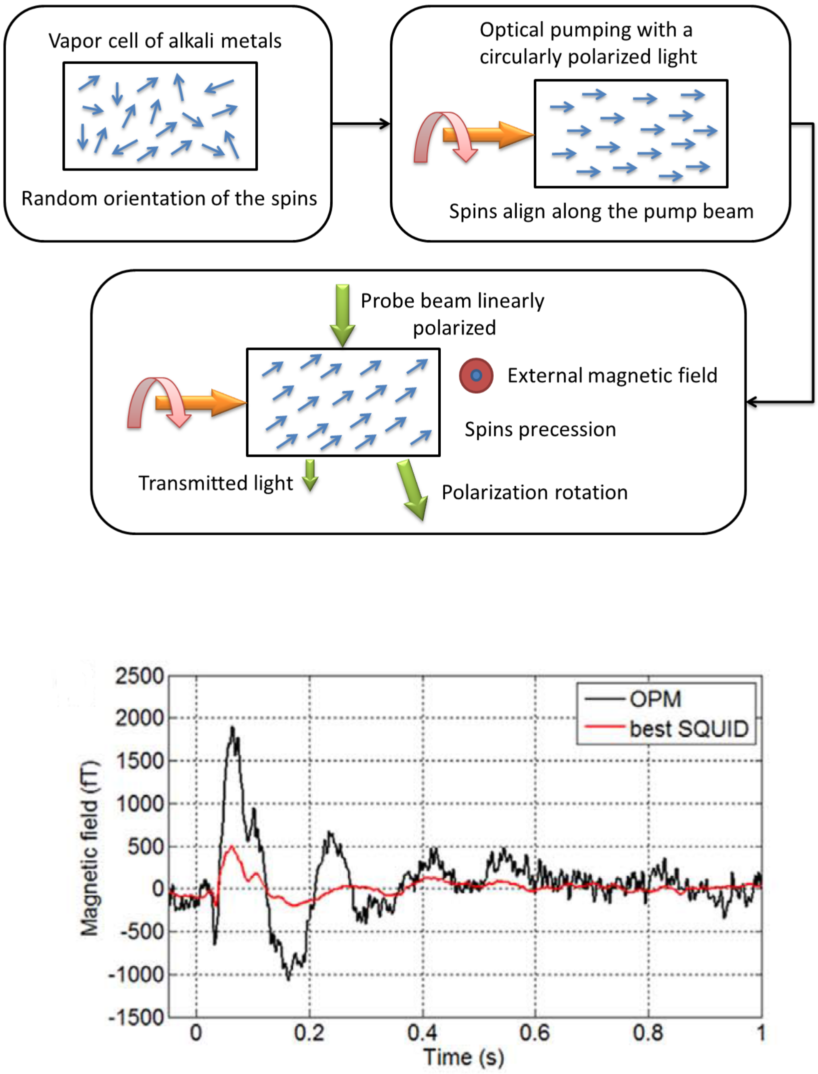

Figure 1.5: **Top:** Optically-pumped magnetometer principle. **Bottom:** Comparison between SQUID and OPM measurements of the magnetic field generated by an evoked response of somatosensory cortex, from [7]. Helium-free OPM measurement allows to be closer to the sources (6 mm, compared to 30-50 mm SQUID-based MEG), so that the amplitude is four times larger (≈ 2 pT) than a traditional SQUID-based acquisition (≈ 500 fT).

1.2 Local-scale neuronal sensing

1.2.1 Theoretical framework

1.2.1.1 Circuit neuroscience

The previous large-scale imaging techniques provide meaningful data to map key functional regions of the brain. Gaining insights into how information is processed implies to bridge the gap between intracellular micro-electrode recordings to centimeter-sized EEG electrode or MEG SQUIDs. This spatial scale spreading over more than five orders of magnitude makes this bridging really non-trivial. Even though EEG and MEG scientists are searching for an improved spatial resolution of their tools, studying higher brain functions compel them to be able to detect coherent signals emerging from tens of thousands of neurons. Many cognitive mechanisms are still beyond our understanding, since they arise from the real-time interactions of massive sets of densely interconnected neuronal networks. These circuits display different dynamics and are governed by connection rules that remain largely unknown so far. Scalp recordings in EEG or MEG suggest that different oscillatory patterns, such as alpha rhythm, are particularly clear during rest [38]. The same applies for anesthesia since large oscillations are measured [48]. In 2004, a pioneering work by Buzsaki studied how conscious behavior influence oscillating networks formed by assemblies of neurons [11]. Talking about bridges, he compared this phenomenon to the tiny oscillations of a bridge, asking whether they are simply "manufacturing" defects or a crucial functionally-relevant part of brain's design. This emerging field, that could be called "circuit neuroscience", will probably be of key importance: being able to correlate the activity of single neurons with the architecture of the circuit, its plasticity and its functional output could improve the comprehension of how the brain carries out operations. However, to achieve this goal, that would requires recordings of every neurons of a given circuit for a sufficiently long time period, novel technologies needs to be developed.

1.2.1.2 Conventional electrodes

The traditional electrodes used by physiologists have brought great advances on the understanding of biophysics of a single neuron. A direct measurement of electrical activity can be provided with a very high signal-to-noise ratio with sub-millisecond time resolution. Electrodes act as a direct translator between the ionic conduction of the intracellular or extracellular medium, and the electron current flowing through their metallic part. The materials are chosen according to their electro-chemical and mechanical properties. Fundamental physical processes at the metal-solution interface are discussed in [8]. To ensure a stable recording, noble metals (Platinum, Iridium) are used because of their resistance to corrosion, but also Tungsten or stainless steel. Another kind of electrode, widely used for intracellular recordings, is the glass micro-pipette. An electrode, usually made of silver/silver-chloride, is immersed into the pipette, filled with a conductive solution that matches the ionic composition of the extracellular bath or of the cytoplasm. The extremity of the tip is around 1 μm so that it enables penetrating the membrane of the targeted neuron without too much damages. The precision of this technique, called patch-clamp, allowed Neher and Sakmann to record currents passing through single ion channel [26, 37], thus improving the comprehension of the fundamental processes underlying the genesis of a spike. The main benefit of intracellular recordings is to get access to information such as the resting potential of the cell, incoming post-synaptic potentials, and spikes. Nevertheless, it requires great experimental skills to master intracellular recordings, especially for *in vivo* configurations. In extracellular recordings, the output signal is a superposition of many biological processes occurring in the vicinity of the electrode: synaptic activity, action potentials, slow fluctuations in glial cells, that are well detailed in [10]. If the sensitive tip is sufficiently close to a firing cell, then action potentials can be clearly identified. An important point to mention is that these extracellular recordings, called local field potential (LFP), depends widely on the size of the electrode. The bigger the electrode, the more neurons contribute to aggregate voltage fluctuations around the tip. Moreover, the relative contributions of the sources depend not only on their distance to the recording point but also on the non-homogenous resistive properties of the brain tissue. All of these points make the interpretation of the extracellular signal non-trivial.

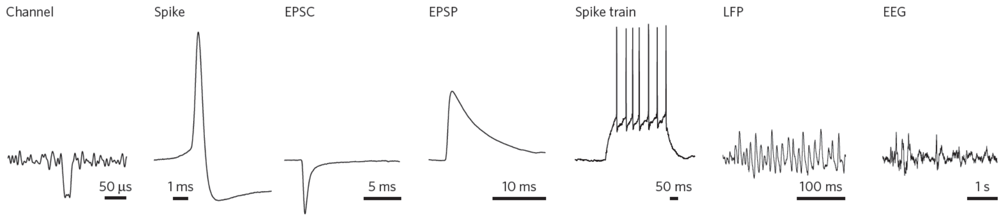

Figure 1.6: **Different kind of neuronal signals recorded over several spatial scales, from [44].** The temporal patterns span over many orders of magnitude and it's worth noticing the very high signal-to-noise ratio. Representative examples shown are of a single channel opening ; an action potential in a cerebellar interneuron; an excitatory postsynaptic current (EPSC), an excitatory postsynaptic potential (EPSP); a spike train from cerebellar granule cells; gamma oscillations (local field potential, LFP) recorded in the hippocampus of an anesthetized rat; and an electroencephalogram from an anesthetized mouse during visual stimulation.

1.2.1.3 Advantage of magnetometry

A critical point about electric measurements is that they provide scalar information. The tip of an electrode collects potential variations due to ionic currents in a global volume, regardless of where they are coming from. Getting access to the propagation direction of these currents would be of great interest to gain a better understanding of the extracellular signal. Concerning action potentials (APs), spatially separated differential scalar measurements would have to be performed to be able to detect which way it propagates or to sense its velocity. That can be done with specific biological system, such as nerve-muscle (see Chapter 3), but, generally, the spatial extent of the AP is longer than the axon, so that the delay between the signals recorded at different locations along the axon is much shorter than the duration of the AP itself. This implies to have a really high signal-to-noise ratio to deduce the velocity. The natural answer to this issue is to perform a vector measurement. Sensing a magnetic field vector yields two kinds of information: the amplitude of the field is proportional to the intensity of the current sources, and its direction might allow a 3D reconstruction of the sources geometries. It has been emphasized that, in MEG, the inverse problem is ill-posed as there is no unique solution for a given recording. For local magnetic sensing, if one considers a multi-channel device, this computation could be easier since there should be no such quiet source.

As stated above, the permeability of brain tissues is similar to the vacuum permeability [25]. This implies that magnetic field can travel the source-sensor distance without undergoing any distortion or filtering effect. It follows that extracellular magnetic recording could provide intracellular information of intact cells, getting rid of the invasiveness of a micro-electrode. This opportunity to detect neuronal activity without any contact with the targeted cells might be of critical importance if one imagines chronic implantable system of magnetic micro-sensors. Long-term biostability is an essential condition for the choice of the material for electric implants. In our case, magnetic sensors could be encapsulated with biocompatible materials, like parylene [27], reducing foreign-body reactions.

Another inherent feature of every electric recording is that the absolute value of a potential at a given point has no physical meaning: every signals are measured with respect to a reference electrode. This reference electrode has to be placed sufficiently far away from the sources. Its location depends on the type of experiments, but it is a prerequisite that the recorded potential difference must not fluctuate if the reference is moved anywhere else in this "far away" zone. Otherwise, the potential of the reference electrode has to be accurately estimated. Yet, it would be ineffective, for example, to plug the reference to the laboratory ground because of the large amount of noise coming from the environment. In most of the cases, a pre-amplifier with a high common-mode rejection rate is integrated to minimize external perturbations. Furthermore, in multi-electrode recordings, the same reference is shared by every channels, which is an issue for analysis of functional connectivity, since the resulting signals are not independent [14]. The possibility to perform reference-free magnetic recordings would overcome this issue.

In a nutshell, local magnetic measurements might provide much additional information and also offer advantages compared to traditional electric techniques: non-invasiveness, reference-free, unperturbed signals, sensitivity to the current direction, high spatial and temporal resolution. So far, only two tools meet this combination of features: nitrogen-vacancy (NV) quantum defects in diamond, and giant magnetoresistance-based sensors (GMR). The latter has been developed in this thesis, while first recordings using NV-based sensors were published in 2016 by the team of R.Walsworth. A summary of this latter technique is given below, to give a comparison basis to the reader.

1.2.2 NV centers

Diamond is an allotrope of carbon, mainly renowned for its extreme hardness and thermal conductivity. It is a wide-bandgap semi-conductor (5,5 eV), which corresponds to an optical transition of 225 nm. Diamond lattice host different kinds of impurities, and they create new energy levels in the gap. They induce optical transitions in the visible range (400-800 nm): a diamond with nitrogen impurities appears yellow, bore impurities give a blue shade and that is why such crystallographic defects are usually called "color centers". When two adjacent carbon atoms are replaced by one nitrogen impurity associated to a vacancy in a neighboring lattice site, this defect is called a NV center. Here is a simplified description of the operating principle of the corresponding magnetometer.

For a negatively-charged NV center, there remains two non-bonded electrons and the system behaves like a trapped atom inside the diamond crystal, with two levels of energy, the ground and the excited state. The interaction between the two electrons splits each energy levels in two sub-levels, noted $|0\rangle$ and $|\pm 1\rangle$, separated by 11.8 µeV (*i.e* 2.87 GHz) for the ground state and 5.8 µeV for the excited state (*i.e* 1.42 GHz). The ground-state sub-levels are nearly equally populated at thermal equilibrium. Optical pumping, via a green laser at 532 nm, puts the NV center in an excited state. The crucial feature is that electrons either decay back to the ground state by emitting a broadband photo-luminescence (PL) signal, or via a non-radiative path from the $|\pm1\rangle$ excited states to the $|0\rangle$ ground state (see Figure 1.8). This optical pumping induces a polarization of the NV center in its $|0\rangle$ ground state. Then, an oscillating microwave field drives transitions between these ground sub-levels. If the frequency of this microwave source reaches the resonance around 2.87 GHz, the fluorescence of the NV center decreases down to 20%. Applying a magnetic field $\mathbf{B}$ to the NV center will induce Zeeman splitting of the $|\pm1\rangle$ sub-levels, proportional to $\mathbf{B}$, that can be detected as a shift in the fluorescence spectrum. For a well-chosen reference point, the number of photons collected will be proportional to the magnetic field.

Since each NV center is an atomic-sized magnetic sensor, the concentration of NV centers at the top surface of the diamond chip used for the experiments has to be the highest possible ($\approx 3.10^{17}$ cm^{-3}). A study, published in 2012 [24], reported the magnetic field that would be generated by an action potential propagating along a crayfish axon, and showed the compatibility between the computed signal and the sensitivity range of a NV-based sensor. The resulting magnetic field, for a source-sensor distance of 100 nm, displays a biphasic shape, ranging from +20 nT to -10 nT, and lasting 2 ms (see Figure 1.7e). In order to confirm experimentally these results, *in vitro* and *in vivo* surface measurements were performed by [3], first using an excised giant axon from a marine worm, then by placing a whole living organism above the NV structure (see Figure 1.8). The sensing volume was $(13 \times 200 \times 2000)\mu\text{m}^3$ and the sensor achieved a sensitivity of 15 pT/$\sqrt{\text{Hz}}$. *In vitro* magnetic recording shows a similar biphasic shape, and a peak-to-peak amplitude of 4 nT (see Figure 1.9). A large signal-to-noise ratio (SNR) of 15 was obtained after averaging 150 trials. As the SNR scales with the square root of the number of trials, one can infer a SNR of 1.2 from a single action potential recording. The frequency bandwidth was set to 4 kHz. *In vivo* experiments carried out on an undissected worm led to a peak-to-peak amplitude of 1 nT, because of a larger distance, estimated around 1.2 mm, between the NV sensing layer and the axon inside the specimen. The number of averaged trials had to be increased to 1650.

Based on these recent results, further developments of NV-based magnetometers raise expectations for a real-time single-neuron action potential detection. However, one has to distinguish the different experimental conditions: biological preparations such as giant axon or invertebrates are relatively easy to handle: the magnetic field of a nerve impulse was first measured in 1980, using a combination of a SQUID and a toroidal pick-up coil through which the nerve had to be pulled [2]. This method is not compatible with *in vivo* diagnostics and yields magnetic field values which are much higher than that in an animal because the return currents in the surrounding tissue are not cancelling. However, the high spatial and temporal resolution of NV-based technology could make it a great candidate to provide new insights into neuronal activity. There remain a few challenges to face, such as implanting a sufficiently dense array of NV center near the surface layer, and to elaborate a customized device that could be used for *in-vivo* experiments in cortical regions, which is, for the moment, incompatible with the bulky setup (see Figure 1.8B) required throughout this study.

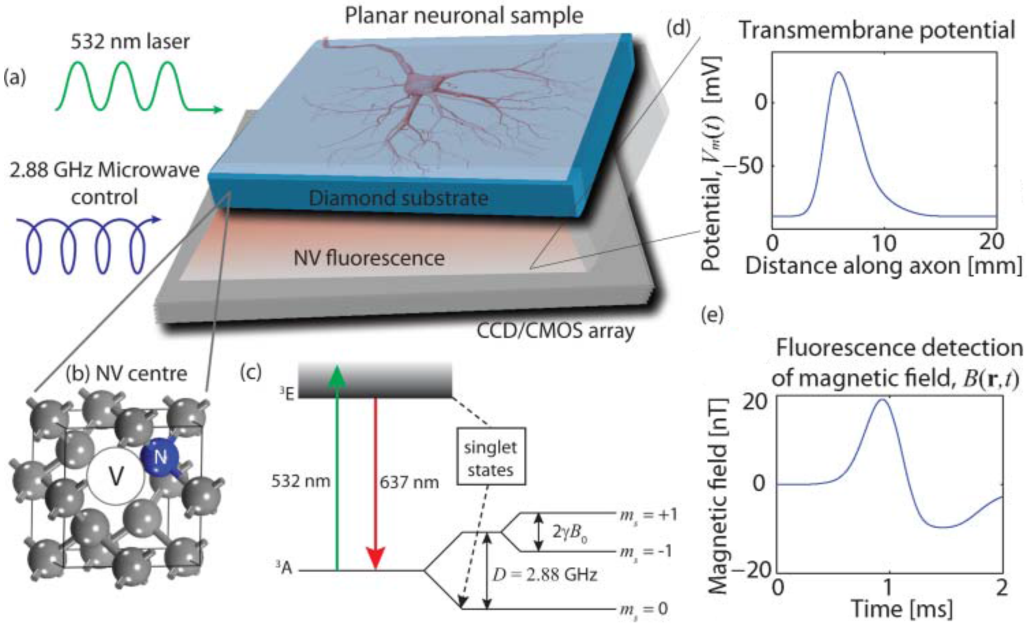

Figure 1.7: **Theoretical study of NV-based biomagnetometry** (a) Diamond substrate with an enriched surface of NV centers, a biological sample placed on top. Read-out by a wide-field CCD (charge coupled device). (b) Atomic lattice structure of an NV center (c) Energy levels: a green laser pumps the NV into the excited state, the decay path is either radiative (red fluorescence), or non-radiative via a metastable state. Zeeman splitting of the $|\pm1\rangle$ levels due to the external field B_0. (d) Longitudinal variation of the action potential propagating along a crayfish axon. (e) Computed magnetic field, for a stand-off distance of 100 nm. (adapted from [24])

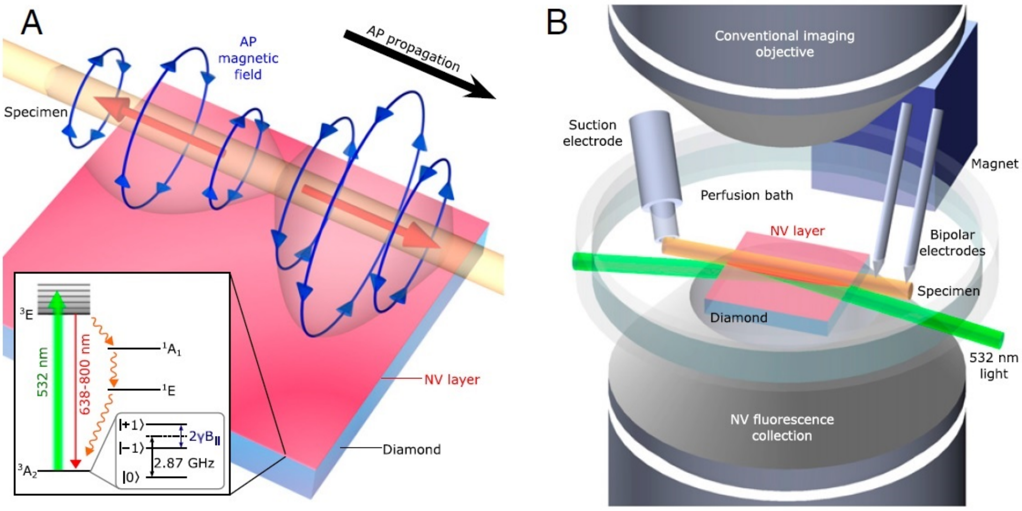

Figure 1.8: **Experimental study of NV-based biomagnetometry** **(A)** The propagation of an AP along the axon induces opposite axial intracellular currents (red arrows) that generate azimuthal magnetic fields. Inset: energy levels of a NV center. **(B)** Setup of the experiment, including the pump laser to polarize the NV centers, a suction electrode that generates an action potential detected by two bipolar electrodes, a rare-earth bias magnet that shifts the resonance around 2.89 GHz, a condenser objective to collect the fluorescence signal. The wire loop used to provide the microwave signal is not shown, from [3].

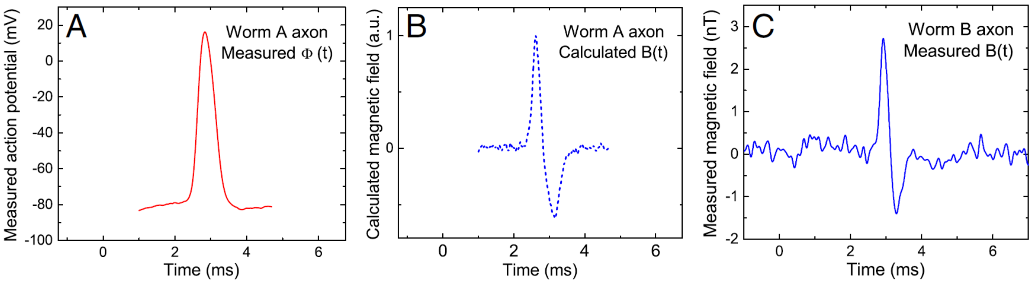

Figure 1.9: **(A)** Intracellular action potential voltage measured on an excised neuron of marine worm *Myxicola infundibulum*. **(B)** Computed magnetic field from (A): in this simple model, the magnetic field is assumed to be proportional to the time derivative of the intracellular voltage. **(C)** Measured magnetic field of the excised giant axon, averaged 150 times, from [3]. The biphasic signal lasts 2 ms and its amplitude reaches 4 nT.

1.3 Conclusion

This first chapter gives an overview of the current main techniques used to study neuronal activity through the magnetic field generated by them.

The primary lesson drawn from this part is the unavoidable trade-off between sensitivity and spatial resolution imposed to every magnetic sensor. Non-invasive methods based on SQUIDs or OPMs are able to detect signals in the femtoTesla range, but their typical spatial resolution, around 1 millimeter, leads to an averaged measurement over thousands of neurons. Developing a micron-sized SQUID would decrease its sensitivity to a prohibitive level to be able to perform successful recordings outside the head of the subject. The same rule governs OPMs: below a cell dimension of 1 mm, the collisions on the walls annihilate the spin polarization and the efficiency of the system. For a cell of 6 mm^3, a sensitivity of 70 $\mathrm{ft}/\sqrt{\mathrm{H}z}$ was reported [46], which is hundreds of times larger than the sub-femtoTesla level achieved by [21, 32]. Neurons have dimensions of the order of 1 to 100 µm. Measuring the activity of a single neuron implies to provide a microscopic sensor, that could be placed at a distance of the same order of magnitude. Room-temperature operation is also an absolute prerequisite for this undertaking. NV centers in diamond are promising, but they require a bulky setup including a laser and microwave irradiation.

The second point is the critical importance of the size of the window through which neuronal activity is observed. Mathematical models have been developed to solve the inverse problem in MEG. Most of them are based on the concept of current dipole that describes the dendritic processes causing the magnetic field measured out of the head. This approximation is successful in MEG [6], because the sensors are supposed to be *far away* from the sources. Experiments based on giant excised axon can also be easily linked to their theoretical estimations [3, 40]. However, considering *in vivo* recordings in the very close vicinity of neurons, such approximations are no longer valid. The irregular geometry of the dendritic branches makes any predictions about the resulting magnetic field uncertain.

Investigating the origins of the MEG signal at a small scale remains an exciting challenge. Local magnetic recordings give an insight on the action potential conduction velocity, which is a critical parameter for the detection of demyelination involved in multiple sclerosis [33]. The difficulties to describes theoretically the expected signal shall not be an impassable obstacle because, as stated in the introduction, groundbreaking experiments have been carried out in EEG and MEG without complete prior modeling. The technique developed during this thesis is based on spin-electronics magnetic sensors. The next chapter presents the physical phenomenons underlying these sensors, their performance, and every step of the whole process that has been carried out in order to obtain the most sensitive device that meets all the requirements described so far to perform local magnetic recordings.

Bibliography

[1] ALEM, O., A. M. BENISON, D. S. BARTH, J. KITCHING et S. KNAPPE. 2014, «Magnetoencephalography of epilepsy with a microfabricated atomic magnetrode», *Journal of Neuroscience*, vol. 34, no. 43, p. 14 324–14 327. 21

[2] BARACH, J., J. FREEMAN et J. WIKSWO JR. 1980, «Experiments on the magnetic field of nerve action potentials», *Journal of Applied Physics*, vol. 51, no. 8, p. 4532–4538. 30

[3] BARRY, J. F., M. J. TURNER, J. M. SCHLOSS, D. R. GLENN, Y. SONG, M. D. LUKIN, H. PARK et R. L. WALSWORTH. 2016, «Optical magnetic detection of single-neuron action potentials using quantum defects in diamond», *Proceedings of the National Academy of Sciences*, p. 201601 513. 29, 31, 32

[4] BAULE, G. et R. MCFEE. 1963, «Detection of the magnetic field of the heart», *American Heart Journal*, vol. 66, no. 1, p. 95–96. 18

[5] BERGER, H. 1929, «Über das elektrenkephalogramm des menschen», *European Archives of Psychiatry and Clinical Neuroscience*, vol. 87, no. 1, p. 527–570. 12

[6] BLAGOEV, K., B. MIHAILA, B. TRAVIS, L. ALEXANDROV, A. BISHOP, D. RANKEN, S. POSSE, C. GASPAROVIC, A. MAYER, C. AINE et collab.. 2007, «Modelling the magnetic signature of neuronal tissue», *NeuroImage*, vol. 37, no. 1, p. 137–148. 32

[7] BOTO, E., S. S. MEYER, V. SHAH, O. ALEM, S. KNAPPE, P. KRUGER, T. M. FROMHOLD, M. LIM, P. M. GLOVER, P. G. MORRIS et collab.. 2017, «A new generation of magnetoencephalography: Room temperature measurements using optically-pumped magnetometers», *Neuroimage*, vol. 149, p. 404–414. 22, 24

[8] BRETTE, R. et A. DESTEXHE. 2012, *Handbook of neural activity measurement*, Cambridge University Press. 26

[9] BROCA, P. 1861, «Remarques sur le siège de la faculté du langage articulé, suivies d'une observation d'aphémie (perte de la parole)», *Bulletin de la Société anatomique*, vol. 6, no. 343, p. 57. 10

[10] BUZSÁKI, G., C. A. ANASTASSIOU et C. KOCH. 2012, «The origin of extracellular fields and currents—eeg, ecog, lfp and spikes», *Nature reviews neuroscience*, vol. 13, no. 6, p. 407–420. 26

[11] BUZSÁKI, G. et A. DRAGUHN. 2004, «Neuronal oscillations in cortical networks», *science*, vol. 304, no. 5679, p. 1926–1929. 25

[12] CANTOR, R., L. LEE, M. TEEPE, V. VINETSKIY et J. LONGO. 1995, «Low-noise, single-layer yba/sub 2/cu/sub 3/o/sub 7-x/dc squid magnetometers at 77 k», *IEEE Transactions on Applied Superconductivity*, vol. 5, no. 2, p. 2927–2930. 21

[13] CARUSO, L. 2015, *Giant magnetoresistance based sensors for local magnetic detection of neuronal currents*, thèse de doctorat, Universite Pierre et Marie Curie-Paris VI. 17

[14] CARUSO, L., T. WUNDERLE, C. M. LEWIS, J. VALADEIRO, V. TRAUCHESSEC, J. TREJO-ROSILLO, J. P. AMARAL, J. NI, C. FERMON, S. CARDOSO et collab.. 2017, «In vivo magnetic recording of neuronal activity», *accepted in Neuron*. 28

[15] CATON, R. 1875, «Electrical currents of the brain.», *The Journal of Nervous and Mental Disease*, vol. 2, no. 4, p. 610. 11

[16] CHERRY, S. R. et M. DAHLBOM. 2006, «Pet: physics, instrumentation, and scanners», dans *PET*, Springer, p. 1–117. 12

[17] CLARKE, J. et A. I. BRAGINSKI. 2006, *The SQUID handbook: Applications of SQUIDs and SQUID systems*, John Wiley & Sons. 19

[18] COHEN, D. 1972, «Magnetoencephalography: detection of the brain's electrical activity with a superconducting magnetometer», *Science*, vol. 175, no. 4022, p. 664–666. 19

[19] COHEN, D. et collab.. 1968, «Magnetoencephalography: evidence of magnetic fields produced by alpha-rhythm currents», *Science*, vol. 161, no. 3843, p. 784–786. 18

[20] COHEN-TANNOUDJI, C. et A. KASTLER. 1966, «I optical pumping», *Progress in optics*, vol. 5, p. 1–81. 21

[21] DANG, H., A. MALOOF et M. ROMALIS. 2010, «Ultrahigh sensitivity magnetic field and magnetization measurements with an atomic magnetometer», *Applied Physics Letters*, vol. 97, no. 15, p. 151 110. 22, 32

[22] FALEY, M., U. POPPE, R. DUNIN-BORKOWSKI, M. SCHIEK, F. BOERS, H. CHOCHOLACS, J. DAMMERS, E. EICH, N. SHAH, A. ERMAKOV et collab.. 2013, «High-tc dc squids for magnetoencephalography», *IEEE Transactions on Applied Superconductivity*, vol. 23, no. 3, p. 1600 705–1600 705. 21

[23] HADAMARD, J. 1902, «Sur les problèmes aux dérivées partielles et leur signification physique», *Princeton university bulletin*, vol. 13, no. 49-52, p. 28. 14

[24] HALL, L., G. BEART, E. THOMAS, D. SIMPSON, L. MCGUINNESS, J. COLE, J. MANTON, R. SCHOLTEN, F. JELEZKO, J. WRACHTRUP et collab.. 2012, «High spatial and temporal resolution wide-field imaging of neuron activity using quantum nv-diamond», *Scientific reports*, vol. 2, p. 401. 29, 30

[25] HÄMÄLÄINEN, M., R. HARI, R. J. ILMONIEMI, J. KNUUTILA et O. V. LOUNASMAA. 1993, «Magnetoencephalography—theory, instrumentation, and applications to noninvasive studies of the working human brain», *Reviews of modern Physics*, vol. 65, no. 2, p. 413. 15, 27

[26] HAMILL, O. P., A. MARTY, E. NEHER, B. SAKMANN et F. SIGWORTH. 1981, «Improved patch-clamp techniques for high-resolution current recording from cells and cell-free membrane patches», *Pflügers Archiv European journal of physiology*, vol. 391, no. 2, p. 85–100. 26

[27] HASSLER, C., R. P. VON METZEN, P. RUTHER et T. STIEGLITZ. 2010, «Characterization of parylene c as an encapsulation material for implanted neural prostheses», *Journal of Biomedical Materials Research Part B: Applied Biomaterials*, vol. 93, no. 1, p. 266–274. 27

[28] IIVANAINEN, J., M. STENROOS et L. PARKKONEN. 2017, «Measuring meg closer to the brain: Performance of on-scalp sensor arrays», *NeuroImage*, vol. 147, p. 542–553. 23

[29] IOANNIDES, A., J. BOLTON et C. CLARKE. 1990, «Continuous probabilistic solutions to the biomagnetic inverse problem», *Inverse Problems*, vol. 6, no. 4, p. 523. 14

[30] JENSEN, K., R. BUDVYTYTE, R. A. THOMAS, T. WANG, A. M. FUCHS, M. V. BALABAS, G. VASILAKIS, L. D. MOSGAARD, H. C. STÆRKIND, J. H. MÜLLER et collab.. 2016, «Non-invasive detection of animal nerve impulses with an atomic magnetometer operating near quantum limited sensitivity», *Scientific Reports*, vol. 6. 23

[31] KNAPPE, S., T. SANDER et L. TRAHMS. 2014, «Optically-pumped magnetometers for meg», dans *Magnetoencephalography*, Springer, p. 993–999. 22

[32] KOMINIS, I., T. KORNACK, J. ALLRED et M. ROMALIS. 2003, «A subfemtotesla multichannel atomic magnetometer», *Nature*, vol. 422, no. 6932, p. 596–599. 22, 32

[33] KUTZELNIGG, A., C. F. LUCCHINETTI, C. STADELMANN, W. BRÜCK, H. RAUSCHKA, M. BERGMANN, M. SCHMIDBAUER, J. E. PARISI et H. LASSMANN. 2005, «Cortical demyelination and diffuse white matter injury in multiple sclerosis», *Brain*, vol. 128, no. 11, p. 2705–2712. 32

[34] LEE, Y.-H. et K. KIM. 2014, «Instrumentation for measuring meg signals», dans *Magnetoencephalography*, Springer, p. 3–33. 20

[35] MAGUIRE, E. A., D. G. GADIAN, I. S. JOHNSRUDE, C. D. GOOD, J. ASHBURNER, R. S. FRACKOWIAK et C. D. FRITH. 2000, «Navigation-related structural change in the hippocampi of taxi drivers», *Proceedings of the National Academy of Sciences*, vol. 97, no. 8, p. 4398–4403. 10

[36] MCDERMOTT, R., S. LEE, B. TEN HAKEN, A. H. TRABESINGER, A. PINES et J. CLARKE. 2004, «Microtesla mri with a superconducting quantum interference device», *Proceedings of the National Academy of Sciences of the United States of America*, vol. 101, no. 21, p. 7857–7861. 10

[37] NEHER, E., B. SAKMANN et J. H. STEINBACH. 1978, «The extracellular patch clamp: a method for resolving currents through individual open channels in biological membranes», *Pflügers Archiv European Journal of Physiology*, vol. 375, no. 2, p. 219–228. 26

[38] NUNEZ, P. L. et R. SRINIVASAN. 2006, *Electric fields of the brain: the neurophysics of EEG*, Oxford University Press, USA. 25

[39] ÖISJÖEN, F., J. F. SCHNEIDERMAN, G. FIGUERAS, M. CHUKHARKIN, A. KALABUKHOV, A. HEDSTRÖM, M. ELAM et D. WINKLER. 2012, «High-tc superconducting quantum interference device recordings of spontaneous brain activity: Towards high-t c magnetoencephalography», *Applied Physics Letters*, vol. 100, no. 13, p. 132 601. 21

[40] ROTH, B. J. et J. WIKSWO. 1985, «The magnetic field of a single axon. a comparison of theory and experiment», *Biophysical journal*, vol. 48, no. 1, p. 93–109. 32

[41] SALMON, E., B. SADZOT, P. MAQUET, C. DEGUELDRE, C. LEMAIRE, P. RIGO, D. COMAR et G. FRANCK. 1994, «Differential diagnosis of alzheimer's disease with pet.», *Journal of nuclear medicine: official publication, Society of Nuclear Medicine*, vol. 35, no. 3, p. 391–398. 12

[42] SANDER, T., J. PREUSSER, R. MHASKAR, J. KITCHING, L. TRAHMS et S. KNAPPE. 2012, «Magnetoencephalography with a chip-scale atomic magnetometer», *Biomedical optics express*, vol. 3, no. 5, p. 981–990. 21

[43] SARVAS, J. 1987, «Basic mathematical and electromagnetic concepts of the biomagnetic inverse problem», *Physics in medicine and biology*, vol. 32, no. 1, p. 11. 14

[44] SCANZIANI, M. et M. HÄUSSER. 2009, «Electrophysiology in the age of light», *Nature*, vol. 461, no. 7266, p. 930–939. 26

[45] SERGEEVA-CHOLLET, N., H. DYVORNE, J. DABEK, Q. HERREROS, H. POLOVY, G. LE GOFF, G. CANNIES, M. PANNETIER-LECOEUR et C. FERMON. 2011, «Low field mri with magnetoresistive mixed sensors», dans *Journal of Physics: Conference Series*, vol. 303, IOP Publishing, p. 012055. 10

[46] SHAH, V., S. KNAPPE, P. D. SCHWINDT et J. KITCHING. 2007, «Subpicotesla atomic magnetometry with a microfabricated vapour cell», *Nature Photonics*, vol. 1, no. 11, p. 649–652. 32

[47] SILVERMAN, D. H., G. W. SMALL, C. Y. CHANG, C. S. LU, M. A. K. DE ABURTO, W. CHEN, J. CZERNIN, S. I. RAPOPORT, P. PIETRINI, G. E. ALEXANDER et collab.. 2001, «Positron emission tomography in evaluation of dementia: regional brain metabolism and long-term outcome», *Jama*, vol. 286, no. 17, p. 2120–2127. 12

[48] TATUM IV, W. O. 2014, *Handbook of EEG interpretation*, Demos Medical Publishing. 25

[49] TAULU, S., J. SIMOLA, J. NENONEN et L. PARKKONEN. 2014, «Novel noise reduction methods», dans *Magnetoencephalography*, Springer, p. 35–71. 20

[50] TAVRIN, Y., Y. ZHANG, M. MÜCK, A. BRAGINSKI et C. HEIDEN. 1993, «Yba2cu3o7 thin film squid gradiometer for biomagnetic measurements», *Applied physics letters*, vol. 62, no. 15, p. 1824–1826. 21

[51] TURNER, A. M. et W. T. GREENOUGH. 1985, «Differential rearing effects on rat visual cortex synapses. i. synaptic and neuronal density and synapses per neuron», *Brain research*, vol. 329, no. 1, p. 195–203. 13

[52] WEISSMAN, T. A., J. R. SANES, J. W. LICHTMAN et J. LIVET. 2011, «Generating and imaging multicolor brainbow mice», *Cold Spring Harbor Protocols*, vol. 2011, no. 7, p. pdb–top114. 18

[53] WILLIAMSON, S. J. et L. KAUFMAN. 1981, «Biomagnetism», *Journal of Magnetism and Magnetic Materials*, vol. 22, no. 2, p. 129–201. 15

[54] WU, M.-K., J. R. ASHBURN, C. TORNG, P. H. HOR, R. L. MENG, L. GAO, Z. J. HUANG, Y. WANG et A. CHU. 1987, «Superconductivity at 93 k in a new mixed-phase y-ba-cu-o compound system at ambient pressure», *Physical Review Letters*, vol. 58, no. 9, p. 908. 21

[55] XIA, H., A. BEN-AMAR BARANGA, D. HOFFMAN et M. ROMALIS. 2006, «Magnetoencephalography with an atomic magnetometer», *Applied Physics Letters*, vol. 89, no. 21, p. 211 104. 21

[56] XIE, M., J. SCHNEIDERMAN, M. CHUKHARKIN, A. KALABUKHOV, B. RIAZ, D. LUNDQVIST, S. WHITMARSH, M. HAMALAINEN, V. JOUSMAKI, R. OOSTENVELD et collab.. 2016, «Benchmarking for on-scalp meg sensors», *IEEE Transactions on Biomedical Engineering*. 21

[57] ZHANG, Y., Y. TAVRIN, M. MÜCK, A. I. BRAGINSKI, C. HEIDEN, S. HAMPSON, C. PANTEV et T. ELBERT. 1993, «Magnetoencephalography using high temperature rf squids», *Brain Topography*, vol. 5, no. 4, p. 379–382. 21

[58] ZIMMERMAN, J., P. THIENE et J. HARDING. 1970, «Design and operation of stable rf-biased superconducting point-contact quantum devices, and a note on the properties of perfectly clean metal contacts», *Journal of Applied Physics*, vol. 41, no. 4, p. 1572–1580. 18

Chapter 2

Magnetoresistive sensors

We are all just prisoners here, of our own device.

Hotel California - The Eagles

Contents

2.1 Theoretical basis

2.1.1 Origin of spintronics

The magnetic sensors, as those developed during this thesis, are one of the flagship devices that emerged from the field of spintronics. Traditional electronics exploits the electric charge of electrons, *i.e* the fact that they experience a force in presence of an electric field. However, in specific materials, the electron transport depends on their spin, a property which has led to the emergence of systems based on this further degree of freedom. The spin, an intrinsically quantum properties of elementary particles, designates an angular momentum, distinct from the classical orbital angular momentum. One of the easiest way to describe the concept of spin is to look back at the experiment that demonstrated its existence. It was conducted in Frankfurt in 1922 by Otto Stern and Walther Gerlach [12, 13]. This experiment is described below in the framework of classical mechanics, but a fully quantum approach can be found in [2].

2.1.2 Stern-Gerlach experiment

The Stern-Gerlach experiment consists of sending a beam of silver atoms through an inhomogeneous magnetic field, and to collect them on a detector screen (see Figure 2.1). The atoms are electrically neutral, so that the Lorentz force ($\mathbf{F_L} = q(\mathbf{E} + \mathbf{v} \times \mathbf{B})$), will not have any influence on their trajectories. However, if they carry a magnetic angular momentum μ, this moment will interact with the external field **B**. This interaction is associated to an energy W:

$$W = -\mu \cdot \mathbf{B} \tag{2.1}$$

Since the magnet generates a non-uniform magnetic field along the z axis, the atoms will experience a force, parallel to this z axis, that deflects them before striking the detector screen:

$$F = -\nabla(W) = \nabla(\mu \cdot \mathbf{B}) = -\mu_z . \frac{\partial B_z}{\partial z} \tag{2.2}$$

If the magnetic angular momentum μ is randomly distributed when the atoms enter the system, one should observe a continuous line on the screen. However, in their ground state, silver atoms show no orbital angular momentum **L**, a quantity which is directly linked to μ by the gyromagnetic ratio γ: $\mu = \gamma \mathbf{L}$. Then, since $\mu = 0$ in our case, one would expect no deflection of the beam while passing through the system, and every atom to land at the same position on the screen.

The first hypothesis is to admit the existence of another kind of angular momentum. It would be clearly different from the orbital angular momentum **L**, the latter being due to the rotation of the electrons around the nucleus. This former intrinsic angular momentum is called the spin. As stated above, if one considers a random distribution of the spin magnetic moments when they are emitted from the source, the particles should be deflected continuously along the z-axis (see Figure (2.1)4). Instead, the atoms are only deflected either up or down, and two symmetrical points were measured. It leads to the second hypothesis: the spin can only take two discrete values.

This is why the Stern-Gerlach experiment demonstrated both the existence of the spin, and the fact that it is quantized. A complete theoretical description of this experiment would be provided a few years later by Uhlenbeck and Goudsmith [41]. The fact that the spin of electrons can take only two values will be of critical importance in the next section, where the explanation of the behavior of the sensors will be given. These two configurations will be referred to as "spin-up" and "spin-down".

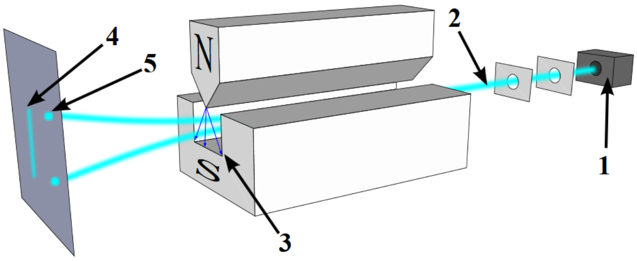

Figure 2.1: **Stern - Gerlach experiment.** This experiment illustrated the existence of an intrinsic magnetic moment of electrons, the spin, that can take only two discrete values. **(1)** Furnace **(2)** Silver-atom beam **(3)** Magnetic field gradient created by specially shaped magnets **(4)** Classical prediction: the atoms are continuously deflected along the *z* axis. **(5)** Actual measurement: only two opposite points are observed

2.2 Magneto-resistive sensors

2.2.1 Anisotropic magneto-resistance

Magneto-resistance reflects how the electrical resistance R of a device depends on the strength of an externally applied magnetic field H. This effect can be characterized by the magneto-resistive ratio MR, defined as:

$$\mathrm{MR} = \frac{\mathrm{R(H)} - \mathrm{R(0)}}{\mathrm{R(0)}} \tag{2.3}$$

where R(H) is the resistance of the sample for an applied field H, and R(0) the resistance corresponding to H = 0. The first magneto-resistive effect was discovered in 1857 by William Thompson (also known as Lord Kelvin) [38]. He observed a variation of resistance of a sample that depended on the relative angle θ between its magnetization and the direction of the applied current. A magnetic sensor based on this effect has been developed later: the Anisotropic Magneto-Resistive (AMR) sensor. The anisotropy is induced either by patterning a rectangular shape with a high aspect ratio, so that the magnetization aligns naturally along the length of the bar, or by applying a strong magnetic field along the length to magnetize it, so that all the magnetic domains in the layer align together in a unique direction. An external magnetic field will make this magnetization rotate, and the global resistance of the sample varies as $\cos^2(\theta)$. Nowadays, commercial AMR sensors (Honeywell HMC1001) exhibit a sensitivity of 23 $\mathrm{pT}/\sqrt{\mathrm{H}z}$ at 100 Hz, but their typical dimensions remain in the millimeter range [46]. A full review explaining the physical effects in detail can be found here [27].

2.2.2 Giant magneto-resistance

The Giant Magneto-Resistance (GMR) effect was discovered in the late 1980s by the groups of Albert Fert [1], from University Paris-Sud, and Peter Grünberg [3], from Jülich, Germany. They were awarded the Nobel Prize in Physics in 2007 for this breakthrough, especially because it has led to significant technological advances in the data storage industry [40]. Pioneering GMR-based hard disks were first put on the market by IBM in 1997 [39], and their performance has not stopped increasing drastically so far.

Before these experiments, the spin was essentially considered through its macroscopic representation: the magnetization of a material. The development of microfabrication techniques, such as the molecular beam epitaxy, allowed to produce samples made of ultra-thin metallic layers, in the nanometer range. Two critical lengths have to be defined to understand electron conduction in metals: the mean free path, which is the average distance traveled by an electron in a crystal before scattering, and the spin diffusion length, λ_s, which is the average distance traveled by an electron before it loses its initial spin orientation, which is called a spin-flip. At room temperature, λ_s is around a few tens of nanometers. On this basis, three properties provide the basis for understanding the GMR effect:

1. In metals, the probability of spin-flip scattering processes is small compared to

the probability of conserving the spin state during a collision: therefore, the spin-diffusion length λ_s is logically larger than the mean free path. The idea underlying the fact that the spin state influences the electrical conduction was introduced by Sir Nevill Mott as early as 1936 [28]. His model proposed that the electrical conduction occurs through two independent conducting channels, one for each polarization of the spin.

2. In ferromagnetic metals (Iron, Nickel, Cobalt), the scattering rate is spin-dependent. The higher the scattering rate, the higher the resistivity for a given spin channel, and the lower its conductivity. This property is due to the asymmetry of the density of states, *i.e* the number of available states to be occupied by the electrons, at the Fermi level, *i.e* the energy level that has a 50% probability to be occupied, according to the spin direction. The two conducting channels described above exhibit two different resistivities, noted $\rho_\uparrow$ and $\rho_\downarrow$. The global resistivity of a ferromagnetic layer is then: $\rho = (\rho_\uparrow . \rho_\downarrow)/(\rho_\uparrow + \rho_\downarrow)$.

3. When two ferromagnetic layers are deposited on top of each other, their magnetizations tend to align in the same direction, via the exchange interaction described above. In 1986, Grünberg reported evidences of an anti-ferromagnetic coupling, *i.e* an anti-parallel magnetization configuration, between two ferromagnetic layers of Iron when they are separated by a non-magnetic layer [14]. This layer, usually made of Copper or Chromium, is called the spacer.

It is then straightforward to explain the GMR effect: let's consider a sample made of two ferromagnetic layers separated by a spacer (see Figure 2.2 right). Let's also assume that the scattering rate is higher for electrons whose spins are anti-parallel to the magnetization of a layer, $R_{\uparrow\uparrow} \leq R_{\uparrow\downarrow}$.

- Without external magnetic field, the magnetization of the two layers are respectively ↑ and ↓ because of the anti-ferromagnetic coupling. The probability for the spins ↓ to be scattered will be high when passing through the first layer but much lower when reaching the second one, and vice-versa for the spins ↑. The global resistance can be expressed as $R_{AP} = (R_{\uparrow\uparrow} + R_{\uparrow\downarrow}) // (R_{\downarrow\uparrow} + R_{\downarrow\downarrow}) = (R_{\uparrow\uparrow} + R_{\uparrow\downarrow})/2 \approx R_{\uparrow\downarrow}/2$

- When a magnetic field is applied, both magnetizations are parallel, say in the ↑ direction. The spins ↑ will travel through the layers easily, while the spins ↓ will be strongly scattered. The global resistance can be expressed as $R_P = (2R_{\uparrow\uparrow}) // (2R_{\downarrow\uparrow}) \approx 2R_{\uparrow\uparrow}$

The first experiments made by Fert were conducted on a multilayer sample of Iron and Chromium (see Figure 2.2 left). The MR ratio between R_P and R_{AP} reached up to

80%. This value, much larger than the anisotropic effect presented above, made him coined the term "giant" magneto-resistance.

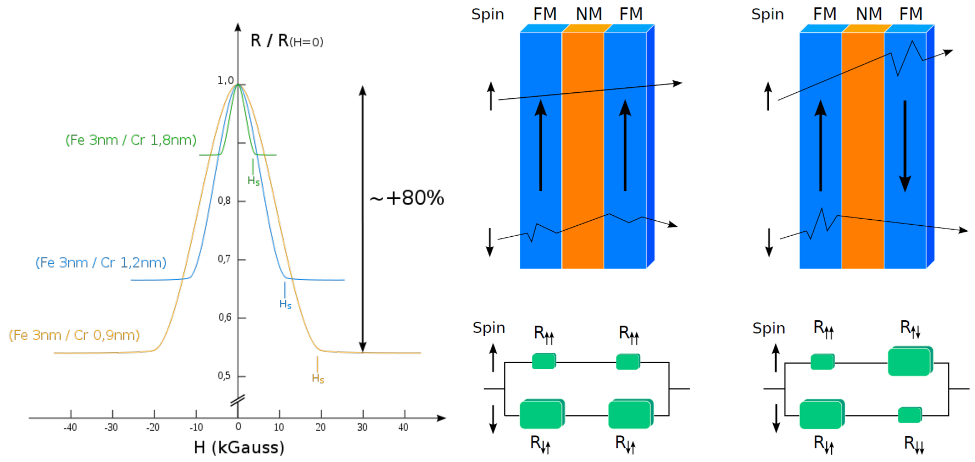

Figure 2.2: **Left**: Initial measurement of the giant magneto-resistance effect by Fert et al. [1]. The magnetic field needed to switch from the anti-parallel state to the parallel state was 20 kGauss, *i.e* 2 Tesla. The sample was cooled down to 4.2 K. At room temperature, Grünberg et. al reported a MR ratio of 1.5%. **Right**: Illustration of the spin-dependent scattering in ferromagnetic materials (FM). The spacer is non-magnetic (NM). The equivalent electrical circuit with two conducting channels is shown under each configuration. For parallel magnetizations, $R_P \approx 2R_{\uparrow\uparrow}$, and $R_{AP} \approx R_{\uparrow\downarrow}/2$ in the anti-parallel state.

2.2.3 Spin valve structure

After the discovery of Fert and Grünberg, a few technological issues remained towards industrial production of GMR sensors. The multilayer structures had been deposited by molecular beam epitaxy, which is a slow process, incompatible with mass production. In 1990, Parkin et. al reported the successful deposition of Fe/Cr, Co/Ru, and Co/Cr layers by sputtering techniques [31]. The next question is how to get a large magneto-resistance effect at room temperature and without using such strong field. The strength of the magnetic field used by Fert to switch from the anti-parallel state to the parallel state was 2 Tesla, which is also incompatible with industrial applications.

The answer was provided in 1991 by Dieny et. al, when they developed a device called a spin valve [7]. A spin valve is made of only two ferromagnetic layers, separated by a spacer. As stated above, in a multilayers structure, the thickness of the non-magnetic spacer is of key importance, because it will induce either a ferromagnetic coupling between two adjacent layers (↑↑), or an anti-ferromagnetic coupling (↑↓), the latter configuration being used by Fert and Grünberg to get a high resistance at zero field. In a spin valve, the spacer is a little thicker, so that there is no more coupling between the two ferromagnetic layers. Then, it becomes possible to switch the magnetization direction of one of the two layers, while the other keeps the same magnetization. The first one, which aligns along the external field, is called the free layer. The second one is called the hard layer or pinned layer, since its coercive field, the magnetic field that switches its magnetization, is really high compared to the free layer. Instead of measuring the resistance of the structure in the parallel or anti-parallel state, one can get access to a continuum of resistance values corresponding to the angle between the magnetization of the free layer and the hard layer (see Figure 2.3). The materials that composed the spin valves and the specific design are described in the following section.

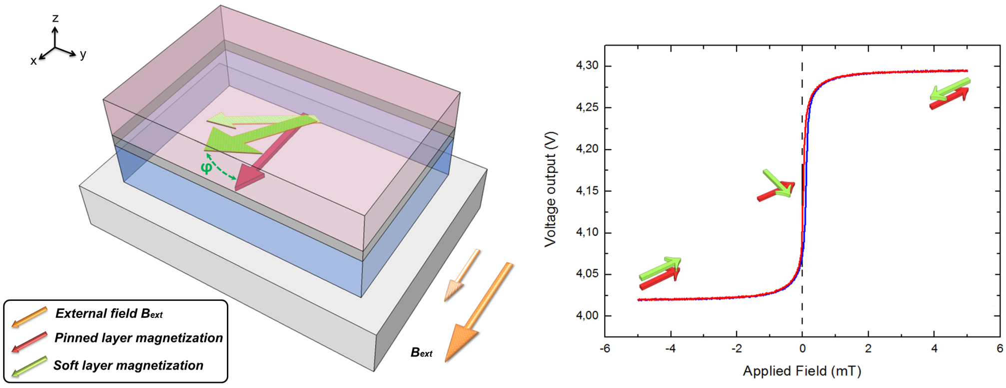

Figure 2.3: **Left: Spin valve principle.** The stack is deposited on a silicon substrate (light gray). The pinned layer (light blue) has a fixed magnetization along a specific direction (red arrow), while in the free layer (light pink) magnetization rotates (green arrows) when an external field is applied on the plane of the stack (illustrated with light and dark orange arrows according to the field strength). The resistance of the stack varies as function of the angle ϕ between the free and the hard layer. **Right: Response of a spin valve sensor to an in-plane magnetic field.** The sensor is fed with a DC current and the output voltage is plotted. The resistance is low when the free layer and the hard layer are in the parallel state ($\phi = 0$ deg), and becomes maximal when they are in the anti-parallel configuration ($\phi = 180$ deg). In order to make the resistance of the structure vary linearly between these two saturated states, the angle between the free layer and the hard layer magnetization is set at $\phi = 90$ deg. It can be done by placing a bias magnet under the sensor, or, for sub-micrometer sizes, by patterning a rectangle with a high aspect ratio. Red (blue) curve is obtained when the field is swept from negative (positive) values to positive (negative) values.

2.3 Sensor microfabrication process

2.3.1 Stack deposition

In order to make the spin valve an efficient magnetic sensor, each layer has to meet several criteria. The choice of materials and their thicknesses are key parameters (see Figure 2.4). Here is the detailed composition of the stacks:

- **The free layer:** its role is to align its magnetization along the field of interest. The sensitivity of the sensor depends on how easily and how smoothly the rotation occurs. The free layer is made of a bilayer of an alloy of $NiFe$ coupled to a layer of $CoFe$. The $NiFe$ is a very soft material, which means that its coercivity is really low. The $CoFe$ is chosen because of its high spin-polarization, in order to enhance the MR ratio. There is a direct coupling between these two layers, so that the magnetization of the $CoFe$ layer will follow any rotation of the $NiFe$ due to the magnetic field.

- **The spacer:** its role is to decouple the free layer from the hard layer. To achieve an efficient decoupling without decreasing the MR ratio, its thickness must be between 2.0 and 2.2 nm [11]. The spin-state of the conducting electrons passing through the spacer has to remain unchanged to conserve the GMR effect. That is why the thickness needs to be inferior to the spin diffusion length or to the mean free path, according to the contact configuration (see below). The spacer is made of Copper in every stacks developed in this work. If the spacer is made of an electrical insulator which is sufficiently thin, then the electrons can tunnel through this barrier. This gives rise to a tunnel magneto-resistance (TMR) effect. Originally discovered in 1975 [20], before the GMR effect, the TMR ratio can be much higher. The development of device using crystalline magnesium oxyde (MgO) as a spacer, since the early 2000's, has led to TMR ratio of 180% [32, 45]. The highest TMR ratio reported so far is 604% at 300 K, and 1104% at 5 K [18]. However, although TMR-based sensors exhibit a higher sensitivity, their intrinsic noise is also greater than GMR sensors in the low-frequency range, so that their detectivity is on the same order of magnitude. Moreover, the micro-fabrication process of a TMR sensor is more complex, so it has not been developed in this work.

- **The hard layer:** its role is to keep its magnetization in the same direction, whatever the strength of the external field, in order to be used as a magnetic reference. The basic configuration is to couple a ferromagnetic layer of $CoFe$ to an anti-ferromagnetic layer of $IrMn$ or $PtMn$. To increase the pinning effect, one can also create a synthetic anti-ferromagnetic (SAF) [23], based on the same principle than the multilayers presented previously. Two layers of $CoFe$ are separated by a spacer of Ruthenium, whose thickness is chosen to create an anti-ferromagnetic coupling between them [42]. One of the main advantage of this SAF-based configuration is that, in microscopic structures, the static field created by the pinned layer on the free layer is nearly canceled because of the anti-parallel alignment of the two $CoFe$ magnetizations [6]. As the free layer is not affected by this stray field, it improves the sensitivity of the spin valve [15]. Moreover, a stronger pinning ensures a stability that allows the sensor to operate at higher fields.

Two layers of Tantale are deposited on both sides of the stack, acting as binder layers, to ensure a good adhesion with the adjacent layer. The stacks are usually deposited on a silicon substrate of 700 µm, insulated by 1 µm of SiO_2. Most of the stacks used for this work were purchased from an external supplier, but the very last samples were deposited in-house with a sputtering machine Rotaris. It opens new possibilities for improving the quality of the stacks, studying deeply the coupling between every layer, and understanding the influence of their thickness.

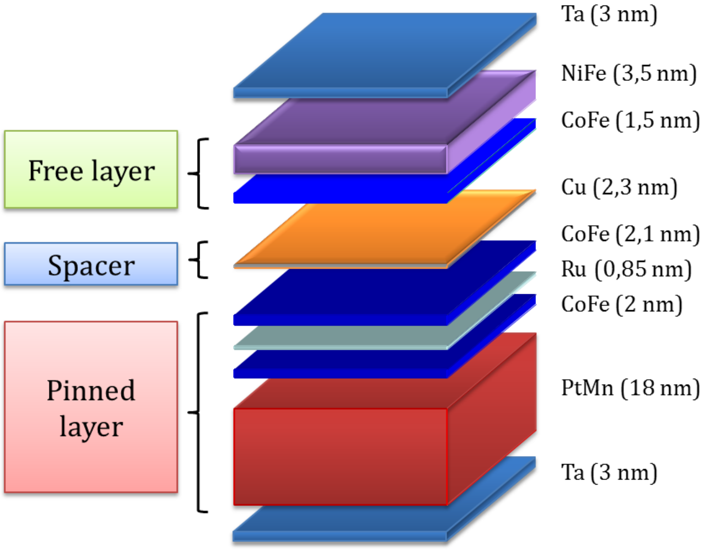

Figure 2.4: **Typical spin valve stack composition.** The order of deposition of each layers is chosen so that the two $CoFe$ layers, which have a high spin polarization, surround the spacer. Adding a synthetic anti-ferromagnetic increases the coercivity of the hard layer and cancels its stray field, that would affect the free layer and lower the sensitivity of the sensor. This configuration has been used for every spin valve fabricated throughout this work.

2.3.2 Probe design

One of the fundamental properties of every kind of sensor is the linearity of its response to an input quantity. In the case of a spin valve, the linearity is ensured if every spin of the free layer aligns and rotates perfectly with the applied magnetic field. It means that one can consider the free layer as a single magnetic domain. A magnetic domain is defined as a region within a material where the magnetization is homogeneous. However, for a piece of ferromagnetic material larger than a few microns, a spontaneous division in many domains occurs, in order to minimize the global energy of the system [10]. This effect is illustrated by numerical simulations in Figure 2.5. As each domain's magnetization will reverse one after another, the response of the sensor will exhibit both an hysteresis and discontinuities in its sensitive part. One way to obtain a mono-domain free layer, is to place a flat magnet below the sensor, in order to create a magnetostatic field that forces the magnetic moments to align parallel to each other. Another way, which is only valid for a microscopic structure, is to pattern a rectangular shape with a high aspect ratio so that the magnetization will tend to align along the length of the bar, which is called the easy axis. The most efficient shapes that allow domain structures to be avoided are the yoke shape and meanders [30]. One of the advantages of the GMR technology is that the sensors are highly malleable in shape, from a few microns to several millimeters, so that they can be adapted to the two specific biological experiments presented in the following chapters. The design of the sensors has been made using a lithography process, presented below.

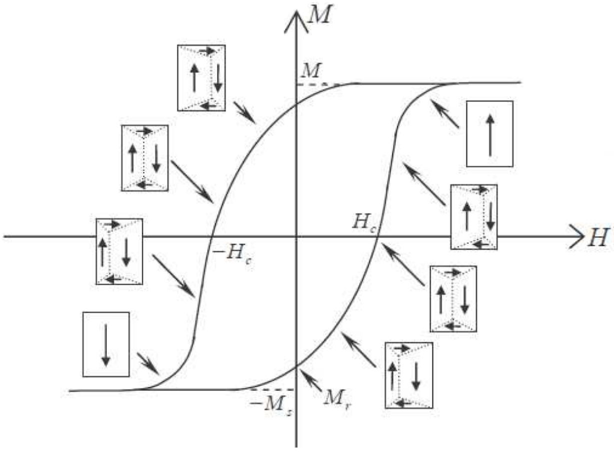

Figure 2.5: **Magnetization of a ferromagnetic bar as a function of the applied field [33].** The creation of magnetic domains within the free layer induces a large hysteresis. The variation of resistance of the sensor will not be perfectly linear because of these discontinuities.

2.3.3 Photo-Lithography

When the spin valve stack has been deposited on a substrate, patterning the desired shape is made with a photo-lithography process. Since the size of the sample can go down to a few micrometers, the whole process is realized in a clean-room to avoid any impurities. Here are the different steps of a lithography process:

1. A few drops of a photo-sensitive polymer resin, called photoresist, is deposited over the whole sample, and a homogeneous thickness is obtained by spin-coating. The substrate is placed on a chuck and maintained in vacuum while rotating at 5000 rpm. The thickness of the photoresist varies between 1 to 10 µm.
2. The sample is placed for 3 minutes on hot plate at 110°C, in order to make the solvent evaporate and to keep nothing but the active polymer chains of the photoresist.
3. A UV beam is shined on the sample through a mask on which the desired patterns are sketched. The mask is made of quartz, and the patterns of Chromium, which is opaque to the UV light. When the beam reaches the exposed parts of the photoresist, the carbon chains of the polymer are broken, so that they will be easily removed in a basic solution.
4. The sample is immersed into a basic developer (pH = 12) for 60 seconds in order to remove the photoresist from the exposed areas and to reveal the latent patterns. Finally, the sample is rinsed in deionized water and dried.

Since the polymer resin is sensitive to UV light, all the process is realized in a specific room, shielded against the UV radiation. The choice of the photoresist and its thickness depends on the following step:

- Etching process: the photoresist has to remain on the regions that have to be conserved so that they will be protected during the etching process. In this case, the required thickness is quite low, around 1 µm.
- Deposition process: a given material will be deposited all over the sample. The photoresist has to remain on the regions where there should be no deposition. Then, when the sample is immersed into acetone to dissolve the photoresist, the deposited material will be removed. This is called a "lift-off" process, and is commonly used when the chosen materials are difficult to etch. The thickness of the resin needs to be around 3 times the one of the deposited material to obtain a clean lift-off.

One of the main issues in the field of micro-fabrication is the improvement of the spatial resolution. It is intrinsically limited by the diffraction of the light beam when passing through the mask. The size of the diffraction spot on the sample is proportional to the wavelength of the beam. In order to get the highest resolution, the sample needs to be as close as possible from the mask, and the wavelength to be the lowest possible, that is why UV light ($\lambda \approx 300$ nm) has been chosen. The creation of patterns in the nanometer range implies the use of accelerated electrons, as their wavelength can be much smaller. This method is known as electron lithography. However, the dimensions of the GMR sensors are adapted to the size of neurons, *i.e* a few micrometers, so optical lithography technique has been used throughout this work.

2.3.4 Etching

This step consists of etching the regions of the sample that are no more protected by the photoresist. Different etching techniques are commonly used. Ion beam etching is obtained by bombarding the sample with highly energetic ions of Argon, which knock atoms from the surface of the sample. Another method based on a chemically reactive plasma, called reactive-ion etching, can be used. These techniques are usually referred to as "dry" etching. In contrast, the sample can be immersed in a bath of etchants that will remove the parts to be etched via chemical reactions, which is called a "wet" etching. A dry etching has been performed because of its anisotropic property: the ions strike the sample vertically, which provides sharp and well-shaped features, contrary to chemical etching that erodes the sample in every direction. Once the etching is done, the sample is bathed into acetone to remove the residual photoresist layer on the GMR stack, so that contact lines can be deposited above.

Step	Technique	Parameters
GMR shape	UV Litho	Photoresist S1813, spin-coating 60 s at 5000 rpm
		Baking 3 min at 110°C
		Exposure 20 s - Remover MF319 45 s
	Ion Beam Etching	20 min

2.3.5 Deposition techniques

Once the stack has been etched, three operations combining a lithography and a deposition process are executed:

1. Gold lines for electrical contacts to the sensor

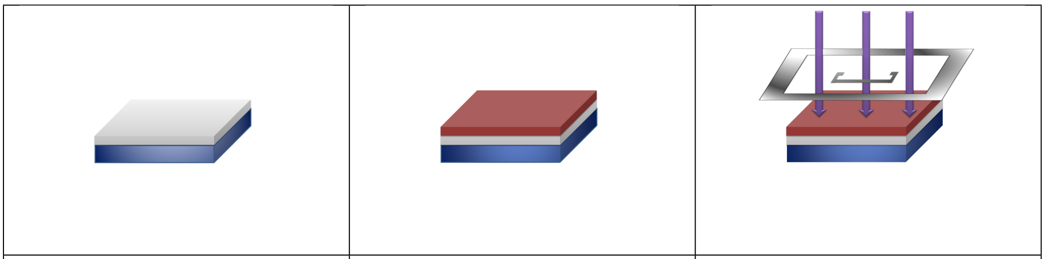

GMR stack (grey) Silicon substrate (blue)

Spin-coating of photoresist (red)

UV Lithography through the mask

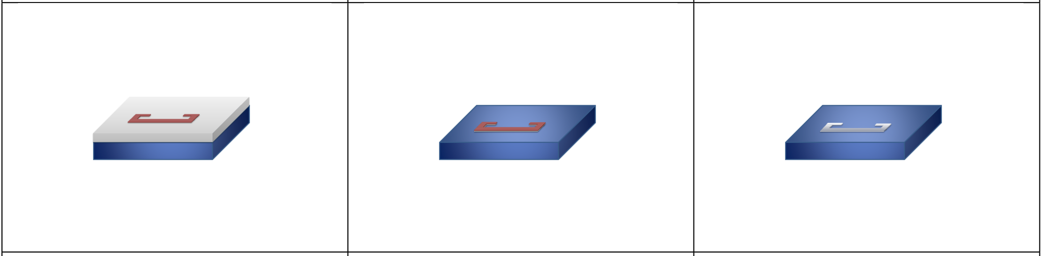

GMR protected before the etching process

After the etching process

Removal of residual photoresist

Figure 2.6: **Etching of the GMR stack**

2. Platinum electrodes to measure the local potential (*in vivo* probes only)
3. Alumina passivation layers to avoid any leakage to or from the conductive medium

Two techniques of deposition can be implemented according to the material, either an evaporation or a sputtering process. In both cases, the deposition is performed in ultra-vacuum. The pressure is maintained around $P = 10^{-8}$ mbar. When the pressure is so low, the particles propagate directly from the target to the sample without reacting or colliding with particles of the residual gas. For example, the mean free path of a gold particle is given by $l = \frac{k_B T}{\sqrt{2}\pi d^2 P} \approx 50$ km, where d is the diameter of the particle (135 pm). The thickness of the deposition can be read directly on a quartz-based micro-scale. The quartz is fed with an alternating current and vibrates at its mechanical resonance frequency. This frequency decreases with the amount of material increasing on the sample. The deposition rate varies between 1 and 15 nm/min. During the evaporation process, the material to be deposited is heated above its boiling point by a high-energy electron beam, then it condensates on the sample. A sputtering process relies on a plasma that creates energetic particles that bombard the target of the material to be deposited. An Argon plasma it generally used, because it will not react with the target material. Sputtering is particularly efficient for the deposition of compounds, since different components would otherwise tend to evaporate at different rates.

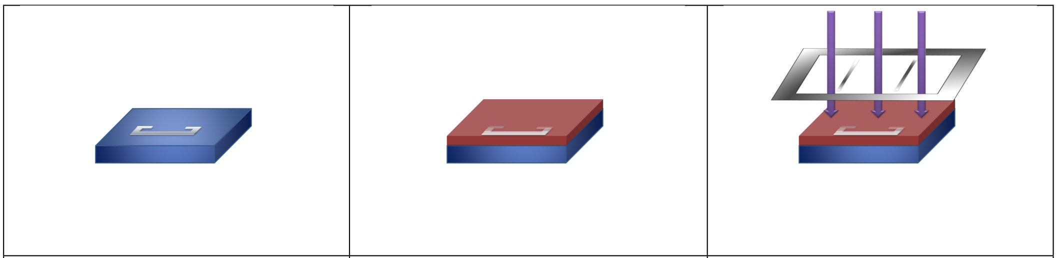

Yoke-shaped GMR (grey)
Silicon substrate (blue)

Spin-coating of
photoresist (red)

UV Lithography
through the mask

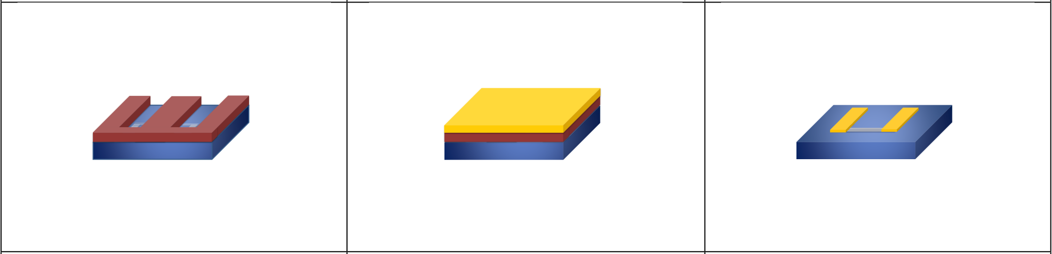

Contact lines
are patterned

Titanium/Gold evaporated
across the sample

After the lift-off
process

Figure 2.7: **Deposition process**

Step	Technique	Parameters
Contacts	UV Litho	Photoresist S1818, spin-coating 60 s at 5000 rpm
		Baking 3 min at 110°C
		Exposure 25 s - Remover MF319 60 s
	Deposition	Pre-etching 30 s
		Evaporation Titanium, 15 nm
		Evaporation Gold, 100 nm
		Evaporation Titanium, 15 nm

2.3.6 Cutting of the sample

The very first step of the process consisted in etching the GMR stack to define the shape of the sensitive part. However, the thickness of this stack was about only 40 nm. Here, the sample has to be released from the silicon substrate, which thickness varies between 200 and 700 µm. The typical commercial substrate is 700-µm thick, and can be ground down to 200 µm, as the needle-shaped probe developed for *in vivo* experiments has to be as thin as possible. The sensors used for the muscle experiment are not subject to this constrain and therefore they are much more robust. This is why these probes have been directly diced with a diamond tip. Concerning the *in vivo* probes, the cutting technique has to be accurate within a few micrometers. During the first two years of this work, the silicon substrate of these sensors was etched by a Deep Reactive-Ion Etching (Deep-RIE) process, performed at the Institut d'Electronique Fondamentale, in Orsay. Then, a new laser cutting machine was purchased by the laboratory, so that the whole process was carried out in-house.

2.3.6.1 Deep-RIE

The Deep-RIE technique was developed by the company Bosch in the early 1990s [22]. It enables very deep etching in silicon (≥ 1 mm), with a very high aspect-ratio (≥ 100), at a rate that can reach 10 µm per minute [21, 25]. This Bosch process performs a highly-anisotropic etch by alternating two steps: a chemical SF_6-based etching and a deposition of a chemically inert passivation layer of C_4F_8. The chemical etching is isotropic but if the steps are kept short, one can achieve clean deep anisotropic etching. In our case, the Bosch process lasted around 30 minutes to etch 200 µm of silicon, but a lithography step had to be carried out to protect the sensor, involving a thick photoresist of 9 µm that had to be baked for 1 hour.

Step	Technique	Parameters
Cutting	UV Litho	Photoresist AZ4562 (9 µm), spin-coating 30 s at 2000 rpm
		Baking 1h at 90°C
		Exposure 60s - Remover AZ400K 5 min
	Deep-RIE	Etching SiO_2 with CHF_3 300 s
		Etching Si with SF_6 400 cycles of 5 s

2.3.6.2 Laser cutting

The very last fabricated sensors have been shaped by laser cutting. This technique brings many advantages compared to the Deep-RIE process: no need for a lithography step, flexibility for the desired shape that was previously set by the mask, possibility to etch different type of wafers such as Silicon, Sapphire, glass, ceramics, etc... An excimer laser operates at 193 nm, and its focused beam heats the surface of the sample to the boiling point. However, the main limitation of this technique is the width of the furrow that is around 100 µm, especially since the laser has to run several times the same path to cut through the wafer. Optimization effort will be required to obtain the same etching quality than with the deep-RIE process. The probe was then mounted on a printed circuit board (PCB) by glueing its upper side and then contacted to the copper lines by wire-bonding. Wire-bonds were 25-µm thick and were protected by encapsulation in thin araldite glue. The sensor is now ready to undergo a series of standardized tests, in order to characterize its magneto-resistance and its noise level.

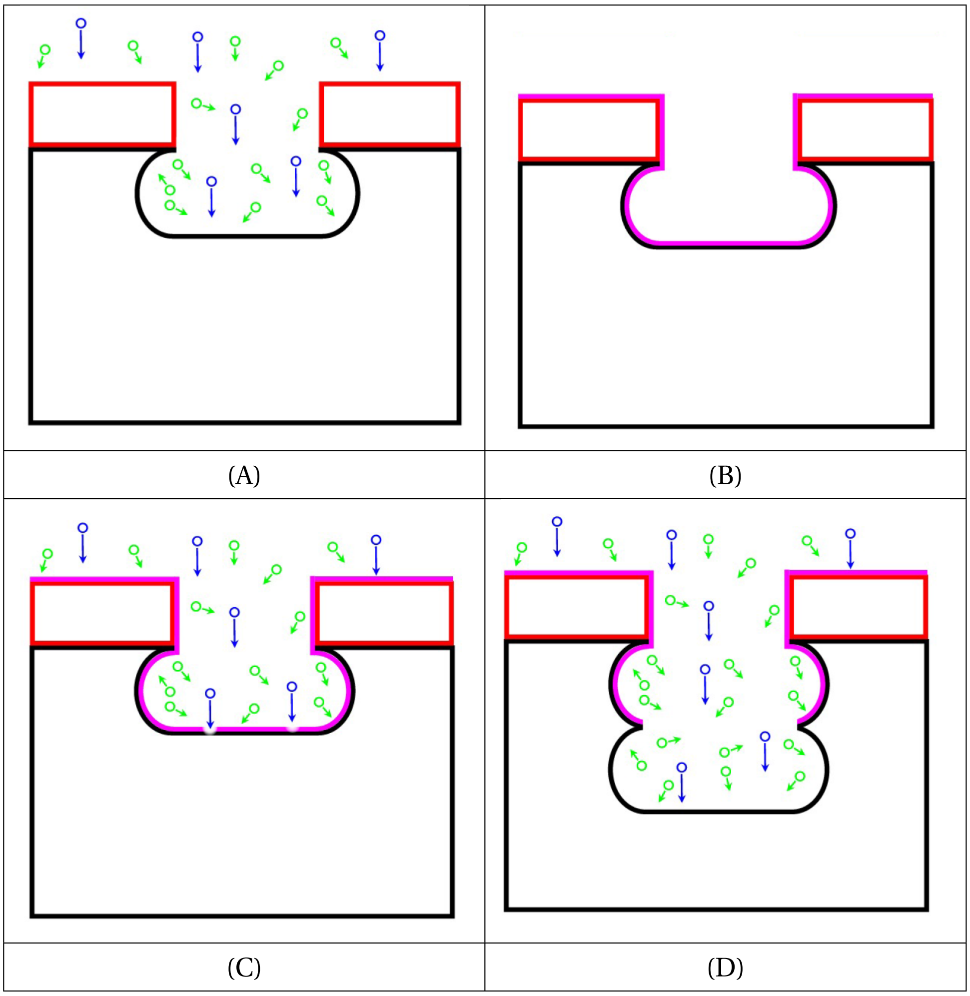
(A) (B) (C) (D)

Figure 2.8: **Deep Reactive-Ion Etching process.** **(A)** The part of the silicon substrate (black) which is not protected by a thick layer of photoresist (red) is etched by both directional ions (blue) and reactive chemical species (green). **(B)** Deposition of a chemically inert passivation layer (pink) so that all the surfaces are coated. **(C)** Energetic ions break through the passivation at the bottom of the trench, exposing the silicon to the chemical etchant. **(D)** Repeating short steps allows to obtain an anisotropic etch of the substrate. Each cycles lasts around 5 s, 400 cycles are required to etch a 200-µm thick silicon substrate.

2.4 Performance of GMR sensors

2.4.1 Magneto-transport

The first step is to measure the response of the spin valve to an applied magnetic field, *i.e* its resistance variation. The sensor is placed at the center of a Helmholtz coil, which is made of two solenoids located symmetrically along the same axis, and separated by a distance equal to the radius of the coils. This configuration makes the magnetic field very uniform at the center. The sensor is fed by a DC current of 1 mA, and its output voltage is directly proportional to the value of the resistance, according to the Ohm's law.

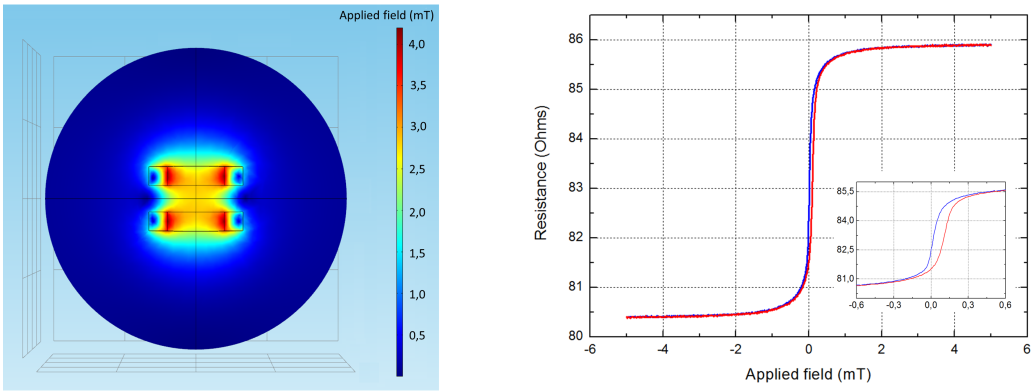

Figure 2.9: **Left:** Simulation of the magnetic field created by the Helmholtz coil used for the measurements. Each solenoid is made of 80 loops and carries a current of 6 A. The sensor is placed at the center where the uniformity of the field is maximum. **Right:** Resistance variation of the spin valve for a magnetic field varying between ±5 mT. In this case, $R_{AP} = 86$ Ohms and $R_P = 80.5$ Ohms. It gives a MR ratio of 6.6 %. Inset: zoom around $B = 0$, the coercive field of the free layer is about 0.1 mT.

The typical response of a probe used for *in vitro* experiments is given Figure 2.9. It provides the following information:

- **Magneto-resistive ratio:** several definitions can be found in the literature, the one chosen along this work is widely used for spin valve structures, and is defined as follows:

$$MR = \frac{R_{AP} - R_P}{(R_P + R_{AP})/2} \tag{2.4}$$

where R_P (resp. R_{AP}) refers to the resistance of the structure when the free layer and the hard layer are aligned in a parallel (resp. anti-parallel) configuration. For the response presented here, $R_{AP} = 86$ Ohms and $R_P = 80.5$ Ohms, the MR ratio is 6.6 %.

- **Sensitivity:** corresponds to the slope of the response around zero, defined as:

$$s = \frac{\Delta R}{\Delta B} = \frac{R_2 - R_1}{(R_1 + R_2)/2} \times \frac{1}{B_2 - B_1} \tag{2.5}$$

  Let's take two symmetric points from the plot 2.9: ($B_1 = -0.1$ mT ; $R_1 = 81$ Ohms) and ($B_2 = 0.1$ mT ; $R_2 = 85$ Ohms). The sensitivity is around 24 %/mT.

- **Magnetic hysteresis:** as stated above, the creation of magnetic domains in the free layer generates a different response depending on whether the magnetic field is swept back or forth between two opposite values. In this case, the two curves are nearly identical.

- **Centering around zero field:** a small dipolar coupling between the free layer and the hard layer or the roughness of their interfaces can induce a positive or negative shift of the response. The sensitivity decreases drastically with such a shift.

- **Linearity:** the switching of magnetic domains contributes also to a deterioration of the smoothness of the curve in the sensitive part.

If one of these defects appears, one can put a magnet close to the sensor. It generates a bias field, so that the spins of the free layer are slightly held back. The hysteresis will be reduced as well as the jumps of resistance (see Figure 2.10). However, the choice and the positioning must be very precise, since an excessive bias field would flatten the slope and reduce sensitivity.

2.4.2 Noise

2.4.2.1 Noise sources

As defined above, the sensitivity is a key performance indicator of the sensor. However, the most important characteristic is the signal-to-noise ratio (SNR) that can be obtained. In fact, if the intrinsic noise of the device is high, even the best sensitivity won't enable the detection of an ultra-low field. Magneto-resistive sensors are subject to different kinds of noise that are described below. They are all described in terms of power spectral density, expressed in $V/\sqrt{Hz}$, in order to simplify their handling:

- **Thermal noise:** the thermal motion of electrons in a conductor produces a spontaneous random variation of potential between the ends of the conductor. This

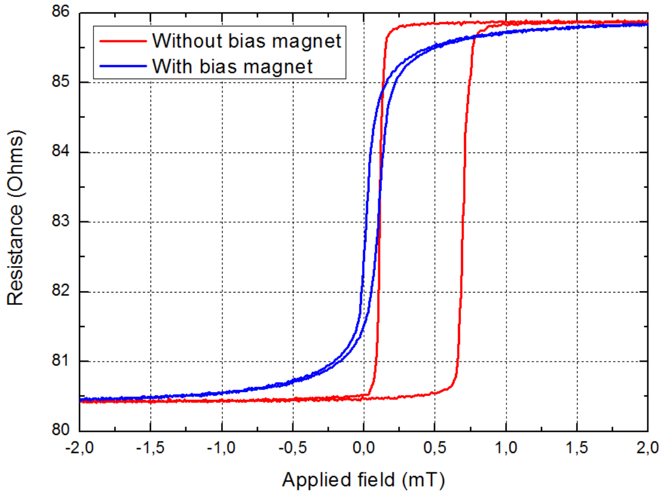

Figure 2.10: **Effect of a bias magnet on the response of the sensor.** Resistance variation of the spin valve with (blue) and without (red) the biasing magnet. The hysteretic behavior is largely reduced, the sensor exhibits a linear variation around zero field.

effect is sometimes called the Johnson-Nyquist noise, since it has been discovered experimentally by J.B Johnson [19] and described theoretically by H. Nyquist in 1928 [29].

$$\sqrt{S_v(f)} = \sqrt{4k_B T R} \tag{2.6}$$

where k_B is the Boltzmann constant, T represents the temperature, and R is the resistance of the device. One can notice that this expression is valid for every material, and is independent of the frequency as long as $f < (k_B T/h) \approx 6$ THz. It means that the power spectrum is nearly constant and represents a "noise floor" that can be easily calculated for each sensor being measured. The agreement between the predicted noise floor and the measurement is used to ensure the reliability of the result.

- **Low-frequency noise:** is the main limiting factor for the detection of ultra-low field in the frequency range of [0.1 Hz – 10 kHz], since it overcomes the contribution of the thermal noise. For example, considering trapped charge carriers that are released with a time constant τ, then, for an infinite number of uniformly distributed time constants, the spectral power density assumes a pure $1/f$ distribution. However, with as few as three time constants spread over one or two decades, the spectrum is approximately $1/f$, that is why this form of noise is very common [35].

The power spectral density $S_v(f)$ of these fluctuations is noted $1/f^\beta$ $(0.5 < \beta < 1.5)$. The research work carried out in 1969 by Hooge [16] on small conductors led to an empirical formulation which is still considered as a reference to describe this phenomenon:

$$\sqrt{S_v(f)} = \sqrt{\frac{\gamma}{N_c f^\beta}}.(RI) \tag{2.7}$$

where γ is the dimensionless Hooge parameter, $(0.5 < \beta < 1.5)$, and N_c the number of charge carriers in the conductor, which is related to the volume of the structure. This means that the low-frequency noise is inversely proportional to the volume of the sample and becomes more and more dominant in small devices.

- **Random Telegraphic Noise (RTN):** is characterized by random fluctuations between metastable states of the magnetic domains of the free layer. This phenomenon induces unwanted resistance variations of the device, which are dependent on the bias current. As shown previously, an optimized yoke-shaped sensor will tend to keep the free layer as a mono-domain. This probability could be increased by depositing a thicker free layer, but this would induce a larger coercivity. The optimal thickness that gives the best trade-off between the coercivity and the RTN noise is around 5 nm [34].

The SNR of the sensor can be deduced from the expressions given above, considering a sensor that does not exhibit RTN noise. For a working bandwidth Δf, the SNR can be written as:

$$\mathrm{SNR} = \frac{S}{N} = \frac{RI}{\sqrt{4k_B T R \Delta f} + \sqrt{\frac{\gamma \Delta f}{N_c f^\beta}}.(RI)} \tag{2.8}$$

The SNR increases with the volume and the resistance of the structure. For local biological experiments, no cooling system can be set up so the operating temperature remains fixed. This expression also underlies the fact that increasing the bias current is an effective solution only at high frequencies, in the thermal noise regime.

2.4.2.2 Measurement setup

The acquisition chain sets up to measure the noise of every device is the same as the one used from the biological experiment (see Figure 2.11). This gives a reliable reference about the performance of the sensor. All the measurements are made in a magnetically shielded room. This room is made of mu-metal, a nickel-iron alloy exhibiting a very high permeability, and aluminum layers. Any external static field will follow the path of highest permeability, as described in the previous chapter related to MEG measurement environment. It ensures that the environmental noise remains lower than the intrinsic noise of the sensor and does not disturb the experiments. The residual field inside this shielded room is 0.02 $\mathrm{fT}/\sqrt{Hz}$ at 100 Hz.

The GMR is inserted in a Wheatstone bridge, which is the best configuration to measure accurately tiny resistance variations. The bridge is powered by batteries, as are the two low-noise amplifiers, in order to get rid of interference at the power line frequency (50 Hz and its harmonics). Since the aim is to get access to the intrinsic noise of the sensor, one has to make sure that the noise brought by the acquisition chain does not influence the recording. Two points confirm that this condition is met:

- Considering two amplifiers connected one after the other, with respective gains G_1 and G_2, and their input noise levels N_1 and N_2. The SNR of the system is given by:

  $$(\mathrm{SNR})^2 = (\frac{S}{N})^2 = \frac{(SG_1G_2)^2}{(N_1G_1G_2)^2 + (N_2G_2)^2} = \frac{S^2}{(N_1)^2 + (N_2/G_1)^2} \approx \frac{S^2}{(N_1)^2} \tag{2.9}$$

  The noise level of the second amplifier is negligible, provided the gain of the first amplifier is sufficiently high. This is why the first gain stage is of key importance, as it set the noise of the global system. In our case, the first amplifier is an INA103, which exhibits a gain of 500 and an input voltage noise of 1 $\mathrm{nV}/\sqrt{Hz}$, while the noise of the second one, a SR560, is 4 $\mathrm{nV}/\sqrt{Hz}$.

- For an ideal amplifier, the noise floor of a 1kΩ GMR sensor is given by:

  $$\sqrt{S_{out}} = \sqrt{4k_B T R} = 4.1\, n\mathrm{V}/\sqrt{Hz} \tag{2.10}$$

  The input voltage noise $S_{in-voltage}$ and the input current noise $S_{in-current}$ need to be taken into account. They are respectively $\sqrt{S_{in-voltage}}$ = 1 $\mathrm{nV}/\sqrt{Hz}$ and $\sqrt{S_{in-current}}$ = 2 $\mathrm{pA}/\sqrt{Hz}$. That gives:

  $$\sqrt{S_{out}} = \sqrt{4k_B T R + S_{in-voltage} + (R)^2 S_{in-current}} = 4.6\, n\mathrm{V}/\sqrt{Hz} \tag{2.11}$$

  The noise level increases from 4.1 to 4.6 $\mathrm{nV}/\sqrt{Hz}$, so the thermal noise introduced by the acquisition chain is still much lower, around 12%, than the noise of the sensor.

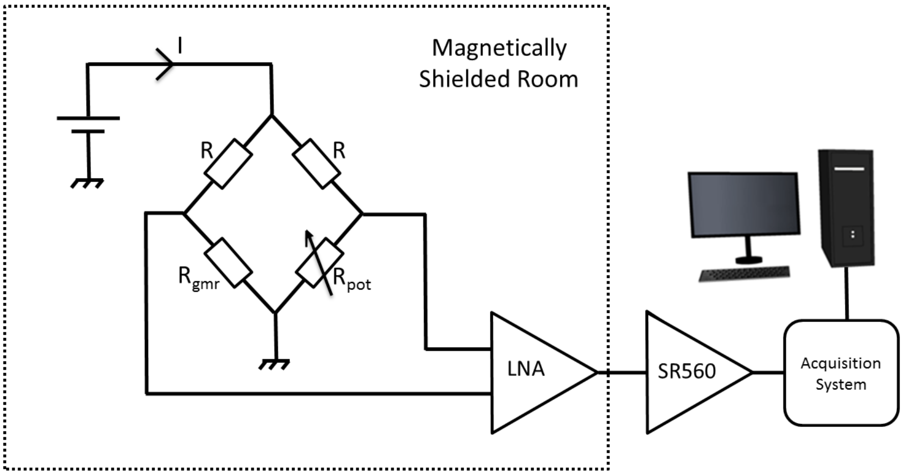

Figure 2.11: **Noise measurement setup.** The GMR sensor is included into a Wheastone bridge which is supplied by a DC current. The output of the bridge is zero when the adjustable resistance R_{pot} is equal to the one of the sensor R_{gmr}. The signal is amplified first by a Low-Noise Amplifier (LNA) INA103 and then by a second one (SR560) which also acts as a band-pass filter.

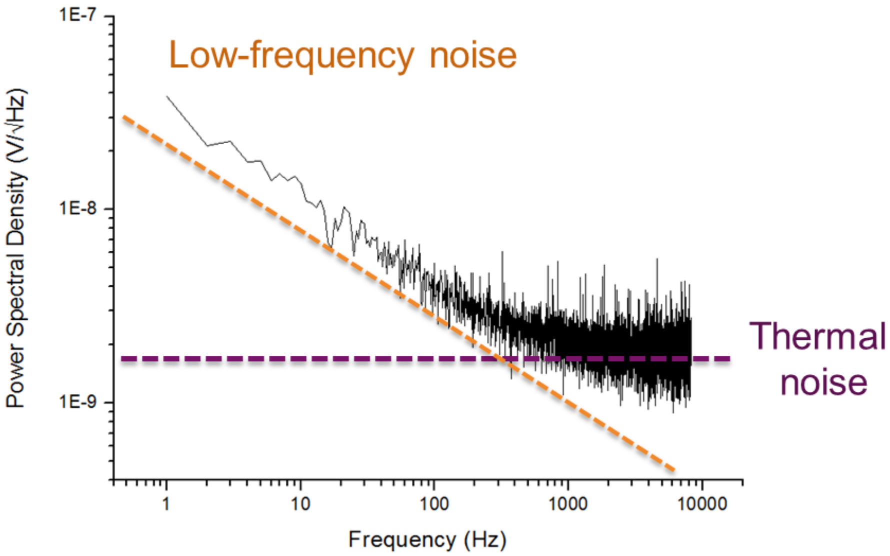

Figure 2.12: **Noise level of a GMR sensor.** The square root of the PSD exhibits two components: thermal noise and the low-frequency noise, which becomes dominant below 1 kHz. The resistance of the GMR sensor is $R = 85\Omega$, and the measurement is performed at room temperature $T = 300\mathrm{K}$. The noise floor can be deduced from $\sqrt{S_v(f)} = \sqrt{4k_B T R + S_{in-voltage} + (R)^2 S_{in-current}} \approx 1.5\, nV/\sqrt{Hz}$

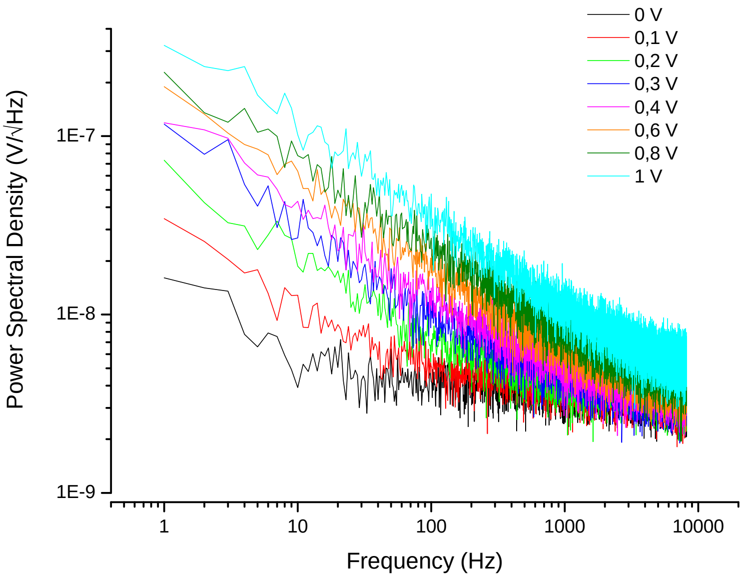

Figure 2.13: **Noise level for different bias.** The input voltage varies from 0 to 1 V. The low-frequency noise increases, as predicted by the formula defined by Hooge. The black curve (0 V) corresponds to the noise of the amplifier. The sensor was a meander made of 5 segments of 4x50 μm^2.

2.5 Low-frequency noise canceling

2.5.1 State of the art

For several decades, 1/f-noise has been observed in many various field: condensed matter systems [8], DNA base sequences [43], rate of traffic flow [37], economic data [24], music [44], rate of insulin uptake by diabetics [5], etc. This list is hardly exhaustive, however, no general theory have been developed so far to explain the widespread occurrence of 1/f-noise. Experiments have been carried out to determine the slope of the power spectral density at very low frequency, to check whether the shape would be modified or not. The 1/f noise in metal-oxide-semiconductor field effect transistors (MOSFET) has been measured down to $10^{-6.3}$ Hz, which corresponds to one cycle every three weeks [4], and no change was observed. The real physical origin of 1/f noise is still an open question [8].

Magneto-resistive sensors undergo low-frequency fluctuations that are believed to arise from two effects. The first component has an electric origin and is valid for every conductor. The trapping of charge carriers due to crystallographic defects, surface roughness or edge effects can induce these conductivity fluctuations. The second component has a magnetic origin, as it can be attributed to slow fluctuations of domains in the free layer. This thermal motion of domains appears to scale with the sensitivity of GMR sensors [36].

During this thesis, a modulation technique, that would theoretically suppress most of the low-frequency noise in GMR sensors, was developed. It implied the micro-fabrication of specific samples and dedicated electronic devices that are detailed below, beginning with the fundamental principle.

In AMR sensors, a method based on the modulation of the current direction has already been developed [26]. This technique can not be applied to GMR sensors, since their resistance and their resistance fluctuations do not depend of the current direction. Another strategy is to shift the operating frequency by using flux concentrators on a micro-electro-mechanical system (MEMS) that oscillates at kilohertz frequencies [9, 17]. However, these techniques remain hard to set up and are quite expensive.

2.5.2 Theoretical principle

The technique has started to be developed at the very end of this thesis and should represent an easy way to suppress the noise due to non-magnetic resistance fluctuations. The standard working mode of a magneto-resistive sensor is chosen to get the most sensitive response, *i.e* at the steepest part of the slope of the R(B) function. Here, the main idea is to switch very fast between this and other operating point, where the sensor is in a saturated state. To do that, a thin conductive line is deposited above the sensor. Current pulses are sent through this line to create a magnetic field that put the GMR in a saturated state. Consequently, the sensor oscillates between a sensitive state and a saturated state. An electronic circuit, known as a sample and hold, can lock the value of the signal during a given interval, that corresponds to half the modulation period in that case. Using two of them, one can extract two signals corresponding to both operating points. The first signal is carrying the information about the applied field and the intrinsic noise of the sensor, while the second one remains independent of the external field and carries nothing but the intrinsic noise. A linear combination of these two signals, using a differential amplifier, leads to a clean signal without the low-frequency noise. If this modulation of sensitivity occurs at a much larger frequency than the low-frequency noise limit, reconstructing any applied magnetic field becomes feasible. The global setup is shown Figure 2.14 and the corresponding shape of the expected signals have been simulated in Figure 2.15.

2.5.3 Custom-made sensors

Testing the theoretical principles described above required to develop specific sensors. A whole micro-fabrication process that meets the previous requirements has been carried out. The masks used for the lithography steps were designed to obtain four pairs of two yoke-shaped probes (see Figure 2.16). The two GMR sensors are placed very close, so that they feel the same external field, and their dimensions are identical. They are sensitive along the same direction, but their hard layers exhibit anti-parallel magnetizations: a given magnetic field will increase the resistance of one sensor, while the other one will decrease. As stated above, this configuration is used to obtain a larger signal at the output of the Wheatstone bridge. When the contact lines are deposited, a passivation layer is sputtered over the sample to ensures a protection against short-circuits that could occur after the deposition of the lines carrying the modulation current just above the sensors. The final shape of the sensor is obtained by laser cutting. Then, the sample is glued into a QFN package (Quad-Flat No-leads) and mounted on a printed circuit board to facilitate its handling. The full potential of this technique has not been validated experimentally so far because of the too large proportion of magnetic noise in our GMR stack. Illustrating results are shown Figure 2.17.

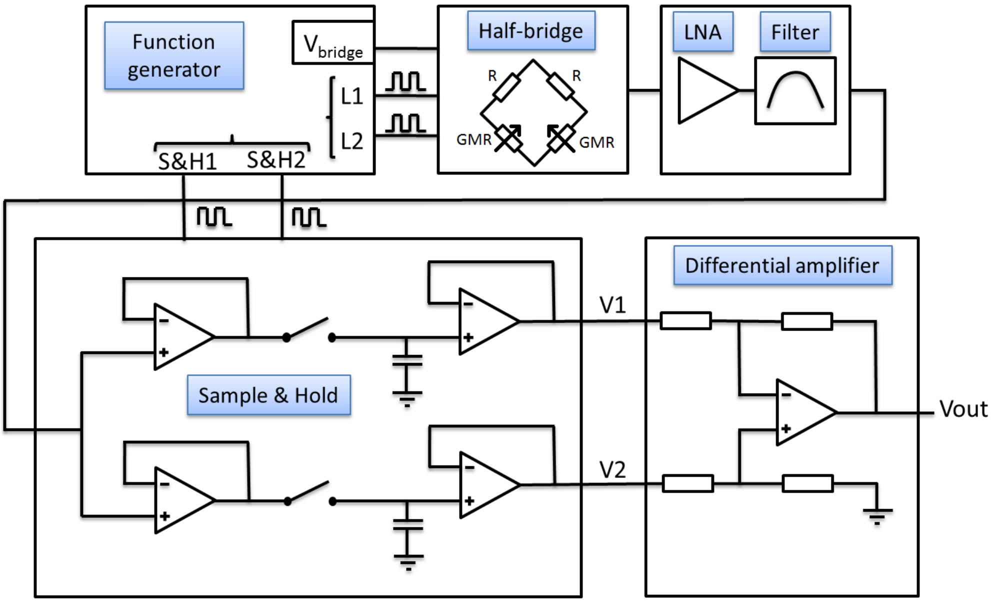

Figure 2.14: **Low-frequency noise canceling setup.** Two GMR sensors are included in a half-bridge configuration. Black arrows represent the anti-parallel magnetizations of their hard layers: a given magnetic field will increase the resistance of one GMR, while the other one will decrease. This configuration gives a larger signal at the output of the Wheatstone bridge. The bridge is supplied by a DC source V_{bridge}. Two in-phase square current pulses, L_1 and L_2, are sent through the lines passing just above the sensor, in order to modulate their sensitivities. The signal is amplified and filtered before going through the "sample-and-hold" circuit. To sample the input signal, the switch connects the capacitor to the output of a buffer amplifier. The buffer amplifier charges or discharges the capacitor so that the voltage across the capacitor is equal to the input voltage. In hold mode, the capacitor is disconnected from the buffer and maintains the output voltage at the previous input level. The switches are controlled by two square signals generated by the function generator, in order to set one of them in-phase with the current pulses and the other one out-of-phase. The V_1 output is based on each acquisition in the sensitive regime, while V_2 corresponds to the acquisitions in the saturated state. A differential amplifier gives an output signal V_{out} which is cleaned from the electric low-frequency noise. The sample-and-hold circuits and the differential amplifier could be also replaced by a digital signal processing unit.

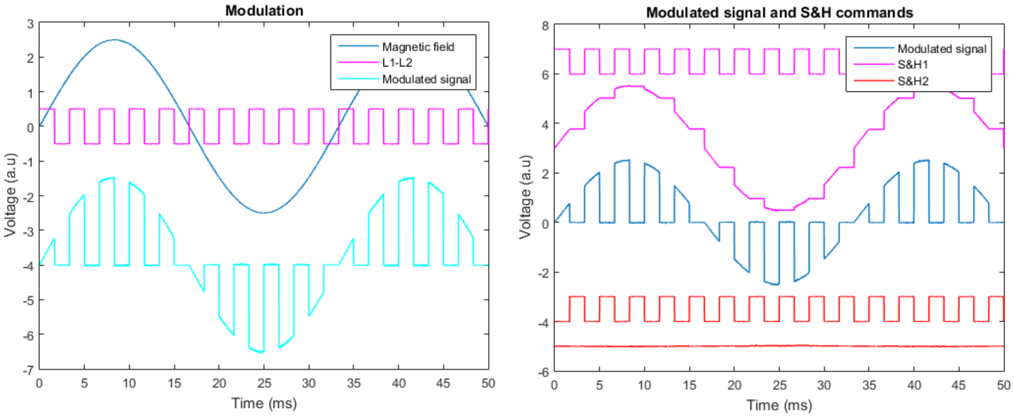

Figure 2.15: **Left:** An external sinusoidal magnetic field is applied to the sensor (blue). At the same time, a square wave is sent through the lines to put the sensor either in its sensitive mode or in its saturated state (pink). This gives a modulated signal (cyan, offset for clarity). **Right:** This modulated signal (blue) is sent to two sample and hold circuits. The two out-of-phase square commands are sent to each switch. The principle is to sample each working mode to reconstruct a signal that carries both the field to detect and the intrinsic noise (pink curve), and a signal that carries only the noise (red curve), so that they can be substracted right after. The modulation frequency is chosen sufficiently low for clarity. However, in practice, the function generator can easily drive hundreds of kilohertz wave, and one can see that the higher the modulation frequency, the cleaner the output will be.

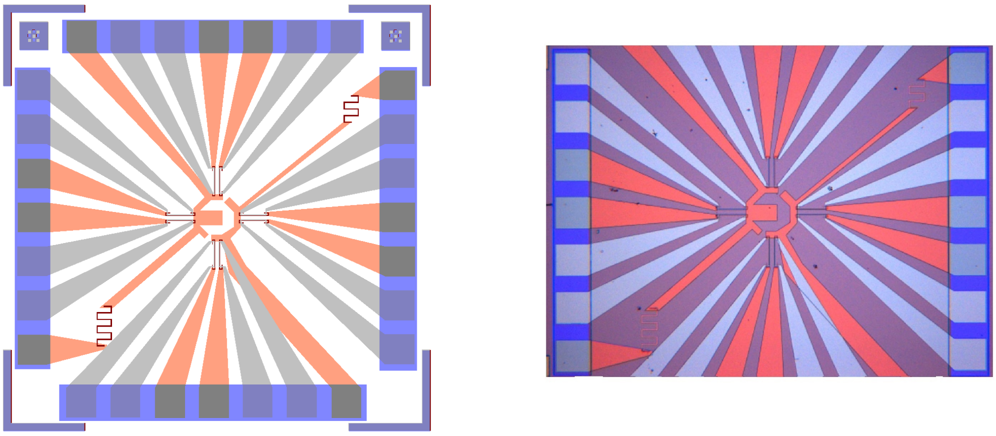

Figure 2.16: **Left:** Sketch of the masks used along the micro-fabrication process. Four pairs of yoke-shaped GMR sensors (red), are contacted by Tantalum/Copper lines (orange). Current lines passing above each sensors appear in grey. The whole sample is passivated, except the ends of the lines to enable wire-bonding (blue). Two resistances of different values allow to identify the way the sample is oriented once it is packaged. **Right:** Microscope image of the sample. The total width is 3 mm.

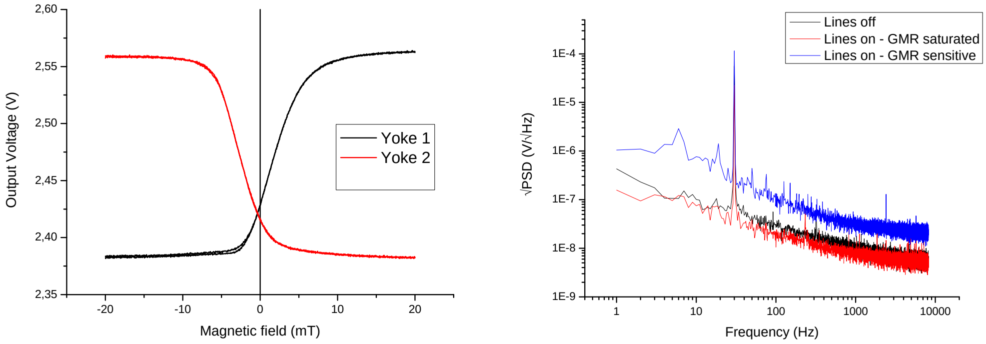

Figure 2.17: **Left:** Responses of two adjacent GMR sensors to an external magnetic field. Their hard layer magnetizations are set anti-parallel so that the half-bridge configuration will be efficient. Based on these curves, one can deduce that the field generated by a current pulse in the lines has to be at least of -5 mT (resp. +5 mT) for the yoke 1 (resp. yoke 2) to be saturated. **Right:** Noise level of the output signal in three cases: without any current pulses (black), with a current pulse that sets the sensor in its saturated state (red), with a current pulse that sets the sensor in its sensitive state (blue). The noise is much higher when the sensors are polarized in their sensitive state. This difference between the two states is necessarily due to intrinsic magnetic noise. The fact that the two working points exhibit a different noise level prevents any efficient noise subtraction. Future experiments based on a GMR stack that exhibits less magnetic noise should provide more significant results.

2.6 Conclusion

This second chapter describes how a leading technology has arisen from the discovery of a quantum property, the spin. It is worth noting that well before the concrete implementation of the sensors, most of the physical principles underlying the behavior of electrons in a ferromagnetic stack were already known. Perceiving the effects of the spin implies the fabrication of systems whose dimensions do not exceed the spin-diffusion length, around a few nanometers. The improvement of deposition techniques in the late 1980s enabled the production of ultra thin films, and the expected results followed right after.

Optimizing the properties of a magnetic structure is a very challenging task that was not addressed during this work as it would require a competitive in-house deposition machine that is still being implemented. However, the whole micro-fabrication process, described in this chapter, has been carried out in the clean room of the laboratory. It was a considerable advantage, taking into account the large number of parameters in such a process (photoresist thickness, coating speed, UV exposition power, time of removal, etching depth, etc...).

When one wants to measure the tiniest signal amplitudes, the performance of the sensors is obviously the key parameter. However, even the best sensor has to be included in a well-designed acquisition chain, so as not to see the efforts put in the fabrication being spoiled by a noisy environment. A novel method to reduce the electric low-frequency noise has been proposed, and should be validated soon.

Room-temperature, micron-sized GMR sensors able to detect magnetic field in the nanotesla range, all these advantages provided by this technology make it a serious candidate to perform magnetophysiology. Before going straight into the cortex, a simpler biological system was chosen to measure bio-magnetic fields: the mouse soleus muscle, whose magnetic signature is easily predictable. This study is presented in the next chapter.

Bibliography

[1] BAIBICH, M. N., J. M. BROTO, A. FERT, F. N. VAN DAU, F. PETROFF, P. ETIENNE, G. CREUZET, A. FRIEDERICH et J. CHAZELAS. 1988, «Giant magnetoresistance of (001) fe/(001) cr magnetic superlattices», *Physical review letters*, vol. 61, no. 21, p. 2472. 45, 47

[2] BASDEVANT, J.-L., J. DALIBARD et M. JOFFRE. 2002, *Mécanique quantique*, Editions Ecole Polytechnique. 43

[3] BINASCH, G., P. GRÜNBERG, F. SAURENBACH et W. ZINN. 1989, «Enhanced magnetoresistance in layered magnetic structures with antiferromagnetic interlayer exchange», *Physical review B*, vol. 39, no. 7, p. 4828. 45

[4] CALOYANNIDES, M. 1974, «Microcycle spectral estimates of 1/f noise in semiconductors», *Journal of Applied Physics*, vol. 45, no. 1, p. 307–316. 64

[5] CAMPBELL, M. J. et B. W. JONES. 1972, «Cyclic changes in insulin needs of an unstable diabetic», *Science*, vol. 177, no. 4052, p. 889–891. 64

[6] DIENY, B., M. LI, S. LIAO, C. HORNG et K. JU. 2000, «Quantitative interpretation of the magnetoresistive response (amplitude and shape) of spin valves with synthetic antiferromagnetic pinned layers», *Journal of Applied Physics*, vol. 87, no. 7, p. 3415–3420. 50

[7] DIENY, B., V. S. SPERIOSU, S. S. PARKIN, B. A. GURNEY, D. R. WILHOIT et D. MAURI. 1991, «Giant magnetoresistive in soft ferromagnetic multilayers», *Physical Review B*, vol. 43, no. 1, p. 1297. 47

[8] DUTTA, P. et P. HORN. 1981, «Low-frequency fluctuations in solids: 1/f noise», *Reviews of Modern physics*, vol. 53, no. 3, p. 497. 64

[9] EDELSTEIN, A., G. FISCHER, M. PEDERSEN, E. NOWAK, S. F. CHENG et C. NORDMAN. 2006, «Progress toward a thousandfold reduction in 1/ f noise in magnetic sensors using an ac microelectromechanical system flux concentrator», *Journal of applied physics*, vol. 99, no. 8, p. 08B317. 65

[10] FEYNMAN, R. P., R. B. LEIGHTON et M. SANDS. 2015, *The Feynman Lectures on Physics, Vol. II: The New Millennium Edition: Mainly Electromagnetism and Matter*, Hachette UK. 51

[11] FREITAS, P., R. FERREIRA, S. CARDOSO et F. CARDOSO. 2007, «Magnetoresistive sensors», *Journal of Physics: Condensed Matter*, vol. 19, no. 16, p. 165 221. 49

[12] GERLACH, W. et O. STERN. 1922, «Der experimentelle nachweis der richtungsquantelung im magnetfeld», *Zeitschrift für Physik A Hadrons and Nuclei*, vol. 9, no. 1, p. 349–352. 43

[13] GERLACH, W. et O. STERN. 1924, «über die richtungsquantelung im magnetfeld», *Annalen der Physik*, vol. 379, no. 16, p. 673–699. 43

[14] GRÜNBERG, P., R. SCHREIBER, Y. PANG, M. BRODSKY et H. SOWERS. 1986, «Layered magnetic structures: evidence for antiferromagnetic coupling of fe layers across cr interlayers», *Physical Review Letters*, vol. 57, no. 19, p. 2442. 46

[15] HEIM, D. E. et S. S. PARKIN. 1995, «Magnetoresistive spin valve sensor with improved pinned ferromagnetic layer and magnetic recording system using the sensor», US Patent 5,465,185. 50

[16] HOOGE, F. N. 1969, «$1/f$ noise is no surface effect», *Physics letters A*, vol. 29, no. 3, p. 139–140. 61

[17] HU, J., M. PAN, W. TIAN, D. CHEN, J. ZHAO et F. LUO. 2012, «1/f noise suppression of giant magnetoresistive sensors with vertical motion flux modulation», *Applied Physics Letters*, vol. 100, no. 24, p. 244 102. 65

[18] IKEDA, S., J. HAYAKAWA, Y. ASHIZAWA, Y. LEE, K. MIURA, H. HASEGAWA, M. TSUNODA, F. MATSUKURA et H. OHNO. 2008, «Tunnel magnetoresistance of 604% at 300 k by suppression of ta diffusion in co fe b/ mg o/ co fe b pseudo-spin-valves annealed at high temperature», *Applied Physics Letters*, vol. 93, no. 8, p. 082 508. 49

[19] JOHNSON, J. B. 1928, «Thermal agitation of electricity in conductors», *Physical review*, vol. 32, no. 1, p. 97. 60

[20] JULLIERE, M. 1975, «Tunneling between ferromagnetic films», *Physics letters A*, vol. 54, no. 3, p. 225–226. 49

[21] LAERME, F., A. SCHILP, K. FUNK et M. OFFENBERG. 1999, «Bosch deep silicon etching: improving uniformity and etch rate for advanced mems applications», dans *Micro Electro Mechanical Systems, 1999. MEMS'99. Twelfth IEEE International Conference on*, IEEE, p. 211–216. 56

[22] LAERMER, F. et A. SCHILP. 1996, «Method of anisotropically etching silicon», US Patent 5,501,893. 56

[23] LEAL, J. et M. KRYDER. 1998, «Spin valves exchange biased by co/ru/co synthetic antiferromagnets», *Journal of applied physics*, vol. 83, no. 7, p. 3720–3723. 49

[24] MANDELBROT, B. B. et J. W. VAN NESS. 1968, «Fractional brownian motions, fractional noises and applications», *SIAM review*, vol. 10, no. 4, p. 422–437. 64

[25] MARTY, F., L. ROUSSEAU, B. SAADANY, B. MERCIER, O. FRANÇAIS, Y. MITA et T. BOUROUINA. 2005, «Advanced etching of silicon based on deep reactive ion etching for silicon high aspect ratio microstructures and three-dimensional micro- and nanostructures», *Microelectronics journal*, vol. 36, no. 7, p. 673–677. 56

[26] MATEOS, I., J. RAMOS-CASTRO et A. LOBO. 2015, «Low-frequency noise characterization of a magnetic field monitoring system using an anisotropic magnetoresistance», *Sensors and Actuators A: Physical*, vol. 235, p. 57–63. 65

[27] MCGUIRE, T. et R. POTTER. 1975, «Anisotropic magnetoresistance in ferromagnetic 3d alloys», *IEEE Transactions on Magnetics*, vol. 11, no. 4, p. 1018–1038. 45

[28] MOTT, N. F. 1936, «The electrical conductivity of transition metals», dans *Proceedings of the Royal Society of London A: Mathematical, Physical and Engineering Sciences*, vol. 153, The Royal Society, p. 699–717. 46

[29] NYQUIST, H. 1928, «Thermal agitation of electric charge in conductors», *Physical review*, vol. 32, no. 1, p. 110. 60

[30] PANNETIER, M., C. FERMON, G. LE GOFF, J. SIMOLA, E. KERR et J. COEY. 2005, «Noise in small magnetic systems—applications to very sensitive magnetoresistive sensors», *Journal of magnetism and magnetic materials*, vol. 290, p. 1158–1160. 51

[31] PARKIN, S., N. MORE et K. ROCHE. 1990, «Oscillations in exchange coupling and magnetoresistance in metallic superlattice structures: Co/ru, co/cr, and fe/cr», *Physical Review Letters*, vol. 64, no. 19, p. 2304. 47

[32] PARKIN, S. S., C. KAISER, A. PANCHULA, P. M. RICE, B. HUGHES, M. SAMANT et S.-H. YANG. 2004, «Giant tunnelling magnetoresistance at room temperature with mgo (100) tunnel barriers», *Nature materials*, vol. 3, no. 12, p. 862–867. 49

[33] SOLIGNAC, A. 2012, *Réalisation et étude d'hétérostructures à base du manganite La0. 7Sr0. 3MnO3 pour des capteurs magnétiques oxydes ultrasensibles*, thèse de doctorat, Université Pierre et Marie Curie-Paris VI. 51

[34] POLOVY-DU SOUICH, H. 2010, *Capteurs mixtes pour applications médicales*, thèse de doctorat, Paris 6. 61

[35] SPIELER, H. 2002, «Measurements–iii electronic noise», *ICFA Instrumentation School, Istanbul*. 60

[36] STUTZKE, N. A., S. E. RUSSEK, D. P. PAPPAS et M. TONDRA. 2005, «Low-frequency noise measurements on commercial magnetoresistive magnetic field sensors», *Journal of Applied Physics*, vol. 97, no. 10, p. 10Q107. 65

[37] TAKAYASU, M. et H. TAKAYASU. 1993, «1/f noise in a traffic model», *fractals*, vol. 1, no. 04, p. 860–866. 64

[38] THOMSON, W. 1856, «On the electro-dynamic qualities of metals:–effects of magnetization on the electric conductivity of nickel and of iron», *Proceedings of the Royal Society of London*, vol. 8, p. 546–550. 45

[39] TRABESINGER, A. 2008, «Physics is set spinning», *Nature Milestones SPIN S*, vol. 5. 45

[40] TSANG, C., R. E. FONTANA, T. LIN, D. E. HEIM, V. S. SPERIOSU, B. A. GURNEY et M. L. WILLIAMS. 1994, «Design, fabrication and testing of spin-valve read heads for high density recording», *IEEE Transactions on Magnetics*, vol. 30, no. 6, p. 3801–3806. 45

[41] UHLENBECK, G. E. et S. GOUDSMIT. 1925, «Ersetzung der hypothese vom unmechanischen zwang durch eine forderung bezüglich des inneren verhaltens jedes einzelnen elektrons», *Naturwissenschaften*, vol. 13, no. 47, p. 953–954. 44

[42] VELOSO, A. et F. P. P. 2000, «Spin valve sensors with synthetic free and pinned layers», *Journal of Applied Physics*, vol. 87, no. 9, p. 5744–5746. 50

[43] VOSS, R. F. 1992, «Evolution of long-range fractal correlations and 1/f noise in dna base sequences», *Physical review letters*, vol. 68, no. 25, p. 3805. 64

[44] VOSS, R. F. et J. CLARKE. 1978, «"1/f noise"in music: Music from 1/f noise», *The Journal of the Acoustical Society of America*, vol. 63, no. 1, p. 258–263. 64

[45] YUASA, S., T. NAGAHAMA, A. FUKUSHIMA, Y. SUZUKI et K. ANDO. 2004, «Giant room-temperature magnetoresistance in single-crystal fe/mgo/fe magnetic tunnel junctions», *Nature materials*, vol. 3, no. 12, p. 868–871. 49

[46] ZIMMERMANN, E., A. VERWEERD, W. GLAAS, A. TILLMANN et A. KEMNA. 2005, «An amr sensor-based measurement system for magnetoelectrical resistivity tomography», *IEEE Sensors Journal*, vol. 5, no. 2, p. 233–241. 45

Chapter 3

In-vitro magnetic action potential in skeletal muscle

Le succès, c'est d'aller d'échec en échec sans perdre son enthousiasme

Winston Churchill

Contents

Introduction

This third chapter presents the experiments that were conducted at the "Unité de Neurosciences, Information et Compléxité" (UNIC) of the Centre National de la Recherche Scientifique (CNRS). The main goal of this study was to show the compatibility of the GMR technology with local recordings of biological magnetic fields. All the dissections and electro-physiological characterizations have been performed by G. Ouanounou. The modeling part was developed by F. Barbieri. The results have been published in 2016 in *Scientific Reports* [2] and are available in open access. Animal care followed the European Union regulations (O.J. of E.C. L358/1 18 December 1986), and the European directive 2010/63/UE. For all of the results presented in this chapter, 3 to 5-month-old Swiss mice were anesthetized with isoflurane, and cervical dislocated. Dissections were performed within 15 minutes in an oxygenated Ringer solution of the following composition (in mM): 145 NaCl, 3 KCl, 2 $CaCl_2$, 1 $MgCl_2$, 10 HEPES (pH 7.4) and 11 glucose. Intra- and extra-cellular recordings were performed at room temperature in the oxygenated Ringer solution.

3.1 Theoretical framework

3.1.1 Magnetomyography (MMG)

In 1972, a few months after having reported the first MEG recordings of alpha rhythm in a human brain, D. Cohen performed the very first measurements of the magnetic signature generated by muscles [5]. He coined the term *magnetomyography* (MMG), to describe the SQUID-based experiments that led to these results, and, more broadly, every recording of a magnetic field generated by ionic currents in a skeletal muscle. A skeletal muscle is characterized by being under conscious control of the somatic nervous system, and it is attached to bones via a bundle of collagen fibers called tendon. The two other types of muscles are cardiac muscle and smooth muscles (blood vessels, esophagus, stomach, intestine), which are classified as involuntary muscles. However, since the pioneering results of Cohen, most of the researches in biomagnetism focused on MEG or magnetocardiography (MCG). MMG signals were most often presented as artifacts occurring during MEG recordings, because of their higher amplitude [20, 23].

Investigating the magnetic field due to muscular activity is of key interest, for the same reasons as noted earlier for MEG. Contrary to electromyography, which strongly depends on the dielectric properties of the surrounding biological tissues, MMG signals can propagate without distortion, since the permeability of the tissues is the same as free space. However, just as in MEG, one has to take into account the return currents flowing in the extracellular medium that screen the magnetic field of interest. This screening effect will be quantified in the following modeling section. Nevertheless, the transparency of the body to magnetic fields opens the possibility to access deep muscle sources that can not be measured via the skin electric potential. Moreover, assuming that the source configuration is otherwise known, a set of three orthogonal magnetic sensors would provide a complete description of the magnetic field vector, which contains information about the direction of propagation of ionic currents. It could be done without any physical contact with the subject, and the possibility to place the magnetic sensors at various locations over the targeted area opens the way to tomography and imaging.

The activation of a muscle fiber is similar to the process occurring in neurons, as the contraction is triggered when an action potential is transmitted via the neuro-muscular junction. The muscle structure shows ideal biophysical features, which are detailed below, to record clearly the magnetic signature of an action potential. The first experiments reported by Cohen revealed the activation of each muscle implied in the contraction of the elbow (biceps, triceps, brachialis) of the subject. The SQUID was placed a few centimeters from the sources to be sensitive to the entire system, but this distance prevents from locating accurately the position of an action potential along the muscle fibers. Measuring the magnetic signature of a single action potential could be done through *in vitro* experiments, so that a single activation could be triggered via a pulse generator. The very first signal was obtained in 1985 on a giant axon of a crayfish, threaded through a toroidal pick-up coil [25]. The first recordings showing clearly the magnetic field due to a single muscular action potential have been reported in 1988 [17] (see Figure 3.1).

3.1.2 Nerve-Muscle features

In order to demonstrate the ability of GMR-based sensors to record locally biological magnetic fields, one of the simplest biological structure has been chosen: the mouse skeletal soleus muscle. The soleus muscle is located in the back part of the lower leg: it starts from the knee and is connected to the heel via Achilles tendon. The soleus is composed of a few hundred of muscle fibers aligned parallel to each other. As well as neurons, muscle fibers are excitable cells that can be activated by an electrical input pulse coming from the nerve. However, as detailed in Chapter 1, neurons fire an action potential only when the summation of post-synaptic potentials, coming from thousands of neighboring cells, reaches a given potential threshold. In the case of soleus muscle, the

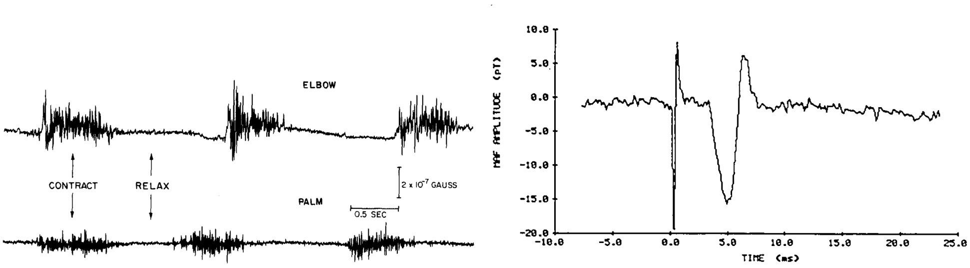

Figure 3.1: **Left:** Very first MMG recordings of the magnetic field generated by a voluntary flexion of human elbow and palm contractions [5]. The SQUID magnetometer was located 4 cm above the elbow, and then inside the palm of the hand, as the hand was wrapped around the Helium Dewar. The amplitude was up to 30 pT. **Right:** Magnetic field induced by an action potential propagating along an excised frog muscle (gastrocnemius) [17]. The SQUID was located 17 mm above the plane of the muscle. The curve represents the averaging of 9 successive responses. The signal has a biphasic shape with a peak-to-peak amplitude of 22 pT. The delay and duration are about 3.5 ms and 4 ms, respectively.

process is much simpler: each muscle fiber is innervated by a single excitatory synapse. Moreover, this synapse exhibits a very high robustness, so that a single nerve stimulus triggers every time an action potential in every fiber of the soleus muscle.

The soleus muscle provides other advantageous features that add to this optimal temporal synchronicity:

- Every synapse is located at the center of its corresponding fiber, so that every action potential propagates symmetrically towards both ends of the muscle, while being spatially synchronized.
- Since the fibers are aligned parallel to each other, the magnetic field induced by all intra-cellular currents will be maximized.
- Contrary to the complexity of cortical networks, this parallel organization simplifies greatly the modeling part, so that the expected magnetic pattern can be determined with good accuracy.
- The efficiency of the synaptic transmission, *i.e* that each stimulus generates an action potential, allows averaging the results of hundreds of trials, improving the signal-to-noise ratio.
- The muscle is about 10-mm long and 1-mm wide, which implies that the specially-designed GMR sensors will have quite large dimensions, and, consequently, a lower noise level in the frequency range of interest.

3.2 Electrophysiology

3.2.1 Action potential dynamics

Before rushing straight to magnetic recordings, the electrical behavior of the soleus muscle has been characterized using electrophysiological techniques. Intra and extracellular recordings have been conducted to access the precise dynamic of the propagation of an action potential in our specific experimental conditions. The results provided access to the shape, amplitude, and propagation speed of the electric signal along the muscle, which have been key information to develop a realistic model and to interpret the magnetic signature measured later.

Muscle fibers operate in a similar way as an axon of a neuron. They can be considered as excitable cables whose membranes are covered with voltage-gated ion channels, exhibiting selective permeabilities. Contraction of skeletal muscles is controlled by electrochemical signals sent by the brain through the nervous system to a motor neuron, that innervates the fibers of the targeted muscle. To perform *in-vitro* stimulations of the muscle, the somatic nervous system is mimicked by a voltage generator: the nerve is sucked up into a glass micro-pipette, filled with a physiological solution, and a voltage drop is applied to excite the soleus. A square step of 6 V lasting 30 µs reached the activation threshold. The action potential travels along every axon of the nerve, until the neuromuscular junction. It triggers the release of acetylcholine, a specific neurotransmitter dedicated, among other functions, to muscle activation, in the synaptic cleft. These acetylcholine molecules bind to their corresponding nicotinic receptors on the membrane of each muscle fibers, initiating the opening of voltage-gated ion channels. In the resting state, the potential difference across a membrane is -90 mV (see Figure 3.3). An inward flow of sodium ions Na^+ raises the membrane potential up to +20 mV, which is called a depolarization phase, and positively charged potassium ions K^+ leak out of the cell to repolarize the membrane back to its resting potential. When this signal arrives at the center of a muscle fiber, this potential variation triggers the neighboring region, so that the action potential propagates symmetrically towards both ends of the fiber. Its amplitude remains unchanged along the whole distance, the same way a wave of falling pieces is transmitted in a chain of dominoes [10].

Based on these electrophysiological considerations, the effects of an action potential propagating along a muscle fiber can be seen through three different points of view:

- Intra-cellular recordings: a micro-electrode inserted inside a muscle fiber gives a direct access to the membrane potential. Measurements at different positions along the muscle enable to compute the conduction velocity of the action potential. However, macroscopic motion of the muscle during contraction avoid conventional intracellular recordings. In order to maintain the intracellular recording in the moving tissue, a "floating electrode" technique, inspired from [14, 27], was developed by G.Ouanounou (see Figure 3.2).

- Extra-cellular recordings: a micro-electrode put in the extracellular medium, close to the muscle, records the local variations of potential due to inward and outward transmembrane currents.

- Axial currents: the internal potential gradients around the depolarized active zone, *i.e* ranging from -90 mV to +20 mV, generate intra-cellular flows of ions that are not directly measured with classical electrophysiological techniques. This is why the magnetic sensor developed for this experiment could bring additional information concerning the activation of muscle cells, by measuring the field created by these axial currents and by getting access to their direction of propagation.

3.2.2 Results

Intracellular recordings

The soleus muscle is 1 cm long, which allowed to record its membrane potential at several locations along its length. Intra-cellular recordings (Figure 3.2 blue curves) were performed at five different positions: one is located at the synaptic region in the center of the muscle, the four others are situated at 1.5 mm and 4.5 mm on both sides of the central area. When the voltage stimulus is applied to the nerve, the time due to synaptic transmission causes a delay of 2 ms between the stimulus and the emergence of the action potential at the center of the muscle. Then, the signal triggers two identically-shaped action potentials traveling in opposite directions. At 1.5-mm and 4.5-mm distance, the action potential is delayed by 2.6 ms and 4.8 ms, respectively. The same timing is found on both sides. The actual conduction velocity is easily derived from these measurements: $v = 4.5/(4.8-2) = 1.6\ \mathrm{m/s}$. Similar values can be found in the literature, varying between 1 and 3 m/s, according to experimental conditions such as temperature and ion concentrations in the bath solution [11, 13, 22].

Extracellular recordings

The extracellular recordings (Figure 3.2 green curves) performed on the two sides of the central synaptic region exhibit a tri-phasic pattern that can be explained as follows. The first and the third positive part of the signal corresponds to the effects on the external potential of the positive transmembrane currents at the front and at the back of the active zone, respectively. The second phase is due to the negative transmembrane currents at the active zone. At the center of the muscle, the extracellular potential shows only two phases, corresponding to the effects of the negative transmembrane currents followed by the effects of the positive currents at the back of the two active zones.

These electrophysiological measurements give indications about how to design the magnetic sensors to measure the magnetic field generated by the axial currents. A single GMR sensor, shaped so that its dimensions are equal to those of the muscle, would average every currents, flowing on both directions, because of the symmetrical configuration of the soleus. The output signal would be zero and no information could be extracted about the muscle activation. Two regions of interest emerge: on the two sides of the muscle, the leading edge of depolarization and the trailing edge of repolarization generate local opposite axial currents during the propagation of an action potential, which are supposed to result in a biphasic magnetic field. Two GMR sensors located around these regions could allow to record independently and simultaneously these two components. The central synaptic part, where the action potential rises, is also worth being measured, in order to check that the symmetrical axial currents are well averaged along the length of the probe and no magnetic signal should be recorded.

Three aligned GMR sensors have been designed to confirm these expectations. The return currents, flowing in the extracellular space, are also expected to generate magnetic fields, but in opposite direction, partially screening the intracellular source. The modeling part presented below has taken all of these features into account to predict accurately the shape and the amplitude of the magnetic signal.

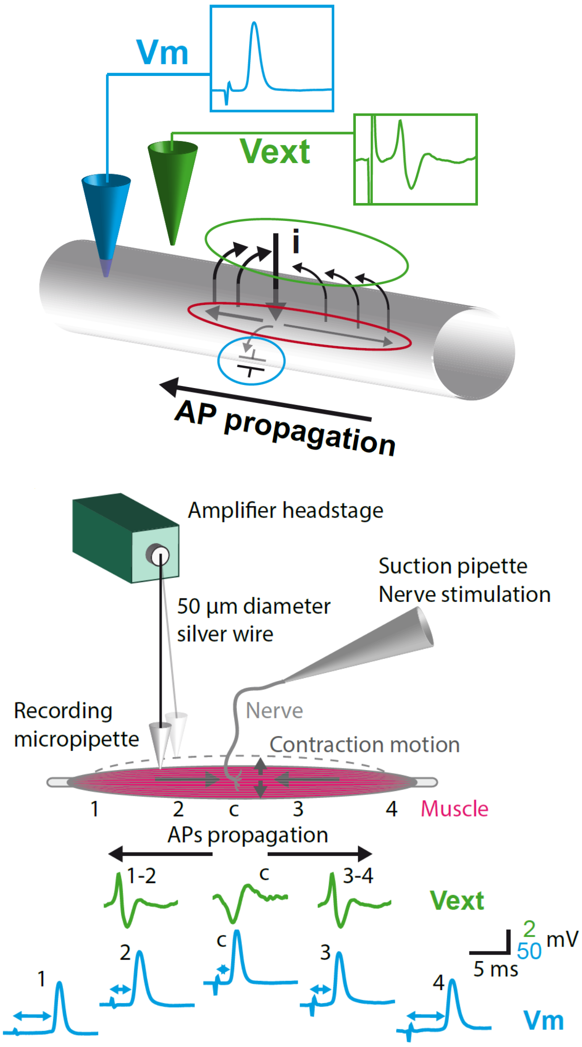

Figure 3.2: **Results of electrophysiological recordings.** Top: Intra-cellular recordings (blue electrode) give access to the membrane potential V$_m$, that reflects the charge of the membrane capacitor. The typical shape of a muscular action potential is obtained with a very high signal-to-noise ratio. Extra-cellular recordings (green electrode) reflect the effect of inward and outward currents on the potential of the medium. Due to this source/sink configuration, a kind of current loop is induced. The extra-cellular currents tend to screen the magnetic field generated by the intra-cellular axial currents (red circle), which are not measured by traditional electrophysiological tools. Bottom: Schematic illustrating the measurement setup. The nerve is introduced into a suction pipette and a voltage pulse is applied to generate an action potential. In order to perform intra-cellular recording despite the muscle contraction, a floating electrode has been set up. The extreme tip of a glass micro-pipette is used as an electrode, and hangs at the extremity of a free moving silver wire, connected by its opposite end to the amplifier head-stage. The absence of pipette holder allows the free moving of the system without being perturbed by the contraction. Blue (resp. green) traces represent the intra-cellular (resp. extra) recordings of the action potential, both at the neuromuscular junction and at different positions (noted 1,2,3,4) in order to measure the velocity of the signal along the fiber.

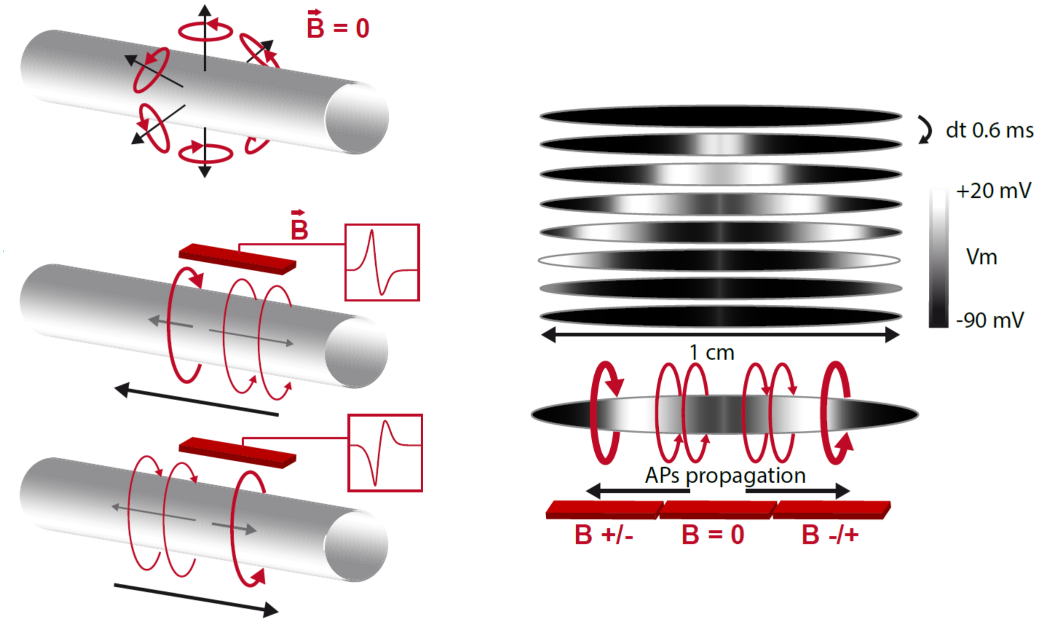

Figure 3.3: **Left: Expected magnetic signatures.** (Top) Since the voltage-gated ion channels are homogeneously distributed over the circumference of a fiber, the contribution of transmembrane currents, because of this cylindrical symmetry, cancels out at a sufficiently large distance compared to the fiber diameter. (Center and bottom) Axial currents create a biphasic magnetic pattern, whose polarity depends on the direction of propagation of the action potential (black arrow). **Right: Membrane potential evolution.** Simulation of the membrane potential rising at the center and traveling along both sides of the muscle. The internal gradients creates two opposite axial currents at the front and at the back of the active region, that are the sources of the targeted magnetic field.

3.3 Modeling

3.3.1 Features of the model

The numbers of parameters used to model this kind of biological system could be large (geometrical dimensions, conductivities, etc). In order to obtain a realistic model in a finite time, most of them were fixed at average values taken from the literature and that seemed to be coherent with the experiment. The mouse skeletal soleus muscle was modeled as follows (see Figure 3.4):

- A bundle of $N = 887$ cylindrical fibers, according to morphometric studies [4, 6].
- Fiber diameter of 40 µm and length of 1 cm.
- Interstitial space between two neighboring fiber 10 µm [7, 16].
- Each fiber is divided into 1000 compartments of 10 µm in length.
- The magnetic field is computed at 30 µm from the muscle, since it is in contact with the probe and that only a passivation layer of about 15 µm separated the sensor from the saline solution.
- Four regions of interest are defined: the fibers, the bundle, the sheath and saline bath.
- The intracellular conductivity of the fiber σ_i is considered homogenous and isotropic, and is set to 1.25 S/m ($\rho_i = 80\ \Omega$.cm) to reproduce the action potential dynamics and is in the range of estimated cytoplasmic resistance [8].
- The conductivity of the saline Ringer solution is also considered homogenous and isotropic, and is set to its typical value $\sigma_e = 1.6$ S/m ($\rho_e = 62.5\ \Omega$.cm)

As shown in the scheme of Figure 3.2, if local source-sink loops of current are present at two different sites along the cable, local charge variations in the extracellular medium create a potential gradient with opposite polarity with respect to the intracellular space. Hence, extra- and intracellular gradients generate currents in opposite directions. Extracellular currents are generally dispersed in a larger volume, in the cortex, for example. On the contrary, inside of the muscle, the fibers are closely packed and the presence of the others fibers limits the diffusion of the extracellular currents along the radial direction in the interstitial space. This geometry boosts the diffusion of these currents along the axial direction in the near surrounding of the fiber surface. Extracellular currents in the muscle are then likely to contribute considerably to the generation of a screening magnetic field. According to these constraints, the bundle itself was modeled as an anisotropic medium, with different conductivities along the radial and axial directions, σ_ρ and σ_z. Therefore, the free parameters that were varied to reproduce the recorded magnetic field are the two conductivities of the bundle, σ_ρ and σ_z, and the conductivity of the sheath σ_s.

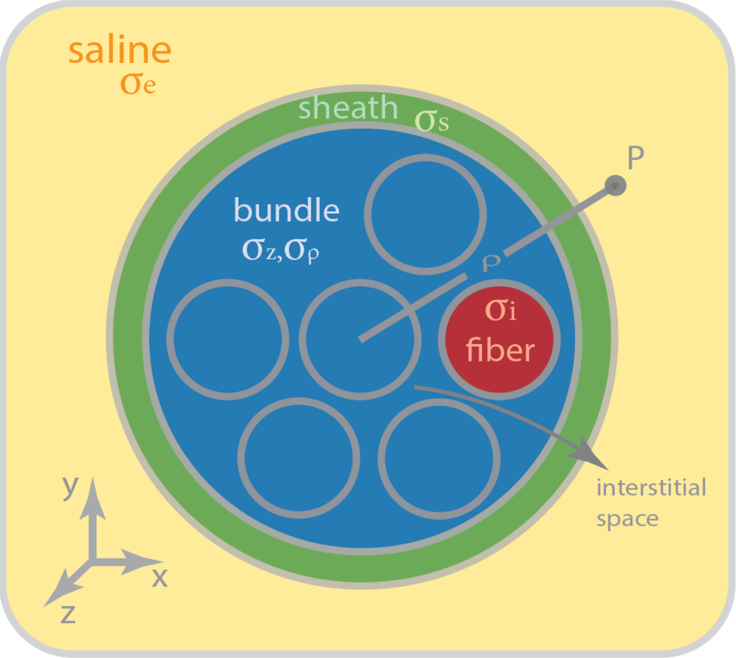

Figure 3.4: **Scheme of the muscle section.** The different sub-regions are depicted in different colors: the fibers (red), the bundle (blue), the sheath (green) and bath saline (yellow). The packed and parallel organization of the fibers inside the bundle is taken into account by inserting two different conductivities in the model, one for the radial direction σ_ρ, and one for the axial direction σ_z. If the ratio σ_z/σ_ρ increases, the current flowing in the bundle along the axial direction of the muscle will increase, and the recorded magnetic field will be strongly screened. This effect is illustrated in Figure 3.6a.

3.3.2 Results

Simulations reproduced the shape of the action potential measured by electrophysiological techniques, and its symmetric propagation from the center toward the two ends of the cable. Figure 3.5 illustrates the membrane potential over the length of the fiber at different times, and the corresponding axial currents flowing along the opposite internal gradients on the two sides of each action potential. Since the internal gradient, at the leading edge of the signal, corresponds to a variation of potential from +20 mV to −90 mV over about 1.5 mm, the corresponding intracellular current can be computed by:

$$I = \frac{\Delta V}{R} = \frac{\Delta V\,S}{\rho_i\,l} = \frac{(110.10^{-3})\,\pi(20.10^{-6})^2}{(0.8).(1.5.10^{-3})} = 115\,nA \tag{3.1}$$

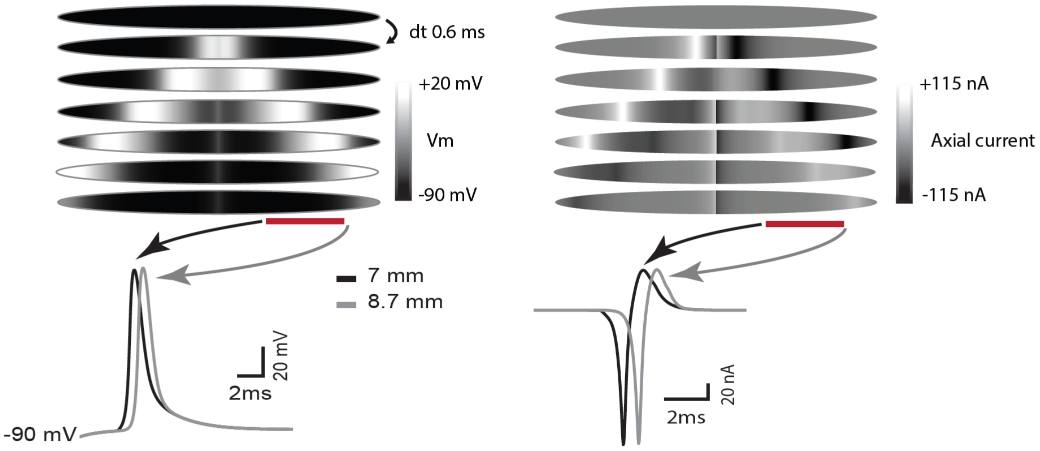

Figure 3.5: **Simulation of the evolution of the membrane potential and the axial current along the muscle fiber for successive times.** (Left) The time evolution of the membrane potential during the propagation of an action potential (top). Shape of the signal at two different sites of the fiber corresponding to the two ends of the probe, which is 1.7-mm long (bottom). The time lapse between the two action potential peaks is 0.7 ms, corresponding to an action potential speed of 2.4 m/s. (Right) Axial currents generated by the membrane potential gradients along the fiber (top), and currents seen by the two ends of the probe (bottom). The spatial averaging operated by the GMR sensor will flatten and broaden the shape of the recorded field, compared to these current shapes.

The calculation of the magnetic fields was based on the analytical model developed in 1985 by Roth and Wikswo [24]. After the definition of the system geometry, the electric potential is computed in each region by solving the Laplace equation. The current density is then deduced from the local Ohm's law, and the magnetic field is obtained by applying the Ampère's law:

$$\oint_C \mathbf{B}\,\mathbf{dl} = \mu_0 \iint_S \mathbf{J}\cdot\mathbf{dS} = \mu_0\,I \tag{3.2}$$

where I is the current passing through the surface S enclosed by the curve C. This equation allows to disentangle the contributions to the global magnetic field of each region: the fibers, the bundle, the sheath of connective tissue and the bath. All the results are summarized in Figure 3.6.

The first plot (top left), confirms that the ratio σ_z/σ_ρ plays an important role on the net magnetic field measured by the sensor. If $\sigma_z = \sigma_\rho$, the conductivity of the bundle is considered to be isotropic. It means that the return currents are spreading in the extracellular medium in a large volume, which reduces the screening effect. In this case, the amplitude goes up to 12 nT. When the ratio increases, the conduction along the fibers is enhanced and the net amplitude decreases.

The second plot (center left) shows that the other free parameter of the model, the conductivity of the surrounding sheath σ_s, does not influence the final result. σ_s varies from 0.1 S/m to 3 S/m but all the curves overlap.

The third plot (bottom left) illustrates the spatial averaging operated by the GMR sensor. The global resistance is directly linked to the orientation of the magnetic moments of the free layer. Since the length of the probe is 1.7 mm, moments located at different positions will not feel the same magnetic field when the action potential propagates over the sensor, at a given point in time. When averaged over the probe's length, the magnetic field was reduced by about 40% and was slightly broader in time.

The last plot (right), corresponds to the computation of the four components, (B_i, B_b, B_s, B_e), for a single fiber. The amplitude of the magnetic field due to the intracellular current in a fiber B_i, measured at 30 μm, is similar to the one due to extracellular current in the interstitial space of the bundle B_b, especially for a fiber located at the center of the muscle. It confirms the intuitive point that the major contribution to the net magnetic field comes from the fibers located on the edges of the bundle. Currents flowing into the sheath or in the saline bath create magnetic fields that have no influence on the net field sensed by the probe. Their amplitudes are two to three orders of magnitude smaller than B_i. Based on these simulations, one can deduce that the screening effect is largely due to B_b. It is estimated to be close to 75%.

The best agreement between theory and experiments was obtained for $\sigma_i = 1.5$ S/m, $\sigma_\rho = 0.01$ S/m, $\sigma_z = 4.5$ S/m and $\sigma_s = 3$ S/m. The computed signal is superimposed in Figure 3.7 (black) and compared to the recorded signal (gray): the agreement between the theory and experiments is excellent both in amplitude and temporal pattern, for a set of biologically plausible values.

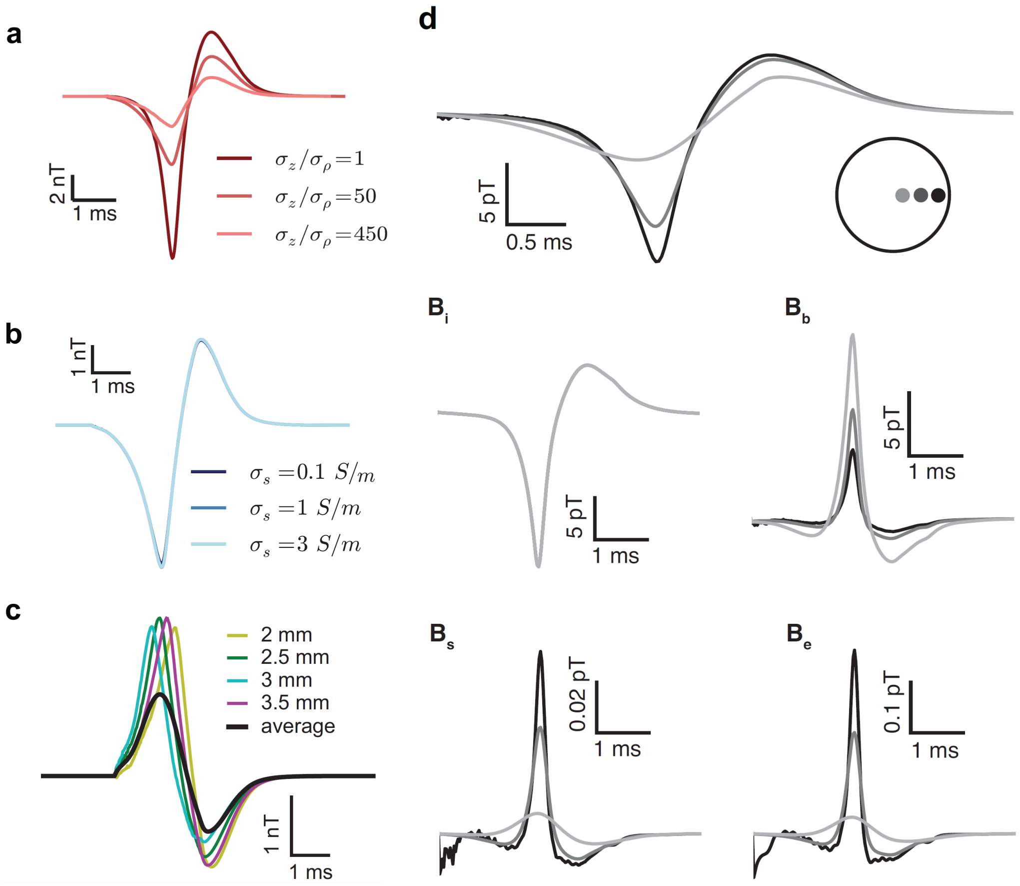

Figure 3.6: **Simulated magnetic fields.** **(a)** Magnetic field generated by the entire muscle at 30 μm from the surface for different values of the ratio σ_z/σ_ρ ($\sigma_s = 3$ S/m). The higher the ratio, the higher the current flowing axially along the muscle through the interstitial space, which induces a large screening effect. **(b)** Same as in (a), but when varying σ_s ($\sigma_{rho} = 0.01$ S/m and $\sigma_z = 3$ S/m). The conductivity of the sheath does not influence the global magnetic field. **(c)** Effect of the averaging over the probe length: the punctual magnetic field generated at 30 μm from the surface is shown for different position along the muscle (colored traces). The black trace represents the time evolution of the average of the magnetic field over the positions spanning the probes length (1.7 mm). **(d)** Behavior of the magnetic field of a single fiber depending on its position inside the bundle. The contribution to the net magnetic field is four times larger for the fibers located on the outer radius in the muscle, compared to a fiber located at the center (top). The different magnetic field components due to the currents flowing in the fiber (B_i), the bundle (B_b), the sheath (B_s) and the saline solution (B_e) (bottom). The same scale is used for the field generated by the current in the fiber B_i and in the bundle B_b. The magnetic field in the saline solution and in the sheath increases when the fiber is located close to the edge of the muscle, since the current can flow outside more easily. However, the scale is divided by 50 for the field in the saline solution B_e, and by 250 for the field in the sheath B_s. This is why extracellular current in the bundle can be considered as the primary source of screening.

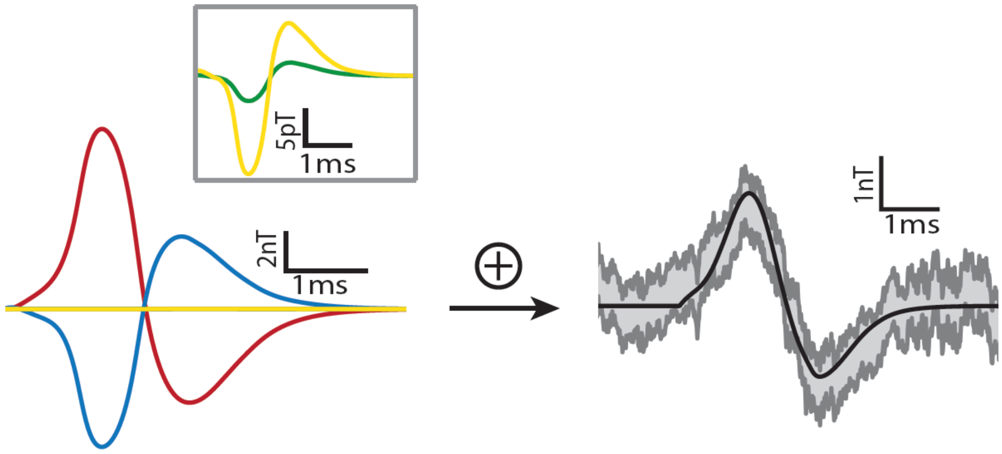

Figure 3.7: **Left:** The components of the calculated magnetic field due to the currents flowing in the different regions depicted in Figure 3.4: the fibers (red), the bundle (blue), the sheath (green) and bath saline (yellow), respectively in the main panel and in the inset. The screening effect, mostly due to the extracellular current flowing in the bundle, is close to 75%. **Right:** The calculated net magnetic field (black) resulting from the superposition of the components shown on the left, is compared with the data (gray) obtained from one muscle ($n = 450$ trials). The best agreement between theory and experiments was obtained for $\sigma_i = 1.5$ S/m, $\sigma_\rho = 0.01$ S/m, $\sigma_z = 4.5$ S/m and $\sigma_s = 3$ S/m.

3.4 Custom-made GMR sensor

3.4.1 Micro-fabrication

Considering the results of the electrophysiological experiments and the numerical simulations, the shape of the sensors was adapted to detect the magnetic field in the regions of interest. Three aligned spin valves of (1.7 mm * 400 µm) have been designed, oriented in such a way that they would be sensitive to the azimuthal component of the magnetic field, generated by the propagation of an action potential along the muscle. A schematic representation is given in Figure 3.8.

The stack of materials used to generate the giant magneto-resistive effect is similar to the one described in Chapter 2. The stack was deposited by sputtering on a 700-µm thick silicon substrate insulated by a SiO_2 layer of 1 µm. The free layer is made of a soft ferromagnetic layer of $NiFe$ (3.5 nm) coupled to a strongly spin-polarized layer of $CoFe$ (1.5 nm). The hard layer is made of an anti-ferromagnetic layer $PtMn$ (18 nm) coupled to a $CoFe$ (2 nm), which is itself part of a synthetic anti-ferromagnet (SAF) since it is coupled to another layer of $CoFe$ (2.1 nm) through a layer of Ruthenium (0.85 nm). The spacer between the free layer and the hard layer is a 2.3-nm thick layer of Copper.

The GMR stack is patterned by laser lithography, and the three segments are etched by ion milling under Argon gas at 10^{-4} mbar. The sensors are contacted via lines of Titanium (15 nm)/Gold (150 nm)/Titanium (15 nm) deposited by evaporation at 10^{-8} mbar through a lift-off process. The sensors are contacted in a "current-in-plane configuration" (CIP), *i.e* electrons will flow in the plane of the stack, contrary to the CPP (current perpendicular to plane) configuration. The GMR effect occurs in both cases since the thickness of the layers is smaller than the spin-diffusion length discussed in Chapter 2, but the CIP configuration implies a much more straightforward fabrication process. Moreover, it leads to an output impedance which is easier to match to the readout electronics (dozens of Ohms, versus mOhms for the CPP configuration). The whole sample is then protected by a passivation bi-layer of Al_2O_3 (150 nm) and Si_3N_4 (150 nm) deposited by sputtering, except at the ends of the contact lines to allow wire-bonding. The square shape of the final probe was defined by dicing it with a diamond tip.

The probe was glued on a printed circuit board (PCB) and contacted to the gold lines by wire-bonding. The wires are made of aluminum and are 30-µm thick. They were encapsulated by a drop of araldite glue because of their fragility and to avoid any short-circuits when placed in the conductive bath. The system was placed into a hollow chamber made of Teflon in which a layer of silicone was poured and baked to handle easily the needles used to fasten the muscle by its tendons. Because of the large dimensions of the sample, defects in the insulating layer could lead to electrical contamination coming from a point contact with the conductive bath, *i.e* artifact recorded at the sample output. To ensure an accurate insulation when the sensors are immersed in the saline solution, the previous layers were topped by a polymer resin (15 µm). A biasing ferrite magnet was placed under the chamber to keep the magnetization of the free layer orthogonal to the one of the hard layer in absence of an applied field. This allows linearization of the response of the sensor around zero field, as discussed in Chapter 2. Microfabrication steps are detailed in the following table.

3.4.2 Performance

For each probe used during the *in-vitro* experiments, the three sensors have undergone the characterization procedure presented in Chapter 2.

The response to an external magnetic field is obtained by putting the sensor inside

Step	Technique	Parameters
GMR shape	Laser Litho	Photoresist S1813, spin 60 s at 5000 rpm
		Baking 3 min at 110°C
		Exposure 20 s - Remover MF319 45 s
	Etching	20 min
Contacts	Laser Litho	Photoresist S1818, spin 60 s at 5000 rpm
		Baking 3 min at 110°C
		Exposure 25 s - Remover MF319 60 s
	Deposition	Pre-etching 30 s
		Evaporation Titanium, 15 nm
		Evaporation Gold, 100 nm
		Evaporation Titanium, 15 nm
Passivation	Laser Litho	Photoresist S1818, spin 60 s at 5000 rpm
		Baking 3 min at 110°C
		Exposure 25 s - Remover MF319 60 s
	Deposition	Pre-etching 30 s
		Sputtering Al_2O_3, 150 nm
		Sputtering Si_3N_4, 150 nm
Cutting	Dicing	Manual dicing with a diamond tip
Packaging	Wire bonding	3 Aluminum wires per contact lines.
	Protection	Gluing of the wires with araldite
	Fixation	Silicone poured in the chamber - Baked 24h at 50°C
	Passivation	Polymer resin topped over the sample

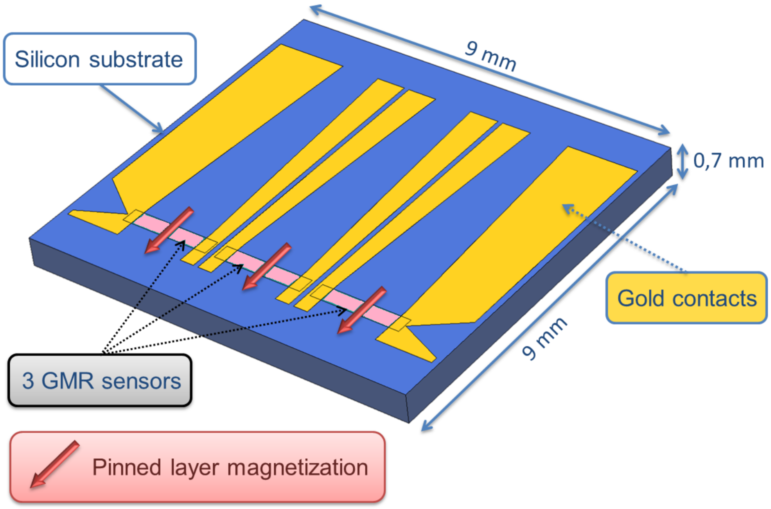

Figure 3.8: **Specially designed sensor for *in vitro* experiments.** The sensor is made of three independent GMR segments (light pink) whose pinned layer magnetizations are perpendicular to the segment length (red arrows). The magnetic field lines are expected to wrap around the muscle fibers, *i.e* being aligned with the sensitivity direction of the sensors, which is fixed by this pinned layer magnetization. Each segment is contacted through two lines of Ti/Au/Ti (yellow). A notch was patterned on the two contact lines on the edges of the sample to make the positioning of the muscle easier.

a Helmholtz coil and by varying the field between ±5 mT along the sensing direction of the spin valves. The magneto-resistive (MR) ratio is usually identical for three sensors of a given probe since they were patterned on the same initial GMR stack. The mean value of MR ratios is around 6.5%. The sensitivity, defined by the slope around zero field, can vary from one sensor to another. It is typically ranging between 5 %/mT and 20 %/mT. However, before each experiment, the converting factor in V/T, between a voltage at the output of the sensor and the corresponding magnetic field, is deduced from the application of a calibrated magnetic signal. This technique is simple and provides a more reliable value than computing the slope of the response. Considering a sensitivity of 10 %/mT and a supply voltage of 1 V, a magnetic field of 1 mT will generate a signal of 100 mV. The expected amplitude being about 1 nT, the output voltage of 100 nV will be amplified about 10000 times before digital processing. Typical responses of three aligned spin valves are plotted in Figure 3.9, as well as the field equivalent noise, measured in a magnetically shielded room.

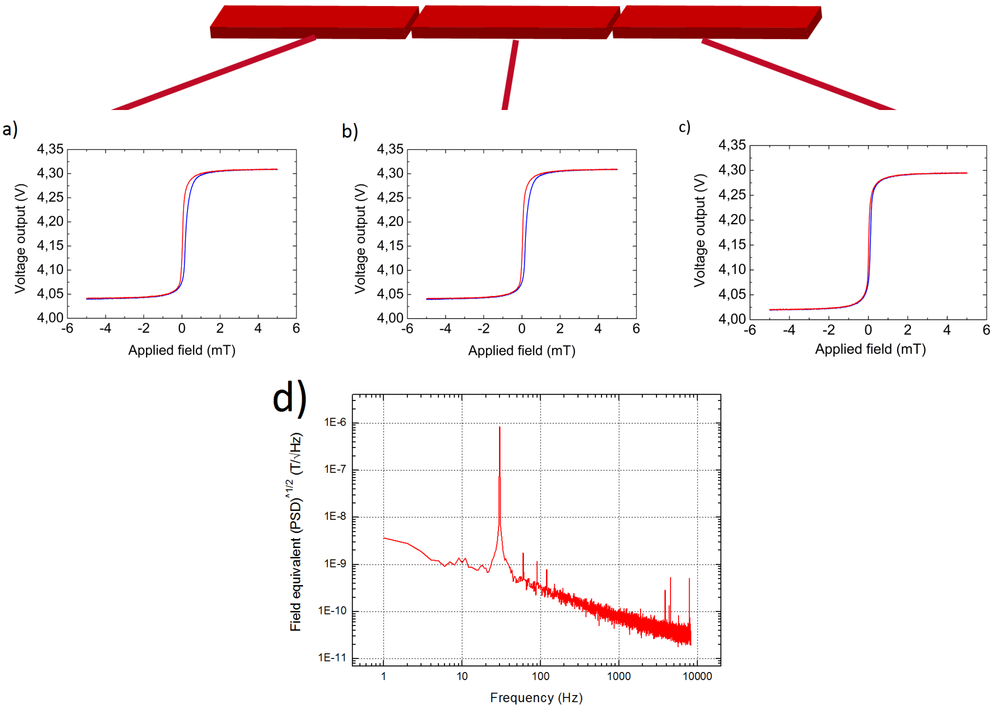

Figure 3.9: **Magneto-resistance and noise level of the GMR sensors.** **(a)** **(b)** **(c)** The output of each of the three spin valves is plotted as a function of the applied field. The magneto-resistance ratio is 6.6% for the three of them, but their sensitivity can vary slightly. To calibrate accurately the recordings on every channel, a sinusoidal signal of 1 µT was applied before each *in vitro* experiments. **d)** The noise level is measured in the magnetically-shielded room and converted to an equivalent field noise level in $[T/\sqrt{Hz}]$ thanks to a calibrated test signal at 30 Hz. Despite the large size of the spin valve (1.7 mm * 400 µm) there is still a dominant 1/f noise component. For the left sensor, the noise level is 1 $nT/\sqrt{Hz}$ at 10 Hz, 300 $pT/\sqrt{Hz}$ at 100 Hz, and 70 $pT/\sqrt{Hz}$ at 1 kHz.

3.5 Magnetic recordings

3.5.1 Experimental setup

The dissection was made on 3 to 5-month-old Swiss mice. The challenging part of this operation consists of extracting the very thin and fragile nerve without any damage. The fat layer that surrounds the muscle has to be removed to increase the proximity between the fibers and the sensors. The nerve-muscle preparation is then fixed on top of the sensor and hold via minutien pins put through the tendons, while the sensor is glued in a hollow chamber (see Figure 3.10). The chamber is filled with an oxygenated Ringer solution to maximize the time available for recording. Generally, the muscle responds properly to stimulations for 3 to 4 hours.

A large battery ensured a stable current feed to the sensors for the measurement time. Their resistance is typically around 80 Ω. Each of the three GMR sensors is fed by a DC current of 20 mA and included in a Wheatstone bridge, whose outputs are connected to three identical low-noise differential amplifiers INA103. A second stage (SR560) filters the signal in the range of 1 Hz - 10 kHz. The gain of the first stage is 500 and the one of the second amplifier is set to 20. The digitization is made using a 16-bit A/D converter. Data processing consisted first in removing the stimulation artifact. Its exponential shape was fitted and subtracted from the initial signal. Considering the total duration of the magnetic pattern, the frequency window was then reduced to 80 Hz - 1.2 kHz to increase the signal-to-noise ratio.

3.5.2 Results

3.5.2.1 Magnetic signature of an action potential

Once the dissection is completed and the whole experimental setup is on, the muscle and the sensors are controlled one last time before running the process. A stimulus is applied to the nerve and the following contraction of the muscle can be observed directly through a binocular microscope. It is worth noting that the actual movement of the muscle starts a few millisecond after the propagation of the action potential, so that there is no artifact coming from the contraction. It has been measured with a force probe connected directly to the soleus. After this check, the noise level on each sensor is measured directly via the oscilloscope. The noise decreases as the square root of the number of trials, that were set up to 500, which reduces the noise by a factor 22. Since the expected amplitude is a few nT, the noise has to be lower than about 30 nT to run

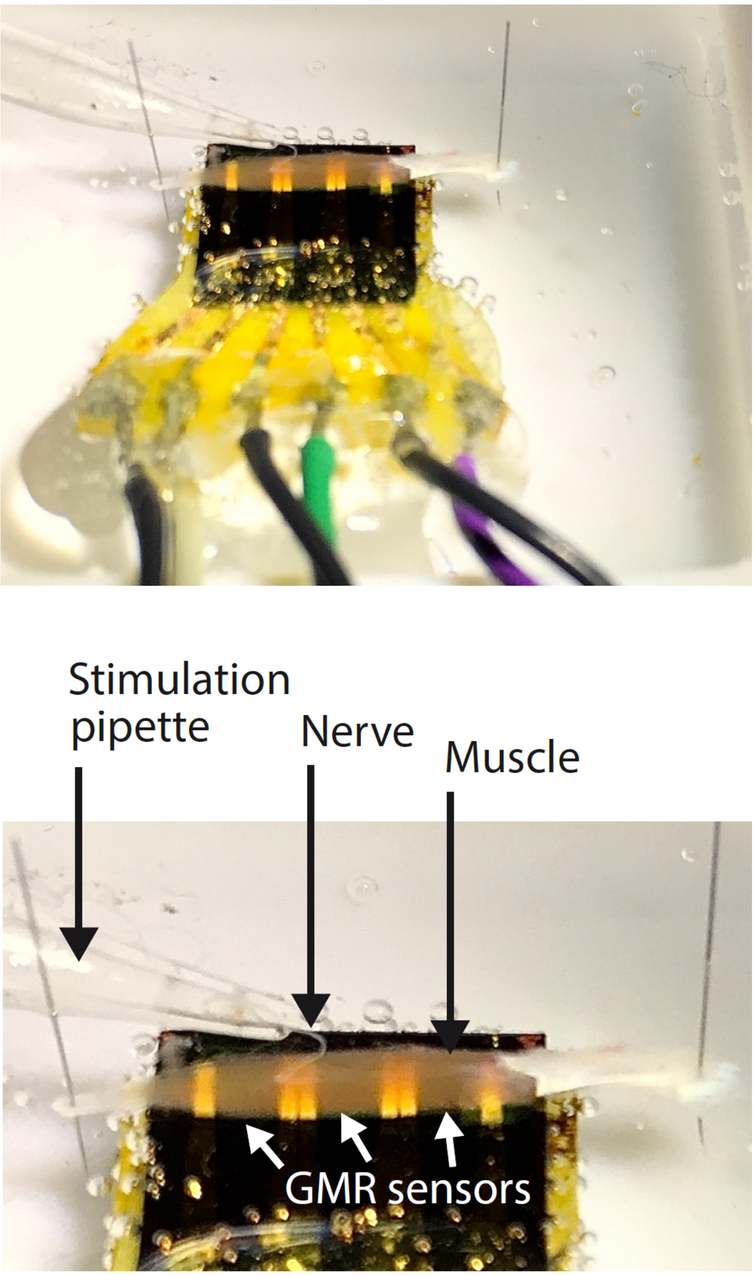

Figure 3.10: **Picture of the *in vitro* experiment.** The soleus muscle-nerve preparation was placed on top of the probe, and held with minutien pins through the tendons. The nerve is sucked up into the stimulating glass pipette, which is filled with saline solution. The probe is also immersed in the saline solution, which requires a perfect electrical insulation of the sensors, the contacts lines, and the wire bonding. Once the action potential is triggered in the nerve by a voltage pulse, it propagates to the neuro-muscular junction at the center of muscle, before being splitted in two identical action potentials traveling towards both ends. The three GMR sensors record simultaneously the azimuthal component of the magnetic field, which is the result of both the axial currents in the fibers and the screening effect of 75% due to return currents.

the experiment with the reasonable conditions. Figure 3.11 shows the main result for a recording session of 500 averaged acquisitions: the magnetic field generated by the propagation of the action potential along the muscle.

As expected by the electrophysiological recordings and by the simulations, the two external sensors measured a magnetic field that exhibits a biphasic shape with opposite polarity. The biphasic shape comes from the two opposite axial currents flowing at the leading and at the trailing edges of the action potential. The peak-to-peak amplitude is 2.7 nT. This value is consistent among the 6 muscles tested: the average amplitude was 2.8 nT and the standard deviation 0.7 nT. The total duration of the magnetic pattern is 4.8 ms, and the temporal delay between the two peaks is 2 ms. Moreover, knowing the sensitivity direction of the GMR sensors, the polarity of the signals is in agreement with the the axial currents directions. This information, due to the vectorial nature of the magnetic field, is of great interest compared to classical scalar electrophysiological recording techniques. At the central region, the magnetic fields generated by the two action potentials propagating in opposite direction are probed simultaneously by the same sensor. The spatial averaging along the segment cancels their contributions and the output signal is flat.

The signal was low-pass filtered at the acquisition with a 10-kHz cut-off frequency (noisy gray traces), and the signal to noise ratio of the averaged signal ($n = 500$ events) was 7.5 on the left sensor and 10 on the right sensor. An additional off-line filtering, with a cut-off frequency of 1.2 kHz (smooth black traces), allowed to raise the SNR to 9.5 and 15 for the left and right segments respectively. Based on these settings, the threshold of detection, *i.e* a signal-to-noise of 2, could be obtained after 10 trials.

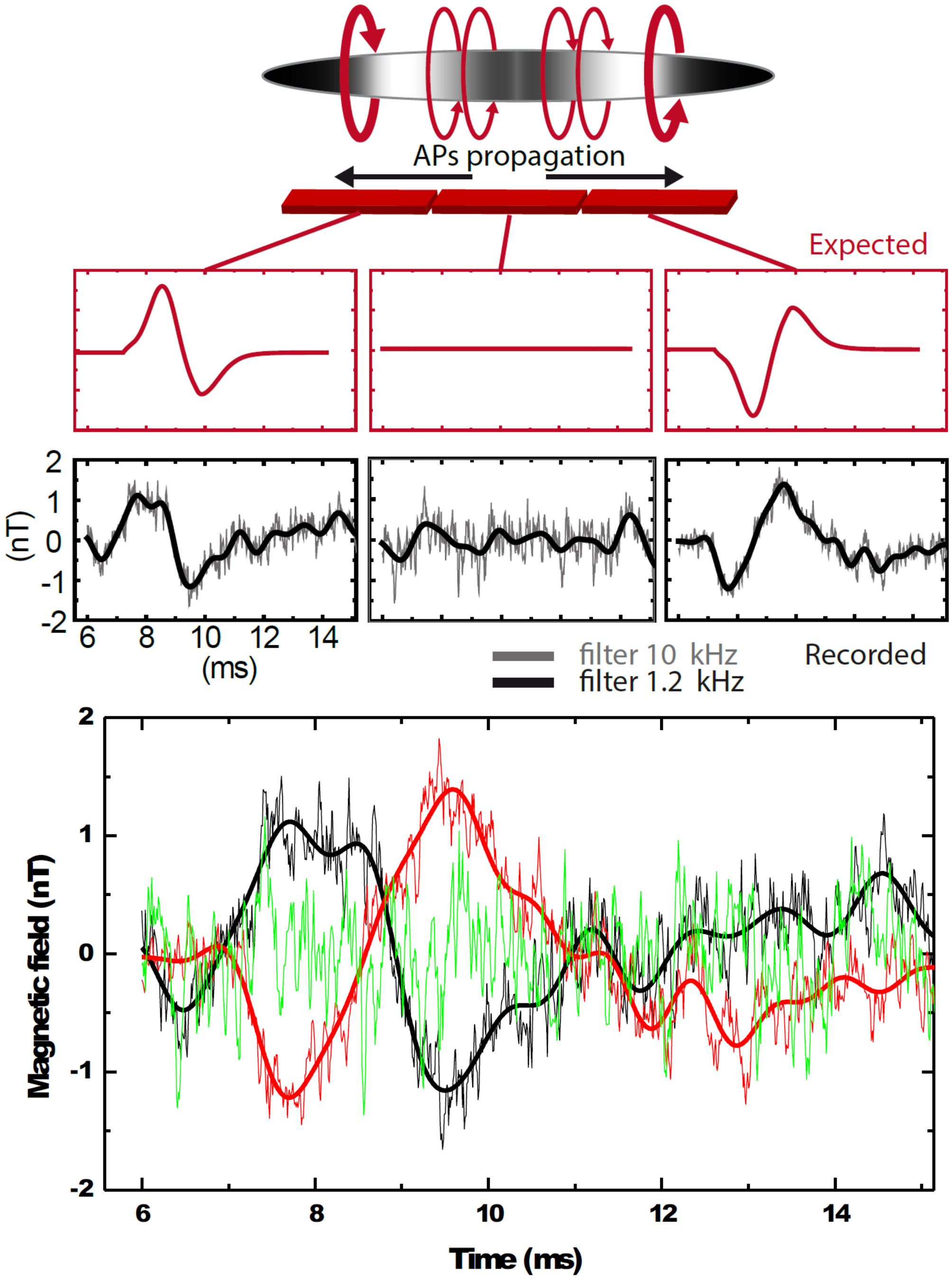

Figure 3.11: **Magnetic signature of the action potential.** (Top) The expected results, obtained from the modeling part (red) and the recorded magnetic field (black). Traces are averaged over 500 trials and low-pass filtered at 10 kHz (gray) or 1.2 kHz (black). The zero of the time scale corresponds to the electric stimulus applied in the pipette. (Bottom) Superposition of the traces of the left sensor (black), right one (red), and the one at the center (green). The sensor at the center averages the contribution of two identical opposite current, while the two sensors on the sides both show a biphasic pattern, with opposite polarity, that matches greatly the theoretical predictions.

3.5.2.2 Control experiments

The pioneering aspect of this kind of experiment requires to take all the necessary precautions to remove any doubt about the veracity of the results. Since the expected pattern looks like a pulse, it could easily be confused with artifacts coming from various sources. For this purpose, three types of control experiments have been conducted on the nerve-muscle preparation to confirm all the results obtained via electrophysiology or via the modeling. All of these checks were successful (see Figure 3.12) and they gave a strong reliability to these results.

- **Magnetic origin:** electrophysiological measurements showed that the transmembrane currents are able to raise the potential of the extracellular medium by several milli-volts. The magnetic field being measured through potential difference across the GMR sensor of a few nano-volts, the electrical insulation of the probe and of the gold connectors is critical to ensure a strictly magnetic measurement. The quality of the insulation, and the absence of electrical contamination of the signal, have been controlled by reproducing the experiment with no feeding current in the GMR sensor. Since the output voltage V_{out} is defined by $V_{out} = R(B).I$, the magneto-resistive effect should not influence the output if $I = 0$. The flatness of the corresponding recording confirms the magnetic origin of the signal.
- **Action potential:** in order to control that the recorded magnetic signal was only due to the muscle activity, the nicotinic receptor antagonist curare was used to block the muscle action potential, while preserving nerve activity. A concentration of 50 µM was added to the Ringer solution, and its effectiveness, *i.e* the absence of contraction, was checked through a binocular microscope. The magnetic pattern disappeared, and it confirms the link between the observed signal and the action potential propagation. The antagonist effect of the curare on the nicotinic receptors being reversible, the solution was washed out, and it restored the muscle activity and its characteristic magnetic signature.
- **Axial currents:** the main assumptions made so far were based on the distributions of the currents inside the muscle. One easy way to make sure that the recorded magnetic signature is associated to axial currents is to modify the geometry of the experiment. The muscle was placed orthogonally to the GMR sensor, so that the azimuthal magnetic component would not be probed. The absence of detectable signal further confirms the assumption that the transmembrane currents have a negligible contribution to the global magnetic field which is mainly due to the axial currents flowing in the direction of the fibers.

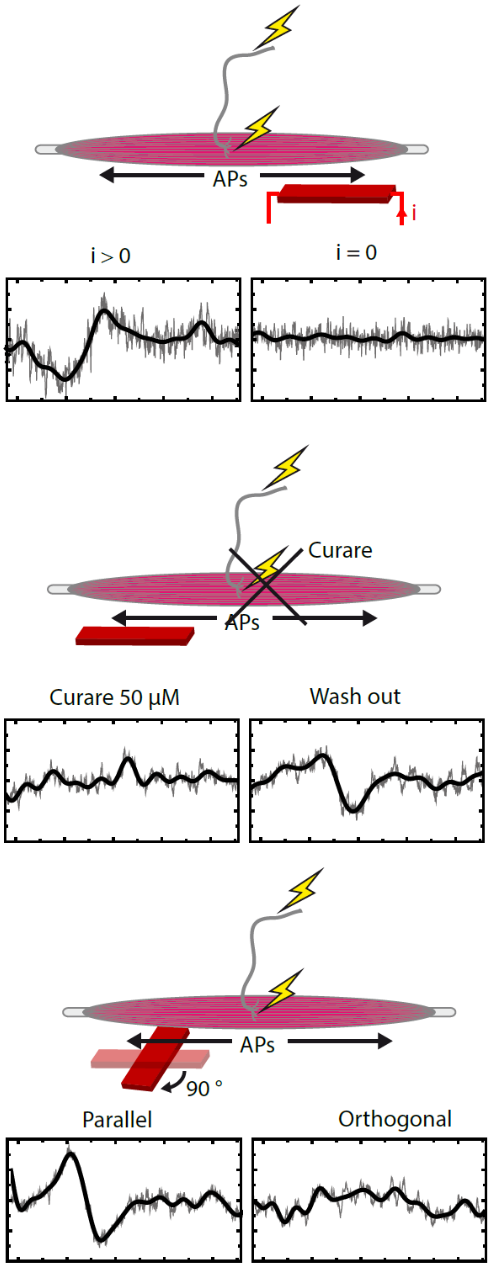

Figure 3.12: **Validation of the results by control experiments.** **(Top)** The same experiment was conducted without feeding the GMR sensors. This measure allows to check whether the signal has a magnetic origin, which makes the resistance of the sensor vary, or if it is an electric contamination due to a permeable insulation layer. **(Center)** The synaptic receptors at the neuromuscular junction, that are supposed to transmit the action potential coming from the nerve to the muscle, are blocked by adding curare to the bath. Washing out restore the signal. **(Bottom)** The muscle is placed orthogonally to the sensors, to validate the fact that the recorded magnetic field is due to axial currents.

3.6 Conclusion

The work presented in this third chapter demonstrates that GMR-based technology can be used to design specific magnetic sensors for biological recordings. In order to validate this idea, the magnetic field associated with the action potential activity in *in vitro* mouse skeletal muscle was successfully recorded. The simplicity of the muscle organization and the high synchronicity of its electrical activity generate a simple, predictable, and large magnetic field. Microfabrication techniques have made possible to optimally shape the sensors to record the signal at specific locations, chosen after a complete electrophysiological study of the system. The agreement between experiments and theory represents a solid validation, all the more robust as the experimental system is simple.

The biphasic pattern of the magnetic signal matched the temporal evolution expected from simple considerations based on the action potential shape and its propagation speed obtained by the electrophysiological recordings. The peak-to-peak amplitude was of the order of 2-3 nano-tesla and also matched the theoretical predictions of the model developed here. These values are comparable to the amplitude measured in worm, whose giant axon is much larger (200-µm radius) with NV centers in diamond by [3]. The large internal potential gradient offered by the AP, the strong synchronicity among muscle fibers, their large diameter and their simple parallel organization, all together can explain that the local magnetic fields we found in the skeletal muscle. The initial assumptions concerning the nature of the sources have been supported through these experiments: the intra- and extracellular currents are the main sources of the net magnetic field, and the contribution of the transmembrane currents is negligible. The model suggests that the local net magnetic field is largely reduced by the screening currents, which hide more than half of the intracellular primary sources. The experimental validation of these principles, applicable to cable-like structures such as neurons in the brain, is the first required step to validate the use of GMR-based sensors in the identification of the cellular generators of the macroscopic MEG signal.

Some attempts have been done in 2011 [1] to use GMR-based sensors for the detection of biomagnetic fields, without being able to achieve a purely magnetic recording. The experiments were carried out on a *in vitro* rat hippocampus brain slice. The recorded signal was 2.5 µT, which is three orders of magnitude higher than the expected and measured values in this work. The authors acknowledged that their probes were picking up an action potential by capacitive coupling. Indeed, variations of the extracellular potential are in the milliVolts range, while the voltage variation in the sensor induced by a magnetic field of the order of a nano-tesla is around tens of nano-volts. In our experiment, in order to differentiate whether the output signal is of magnetic origin or due to an electrical contamination, the sensor potential has been measured in absence of feeding current. The results proved the veracity of the magnetic recordings and that the effectiveness of the electrical insulation. Other possibilities of artifact have been ruled out by pharmacological techniques and by measuring the other components of the magnetic field. The hypothesis of a motion artifact has been rejected since the muscle started to generate a twitch force well after the complete propagation of the action potential. No specific shielding was needed for these signals recorded on the skeletal muscle, but shielding is envisaged for lower magnitudes detection, to avoid ambient noise and to reach the intrinsic limits of the probes.

Since the first magnetic recordings on skeletal muscles in 1972 [5], a very few studies have been reported [9, 12, 15, 19, 21, 26]. They were all based on SQUIDs or toroidal pick-up coils that successfully recorded the magnetic signature of muscular activity, but a much larger effort was put on brain and heart studies. Nevertheless, being able to localize current sources inside skeletal muscle fibers would be of great interest to help determining the healthy state of the muscle. Current leakage from an injured fiber modify the shape of the induced magnetic field, and the mapping of muscle lesions would be more efficient [18]. The experiments presented in this chapter demonstrated that GMR-based sensors offer the required sensitivity and malleability to detect these kind of biomagnetic fields with micro-probes at room temperature. The shape, the amplitude and the duration of the signal are quite similar to those obtained with other types of sensors, since the simplicity of the skeletal muscle structure allows reproducible trials.

In contrast, *in vivo* magnetic recordings of brain activity inside the neuropil, have never been reported so far, and modeling the behavior of a cortical neuronal network is much more complicated. However, by pushing further the technological steps, a GMR-based sensor has been specially designed to perform this new kind of experiments that are addressed in the following chapter.

Bibliography

[1] AMARAL, J., S. CARDOSO, P. FREITAS et A. SEBASTIAO. 2011, «Toward a system to measure action potential on mice brain slices with local magnetoresistive probes», *Journal of Applied Physics*, vol. 109, no. 7, p. 07B308. 100

[2] BARBIERI, F., V. TRAUCHESSEC, L. CARUSO, J. TREJO-ROSILLO, B. TELENCZUK, E. PAUL, T. BAL, A. DESTEXHE, C. FERMON, M. PANNETIER-LECOEUR et collab.. 2016, «Local recording of biological magnetic fields using giant magneto resistance-based micro-probes», *Scientific Reports*, vol. 6. 76

[3] BARRY, J. F., M. J. TURNER, J. M. SCHLOSS, D. R. GLENN, Y. SONG, M. D. LUKIN, H. PARK et R. L. WALSWORTH. 2016, «Optical magnetic detection of single-neuron action potentials using quantum defects in diamond», *Proceedings of the National Academy of Sciences*, p. 201601 513. 100

[4] CADENA, S. M., K. N. TOMKINSON, T. E. MONNELL, M. S. SPAITS, R. KUMAR, K. W. UNDERWOOD, R. S. PEARSALL et J. L. LACHEY. 2010, «Administration of a soluble activin type iib receptor promotes skeletal muscle growth independent of fiber type», *Journal of applied physiology*, vol. 109, no. 3, p. 635–642. 84

[5] COHEN, D. et E. GIVLER. 1972, «Magnetomyography: Magnetic fields around the human body produced by skeletal muscles», *Applied Physics Letters*, vol. 21, no. 3, p. 114–116. 76, 78, 101

[6] CONSOLINO, C. M., F. DUCLOS, J. LEE, R. A. WILLIAMSON, K. P. CAMPBELL et S. V. BROOKS. 2005, «Muscles of mice deficient in α-sarcoglycan maintain large masses and near control force values throughout the life span», *Physiological genomics*, vol. 22, no. 2, p. 244–256. 84

[7] FLESSNER, M. F., J. LOFTHOUSE et collab.. 1997, «In vivo diffusion of immunoglobulin g in muscle: effects of binding, solute exclusion, and lymphatic removal», *American Journal of Physiology-Heart and Circulatory Physiology*, vol. 273, no. 6, p. H2783–H2793. 84

[8] FOSTER, K. R., J. M. BIDINGER et D. CARPENTER. 1976, «The electrical resistivity of cytoplasm», *Biophysical journal*, vol. 16, no. 9, p. 991–1001. 84

[9] GIELEN, F., R. FRIEDMAN et J. WIKSWO. 1991, «In vivo magnetic and electric recordings from nerve bundles and single motor units in mammalian skeletal muscle. correlations with muscle force.», *The Journal of general physiology*, vol. 98, no. 5, p. 1043–1061. 101

[10] HÄMÄLÄINEN, M., R. HARI, R. J. ILMONIEMI, J. KNUUTILA et O. V. LOUNASMAA. 1993, «Magnetoencephalography—theory, instrumentation, and applications to noninvasive studies of the working human brain», *Reviews of modern Physics*, vol. 65, no. 2, p. 413. 79

[11] JUEL, C. 1988, «Muscle action potential propagation velocity changes during activity», *Muscle & nerve*, vol. 11, no. 7, p. 714–719. 80

[12] KOGA, S. et A. NAKAMURA. 1982, «Magnetic signals from human skeletal muscles», *Japanese Journal of Applied Physics*, vol. 21, no. 5A, p. L272. 101

[13] KOSSLER, F., F. LANGE, G. CAFFIER et G. KUCHLER. 1991, «External potassium and action potential propagation in rat fast and slow twitch muscles», *Gen Physiol Biophys*, vol. 10, no. 5, p. 485–98. 80

[14] KUNZE, W. A. 1998, «A mobile intracellular microelectrode designed to record from neurons in contracting tissue», *Brain Research Protocols*, vol. 3, no. 1, p. 94–99. 80

[15] LEWIS, M. J. 2003, «Biomagnetism: a new tool in sport and exercise science», *Journal of sports sciences*, vol. 21, no. 10, p. 793–802. 101

[16] MAC GABHANN, F., J. W. JI et A. S. POPEL. 2007, «Vegf gradients, receptor activation, and sprout guidance in resting and exercising skeletal muscle», *Journal of applied physiology*, vol. 102, no. 2, p. 722–734. 84

[17] MACHATTIE, D. B. 1988, *Investigation of the evoked magnetic action flux of skeletal muscle*, thèse de doctorat, McMaster University. 77, 78

[18] MACKERT, B.-M., J. MACKERT, G. WÜBBELER, F. ARMBRUST, K.-D. WOLFF, M. BURGHOFF, L. TRAHMS et G. CURIO. 1999, «Magnetometry of injury currents from human nerve and muscle specimens using superconducting quantum interferences devices», *Neuroscience letters*, vol. 262, no. 3, p. 163–166. 101

[19] MASUDA, T., H. ENDO et T. TAKEDA. 1999, «Magnetic fields produced by single motor units in human skeletal muscles», *Clinical neurophysiology*, vol. 110, no. 3, p. 384–389. 101

[20] MUTHUKUMARASWAMY, S. 2013, «High-frequency brain activity and muscle artifacts in meg/eeg: a review and recommendations», *Frontiers in human neuroscience*, vol. 7, p. 138. 76

[21] NANTEL, N. P. et L. D. PENGELLY. 1991, «Design optimization of a transducer for magnetomyography», dans *Engineering in Medicine and Biology Society, 1991. Vol. 13: 1991., Proceedings of the Annual International Conference of the IEEE*, IEEE, p. 1709–1710. 101

[22] OVERGAARD, K., O. B. NIELSEN, J. A. FLATMAN et T. CLAUSEN. 1999, «Relations between excitability and contractility in rat soleus muscle: role of the na+-k+ pump and na+/k+ gradients», *The Journal of Physiology*, vol. 518, no. 1, p. 215–225. 80

[23] REITE, M., J. E. ZIMMERMAN, J. EDRICH et J. ZIMMERMAN. 1976, «The human magnetoencephalogram: some eeg and related correlations», *Electroencephalography and Clinical neurophysiology*, vol. 40, no. 1, p. 59–66. 76

[24] ROTH, B. J. et J. P. WIKSWO. 1985, «The electrical potential and the magnetic field of an axon in a nerve bundle», *Mathematical biosciences*, vol. 76, no. 1, p. 37–57. 86

[25] ROTH, B. J. et J. P. WIKSWO. 1985, «The magnetic field of a single axon. a comparison of theory and experiment», *Biophysical Journal*, vol. 48, no. 1, p. 93–109. 77

[26] VAN EGERAAT, J., R. FRIEDMAN et J. WIKSWO. 1990, «Magnetic field of a single muscle fiber. first measurements and a core conductor model», *Biophysical journal*, vol. 57, no. 3, p. 663–667. 101

[27] WOODBURY, J. W. et A. J. BRADY. 1956, «Intracellular recording from moving tissues with a flexibly mounted ultramicroelectrode», *Science*, vol. 123, no. 3186, p. 100–101. 80

Chapter 4

In-vivo magnetic action potential in visual cortex

> *L'homme qui s'approche de son*
> *but ne marche plus, il danse.*
>
> Ainsi parlait Zarathoustra -
> Friedrich Nietzsche

Contents

Introduction

This fourth chapter presents the experiments that were conducted with the team of Professor Pascal Fries, at the Ernst Strüngmann Institute (ESI) for Neuroscience in cooperation with Max Planck Society, Frankfurt, Germany. *In vivo* magnetic recordings in visual cortex of anesthetized cats have been performed. The anesthesia and craniotomy was performed by Thomas Wunderle, Christopher Lewis, Patrick Jendritza and Jianguang Ni. The animal experiments were approved by the responsable government office (Regierungspräsidium Darmstadt) in accordance with the German law for the protection of animals. The first two experiments have been reported in the thesis of L. Caruso [7, 8]. They focused on the magnetic field generated by local field potentials, *i.e* low-frequency (< 300 Hz) electric potential variations in the extracellular space around neurons. This chapter reports the results obtained during the third *in vivo* experiment on cat, where the aim was to detect directly the spikes fired by neurons in the vicinity of the *magnetrode.*

4.1 Theoretical framework

4.1.1 Visual cortex

Visual perception requires an outstanding computational process to transform transient light patterns on the retina into a three-dimensional perception of the world. An incredibly large variety of stimuli, varying in form, color, brightness, motion can be discriminated by the visual system through largely unknown mechanisms. However, the anatomical constituents of the visual system and the pathways taken by the signals are well identified. The image that is projected onto the retina is transduced by a large number of photoreceptor cells: the rods and the cones. They are linked to bipolar cells that transmit the signal via synaptic connections to the output cells of the retina, called the retinal ganglion cells. Their long axons form the optic nerve that extends until the lateral geniculate nucleus (LGN), a relay located in the thalamus, which in turn projects to the primary visual cortex. The term "primary" refers to the region of the visual cortex that receives directly inputs from the LGN. While the response of photoreceptors to light consists of a graded variation of their membrane potential, the ganglion retinal cells transmit information to the brain as trains of action potentials. The stunning ability of the visual system is to create a full range of perception based on these streams of seemingly identical signals.

According to morphometric analysis, the thickness of the cat visual cortex is 1.6 mm

[11]. As the other regions of the cortex, the primary visual cortex is divided in 6 horizontal layers, numbered from the outer surface of the cortex (pia mater) to the underlying white matter [5]. Each of them contains a characteristic distribution of neuronal cells and synaptic connections. Layer 4 is the main input center, where most of the afferent axons from the LGN terminate [19]. An extensive study [37] reported on the neuronal cell density through the entire thickness of the cortex in various cortex areas (motor, somatosensory, frontal, temporal, parietal, visual) in five species (mouse, rat, cat, monkey, man). The absolute number of cells appeared to be constant in every area of every animals, with the exception of the visual cortex of monkey and man, where the density is 2.5 times greater (260 cells in a volume of 30 µm by 25 µm through the depth of the cortex).

Two types of neuronal cells constitute most of the visual cortex: pyramidal and stellate cells. Layer 4 is packed with stellate cells, which have a star-like shape due to the specific dendritic configuration radiating from the soma. They are generally smaller than pyramidal cells, and are confined to the primary visual cortex. The long axons of pyramidal cells connect other brain areas, as well as internal wiring between the cortical layers. However, this description is simplified since dozens of cell types have been identified by Lund et al. [23–26]. One of the key features of biomagnetic recordings is the physical organization of these cells. In the cortex, they are arranged vertically into narrow columns running from the pial surface to the white matter. Each cortical column can be defined according to this anatomical configuration or it can be regarded as a functional module that processes a specific stimulus. This configuration recalls the parallel organization of muscle fibers that helped maximizing the evoked magnetic field. The optimal configuration of the visual cortex, coupled to the facts that it is accessible on the surface of the occipital lobe, and that generating activity can be easily made by numerically controlled stimulus, make this brain area a good candidate for *in vivo* local magnetic recordings.

When a visual stimulus is sent into an eye of the cat, the corresponding neurons in the visual cortex respond by firing trains of action potentials. This electrical activity can be measured extra-cellularly or intra-cellularly by microelectrodes, which are either thin metallic micro-wires or glass pipettes filled with an ionic solution. Intracellular recordings reveal directly information about the membrane potential of the targeted cell, the post-synaptic potentials (EPSP/IPSP), or single channel activity. However, *in vivo* intra-cellular recordings are difficult in practice, and, usually, only short measurements of single neurons are feasible. Extracellular recording is the most developed technique when it comes to *in vivo* measurements of neuronal activity. Sharp microelectrodes are inserted within the cortical layers, and the output signal is split in two different components according to their frequency range.

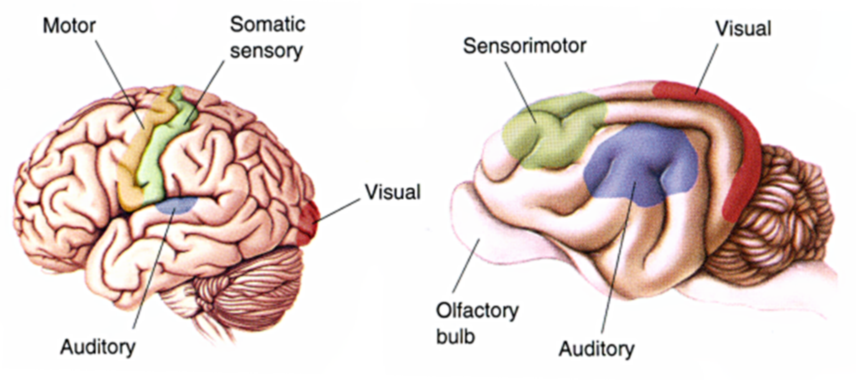

Figure 4.1: **Some functional areas in human (left) and cat (right) brain.** The cortical surfaces are highlighted with different colors corresponding to each functional area: visual, auditory, motor and somatic sensory. The scaling has been adapted by a factor of 3. The visual cortex is easily accessible by craniotomy for the recordings. Adapted from [2].

4.1.2 Local Field Potential (LFP)

The low-frequency part (≤ 500 Hz) of extracellular recordings is called local field potential (LFP) [31]. LFPs are measured with microelectrodes, made of metal or silicon, which are used as either single electrodes or multi-electrode arrays. One of the most widely established technique is based on a so-called Utah array that permits the implantation of 100 electrodes per 16 mm^2 of cerebral cortex [29, 38]. The term *local* can be confusing, but it is traditionally used to discriminate these intracranial measurements from the electroencephalogram, which is recorded at the surface of the scalp with macro-electrodes of a centimeter scale, and from the electrocorticogram (ECoG) recordings made at the surface of the cortex with subdural electrodes of about 1 mm in diameter. Simultaneous recordings of LFPs, ECoG, and EEG displayed the same pattern of oscillations during wake and sleep state [32, 40]. It has been shown that these low-frequency oscillations, up to 4 Hz, have a large coherence range in the order of several millimeters, since they result from a large population of neurons [4]. Ideally, LFPs could bring additional information about the origin of the cortical microscopic events responsible for these oscillations, which would be an important step towards an accurate interpretation of the macroscopic EEG signal. Despite the easy experimental process, there is an ongoing debates about the cellular origin and the interpretation of LFPs.

Local or non-local FP ?

On the one hand, the local aspect of LFP has been suggested by studies that reported different LFP patterns between two electrodes separated by a few hundred microns [20, 41]. The sources are supposed to be within a range of 200-400 µm from the tip of the electrode. However, these studies were restricted to the lateral spreading of the LFP that has been found to be up to 5 mm [22], and they did not observe the vertical diffusion of the signal over centimeter scale [39]. On the other hand, differential recordings between two adjacent electrodes yield amplitudes that are 10 to 100 times smaller than those in single-electrode recordings referenced to ground [16]. Only a source located far away compared to the inter-electrode distance could produce such an effect, which suggests a non-local origin of the LFP. This hypothesis is confirmed by experiments showing that in a curved or folded brain structure, the peak value of the LFP may be located out of the source area [10].

Filtering properties

Although the intracortical recording implies that the LFP signal does not have to propagate through several tissues (cerebrospinal fluid, dura matter, cranium, skin) to reach the electrodes, such as the EEG signal, the high frequency component of the LFP is still strongly attenuated. Then, the extracellular signature of action potentials fired by neurons in the area is largely filtered. This low-pass filtering property of the LFP is both a complex feature to understand and an opportunity in the sense that it prevents from the continuous detection of every extracellular action potentials coming from every neurons of the network, that would make their sorting impossible [9]. Action potential can be recorded extra-cellularly only if the tip of the electrode is located in the close vicinity of the targeted neuron, but the amplitude will vary greatly with its position. Several explanations are suggested to explain these filtering properties of the extracellular environment that limits the contribution of action potentials to LFPs. The return currents flowing out of the cell could be filtered by the membrane [30], the quadrupole configuration could make their contribution decrease quickly [27], or the capacitive properties of the extracellular medium could be responsible of this effect [3].

Relation between LFP and neuronal activity

LFP signal is mostly believed to be due to lower-frequency events, as they need to overlap in time to induce a measurable signal. Inhibitory and excitatory post-synaptic currents are believed to contribute the most to the LFP [6]. Establishing a relationship between spiking activity and the LFP pattern is not straightforward, as many subthreshold post-synaptic currents can be present without triggering an action potential. Even if it seems intuitive that an increase of neuronal activity will lead to stronger LFPs, the causality between spikes and LFPs has not been demonstrated. Moreover, LFPs can be measured in regions where the neurons are not firing, well beyond the boundaries of the activated area since sub-threshold synaptic inputs or inhibitory inputs also generate LFPs [18].

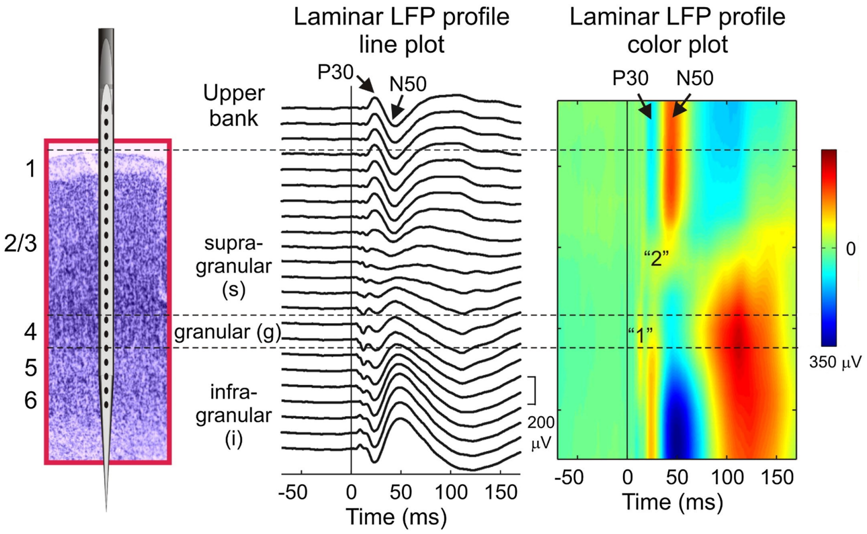

Figure 4.2: **Local field potentials** *In vivo* recordings in the auditory cortex of monkey. A linear array of 23 electrodes separated by 100 µm has been used to measure the LFP in every cortical layers (numbered from 1-6). P30 (resp. N50) represents the positive (resp. negative) response occurring 30 ms (resp 50ms) after the auditory stimulus. The color plot represents the negative deflections in red and the positive deflections in blue, which range between ± 350 µV. Adapted from [18].

4.1.3 Spiking activity

High-pass filtering (≥ 500 Hz) of the extracellular potentials gives information about the spiking activity of the area. A spike is defined as the extracellular signature of an action potential [31]. Figure 4.3 shows the computed extracellular signature of an action potential at different locations along a pyramidal neuron. If the tip of the electrode is positioned sufficiently close to a soma, the spikes are easily detected and, contrary to LFP, the relation between them and neuronal activity is straightforward. In single-unit recordings, an electrode is inserted in the cortex until a clear spike is detected. How-

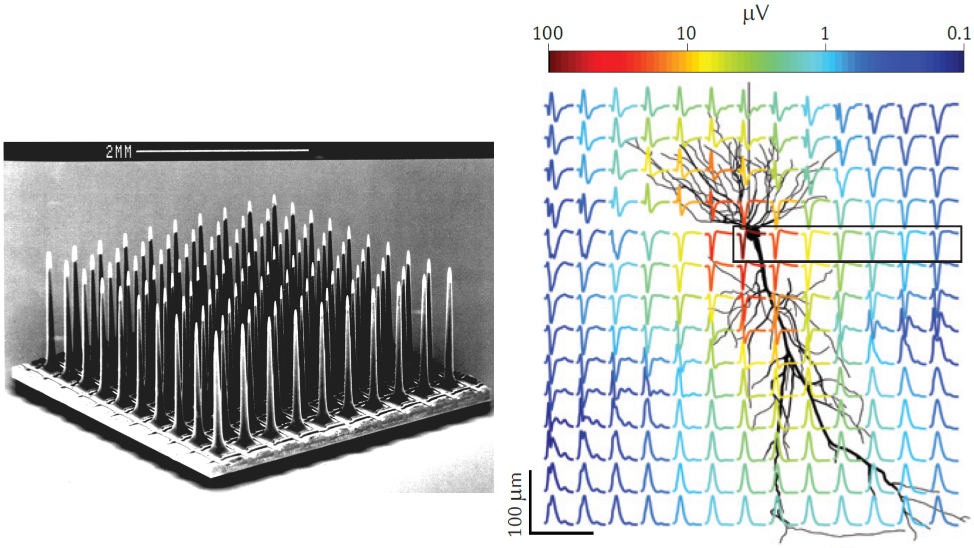

Figure 4.3: **Utah array and the effect of an action potential to the LFP. Left:** Scanning electron microscopic image of a Utah array made of 10*10 electrodes separated by 300 µm. They provide a high spatial resolution, and the position of single active neurons can be estimated by triangulation. These 100 needles are made of silicon and their sensitive part is located at the tip [21]. **Right:** Computation of the extracellular contributions to the LFP of an action potential fired by a pyramidal neuron. The color scale represents the amplitude of the spikes that ranges from 100 µV close to the soma, to 1 µV at a distance of 200 µm. Time scale is 10 ms. Adapted from [6].

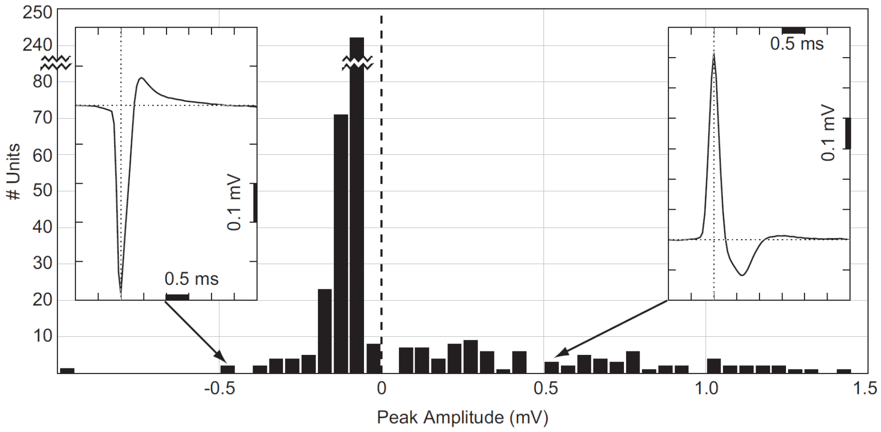

Figure 4.4: **Distribution of extracellular spikes in cat visual cortex.** Extracellular recordings have been performed with a glass micropipette and 453 units cells have been identified using traditional spike sorting processing. 74% of the cells exhibited negative spikes with amplitudes of 50-200 µV. For the negative spikes, the mean amplitude of the peak value was -110 mV, while the mean value for the positive spikes was 0.54 mV. Examples of typical positive and negative spike waveform are shown in the insets. From [12].

ever, the high density of neurons can prevent from sorting which neurons are firing, since many neighboring cells of the same type could be located at the same distance from the sensitive tip of the electrode.

Moreover, the extracellular signature of action potentials fired by neurons in the area is largely filtered. Action potential can be recorded extra-cellularly only if the tip of the electrode is located in the close vicinity of the targeted neuron, but the amplitude will vary greatly with its position. The recorded signal is then a superposition of all these contributions; this is why it is usually referred to as multi-unit activity (MUA). In order to improve spike sorting, *i.e* identifying which neuron is firing, triangulation techniques based on two (stereotrode) or four (tetrode) electrodes have been developed [15].

Since 1926, it is well known that the higher the magnitude of an applied stimulus, the higher the spiking rate of sensory neurons [1]. As stated above, information is encoded in a stream of action potentials, and the research carried out so far was mostly focused on explaining the temporal properties at which these events occur. However, although the actual shape and amplitude of the spikes were not considered as relevant information, except to sort out multi-units, many experiments show that they can vary greatly [17, 28]. In order to classify them, spikes are usually detected using an amplitude threshold and sorted according to their shapes. More complex signal-processing algorithms are developed to perform efficient spike sorting, involving pattern recognition and machine-learning techniques [34]. Modeling studies have been reported to try to describe the biophysical factors responsible for these shape and amplitude variations. As illustrated Figure 4.4, most of the extracellular signature of spikes are negative peaks, but unexplained high amplitude positive spikes, up to 1.5 mV, have been recorded [12]. It emphasized the gap in our understanding of the spike-generation process or of the extracellular recording biophysics.

Performing spike sorting with a magnetic sensor has never been done. The possibility to rely on the electric signal to confirm the actual neuronal activity will be of key importance. A conventional tungsten electrode, positioned close to the GMR sensor, can be used to perform electric spike sorting. Every time a spike is detected, the magnetic field generated during this event is stored and averaged, allowing to perform an original magnetic spike sorting process. Before detailing this technique and the *in vivo* experiments, the development of this needle-shaped GMR-based sensor, referred to as a *magnetrode* is presented.

4.2 Magnetrode

4.2.1 Microfabrication

Considering the columnar orientation of cortical neurons, the intra- and extracellular currents are supposed to flow along the same axis as these columns. This configuration is expected to produce a circular magnetic field, which can't be probed with traditional non-invasive sensors that are sensitive to the radial component of the field (see Chapter 1 Figure 1.3). Since the magnetrode has to be inserted perpendicularly to the cortical surface, *i.e* along the column axis, the sensors have been designed so that the GMR element would be sensitive to this circular component. It has to be emphasized that the thinner the tip of the sensor, the less damage is created when inserted in the cortical layers. The thickness of the probe breaks the local symmetrical arrangement of the cortical columns. However, an infinitely small sensor, placed in the middle of the cortical columns should not measure any magnetic field, so that a certain thickness of the probe remains needful. A spin-valve consisting of 5 segments of 4*50 µm arranged in a meander configuration has been patterned. Compared to a sensor made of a single segment, the sensitive volume of a meander is higher, so that the low-frequency noise, is reduced. The thermal noise level, though, increases with the square root of the global resistance, *i.e* the number of segments.

The GMR stack is deposited by sputtering on a commercial silicon substrate of 700 µm, insulated by a 1-µm thick SiO_2 layer. The wafer is 8 inches (203 mm) in diameter. The deposition is made by sputtering at a partial Argon pressure of 5.10^{-3} mbar. The wafer is annealed at 300°C in a magnetic field of 1 T, applied along the wafer plane and meant to set the magnetization of the PtMn/CoFe layer, which is the magnetic reference layer. After deposition and annealing, the wafer substrate is ground down to 200 µm by mechanical grinding. The composition of the GMR stack is given in Figure 4.5.

The GMR stack is patterned by optical lithography. For each of the five steps of the microfabrication process, a specific chromium mask has been designed. Its dimen-

Material	Ta	PtMn	CoFe	Ru	CoFe	Cu	CoFe	NiFe	Ta
Thickness (nm)	3	18	2	0.85	2.1	2.3	1.5	3.5	3

Figure 4.5: Composition of the GMR stack used for the *magnetrode* process, from the top down to the substrate.

sions, 50 mm * 50 mm, are adapted to the MJB4 (Süss Microtec) mask aligners used in this process. A mask contains up to 10 magnetrodes (see Figure 4.6). A square of the same size is diced from the 8 inches wafer with a diamond tip. The sample is then cleaned with acetone and isopropyl alcohol. A few drops of Shipley 1813 photoresist are poured on the surface and the spin coating is made at 5000 rpm for 60 seconds, which leads to a nominal resist thickness of 1.3 µm. It is then soft baked at 110°C for 3 minutes on a hot plate to evaporate the coating solvent and harden the resist. The sample is placed in contact under the first mask and exposed to UV radiations for 20 seconds under 10 mW/cm^2. After exposure, the sample is rinsed in a developer to remove the exposed parts that will be etched in the following step. A dry etching is made by ion milling under Argon gas at 10^{-4} mbar. After 20 minutes, the sample is put into acetone under ultrasounds for a few minutes, in order to remove the remanent layer of photoresist that protected the meanders during the etching process. Each magnetrode has two meanders made of 5 or 7 segments of 4*50 µm^2.

In a second step, contacts are realized by a lift-off process where a trilayer of Ti (15 nm)/Au (150 nm)/Ti (15 nm) is deposited by electron beam evaporation at 10^{-8} mbar. Each GMR segment is contacted on its short end, along the entire height and width, with the current running in the plane of the stack. Titanium is the most common material used to create adhesion layers that allow both the deposition of gold over the substrate and the deposition of other material over the gold contacts. Considering the thicknesses of these three layers, a Shipley 1818 photoresist was used during the lithography process, in order to obtain a 1.8 µm-thick layer, which is more likely to lift-off the amount of gold deposited above. The complete removal of the remaining parts is obtained in a few minutes or a few hours in the remover (see the next subsection).

The third step consists of depositing an electrode made of Platinum at the tip of the probe. During the *in vivo* experiments, a tungsten electrode is inserted in the cortex close to the magnetrode in order to measure the local potential (either LFP or spikes). The possibility to get rid of this electrode by putting a local electrode a few microns away from the GMR sensor would be of great interest. Therefore, a square of 20*20 µm^2 and 200-nm thick of Platinum is deposited by evaporation. However, this platinum electrode has led to a noisy signal compared to the traditional tungsten electrode.

Passivation of the structure is insured by sputtering a bilayer of Al_2O_3 (150 nm)/Si_3N_4 (150 nm) across the entire probe surface, except for the contact pads on the opposite side of the probe and for the platinum electrode. Deposition of the passivation bilayers is done at 5.10^{-3} mbar for 2*1h30. After passivation, resistance leakage can be quantified by putting the probe into a conductive bath to check the efficiency of the insulation.

Finally, a deep-reactive ion etching (DRIE) process was used to define the tip-shape of the overall probe. Deep etching uses the Bosch process described before, also known as time-multiplexed etching that alternates repeatedly between etching and passivation modes to create deep vertical penetration with a highly anisotropic profile. The photoresist used to protect the sensor was much thicker, 9 µm, and its baking time was 1 hour. Then, 400 cycles of etching/passivation were used to etch down the 200 µm-thick silicon substrate to define the final shape of the probe. The parameters used during the whole process are given in the following table, as well as a scanning electron microscopy picture of a final magnetrode on Figure 4.8.

Just as the muscle sensor, the magnetrode was glued on a printed circuit board (PCB) and contacted to the gold lines by wire-bonding. The wires are made of aluminum and are 30-µm thick. They were encapsulated by a drop of araldite glue because of their fragility and to avoid any short-circuits when placed in the conductive bath. Using a biasing ferrite magnet to improve the response of the spin-valve is a little more tricky, since the tip has to extend beyond the PCB by several millimeters.

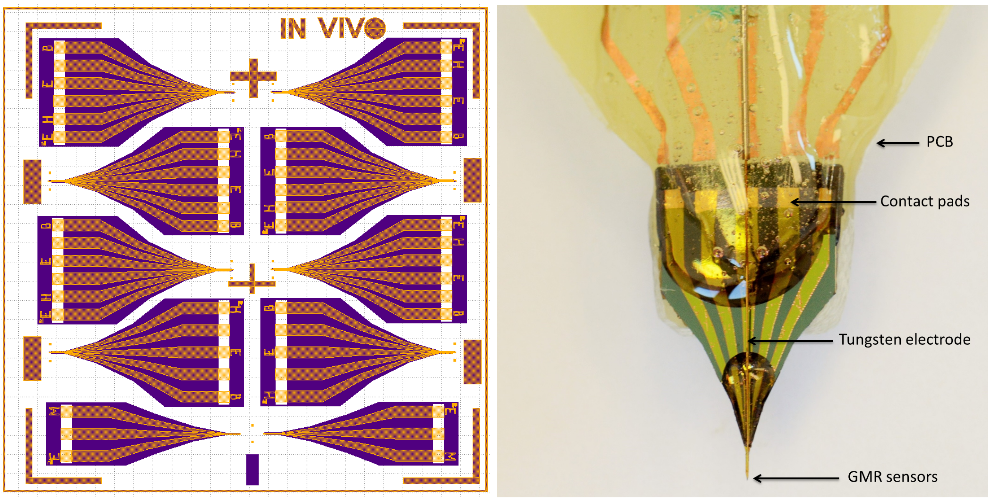

Figure 4.6: **Left:** Schematic of the mask used for lithography processes. Up to 10 magnetrodes can be produced during a single complete microfabrication process. The sides of the mask are 50 mm long, and the side of the grid dotted squares is 200 µm. **Right:** Picture of the magnetrode mounted on a printed-circuit board. A first drop of araldite glue allows to protect the wire bonds between the contact pads of the probe and the copper lines of the PCB. The drop of glue located just above the tip was used to fix the tungsten electrode against the magnetrode to detect spiking activity in the close vicinity of the GMR sensor.

Step	Technique	Parameters
GMR shape	UV Litho	Photoresist S1813, spin 60 s at 5000 rpm
		Baking 3 min at 110°C
		Exposure 20 s - Remover MF319 45 s
	Etching	20 min
Contacts	UV Litho	Photoresist S1818, spin 60 s at 5000 rpm
		Baking 3 min at 110°C
		Exposure 25 s - Remover MF319 60 s
	Deposition	Pre-etching 30 s
		Evaporation Titanium, 15 nm
		Evaporation Gold, 100 nm
		Evaporation Titanium, 15 nm
Electrode	UV Litho	Photoresist S1818, spin 60 s at 5000 rpm
		Baking 3 min at 110°C
		Exposure 25 s - Remover MF319 60 s
	Deposition	Pre-etching 10 s
		Evaporation Platinum, 200 nm
Passivation	UV Litho	Photoresist S1818, spin 60 s at 5000 rpm
		Baking 3 min at 110°C
		Exposure 25 s - Remover MF319 60 s
	Deposition	Pre-etching 30 s
		Sputtering Al_2O_3, 150 nm
		Sputtering Si_3N_4, 150 nm
Cutting	UV Litho	Photoresist AZ4562 (9 µm), spin 30 s at 2000 rpm
		Baking 1h at 90°C
		Exposure 60s - Remover AZ400K 5 min
	Deep-RIE	Etching SiO_2 with CHF_3 300 s
		Etching Si with SF_6 400 cycles of 5 s
Packaging	Wire bonding	3 Aluminum wires per contact lines.
	Protection	Gluing of the wires with araldite

Figure 4.7: **Tracking table of the microfabrication process.**

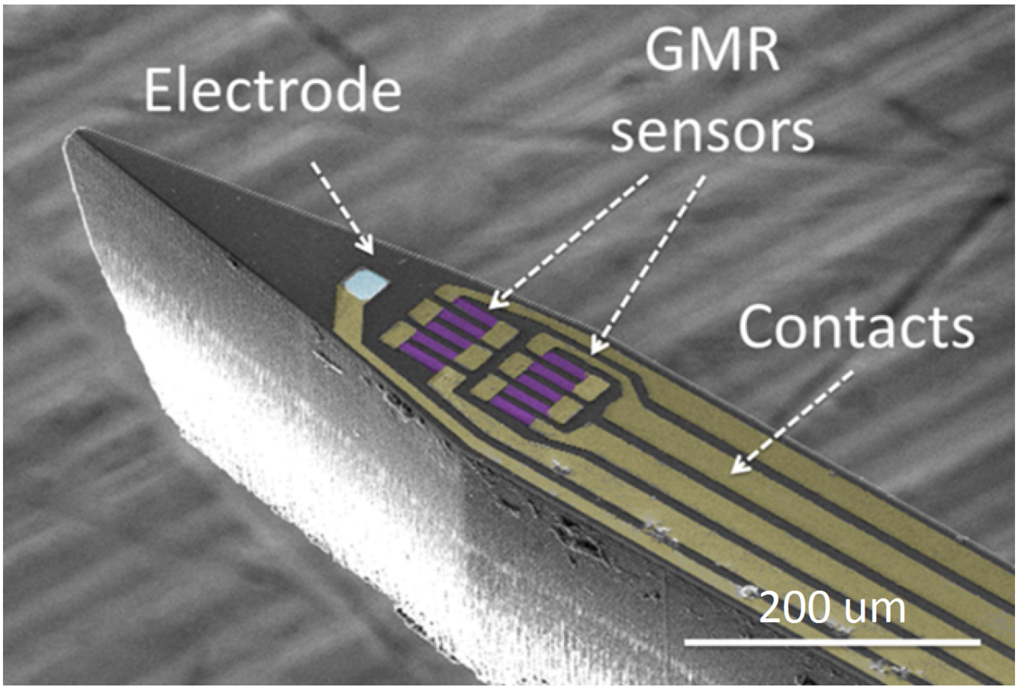

Figure 4.8: **Scanning electron microscopy picture of the magnetrode designed sensor for *in vivo* experiments.** Two GMR-based sensors are made of five GMR segments of 4*50 µm organized in a meander shape (light pink) whose pinned layer magnetizations are perpendicular to the segment length. The sensitivity direction of the sensors, which is fixed by this pinned layer magnetization, is in the plane of the GMR elements and perpendicular to the long axis of the tip. Each segment is contacted by lines of gold/titanium (yellow). The corners of the meander are short-cutted to prevent the magnetic noise due to inhomogeneities located at the edge of the segments. A platinum electrode of 20*20 µm^2 has been deposited close to the sensors to get access to the local electric potential. The silicon substrate is 200-µm thick and was etched by deep reactive ion etching. The scale bar is 200 µm.

4.2.2 Difficulties encountered

Before mastering the complete microfabrication process, many attempts were carried out without success. The large number of parameters has been optimized trial after trial to finally reach a process that can be replicated in a productive way. The cutting of the probe based on the DRIE process was very effective, but it had to be performed in another laboratory, the CTU-MINERVE. A few attempts to define the sharp shape of the probe by an in-house laser cutting machine have been done, however, the system has to be improved to reach the same quality of etching. The basic issues met during each stage of the process are illustrated below.

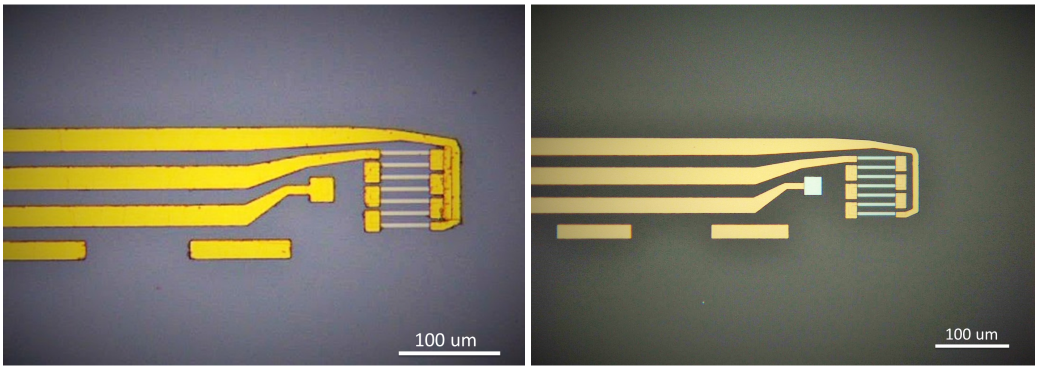

Figure 4.9: **Left: Failed lift-off.** The space between the edges of the segments and the contact line is getting too thin (≈ 2 µm), and the gold layer does not lift, even after several hours of bathing in a remover solution using ultrasound. The current will only flow through the top segment, while the other segments are short-circuited. **Right:** Successful lift-off.

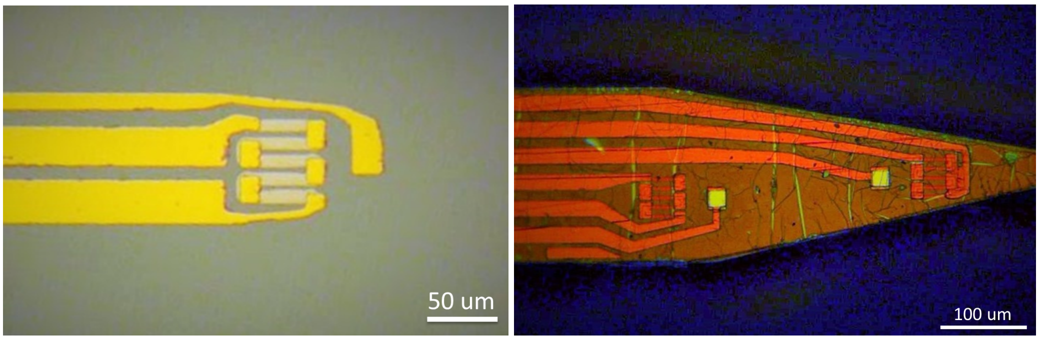

Figure 4.10: **Left: Failed etching.** If the mask and the sample are not completely in contact during the UV lithography process, diffraction will induce larger GMR elements (10 µm instead of 4 µm). The contact pads that are supposed to short-circuit the corners of the meander are too small. The sample will exhibit a large magnetic noise due to the fluctuations of the domains in the corners. **Right: Bad passivation.** The passivation layer is cracking. The electrical insulation will not be efficient when the probe is inserted into a conductive medium such as the cortex.

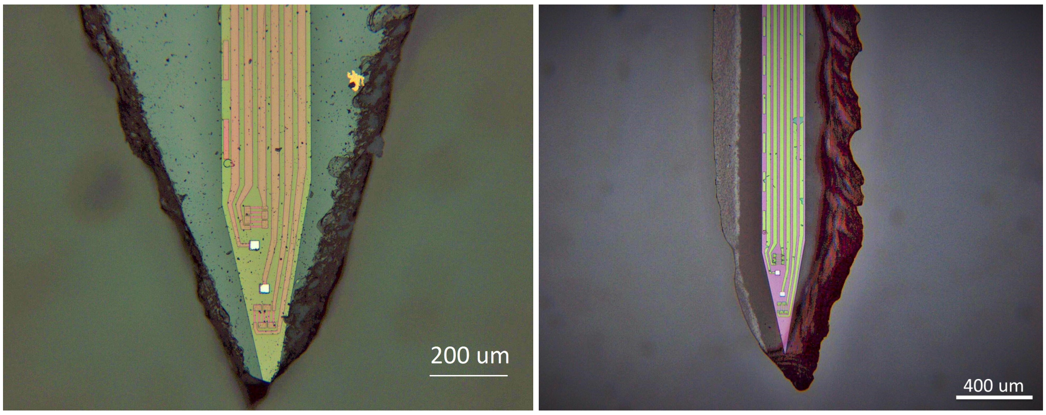

Figure 4.11: **Cutting of the sample. Left:** Picture of a probe after an attempt to define a sharp extremity using a diamond tip. **Right:** Picture of a probe after laser cutting. The contours are better defined, but the physical damages that would be made by inserting this tip inside the neuropil would be too significant.

4.2.3 Performance

The magnetrodes undergo the two basic tests presented earlier in order to measure their magneto-resistive response and their intrinsic noise. Since the same GMR stack has been used most of the time, the magnetoresistive ratio is always in the range of 6-7%. A few processes based on new stacks deposited in the laboratory have been run, but no biological experiments have been carried out with probes from these new stacks. The sensitivity of each sensor is computed from the slope around zero field. Values ranging between 2%/mT and 4%/mT have been obtained.

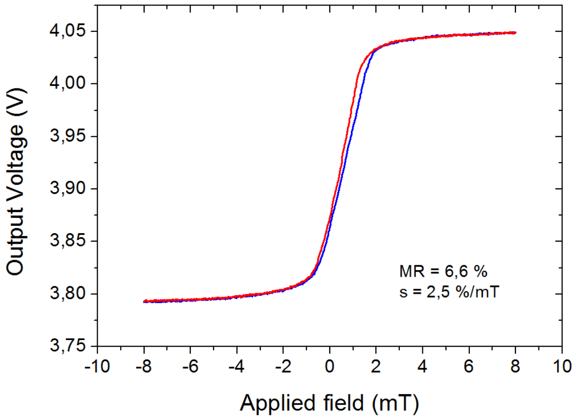

Figure 4.12: **Output voltage of the GMR sensor as a function of the magnetic field.** The magnetoresistance of the sensor is 6,6% and its sensitivity is 2,5 %/mT. For a supply voltage of 1 V, a field of 1 nT would create a variation of 25 nV across the spin valve.

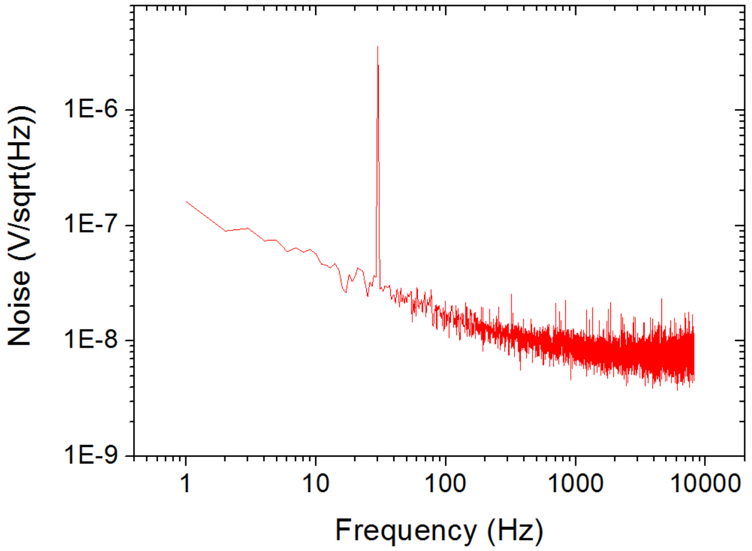

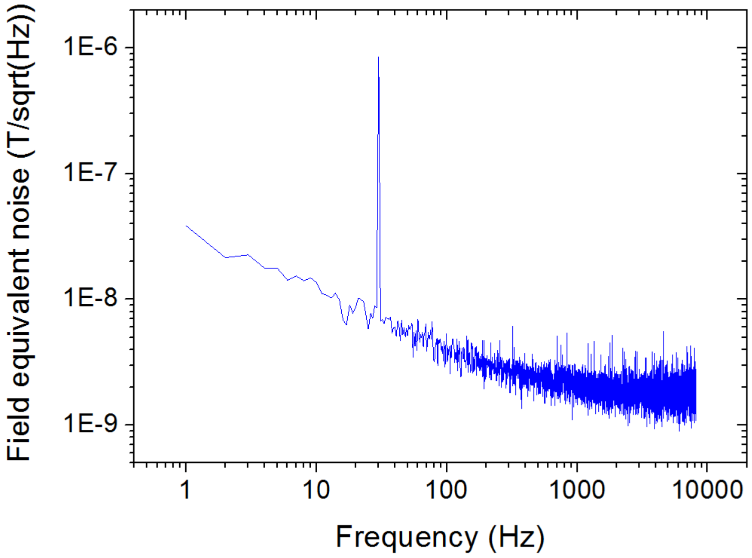

Figure 4.13: **Top:** Noise level (square root of the power spectral density) of the sensor. The 1/f noise is dominant under 1 kHz. The thermal noise level is around 5 nV/$\sqrt{Hz}$. The large peak at 30 Hz is a sinusoidal magnetic field used to get the detectivity of the sensor. **Bottom:** Field equivalent noise level. The detectivity is 10 nT/$\sqrt{Hz}$ at 10 Hz, 4 nT/$\sqrt{Hz}$ at 100 Hz, and 1.5 nT/$\sqrt{Hz}$ above 1 kHz. The global RMS noise on the working bandwidth 500 Hz - 8000 Hz is around 130 nT.

4.3 Experimental setup

4.3.1 Biological procedures

Anesthesia was initiated intramuscularly with 10 mg/kg ketamine hydrochloride and 0.05 mg/kg dexmedetomidine supplemented with 0.04 mg/kg atropine sulfate. Anesthesia was maintained after tracheotomy by artificial ventilation with a mixture of N_2O/O_2 (70%/30%) with 0.8% isoflurane. Analgesia was maintained by intravenous infusion of sufentanil (2 µg/kg/h) together with electrolytes (3 ml/kg/h) and glucose (24 mg/kg/h). After all surgical procedures had been terminated, the animals were paralyzed by intravenous infusion of vecuronium bromide (0.25 mg/kg/h). Atropine was topically applied to the eye in order to dilate the pupil. Depth of anesthesia was controlled by continuously monitoring the electrocardiogram and CO_2 level. Dexamethasone was administered every 48 hours and if needed. A craniotomy was performed around the central part of the primary visual cortex area 17 (homologue to V1 in primates). The dura mater was removed in a small window to allow easy insertion of the recording probes.

4.3.2 Technical features

A shielding box made of aluminum was used for the recordings, in order to reduce line-noise artifacts. The box had to be designed and tailor-made because of the constraints implied by the requirements of life support. Specifically, the animal was connected to an ECG monitor, it received intra-venous infusions, its body temperature was recorded via a rectal thermo probe, which was connected to a control unit, which in turn drove a heating pad. For the present experiment, averaging over multiple stimulus repetitions was effective in revealing the stimulus evoked responses even in the presence of noise.

Electrical recordings were performed with tungsten electrodes (1 MΩ impedance). At first, the electrode and the magnetrode were held by separate micro-manipulators allowing for a precise positioning and careful insertion into the cortex under microscope inspection. The magnetrode was inserted first, about 1 mm below the cortical surface, and angled such that the probe penetrated the cortex as perpendicularly as possible. Subsequently, the tungsten electrode was inserted in close vicinity to the magnetrode. However, once the probes are inserted in the cortex, positioning their sensitive tip at the same position is a quite complex operation. The results presented in the next part were obtained after the tungsten electrode had been glued over the magnetrode, as shown in Figure 4.15. The cortical thickness of the cat being 1.6 mm, the sensors were expected to be located near cortical layer 4, the input layer. Signals from the magnetrode and the electrode were recorded with a standard acquisition system (Tucker Davis Technologies). To this end, signals were buffered by a unity gain headstage, high-pass filtered at 1 Hz, low-pass filtered at 10 kHz and digitized at 20 kHz.

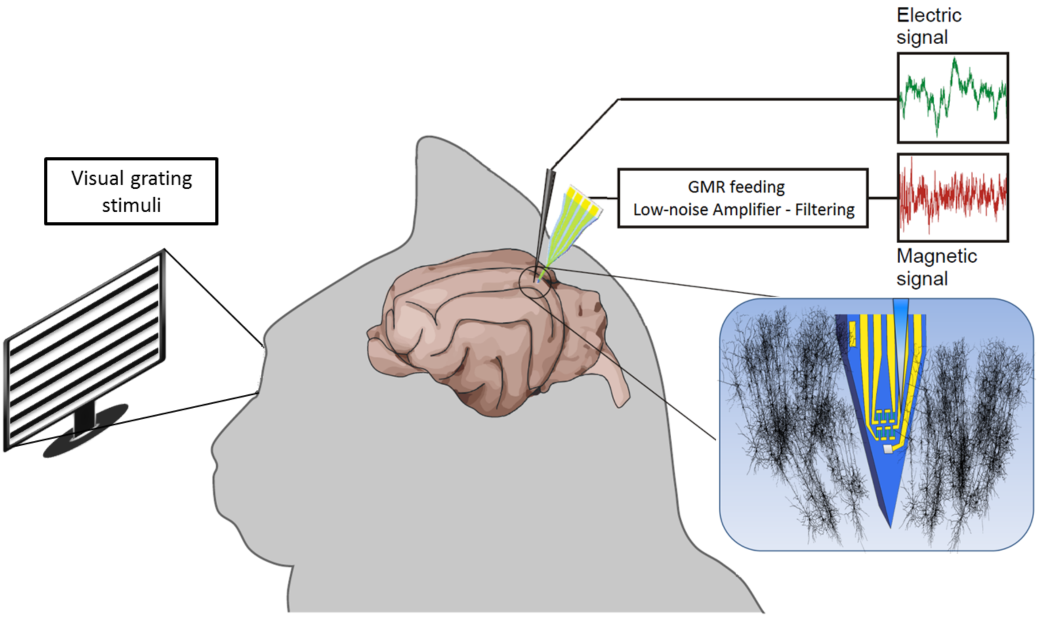

Figure 4.14: **Schematic representation of the *in vivo* experiment.** Recordings were performed in the primary visual cortex of the anesthetized cat. To activate the area, a visual stimulus was applied directly to the contralateral eye using either blue LED light or gratings. The magnetrode, containing the GMR sensor, was positioned within the visual cortex. The tungsten electrode was first inserted as close as possible of the GMR sensor, then the electrode was glued to the magnetrode (see Figure 4.15) so that the recorded signal corresponds to the potential in the very vicinity of the GMR sensor. The supply voltage is delivered by a battery, and the output signal is filtered and amplified before being digitized.

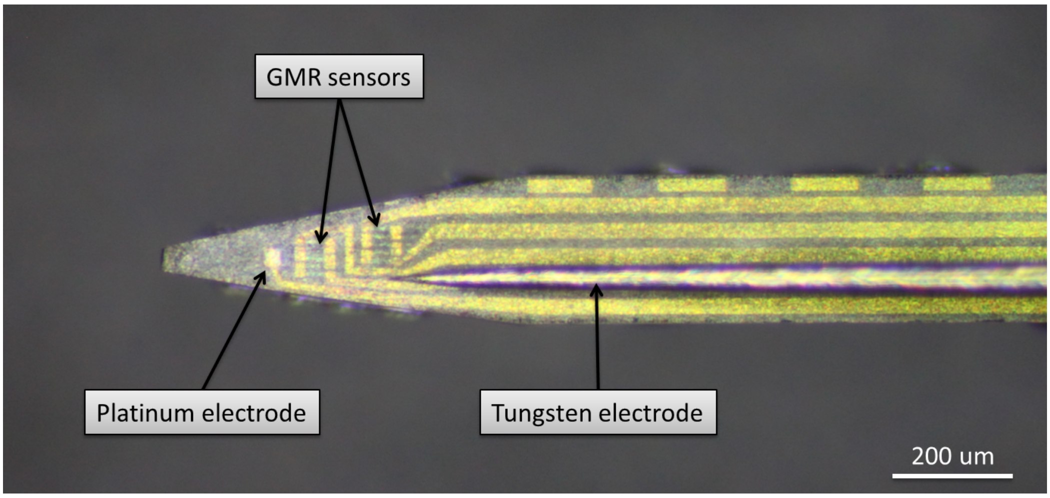

Figure 4.15: **Picture of the magnetrode and the tungsten electrode.** The tungsten electrode has been glued over the magnetrode so that the extremity of the tip is located right next to the upper GMR sensor. The distance between the platinum electrode and the tip of the tungsten electrode is 150 µm.

4.4 Results

4.4.1 Local field potentials

Drifting gratings made of black and white lines are projected to one eye of the cat for 1 second. This stimulus was repeated every 2 seconds, with a variable inter-stimulus interval to avoid adaptation. The stimulus is presented 1000 times, in order to reduce the noise level by a factor $\sqrt{1000} = 31$. The evoked response potential in the visual cortex is recorded both by the tungsten electrode and by the platinum electrode, as shown in Figure 4.16. The main idea is to measure the local field potential at these two different sites, separated by 150 µm. If LFP are indeed really *local*, the two electrodes should record a slightly different signal, which lead to extracellular current between the two sites. The current is supposed to flow along the axis of the magnetrode, and to create a circular magnetic field that can be detected by the meander, since its sensitivity direction is orthogonal to the axis.

The local field potentials recorded by the two electrodes are shown Figure 4.17. The two signals exhibit similar shapes and amplitudes. The onset consists in two large oscillations ranging between 20 µV$_{pp}$ and 80 µV$_{pp}$. They occur 30 ms after the beginning of the stimulus, which can be attributed to the transmission delay between the retina and the visual cortex. The period of one oscillations is about 35 ms, *i.e* a frequency of 28 Hz. The potential varies more slowly at the offset. A single bump lasting 25 ms (4 Hz)

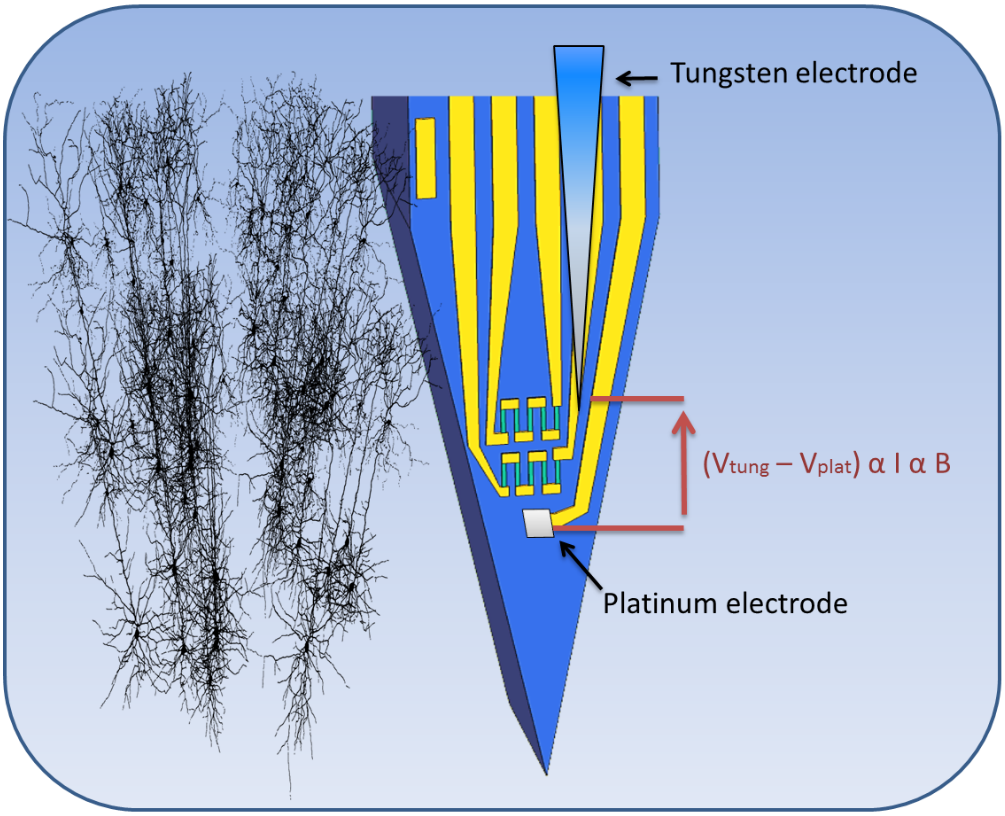

Figure 4.16: **Local field potential measurement.** The tungsten electrode and the platinum electrode are located, respectively, just above and below the GMR sensor. The distance between them is 150 µm. Any potential difference between the two electrodes, noted ($V_{tung} - V_{plat}$), induces a current I that generates a magnetic field B whose direction is compatible with the sensitivity direction of the meander.

can be observed, with an amplitude of 40 μV_{pp} on the platinum electrode, and 55 μV_{pp} on the tungsten electrode.

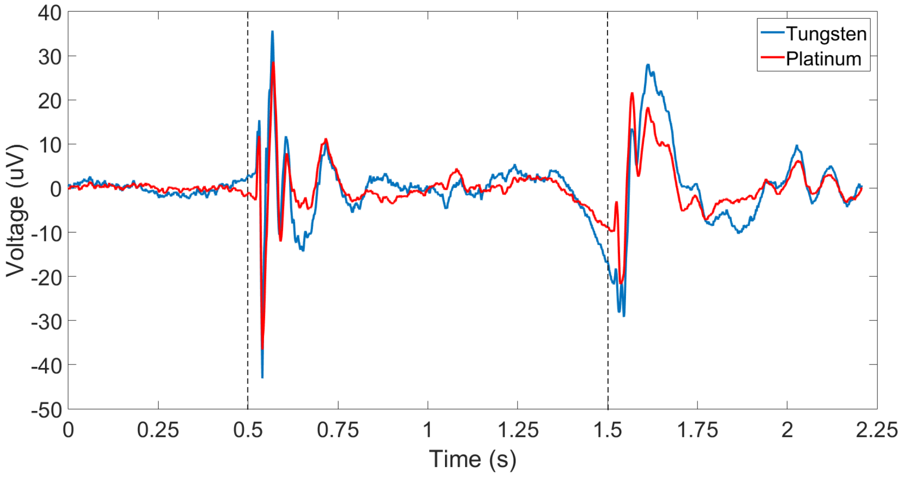

Figure 4.17: **Local field potential in cat visual cortex.** A visual stimulus is applied for 1 second. The vertical dotted lines indicate the onset and the offset of the stimulus. The evoked potential recorded by the tungsten electrode (blue trace) is similar to the one recorded with the platinum electrode (red trace). Both signals are averaged over 1000 trials, and the passband is set to 1 Hz - 300 Hz.

Since the two signals recorded at two different sites are very similar, the gradient of extracellular potential is expected to be small. The subtraction ($V_{tung} - V_{plat}$) gives maximal amplitudes of 20 μV. The component of the induced current, that is supposed to flow between the two electrodes and generate a magnetic field that can be detected by the GMR sensor, is along the axis of the probe, noted $\mathbf{j_z}$. In a simplified point of view, let's consider the extracellular medium as a linear and ohmic, with an isotropic and frequency-independent conductivity σ. From the local Ohm's law $\mathbf{j_z} = \sigma \mathbf{E_z}$, one can deduce the current of interest. The geometry is approximated by a cylinder of 200 μm of radius, and 150-μm long. The conductivity is fixed to 0.3 S/m [14].

$$I_z = \frac{\sigma \Delta V S}{l} = \frac{0.3\, 20.10^{-6}\, \pi (200.10^{-6})^2}{150.10^{-6}} \approx 5\, nA \tag{4.1}$$

The magnetic field **B** seen by the sensor can be estimated by the Ampere's law, considering the 300-nm thick passivation layers. For a distance of 100 μm, it scales as:

$$B = \frac{\mu_0 I_z}{2\pi r} = \frac{4\pi.10^{-7}\, 5.10^{-9}}{2\pi\, 100.10^{-6}} \approx 10\, pT \tag{4.2}$$

The computed magnetic field is plotted on Figure 4.18. Despite the large simplifications of this model, it appears that the range of amplitude, a few tens of picoTesla, is not accessible by GMR sensors. Moreover, the very similar shape of the two recorded signals suggests that local field potentials are not extremely spatially localized and spread nearly unattenuated over hundred of microns. Combined to the low resistivity of the extracellular medium, these features do not tend to create large current and magnetic field that could be sensed by a GMR sensor. In previous experiments reported in [7, 8], no electrical recordings could have been made with the platinum electrode, and the tungsten electrode was not glued over the magnetrode but located in its vicinity, so the present simplified model does not apply in this previous case. Moreover, Figure 4.2 shows the importance of the positioning of the probe down the cortex, since gradients of LFP recorded by a multi-electrodes can vary subsequently and induce either very small or larger currents.

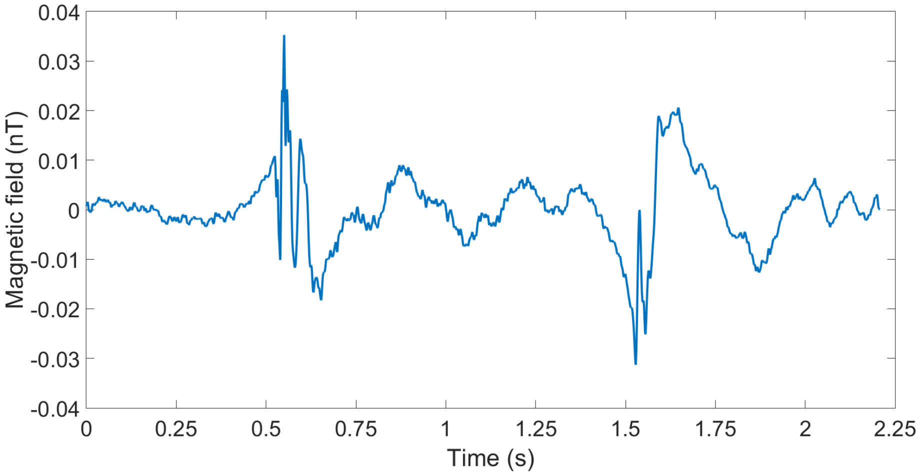

Figure 4.18: **Computed magnetic field from LFPs recordings.** The potential difference between the tungsten and the platinum electrodes reaches up to 20 µV. However, the 150-µm distance between them leads to an estimated current of 5 nA that creates a field of around 10 pT on the GMR sensor. Maximal amplitudes are obtained at the onset (0.5 s) and at the offset (1.5 s) of the visual stimulus. It has to be emphasized that this calculation must be taken with caution since the potential difference has been recorded by two electrodes that are different in size, shape and material.

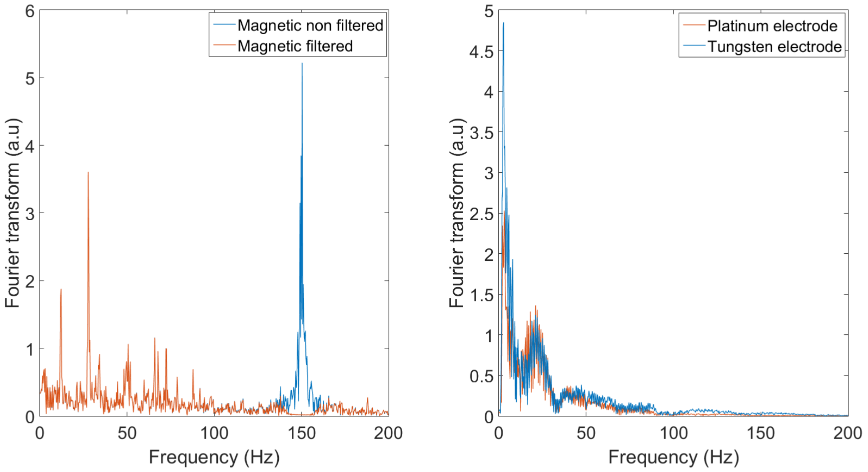

Figure 4.19: **Spectrum of magnetic signal and LFPs.** The frequency distribution of the magnetic signal before (blue trace) and after (red trace) band-stop filtering of the 150 Hz component is illustrated on the left plot. Two peaks can be observed at 12 Hz and 28 Hz. The right plot represents the spectrum of the voltages recorded by the tungsten electrode (blue trace) and the platinum electrode (red trace). Most of the power is concentrated below 30 Hz, and a very large peak appears around 3 Hz. Surprisingly, the two peaks measured on the magnetic signal are not correlated to their electric counterpart.

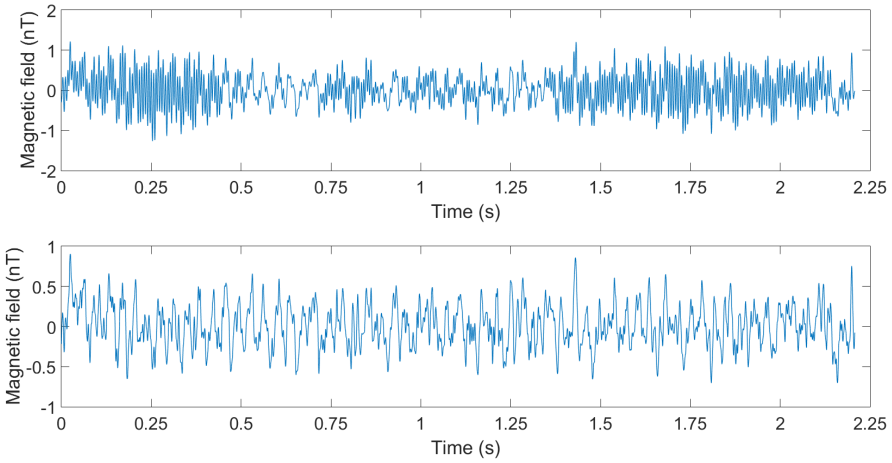

Figure 4.20: **Magnetic signal recorded by a GMR sensor.** The top plot represents the raw signal in the 1 Hz - 300 Hz band, after averaging over 1000 trials. It exhibits a large contamination due to the 150-Hz component. A band-pass filter is applied to suppress this component. The bottom plot shows the filtered signal which lays in the ±0.5-nT range. In order to be able to detect the estimated field of 30 pT, the number of required trials would be around 3.10^5, which represents an impractical acquisition time of 69 hours.

4.4.2 Magnetic spikes

Filtering stage

Spikes coexist with the local field potentials in the raw data. The same signals, whose low-frequency parts have been processed for the detection of LFPs, are used for spike detection. A digital bandpass filter is set to extract the higher frequency range: 500 Hz - 8 kHz. Figure 4.23 shows a superposition of 400 trials of these filtered data. This first step has to be conducted carefully, since a non-linear phase response of the filter could induce either artifacts exhibiting a shape similar to real spikes, or it could distort the spike shape. The first hardware filter that was applied during the acquisition has its frequency cuts (0.3 Hz and 10 kHz) far from the range of interest. Online spike detection can be used in certain applications like prosthetic devices, whose response depends on the instantaneous activity. It is not the case here, which allows to perform offline filtering with zero-phase response for all frequencies. It can be done by processing the data in both the forward and reverse direction (Matlab *filtfilt* function). Once the slow fluctuations of the signal are suppressed, the second step consists in computing a threshold that will be set to a given amplitude to extract the spikes from the noise.

Detection threshold

The choice of the amplitude threshold is a tradeoff between the number of spikes and their veracity. If the threshold is too low, noise fluctuations can be counted as real biological spikes. If the threshold is too high, the number of cells that can be detected decreases. During the *in vivo* experiments, a threshold was set manually over the envelope of the background. However, offline processing allows to compute an automatic threshold for each of the 1000 trials. This technique is much more efficient since the noise level can vary during the 20 minutes of acquisition. Figure 4.21 illustrate the evolution of the noise level for each trial and for the two electrodes. The platinum electrode becomes unstable after 460 trials, and the tungsten electrode noise has a quite stable behavior, oscillating between 7 µV and 9 µV. Once the stable trials have been extracted, the computation of the automatic threshold is performed. A simple technique is to use a value comprises between 3 or 5 times the standard deviation of the signal [33]. An alternative technique proposed by [35, 36] and based on the median absolute deviation of the signal has been shown to be more robust. For each trial, the threshold T_n has been computed as follows:

$$\sigma_n = median(\frac{|x|}{0.6745}) \tag{4.3}$$

$$T_n = 4\,\sigma_n \tag{4.4}$$

It gives a threshold of detection of around ±28 μV for the traces recorded by the tungsten electrode, and ±16 μV for the signal recorded by the platinum electrode. Another threshold was set at 15 σ_n in order to remove all the traces that contain a very large artifact.

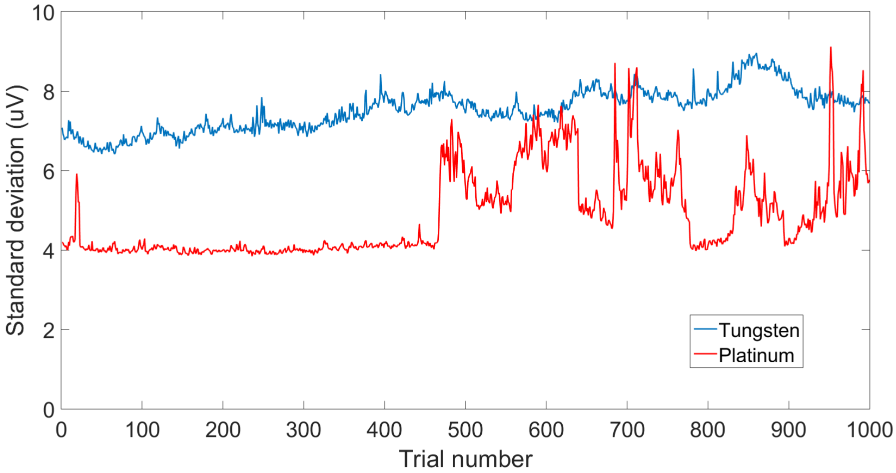

Figure 4.21: **Standard deviation of electric recordings.** The threshold used for spike detection is computed for each of the 1000 trials, for both the tungsten-based recordings (blue trace), and the platinum-based (red trace). Its calculation is based on the formula 4.3, which gives a slightly different result from the classical standard deviation. The evolution of the noise level throughout the acquisitions gives a direct indication about the stability of the electrical recording. The noise level of the blue trace is almost constant, ranging between 7 μV and 9 μV, while the platinum electrode becomes suddenly unstable after 460 trials. The other 540 trials will not be taken into account for the spike extraction process.

Tungsten / Platinum electrodes

Figure 4.22 shows single traces recorded by the two electrodes, and illustrates where the thresholds of detection are placed. The increase of spiking activity during the stimulus is clearly measured by the tungsten electrode, while the platinum electrode signal V_{plat} shows no particular response. It is even clearer when hundreds of traces are superimposed (see Figure 4.23). The envelope of the electric signal V_{tung} shows two bumps of 0.5 seconds, while V_{plat} remains noisy throughout the acquisition. Figure 4.24 illustrates how the spiking rate measured by the tungsten electrode rises from 15 spikes/s up to 230 spikes/s. On the contrary, the spiking rate remains constant, around 4 spikes/s, when recorded by the platinum electrode, which confirm its insensitiveness to the evoked response. Finally, the huge peaks measured by the GMR sensor, above 50 nT and too large to be considered as relevant, appeared to be strongly correlated to the ones occurring on the platinum electrode. If the physiological origin of the spikes recorded by the tungsten electrode is trustworthy, the signal recorded by the platinum electrode prevents from certifying the veracity of these spikes.

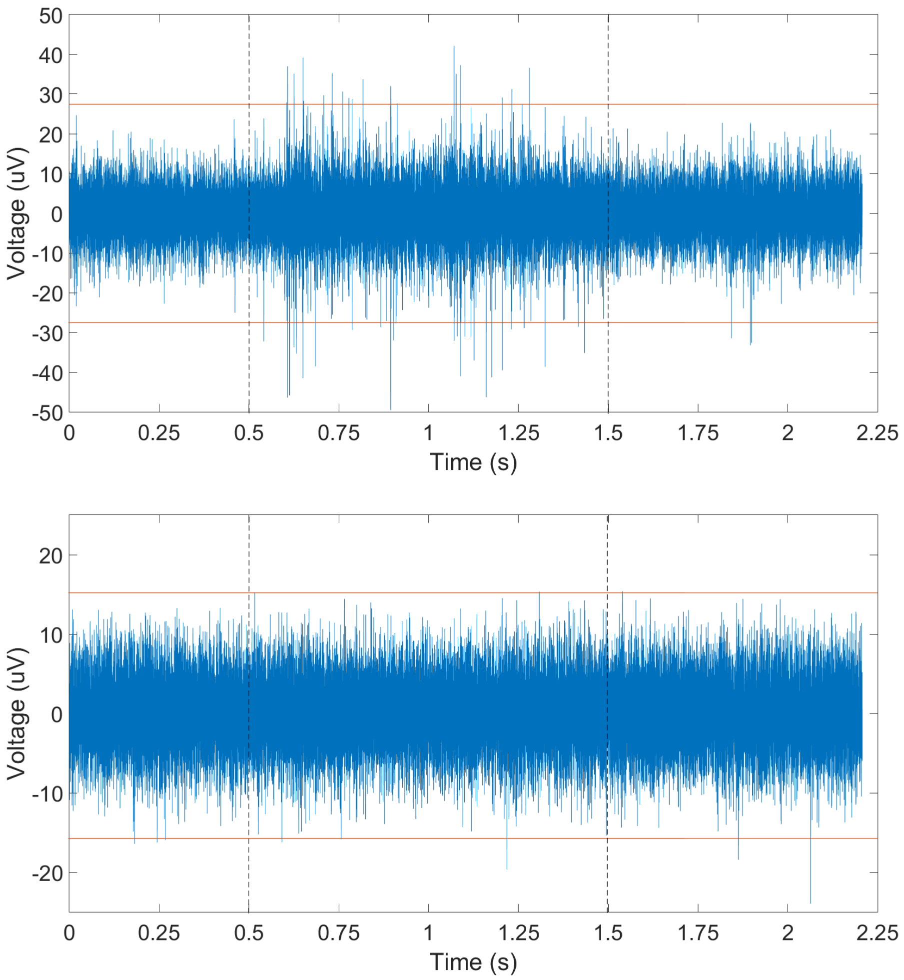

Figure 4.22: **Single traces of spiking activity in cat visual cortex.** Simultaneous extracellular recordings by both electrodes, made of tungsten (top) and platinum (bottom). In both cases, the vertical dotted lines indicate the onset and the offset of the stimulus, and the two red horizontal lines represent the threshold of detection for both positive and negative spikes, which is set to ± 4 σ.

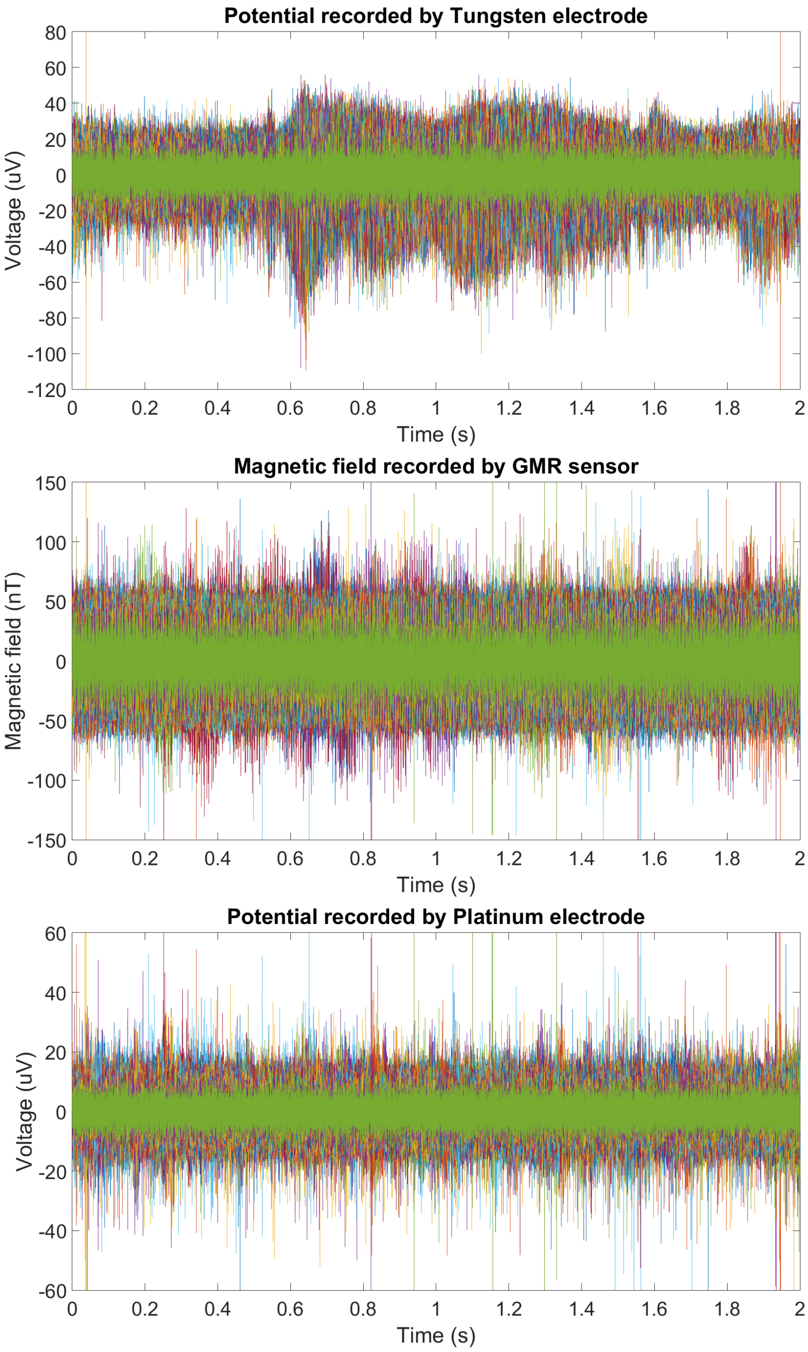

Figure 4.23: **Spiking activity in cat visual cortex.** Superposition of 400 traces corresponding to the extracellular potential filtered to the range 500 Hz - 8 kHz, recorded by the tungsten electrode (top) and by the platinum electrode (bottom). The magnetic field is measured simultaneously by the GMR sensor (center). The outer envelope of the signal recorded by the tungsten electrode shows clearly that the spiking activity increases during the stimulus time range 0.5 s - 1.5 s. On the other hand, the very large peaks, around 100 nT, measured by the GMR sensor, are strongly correlated to the ones occurring on the platinum electrode.

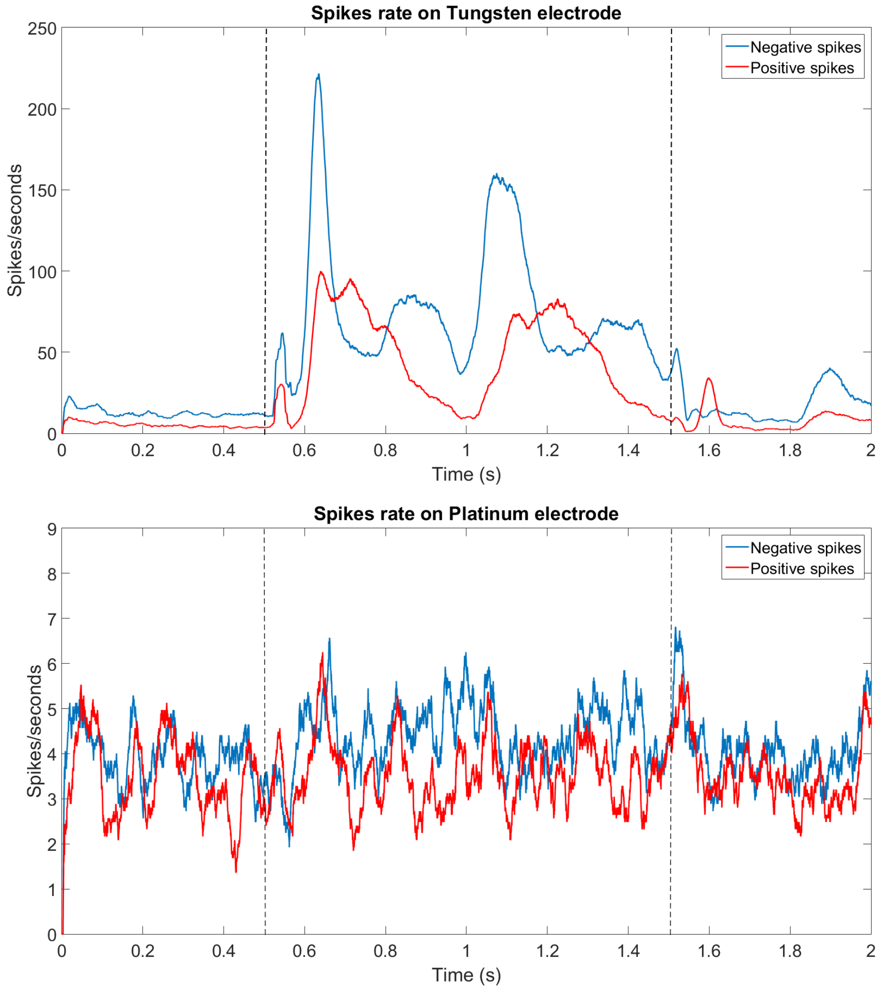

Spikes rate on Tungsten electrode

Spikes rate on Platinum electrode

Figure 4.24: **Spike rates recorded by Tungsten and Platinum electrodes.** The number of spikes recorded per second by the tungsten electrode (top) and the platinum electrode (bottom) is plotted. The vertical dotted lines indicate the onset and the offset of the stimulus. This measurement indicates clearly that the tungsten electrode measures real biological spikes, as the rate increases from 20 spikes/s to around 100 spikes/s when the stimulus is applied. Moreover, the firing rate of negative spikes is higher than the firing rate of positive spikes. On the other hand, the stimulus has no effect on the firing rate recorded by the platinum electrode. It remains constant between 4 and 5 spikes/s, which suggests that the peak values reaching the threshold might not be real spikes and could be noise artifacts.

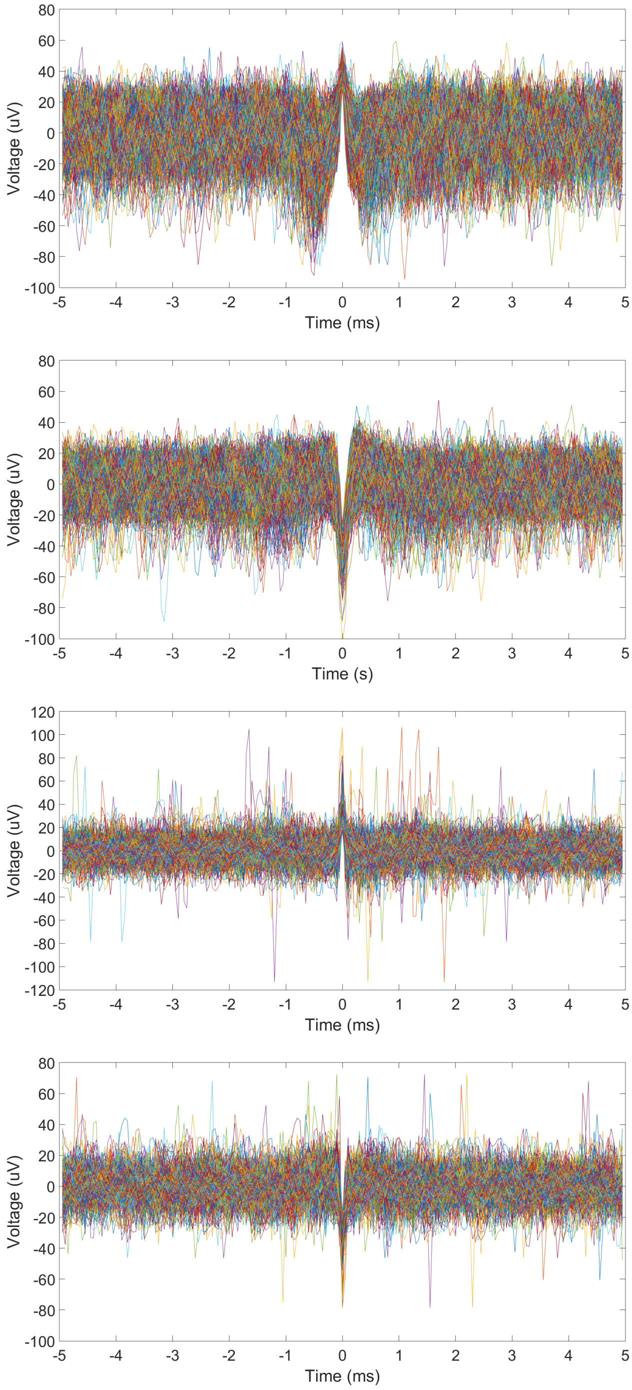

Figure 4.25: **Spiking activity.** Superposition of each positive and negative spike detected by the tungsten electrode (top) and by the platinum electrode (bottom). Each spike is isolated in a time window of 10 ms. Their respective amplitude are plotted on the histograms in Figure 4.26. Another point that suggests the presence of artifacts on the platinum electrode is that a few large spikes of the same amplitude seem to appear in the ±3 ms interval around the recorded spikes, which is below the refractory period of a neuron.

Amplitude distribution

In a typical spike sorting experiment [36], algorithms based on pattern recognition are set up to sort each spike according to their waveforms, in order to discriminate which neuron is firing. The relatively low sampling frequency used during these experiments, 20 kHz, does not allow for such sorting that also requires important software development. Moreover, once the spikes were detected, they have been classified according to their amplitude. If the electrode would have been sensitive to a few neurons in the vicinity of the tip, one would expect to see discrete levels of amplitude, each level corresponding to a neuron at a given distance. Figure 4.26 shows that this is not the case: the distribution of amplitude follows a smooth Gaussian shape. This result indicates that the electrode measures the contribution of a large number of neurons, and that an array of several electrodes would be necessary to sort the spikes accurately.

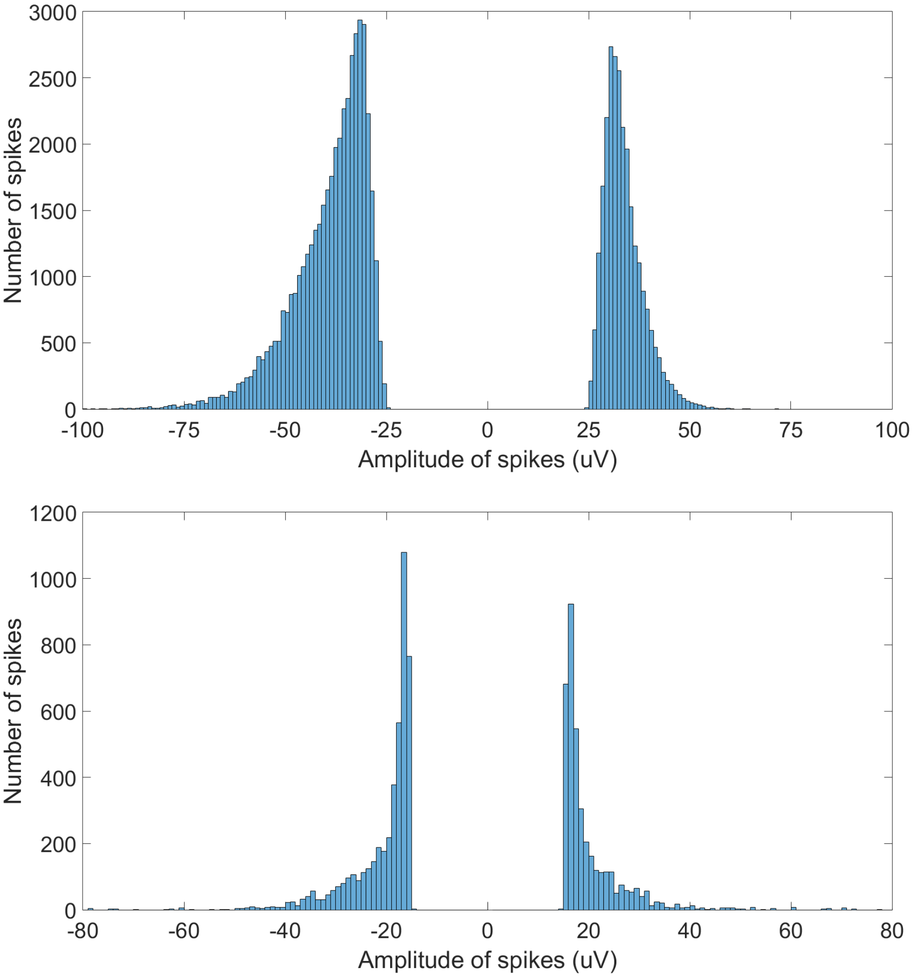

Figure 4.26: **Histogram of spiking activity recorded by Tungsten and Platinum electrodes.** Each bar of the graph represents the number of spikes in a 2 µV range. The tungsten electrode recorded around 46000 negative spikes and 26000 positive spikes, which gives a ratio of 63%-37%. The platinum electrode recorded much less events, 4600 negative spikes and 3900 positive spikes, giving a more balanced ratio of 54%-46%. However, only half of the trials (460/1000) have been taken into account since the recording started to become unstable (see Figure 4.21). The detection of a larger number of negative spikes confirms the veracity of the measurement, since a purely noisy signal would have given an equal symmetric repartition of the events. However, this smooth distribution prevents from identifying how many neurons are firing, which could have been easier if clear steps had appeared. The distribution of this graph is similar to the one presented earlier in Figure 4.4, but, in this case, the maximal amplitude, around 80 µV, does not reach the large reported values of 1.5 mV.

Magnetic signature

Once every spike has been isolated on a time window of 10 ms, the output value of the GMR sensor corresponding to each spikes was extracted on the same window and averaged. This measurement is much more efficient than the previous one, when the aim was to detect the signature of local field potential. Instead of averaging 1000 traces lasting 2 seconds, here, tens of thousands of spikes are recorded and averaged, so that the noise level of the GMR sensor is reduced down to ±0.3 nT. This noise level is sufficiently low to obtain the main result, the first magnetic signature of an action potential recorded *in vivo* inside the cortex.

Figure 4.27 shows a clear magnetic peak, whose maximum is synchronized with the electric spikes. Its averaged amplitude is around 1.1 nT for the positive peaks and -1.3 nT for the negative peaks. It has been shown previously that the expected field due to local field potential was 50 times lower, because of the small potential gradient between the two electrodes, *i.e* the large spatial spreading of the LFPs. When it comes to spiking activity, the signal arises from neurons firing in the very close vicinity of the tip of the electrode, so that the local aspect of the recording is magnified. Sharp gradients of potential are more likely to arise and to induce strong enough current to generate a magnetic field of 1 nT. The complexity of the system makes it really difficult to model and to estimate a relevant value. What is usually described in the literature is the computational methods to predict the shape of extracellular action potential. At first, the transmembrane currents of a neuron are calculated and the Laplace's equation is applied to obtain the extracellular potential. Even though the magnetic contribution of the transmembrane current is assumed to be negligible because of the cylindrical symmetry, its value can reach up to a few nA [13]. These charges loop back in the medium and similar values for the extracellular current could be expected. The model proposed in the previous chapter to suggested that 75% of the magnetic field due to intracellular current was screened by the return current flowing between the fibers of the muscle. A similar reasoning is not appropriate in this case because the arrangement of the cells is not clearly known, especially since the magnetrode is inserted in the middle of the neuropil and the damages are not quantified. Finally, the magnetic signature recorded by the GMR sensor was split in three categories, according to the amplitude of the corresponding electric spikes (see Figure 4.28). It appeared that the lowest amplitude spikes (20-35 µV) induced the largest magnetic field (1.4 nT) and the bigger spikes (35-50 µV) generated a smaller magnetic signal (0.9 nT). This unexpected result can be explained by the arrangement of the cells: a neuron just above the GMR sensor generates a large magnetic field but its electric contribution, measured by the tungsten electrode, is lower than the one of a neuron close to the tip of the latter.

Another important aspect is that the polarity of the magnetic field varies with the polarity of the electric spikes: when the spikes are positive, the magnetic peak is negative and vice versa. However, the sign of the magnetic field depends on the orientation of the pinned layer of the spin-valve. The relevant point is to deduce which way the current that generated this field was flowing, which brings additional information that can not be obtained with an electrical measurement. Here, a positive peak corresponds to a flow of current towards the bottom of the magnetrode, while a negative peak comes from a current flowing upwards. In both cases, it corresponds to radial currents that are not supposed to generate a magnetic component that can be probed by a SQUID placed over the head.

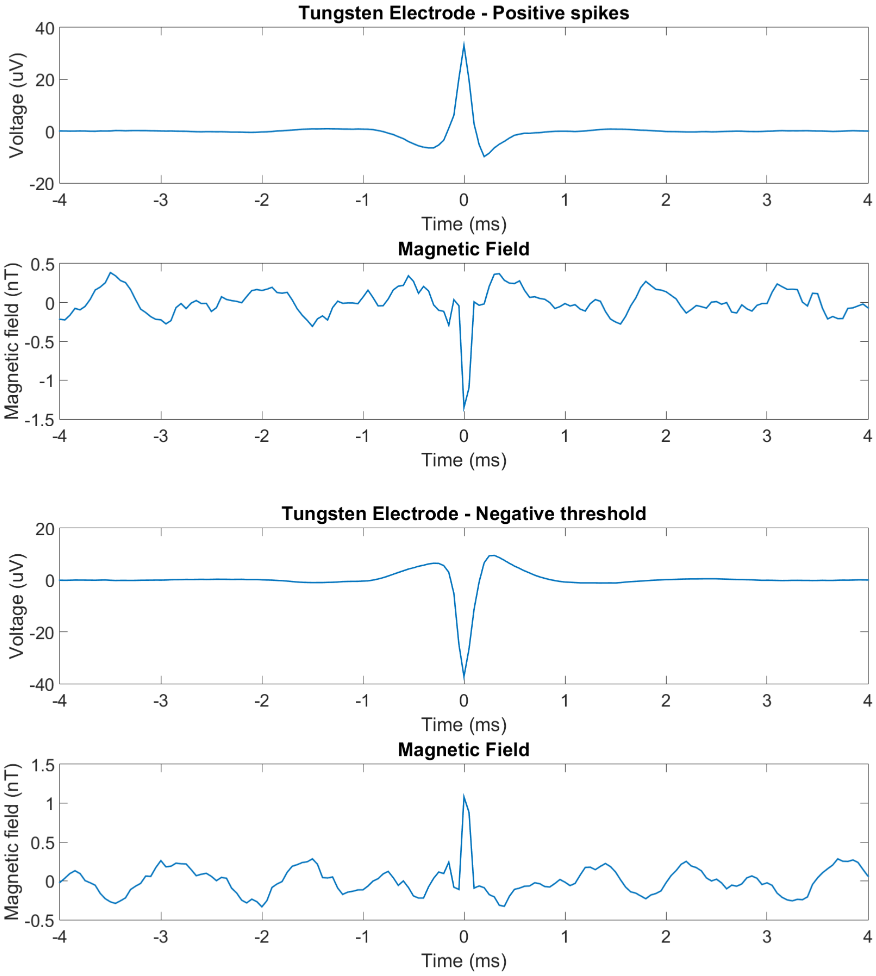

Figure 4.27: **Magnetic signature of spikes triggered on the tungsten electrode.** In order to extract the magnetic signature of action potentials, the 46000 negative spikes and the 26000 positive spikes recorded by the tungsten electrode have been averaged, as well as the magnetic field recorded by the GMR sensor during the corresponding time window of each spike. The noise level of the GMR sensor, around ±60 nT (see Figure 4.23), decreases to ±0.3 nT after 46000 averaged trials. The averaged electric spike has an amplitude of 35 μV, a value which is coherent with the histogram of Figure 4.26. A clear magnetic signal of -1.3 nT is recorded when the positive spikes are detected. When the detection is triggered on the negative spikes, the polarity of the magnetic field is reversed, and a peak of +1.1 nT is measured.

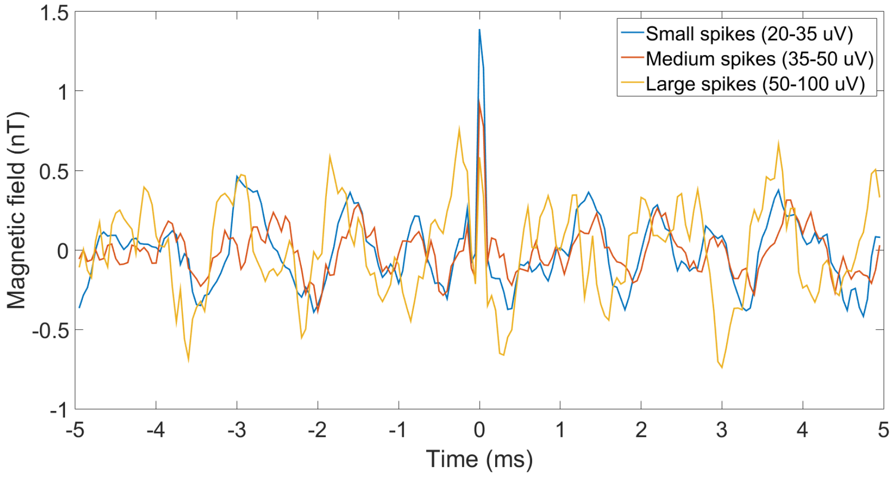

Figure 4.28: **Magnetic spikes according to their electric amplitudes.** The magnetic signal showed Figure 4.27 results from the averaging of tens of thousands spikes. They have been classified in 3 categories according to their peak amplitude, in order to check whether the largest electric spikes would generate the largest magnetic field. The smallest peaks (20-35 µV) lead to a magnetic peak of 1.4 nT, the medium peaks (35-50 µV) and the large peaks (50-100 µV) induce a magnetic peak of respectively 0.9 nT and 0.5 nT. The number of large spikes being small, the signal to noise ratio is lower. This result can be due to the geometry of the system, *i.e* a neuron located next to the tip of the electrode but on its opposite side compared to the GMR sensor will generate a large electric spike and a small magnetic field.

Control experiment

As soon as the previous experiment was successfully carried out, the probes were let at the exact same location in the cortex and another 1000 trials were launched. The only difference was that the feeding current of the GMR sensor was set to zero. As explained in Chapter 3, any variation of resistance of the sensor, due to a magnetic field, would not result in a variation of the output voltage. This technique allows to discriminate whether the signal recorded came from an external magnetic field or was due to electrical coupling through the bath because of a bad insulation. The tungsten electrode still recorded spiking activity and was used as a reference to trigger the spikes, the same way it had been done previously. The results, shown in Figure 4.30, confirm that the signature recorded by the GMR sensor is due to a magnetic field.

The only other factor that could explain a resistance variation of the device would be a local increase of the temperature due to the cellular activity. The variation of the resistance is estimated to be around 0.3%/K. However, such a phenomenon would increase the resistance of the spin-valve and would give a peak that always exhibits the same polarity, whatever the polarity of the electric spike. This hypothesis has been quickly ruled out because of the polarity reversal of this magnetic field.

Another hypothesis consisted in considering that the large peaks, recorded by the platinum electrode, create current pulses flowing along the gold line located close to the GMR sensor (see Figure 4.8). This current induces a magnetic field that could contaminate the recordings, but this effect was also ruled out since the gold line and the GMR sensor are exactly on the same horizontal plane. The circular magnetic field would meet the spin-valve orthogonally, which is not its sensitive axis.

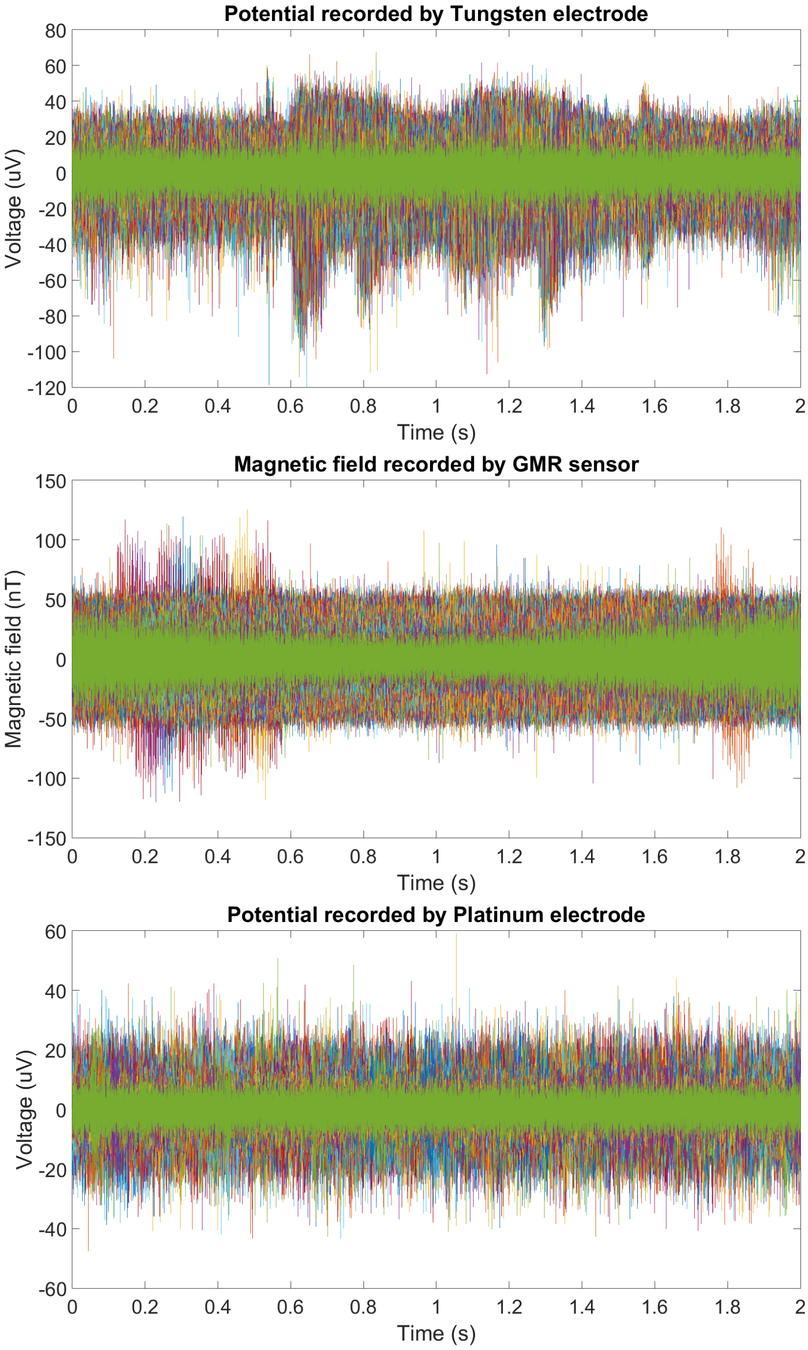

Figure 4.29: **Spiking activity without feeding the GMR sensor.** The same experiment was conducted without feeding the GMR sensor. The envelope of the signal recorded by the tungsten electrode confirms the spiking activity during the stimulation (top). The signal recorded by the GMR sensor (center) should be nothing but noise or artifact due to electric coupling. The superposition of the traces measured by the platinum electrode confirms that it does not detect neuronal response, and that any spikes detected are as likely to be artifact as real biological spikes.

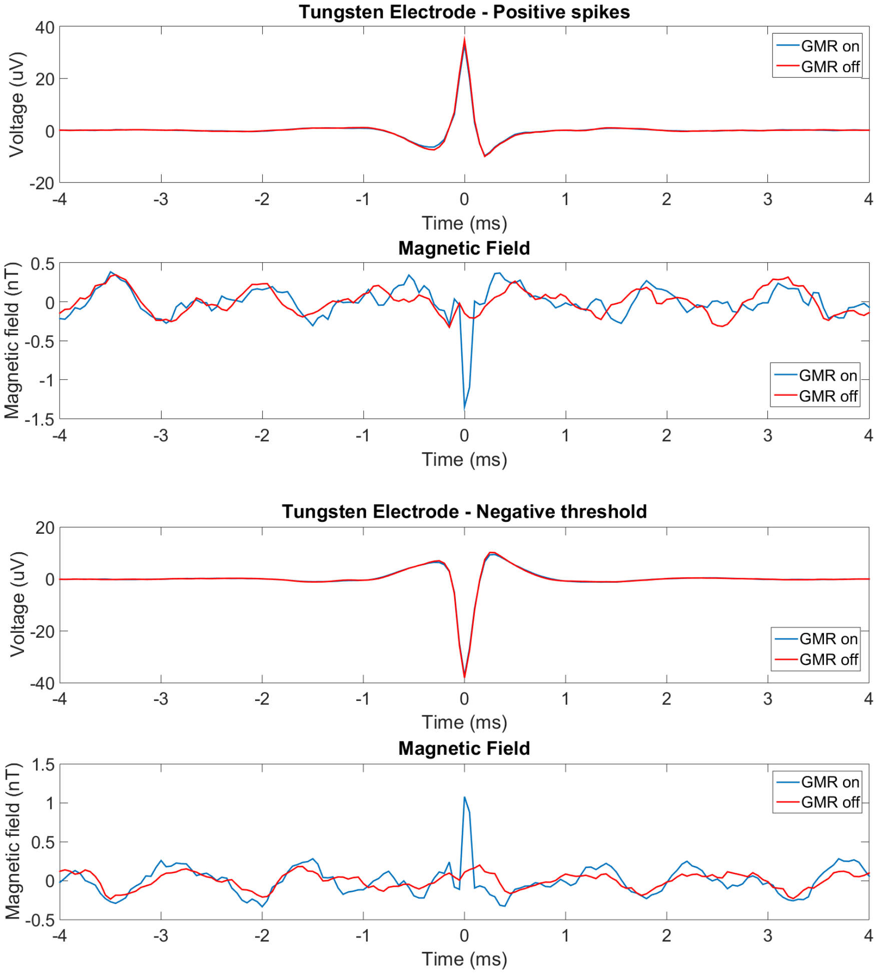

Figure 4.30: **Control of the magnetic origin of the signal.** An identical experiment is performed right after the detection of the magnetic signature of spikes showed in Figure 4.27. The current in the GMR sensor is set to zero, in order to confirm that the spikes recorded previously are due to a magnetic field and not from electrical coupling. The tungsten electrode still records thousands of spikes whose averaged shape (red trace) is identical to the previous experiment (blue trace). The signal recorded with the GMR sensor (red trace) shows no peak, which is a strong argument to support the veracity of the measurement.

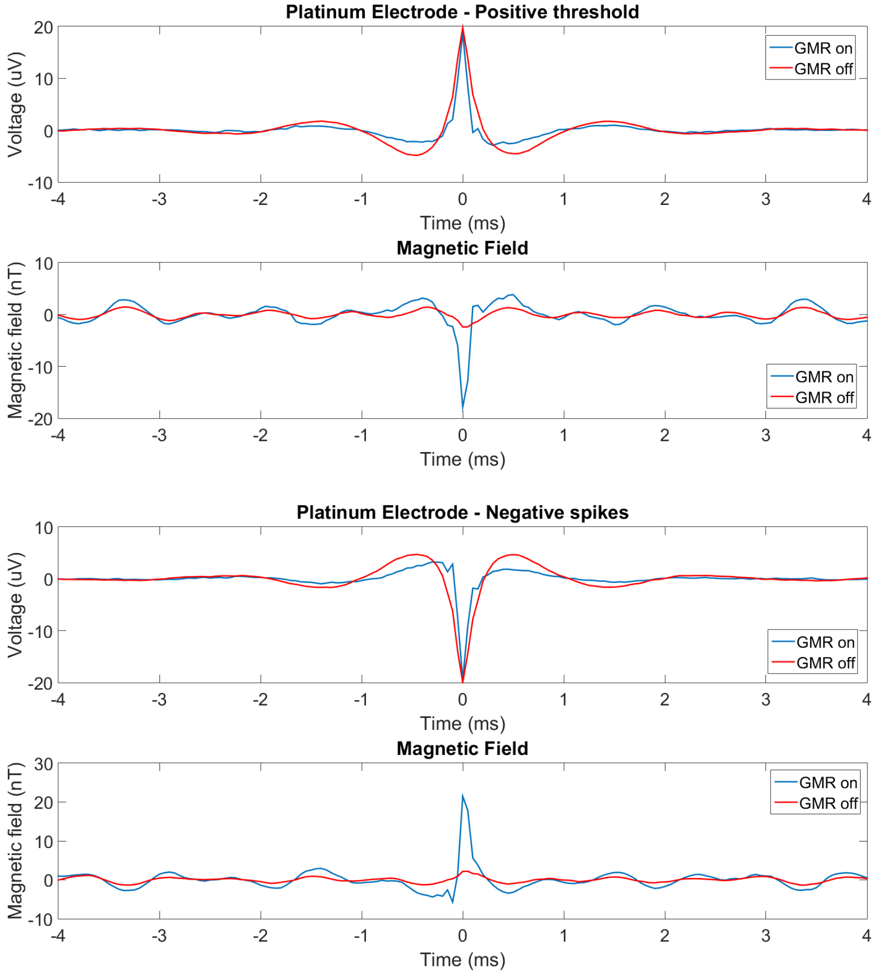

Figure 4.31: **Magnetic signature of spikes triggered on the platinum electrode.** As shown in Figure 4.23, many large spikes in the range of 50-100 nT appeared on the GMR sensor and were strongly correlated to the ones measured by the platinum electrode. After averaging, the remaining magnetic peak reaches respectively -18 nT and +23 nT, despite an upper threshold used to remove all the giant artifacts (±15 σ). The control experiment confirms that these very large peaks are due to a magnetic field. Fortunately, none of these large magnetic peaks were correlated with the spikes recorded by the tungsten electrode, so they do not contaminate the magnetic response.

4.5 Conclusion and perspectives

After the first demonstration of the compatibility of the GMR-based technology with *in vitro* experiments, this chapter presented the very first *in vivo* intra-cortical magnetic recordings of action potentials. Many challenges have been encountered before eventually succeeding in this experiment.

First, it required the development of a microfabrication process to obtain a specially-designed needle-shaped probe carrying a micron-sized GMR sensor. Each step of the process being a source of failure because of the large number of parameters, they all have been optimized to achieve a proper reliability level. From a starting point of 10 magnetrodes that can be lithographed on one mask, a success rate of 80% could be achieved. The last step that consists of cutting the probe with a laser beam is not fully mastered yet. The main advantage to switch to laser cutting was to be able to conduct the whole process in-house and to develop probes on other substrates such as glass, even if the quality of the deep reactive ion etching is still better. The final probe was 200-µm thick, which remains relatively large compared to a conventional electrode. An ambitious objective would be to grind down the substrate even more, but the handling of the system and the risk of fracturing the probe during the experiment would be quite high. For the next experiment, a new probe design will be tested, involving three aligned electrodes located closer to the GMR sensors. Also, it has been demonstrated that two GMR sensors which are sensitive to two orthogonal directions, can be implemented on a single magnetrode. It would represent a great step for the improvement of spike sorting methods.

Secondly, the very small number of *in vivo* experiments limited the possibility to improve the system and to correct the errors that arose. A typical operation lasted about 72 hours, and a measurement involving 1000 trials lasted 40 minutes, thus limiting the tests of multiple configurations. Before launching each measurement, the stability of the signal had to be ensured. Contrary to the *in vitro* setup that could be tested by simply looking at the contraction of the muscle, here, it could take several minutes to find the best placing of the probes that gave a clear evoked response to the stimulus. The reproducibility was much lower, mostly because of the arbitrary insertion of the probes inside the cortex, without being able to control where the sensitive parts were located with respect to the neuronal cells. Moreover, most of the experiments were performed with the magnetrode and the tungsten electrode handled separately by two micromanipulators. The idea to glue the electrode over the magnetrode came up at the very end of the session, but it allowed to trigger the electric spikes close to the GMR sensor, which gave the results presented earlier.

On the other hand, even a small number of experiments results in a very large amount of data. Processing each of the trials involved a lot of software development that had to be adapted continuously. However, the sampling frequency, that was set to 20 kHz, could be increased to refine the signals, even if the file size would increase drastically. The spike detection process was based on a traditional threshold technique, but setting up spike sorting software, implying pattern recognition to link every spike to a neuron, would have extended the time spent on data processing.

Finally, one of the most difficult part of these experiment is to predict which signal is expected. There is no perfect model describing the magnetic field due to an assembly of neurons. The biophysics and the membrane properties of a single neuron are well established, and the imaging techniques allows to localize accurately brain functions. Extracellular recording focuses on the intermediate scale and aim at understanding how the activity of individual neurons contributes to neuronal circuits. Since the information is transmitted through action potentials, detecting the spikes fired by neurons around the electrode is of main interest. However, the morphology of the cells, how they are arranged with respect to each other, their density, the varying amplitude and polarity of the spikes, the placement of the electrode, makes it impossible to model completely this structure. As stated in [36], progress in neuroscience will depend on the understanding of the extracellular recordings of large neural populations. This is all the more reason why the development of new tools is of key importance.

Bibliography

[1] ADRIAN, E. et Y. ZOTTERMAN. 1926, «Impulses set up by touch and pressure», *J. of Physiol*, vol. 61, p. 465. 112

[2] BEAR, M. F., B. W. CONNORS et M. A. PARADISO. 2007, *Neuroscience*, vol. 2, Lippincott Williams & Wilkins. 108

[3] BÉDARD, C., H. KRÖGER et A. DESTEXHE. 2004, «Modeling extracellular field potentials and the frequency-filtering properties of extracellular space», *Biophysical journal*, vol. 86, no. 3, p. 1829–1842. 109

[4] BÉDARD, C., H. KRÖGER et A. DESTEXHE. 2006, «Model of low-pass filtering of local field potentials in brain tissue», *Physical Review E*, vol. 73, no. 5, p. 051 911. 108

[5] BRODMANN, K. 1925, *Vergleichende Lokalisationslehre der Grosshirnrinde: in ihren Prinzipien dargestellt auf Grund des Zellenbaues*, Barth Leipzig. 107

[6] BUZSÁKI, G., C. A. ANASTASSIOU et C. KOCH. 2012, «The origin of extracellular fields and currents—eeg, ecog, lfp and spikes», *Nature reviews neuroscience*, vol. 13, no. 6, p. 407–420. 110, 111

[7] CARUSO, L. 2015, *Giant magnetoresistance based sensors for local magnetic detection of neuronal currents*, thèse de doctorat, Université Pierre et Marie Curie-Paris VI. 106, 127

[8] CARUSO, L., T. WUNDERLE, C. M. LEWIS, J. VALADEIRO, V. TRAUCHESSEC, J. TREJO-ROSILLO, J. P. AMARAL, J. NI, C. FERMON, S. CARDOSO et collab.. 2017, «In vivo magnetic recording of neuronal activity», *accepted in Neuron*. 106, 127

[9] DESTEXHE, A. et C. BEDARD. 2013, «Local field potential», *Scholarpedia*, vol. 8, no. 8, p. 10 713. 109

[10] FERNÁNDEZ-RUIZ, A., S. MUÑOZ, M. SANCHO, J. MAKAROVA, V. A. MAKAROV et O. HERRERAS. 2013, «Cytoarchitectonic and dynamic origins of giant positive local field potentials in the dentate gyrus», *Journal of Neuroscience*, vol. 33, no. 39, p. 15 518–15 532. 109

[11] GABBOTT, P. et P. SOMOGY. 1986, «Quantitative distribution of gaba-immunoreactive neurons in the visual cortex (area 17) of the cat», *Experimental Brain Research*, vol. 61, no. 2, p. 323–331. 107

[12] GOLD, C., C. C. GIRARDIN, K. A. MARTIN et C. KOCH. 2009, «High-amplitude positive spikes recorded extracellularly in cat visual cortex», *Journal of neurophysiology*, vol. 102, no. 6, p. 3340–3351. 111, 112

[13] GOLD, C., D. A. HENZE, C. KOCH et G. BUZSÁKI. 2006, «On the origin of the extracellular action potential waveform: a modeling study», *Journal of neurophysiology*, vol. 95, no. 5, p. 3113–3128. 137

[14] HÄMÄLÄINEN, M., R. HARI, R. J. ILMONIEMI, J. KNUUTILA et O. V. LOUNASMAA. 1993, «Magnetoencephalography—theory, instrumentation, and applications to noninvasive studies of the working human brain», *Reviews of modern Physics*, vol. 65, no. 2, p. 413. 126

[15] HARRIS, K. D., D. A. HENZE, J. CSICSVARI, H. HIRASE et G. BUZSÁKI. 2000, «Accuracy of tetrode spike separation as determined by simultaneous intracellular and extracellular measurements», *Journal of neurophysiology*, vol. 84, no. 1, p. 401–414. 112

[16] HERRERAS, O. 2016, «Local field potentials: Myths and misunderstandings», *Frontiers in neural circuits*, vol. 10. 109

[17] HUBEL, D. H. et collab.. 1957, «Tungsten microelectrode for recording from single units», *Science*, vol. 125, no. 3247, p. 549–550. 112

[18] KAJIKAWA, Y. et C. E. SCHROEDER. 2011, «How local is the local field potential?», *Neuron*, vol. 72, no. 5, p. 847–858. 110

[19] KANDEL, E. R., J. H. SCHWARTZ, T. M. JESSELL, S. A. SIEGELBAUM, A. J. HUDSPETH et collab.. 2000, *Principles of neural science*, vol. 4, McGraw-hill New York. 107

[20] KATZNER, S., I. NAUHAUS, A. BENUCCI, V. BONIN, D. L. RINGACH et M. CARANDINI. 2009, «Local origin of field potentials in visual cortex», *Neuron*, vol. 61, no. 1, p. 35–41. 109

[21] KINDLMANN, G., R. A. NORMANN, A. BADI, J. BIGLER, C. KELLER, R. COFFEY, G. M. JONES et C. R. JOHNSON. 2003, «Imaging of utah electrode array, implanted in cochlear nerve», *Digital Biology: The emerging paradigm*, p. 6–7. 111

[22] KREIMAN, G., C. P. HUNG, A. KRASKOV, R. Q. QUIROGA, T. POGGIO et J. J. DICARLO. 2006, «Object selectivity of local field potentials and spikes in the macaque inferior temporal cortex», *Neuron*, vol. 49, no. 3, p. 433–445. 109

[23] LUND, J. S. 1987, «Local circuit neurons of macaque monkey striate cortex: I. neurons of laminae 4c and 5a», *Journal of Comparative Neurology*, vol. 257, no. 1, p. 60–92. 107

[24] LUND, J. S., M. J. HAWKEN et A. J. PARKER. 1988, «Local circuit neurons of macaque monkey striate cortex: Ii. neurons of laminae 5b and 6», *Journal of Comparative Neurology*, vol. 276, no. 1, p. 1–29.

[25] LUND, J. S. et C. Q. WU. 1997, «Local circuit neurons of macaque monkey striate cortex: Iv. neurons of laminae 1-3a», *Journal of Comparative Neurology*, vol. 384, no. 1, p. 109–126.

[26] LUND, J. S. et T. YOSHIOKA. 1991, «Local circuit neurons of macaque monkey striate cortex: Iii. neurons of laminae 4b, 4a and 3b», *Journal of Comparative Neurology*, vol. 311, no. 2, p. 234–258. 107

[27] MILSTEIN, J. N. et C. KOCH. 2008, «Dynamic moment analysis of the extracellular electric field of a biologically realistic spiking neuron», *Neural computation*, vol. 20, no. 8, p. 2070–2084. 109

[28] MOUNTCASTLE, V. B. 1957, «Modality and topographic properties of single neurons of cat 9s somatic sensory cortex», *Journal of neurophysiology*, vol. 20, no. 4, p. 408–434. 112

[29] NORDHAUSEN, C. T., E. M. MAYNARD et R. A. NORMANN. 1996, «Single unit recording capabilities of a 100 microelectrode array», *Brain research*, vol. 726, no. 1, p. 129–140. 108

[30] PETTERSEN, K. H. et G. T. EINEVOLL. 2008, «Amplitude variability and extracellular low-pass filtering of neuronal spikes», *Biophysical journal*, vol. 94, no. 3, p. 784–802. 109

[31] PETTERSEN, K. H., H. LINDÉN, A. M. DALE et G. T. EINEVOLL. 2012, «Extracellular spikes and csd», *Handbook of neural activity measurement*, vol. 1, p. 92–135. 108, 110

[32] PEYRACHE, A., N. DEHGHANI, E. N. ESKANDAR, J. R. MADSEN, W. S. ANDERSON, J. A. DONOGHUE, L. R. HOCHBERG, E. HALGREN, S. S. CASH et A. DESTEXHE. 2012, «Spatiotemporal dynamics of neocortical excitation and inhibition during human sleep», *Proceedings of the National Academy of Sciences*, vol. 109, no. 5, p. 1731–1736. 108

[33] POUZAT, C., O. MAZOR et G. LAURENT. 2002, «Using noise signature to optimize spike-sorting and to assess neuronal classification quality», *Journal of neuroscience methods*, vol. 122, no. 1, p. 43–57. 129

[34] QUIROGA, R. Q. 2007, «Spike sorting», *Scholarpedia*, vol. 2, no. 12, p. 3583. 112

[35] QUIROGA, R. Q., Z. NADASDY et Y. BEN-SHAUL. 2004, «Unsupervised spike detection and sorting with wavelets and superparamagnetic clustering», *Neural computation*, vol. 16, no. 8, p. 1661–1687. 129

[36] REY, H. G., C. PEDREIRA et R. Q. QUIROGA. 2015, «Past, present and future of spike sorting techniques», *Brain research bulletin*, vol. 119, p. 106–117. 129, 135, 146

[37] ROCKEL, A., R. W. HIORNS et T. POWELL. 1980, «The basic uniformity in structure of the neocortex», *Brain: a journal of neurology*, vol. 103, no. 2, p. 221–244. 107

[38] ROUSCHE, P. J. et R. A. NORMANN. 1998, «Chronic recording capability of the utah intracortical electrode array in cat sensory cortex», *Journal of neuroscience methods*, vol. 82, no. 1, p. 1–15. 108

[39] SCHROEDER, C., C. TENKE et S. GIVRE. 1992, «Subcortical contributions to the surface-recorded flash-vep in the awake macaque», *Electroencephalography and Clinical Neurophysiology/Evoked Potentials Section*, vol. 84, no. 3, p. 219–231. 109

[40] STERIADE, M. 2003, *Neuronal substrates of sleep and epilepsy*, Cambridge University Press. 108

[41] XING, D., C.-I. YEH et R. M. SHAPLEY. 2009, «Spatial spread of the local field potential and its laminar variation in visual cortex», *Journal of neuroscience*, vol. 29, no. 37, p. 11 540–11 549. 109

Chapter 5

Local magnetic stimulation

> *Réserver son jugement implique*
> *un espoir infini*
>
> Gatsby le Magnifique - Francis Scott Fitzgerald

Contents

Introduction

This last chapter describes the work that was carried out at the very beginning of this thesis. The main idea was to study the effect of an external magnetic field on the response of neurons by following the same path as for the sensors, *i.e* going from the brain scale down to the cellular scale. The initial observation was the same: just like there was no microscopic counterpart of MEG systems, the magnetic stimulation remained limited to transcranial magnetic stimulation (TMS), using large coils placed over the head. However, a study published in 2012 reported successful stimulation of neural tissue with micro-coils [8]. Inspired by these results, a stimulation setup has been developed and a few *in vitro* experiments have been performed on rat hippocampus. It highlighted an unlikely artifact source and others experimental issues. In the meantime, the first significant results of GMR-based detection came and the time-consuming microfabrication process has led to push forward this path.

5.1 Transcranial Magnetic Stimulation (TMS)

5.1.1 Early development

After the discovery of "animal electricity" by Galvani and the findings of Faraday about the electromagnetic induction, many experiments to stimulate the brain and nerves have been attempted. The very first successful ones have been carried out on the frog in 1959 [13] and on human peripheral nerves in 1965 [4]. The relatively long excitation signal (40 ms) precluded any physiological recording of the induced activity. The first demonstration of cortical magnetic stimulation was reported in 1985 by Barker et. al [2]. They applied a brief stimulus ($\approx 200\,\mu s$) of 4000 A in a flat coil of outside diameter of 100 mm, placed on the scalp. When located over the motor cortex, a stimulus triggered movements in the opposite foot and elbow of the subject, and action potential occurring 7 ms later (elbow) and 23 ms (foot) were recorded. The main advantage of TMS over electrical stimulation via surface electrode is that current does not pass through the skin (see Figure 5.1), which creates a painful sensation, since this is where most of the pain fiber nerve endings are located [1].

Since then, TMS has been widely developed to study the relationship between the activation of a specific cortical area and behavior, and for investigating area-to-area neuronal connections. Usual functional imaging techniques such as EEG [12, 21, 34, 35], PET [9], or fMRI [6] can be combined with a TMS system to record the evoked activity. However, integrating a TMS-compatible EEG system is challenging since the very strong induced electric field results in a large artifact that may saturate the amplifiers of the recording chain. One of the reasons of the interest for TMS is the ease of use of a TMS system. The typical setup is simply based on a capacitor discharge system, described in the next section, and a hand-held circular coil of a few centimeters. An individual stimuli of 1-2 Tesla, lasting around 300 µs and so inducing an electric field of 100 V/m, is usually required to elicit significant neuronal activation [11]. From a clinical point of view, the use of TMS as a therapeutic tool seems to be efficient for the treatment of a number of neurological disorders, such as medication-resistant depression [19] or for presurgical cortical mapping [26].

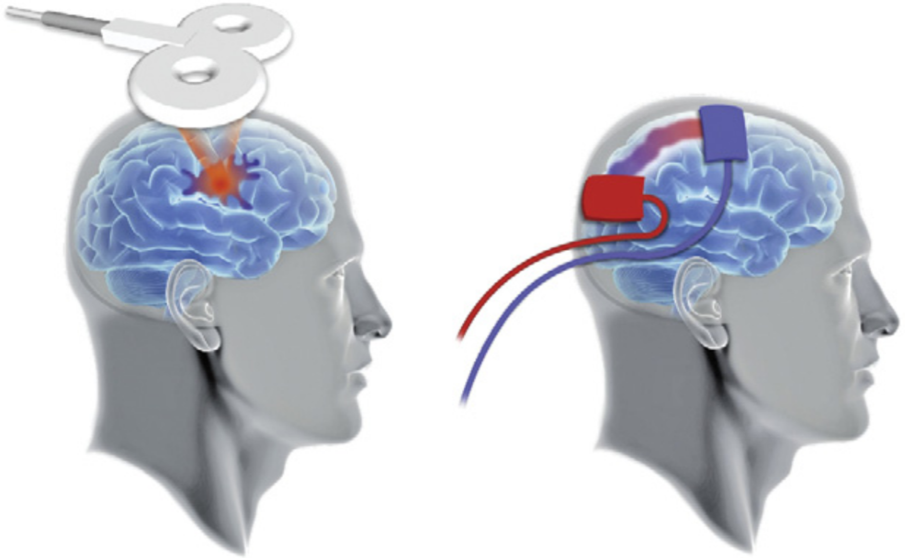

Figure 5.1: **Transcranial Magnetic Stimulation vs. Transcranial Direct Current Stimulation (TDCS), from [33]. Left:** A figure-of-eight coil is placed over the head and a pulse of current creates electromagnetic induction inside the cortical network. **Right:** Electrodes are placed over the scalp and alternating currents of around 1 mA are applied to stimulate neuronal activity. Different frequencies can be used, up to 250 Hz. This methods induces painful sensations for the patient, contrary to TMS.

5.1.2 Basic principles

The first point which is worth clarifying is the semantics. TMS differs from transcranial electrical stimulation since there is no need of electrodes placed in contact with the scalp. The pulses of current are not sent directly through the tissues but in a coil placed over the head, which makes TMS totally painless. However, the stimulation of the neurons occurs because of the ions flow that can modify the membrane potential of the targeted cells, thus increasing or decreasing its probability to fire an action potential. This movement of ions is not triggered by the magnetic field but the electric field. The mechanism of action is based on electromagnetic induction. The magnetic field can be up to several Teslas, there is no chance of stimulating a cell if the field does not vary in time and so does not generate induced currents. The Maxwell-Faraday's equation indicates that the electric field is proportional to the rate of change of magnetic field:

$$\nabla \times \mathbf{E} = -\frac{\partial \mathbf{B}}{\partial t} = -\frac{\partial (\nabla \times \mathbf{A})}{\partial t} \tag{5.1}$$

Where **A** is the magnetic vector potential, which can be computed by:

$$\mathbf{A}(\mathbf{r}, t) = \frac{\mu_0\, i(t)}{4\pi} \int \frac{\mathbf{dl}(r')}{|\mathbf{r} - \mathbf{r}'|} \tag{5.2}$$

The total electric field in the brain can be expressed as the sum of two terms:

$$\mathbf{E} = -\frac{\partial \mathbf{A}}{\partial t} - \nabla \mathrm{V} \tag{5.3}$$

The first term $-\partial \mathbf{A}/\partial t$ is controlled by the pulse sent in the coil and can be easily computed from the expression of **A**. In an unbounded medium whose conductivity is uniform, there would be no accumulation of electric charges and thus no gradient of potential $\nabla \mathrm{V}$. In this ideal case, a modeling study reported that for a single straight axon, the action potential is triggered at locations where the spatial gradient of electric field along the axon is maximum [29]. Intuitively, one would apply the electric field transverse to the membrane, to change directly the membrane potential of the cell. However, since the resting potential is around -70 mV, and the thickness of the membrane estimated to be a few nanometers, the local electric field is around 10^7 V/m, which is out of the range of the TMS systems. A schematic illustration of the activating mechanisms for different configuration is given on Figure 5.2.

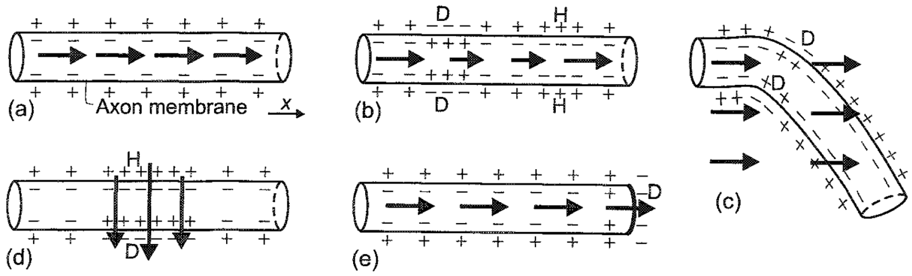

Figure 5.2: **Model of activation mechanisms by TMS, from [11].** Black arrows represent the electric field. **(a)** Uniform electric field along the axon: the similar flow of charges inside and outside the cell do not modify the membrane potential. **(b)** A positive (resp. negative) gradient of electric field $\partial E_x/\partial t$ creates an hyperpolarization (H) or a depolarization (D). **(c)** An artificial gradient can be obtained when a bent axon is placed in a homogenous electric field, which is probably the most common activation process. **(d)** The electric field is applied perpendicularly to the membrane, but the local transmembrane electric field is 10^4 times greater than the strength that can be applied with a coil. **(e)** Depolarization generated by an homogenous electric field at the axon ending.

5.2 Local Magnetic Stimulation (LMS)

5.2.1 Motivations

Despite the actual benefits of electrical and transcranial magnetic stimulation as research tools or as a therapeutic strategy, these techniques have several limitations. The benefit of the non-invasiveness of TMS is balanced on the other side by a poor spatial resolution. The size of the coils, in the centimeter range, and their positioning above the head of the patient, precludes any accurate targeting of a given neuronal population, unless performing navigated TMS [30]. Moreover, the activation zone of TMS is limited to superficial cortical layers, and deeper structures are beyond the range of current devices [32]. It requires large power sources to deliver magnetic pulses reaching the threshold of activation, and the long duration of the treatment requires long clinical stays [8].

Brain regions can also be activated simply in applying current between two relatively large electrodes (35 cm^2 each) placed over the scalp. This technique is referred to as transcranial direct current stimulation (TDCS). The underlying physiological mechanisms of TDCS have been intensively investigated for decades. Although most of the studies suggest for example that the activity of the area located under the anode increased, while cathodal stimulation reduces cortical excitability [23], there remain elusive issues about the precise effect of an electrical pulse to a brain region. The success of electrical stimulation is due to the possibility to design implantable microelectrodes, that allows to target accurately very specific zones. This methods is referred to as Deep Brain Stimulation (DBS). Important clinical advances based on DBS have been reported: restoring hearing with cochlear implants and motor functions to Parkinsonian patients with basal ganglia stimulation [31]. Its therapeutic efficiency contrasts with the many hypothesis proposed in the literature to explain the biophysics that rules this stimulation technique [20, 22].

Technical limitations come with the implementation of a DBS system. The implantation generates inflammatory reactions: the contact with an electrode leads to the formation of scars around the tip, involving subsequent decrease of stimulation efficacy [10]. Over the time, this immune reaction also increases the threshold of activation of the targeted cells. Moreover, patients carrying a DBS system should not undergo an MRI examination without a complete test procedure, in order to ensure the safety of the patient. The current induced by an MRI signal could lead to a large heating at the tip of the conductive electrode, resulting in serious neurological damage [28]. Finally, if the electrode is not perfectly placed by the neurologist, the stimulating pulses of currents can spread to surrounding areas that were not initially targeted, which might generate side-effects [3].

On this basis, the same observation can be drawn for the stimulation techniques as it has been done for the imaging ones in the previous chapters. Sensing the electric response of neuronal activity can be made at the brain scale by EEG, and at the cellular level by electrophysiology techniques. The magnetic signature of this activity was only recordable at the brain scale by MEG, and GMR-based technology has been proposed to perform local magnetophysiology. Concerning stimulation systems, TDCS and DBS are proven methods but they have intrinsic drawbacks, cited above. TMS is a powerful tool, but there is no microscopic counterpart of magnetic stimulation system. The large amplitude of field required to induce neuronal activity in TMS, *i.e* a variation of 1-2 Tesla in 100 μs that induces an electric field of 100 V/m, was thought to be out of the range of microscopic coils. However, microcoils could be a great alternative to perform local magnetic stimulation. The spatial resolution would be largely improved by implanting them in the close vicinity of the targeted cells. Microcoils would be MRI-compatible, and, coated with a biocompatible materials, the coil would not create any inflammation or immune rejection by the body.

A recent study, published in 2012, reported the first experiment that elicited neuronal response with micro-coils [8]. A square coil of 0.5 x 0.5 mm^2 and 1-mm long was placed 300 µm above the biological sample, retinal ganglion cells of rabbit. The spiking activity was recorded by a patch-clamp electrode, and two kinds of activation have been reported. Direct activation of the cells corresponds to the firing of an action potential with a latency of 1 ms (see Figure 5.3), while indirect activation corresponds to burst of spikes appearing tens of milliseconds after, suggesting synaptic activation. The most surprising result is that the electric field produced by these microcoils was estimated to be 1 V/m, two orders of magnitude below the conventional values. Indirect activation mechanism is still unknown, but it could be due to surrounding neurons that were close to reach their firing threshold at the instant of the stimulation. Nevertheless, being able to trigger directly an action potential with such a low electric field seemed both surprising but also promising. Based on these results a local magnetic stimulation setup, presented in the next section, was developed.

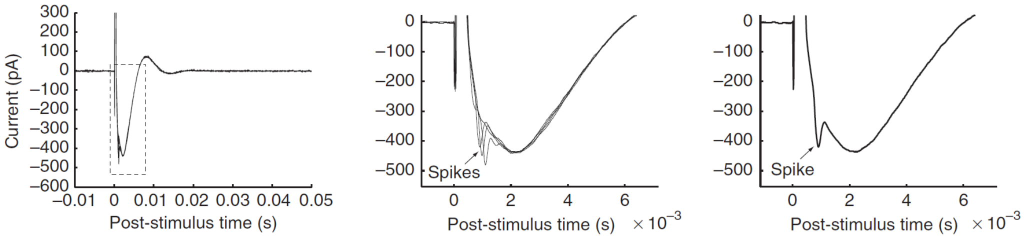

Figure 5.3: **Recordings of neuronal activity after micro magnetic stimulation, from [8]. Left:** Response of retinal neurons to a single pulse of magnetic field. **Center:** Zoom of the dashed zone on the left graph. Overlay of five trials, suggesting the firing of action potential by the targeted cell, 1 ms after the stimulus. **Right:** Recording of one single trial.

5.2.2 LMS setup

The setup is similar to the conventional ones implemented in a TMS system. The need of a high current (tens of Amperes) precludes the use of a pulse generator. It can be obtained by discharging a large capacitor, 330 µF, connected in series with the coil by a switch. A schematic presentation of the magnetic stimulation system is shown in Figure 5.4. An IGBT (Insulated Gate Bipolar Transistor) behaves like a switch controlled by the output of the switch driver signal V_{trig} :

- if $V_{trig} = 0\,V$, the transistor is blocked, no current flows into the coil, and the DC source charges the capacitor through the charge resistance with a time constant $\tau = R.C = 2.10^3.330.10^{-6} = 0.7$ s.
- if $V_{trig} = 5\,V$, the transistor is saturated, all the charge stored in the capacitor is

flowing through the coil. If the coil had zero resistance, the charges would go alternatively from the coil to the capacitor in a sinusoidal way, but here $R_{coil} = 1,25\Omega$, so the damping due to Joule effect induces a current with only one semi-sinusoidal shape lasting about 100 µs.

The inductance of the coil used for the experiments is L = 35 µH and its inner radius is 5 mm. It has been shown that a coil wrapped around a cylindrical magnetic core does not provide any advantage over an air-core coil [27]. The design of the coil was guided by simulations of the RLC circuit to induce high electric field with a pulse width in the range of 100 µs. The equation of induction given above suggests to create a pulse as short as possible, in order to maximize the rate $-\partial\mathbf{A}/\partial t$. However, the stimulation of a given tissue is due to the amount of electrical charges displaced that makes a cell reaches its threshold potential. It means that the intensity of the stimulus and its duration are linked by an inverse law, which is called a strength-duration curve:

$$I_{th} = \frac{I_r}{1 - e^{-t_s/\tau}} \tag{5.4}$$

In this equation, I_{th} is the current stimulus threshold sufficient to generate a neuronal response in 50% of the trials, t_s is the duration of the stimulus pulse, and τ is the membrane time constant as defined $\tau = r_m.c_m$, where r_m and c_m represent the membrane resistance and capacitance. I_r is the minimum current amplitude of infinite duration that results in the depolarization threshold of the membrane being reached. Chronaxy is defined as the duration that elicits a response when the stimulus strength is twice the rheobasic value. The power efficiency is maximal when $t_s = t_{chronaxy}$. According to the strength-duration curve, the coil has been designed to obtain a pulse width of ≈ 100 µs, which is the typical value used in TMS. In order to measure the induced electric field, a pick-up loop of the same radius was placed below the coil, so that the variation of magnetic flux generates an electromotive force during the discharge of the capacitor. This electromotive force is given by:

$$\varepsilon = \oint_C \mathbf{E.dl} \tag{5.5}$$

The circular geometry of the pick-up loop gives directly the electric field induced by the coil: $E = \varepsilon/(2\pi R)$. The measured waveform of ε showed in Figure 5.5 has a peak amplitude of 120 mV. It leads to an electric field of 3.8 V/m, which is very low compared to TMS but in the same range as the study presented above [8]. A numerical model of the coil was also developed to compare the amplitude with this characterization test. The exact same parameters were chosen for the size of the coil and the number of turns. Figure 5.6 provides coherent results.

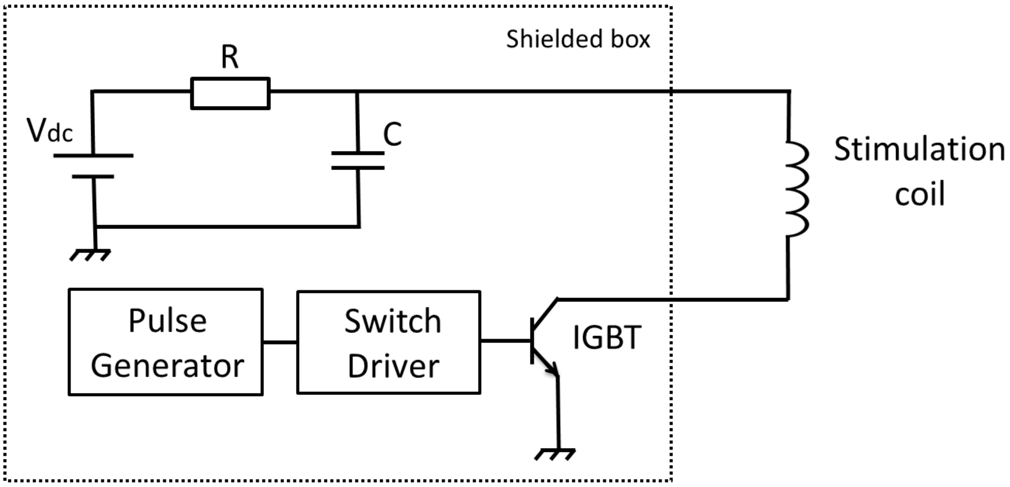

Figure 5.4: **Electronic circuit used to generate current pulses in the stimulation coil.**

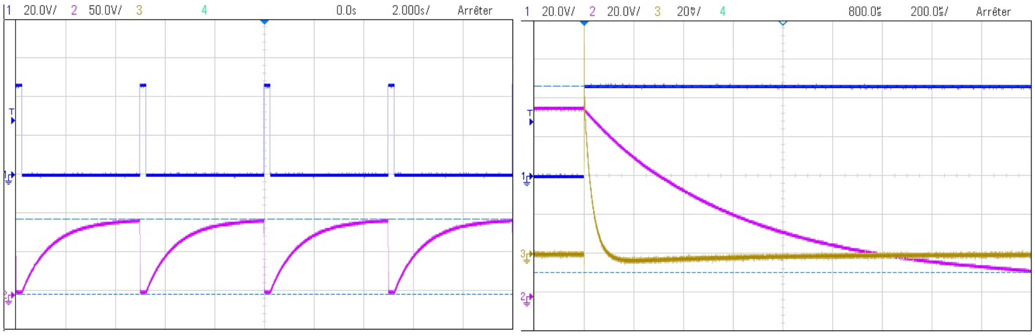

Figure 5.5: **Signal waveforms. Left:** evolution of the voltage across the capacitor (pink trace) when a trigger signal (blue trace) saturates the transistor: a full discharge can not be repeated at a faster rate than 4 seconds. It may be possible to reduce this value to 1 second, depending on the capacity of the charge resistance to dissipate the peak power at the opening of the switch. **Right:** Stimulation signal when the transistor gets saturated (blue curve). It was measured with a pick-up coil with the same diameter placed at the edge of the stimulation coil. The maximum amplitude is about 100 mV, which corresponds to an induced electric field **E** of $E = \frac{120.10^{-3}}{2\pi r} \approx 3.8$ V/m

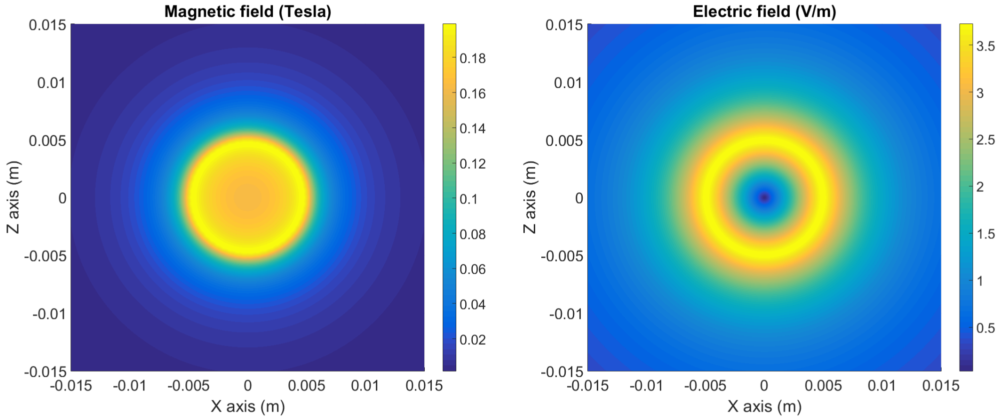

Figure 5.6: **Computed magnetic and electric field generated by current pulse in the coil.** The parameters used for this simulation correspond to the setup: the coil has a diameter of 5 mm and comprises 40 turns. A pulse of 50 A lasting 100 µs generates a magnetic field of 180 mT and a circular electric field of 3.5 V/m, in a plane located 500 µm under the coil.

5.2.3 Experiments

The *in vitro* experiments were conducted at the "Unité de Neurosciences, Information et Compléxité" (UNIC) of the Centre National de la Recherche Scientifique (CNRS). Dissection of a 6 week-old male Sprague-Dawley rat and extraction of the hippocampal slices were performed by A. Mikroulis. The coil was positioned as close as possible to the slice, with its axis oriented orthogonally to the plane of the slice. As illustrated by the simulation results in Figure 5.6, the electric field is maximum under the wires of the coil but is zero at the center, which explains the actual position of the coil compared to the slice. A recording electrode placed in the extracellular space was used to measure the evoked response and the reference was put further away in the preparation. The output was sampled at 20 kHz and low-pass filtered at 10 kHz. A picture of the experiment is shown in Figure 5.7.

The first experimental issue came from the huge size of the stimulation artifact, that saturated the elements of the acquisition chain. Then, the charge voltage of the capacitor was largely reduced and increased slowly to get both a sizable electric field and a artifact-compatible recording. The first consistent set of recordings is shown in Figure 5.8. Five stimuli were sent with a 5-s interval. The stimulation artifact lasted about 3 ms, and no distinct activity, referred to as indirect activation in [8], was perceived after this delay. However, a small response, occurring 1 ms after the stimulation, was hidden in the middle of the artifact (see Figure 5.8 center). The persistence of this signal was confirmed for several amplitudes of stimulation. Its identification, though, became more and more tricky when the charging voltage increases. The artifact was larger and still decreased exponentially, leading to a steeper slope that made the sorting of the spike more difficult. This exponential decrease of the artifact was fitted and subtracted to reveal the actual shape of the spike, expected to be similar to the extracellular action potential pattern recorded previously.

The signal obtained after the artifact removal was biphasic, lasted around 500 µs, and its amplitude was 600 µV. The great similarity, in terms of shape and temporal delay with the signals presented as spikes in the article of Bonmassar et. al [8] (see Figure 5.3), suggested the efficacy of local magnetic stimulation to trigger action potentials with electric field two orders of magnitude below the conventional values used in TMS. However, control experiments, that were not presented in [8], are necessary to get rid of other sources of artifact, just like GMR sensors were turned off to prove the magnetic origin of the recorded signals.

The first control experiment consisted in applying tetrodotoxin (TTX) in the bath. The role of TTX is to inhibit the firing of action potentials by blocking the flow of sodium ions into their corresponding channels [5]. This test, which is supposed to confirm the stimulation of the hippocampal neurons, ruled out this hypothesis, as the peak was still visible. The hypothesis of a physiological origin of the recorded signal was definitely rejected by repeating the experiments without the hippocampal slice and measuring the same signal again. After investigating the possible sources of this artifact, it appeared that the current discharge through the coil induced very tiny mechanical resonance of a few loops. An UV-polymerizable adhesive was applied all over the coil to make sure all the wires stick together without moving under stimulation. The absence of signal in the following experiments confirmed the mechanical cause of this artifact. However, no spikes could have been recorded with this system, as the size of the artifact limited drastically the stimulus strength that could be applied to the neurons.

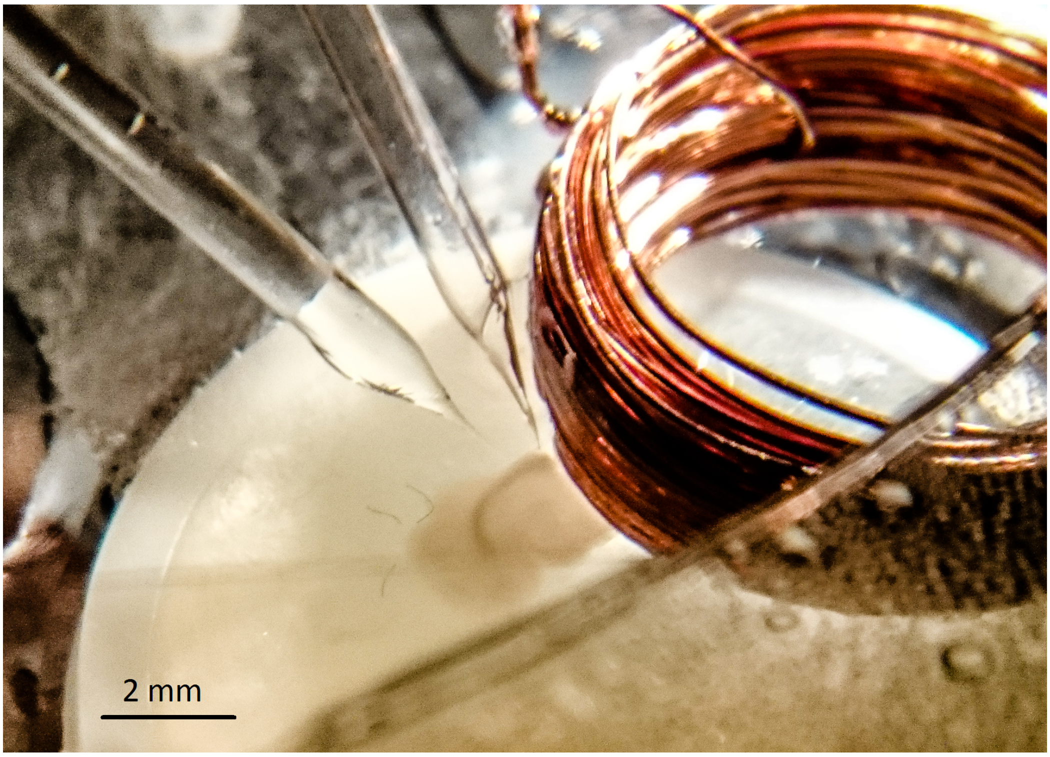

Figure 5.7: **Picture of the *in vitro* local magnetic stimulation experiment.** The 5-mm radius coil is placed just above the hippocampal slice but shifted so that the slice is located in the highest electric field zone. Next to the coil, the glass pipette records the activity in the extracellular space of the slice. The reference electrode is on the left side, in the bath.

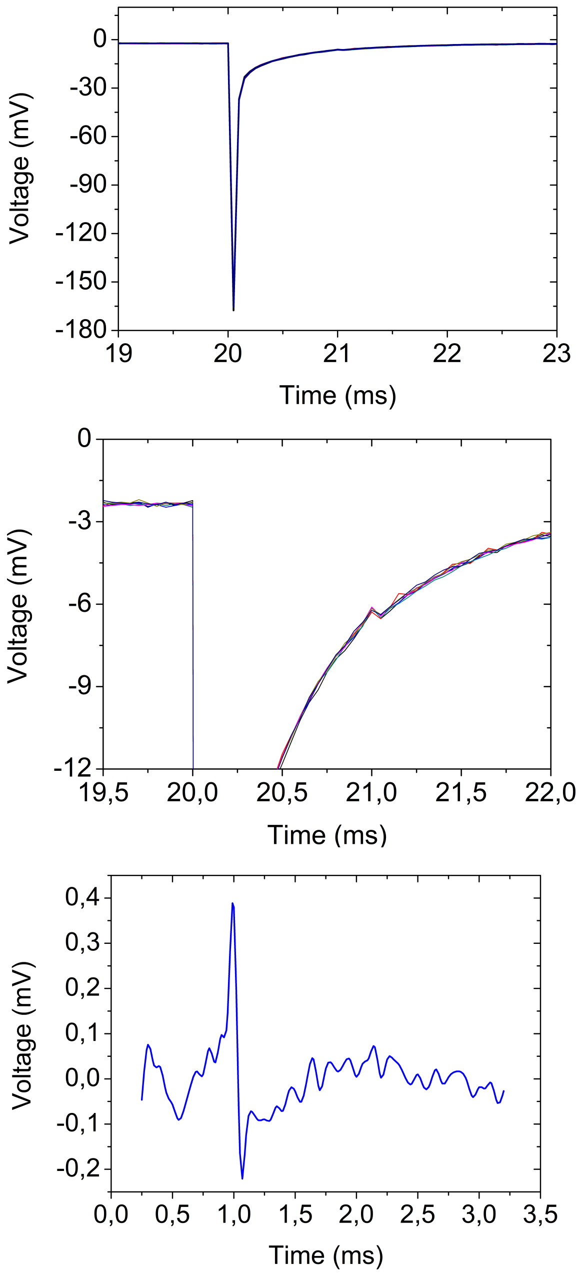

Figure 5.8: **Response to local magnetic stimulation recorded by the electrode. Top:** Artifact occurring during the stimulation. The intensity of stimulation had to be reduced until the artifact does not saturate the acquisition chain. **Center:** Zoom on the region of interest from the top graph. A spike seems to appears 1 ms after the stimulus, and is reproducible in every of the 5 overlying trials. **Bottom:** Signal extracted from the stimulation artifact. Despite compatible shape and amplitude with a real action potential, and a significant similarity with the signal presented as spikes in Figure 5.3, control experiment without the slice proved the artifact was due to the mechanical vibration of the coil created by the stimulation.

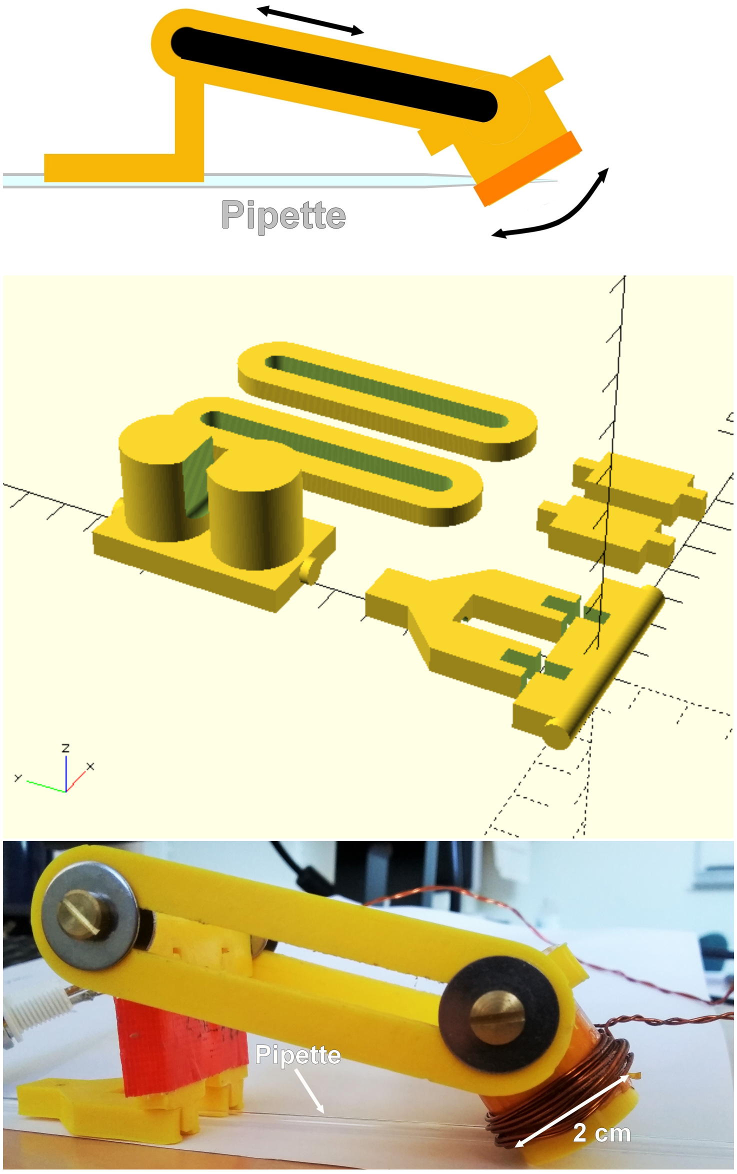

Figure 5.9: **3D printed system for future LMS experiments.** This system will allow to wire a figure of eight coil that generates a maximal electric field at the center, twice as large as a circular coil. The system can be oriented. Moreover, the pipette, through which the nerve is sucked up, can be mounted on a specially designed holder. The coil can rotate around the axis perpendicular to the pipette, to test the efficacy of the different orientation of the electric field compared to the nerve. The printing was realized in-house and the CAD design by J.Boutzen.

5.3 Conclusion

This final chapter sums up the work carried out at the beginning of this thesis before dedicating the remaining time to the development of magnetic sensors. The study reported in 2012 about the magnetic stimulation of cells with micro-sized coils had provided hope to perform successfully microTMS. The next publications [7, 15–18, 25] from the same team still reported microstimulation, but through indirect activation. The direct activation, *i.e* a single spike triggered on a single pulse, seems to be out of the range of such micro systems.

For future experiments, a simple way to check the efficacy of the magnetic stimulation would be to perform *in vitro* magnetic stimulation on a mouse muscle. The main advantage would be the possibility to check directly the success of the stimulation by visualizing the contraction of the muscle through a microscope. To this end, a 3D printed system, presented in Figure 5.9 has been designed for future experiments. Moreover, performing intracellular recordings during magnetic stimulation would give insights about how the membrane potential is varying and how far the neuron is from firing, so that the intensity of the stimulus could be adjusted just over the activation threshold.

Finally, a future project will consist in developing device for prosthetic rehabilitation of the retina based on local magnetic stimulation. Coil-based implants have been recently suggested as an alternative to conventional electrodes [14]. The idea is to provide a solution for patients suffering from retinal degenerations, by stimulating retinal ganglion cells that will transmit an information that can be processed by the visual system. An array of planar inductors would be inserted on a spherical shaped scleral explant, to create a kind of contact lens whose inductors would be activated according the image acquired by a camera placed next to the eye of the patient. The beginning of a future collaboration with the Institut de Neurosciences de la Timone (INT) in Marseille, has already led to a patent filing [24].

Bibliography

[1] BARKER, A. T. et I. FREESTON. 2007, «Transcranial magnetic stimulation», *Scholarpedia*, vol. 2, no. 10, p. 2936. 152

[2] BARKER, A. T., R. JALINOUS et I. L. FREESTON. 1985, «Non-invasive magnetic stimulation of human motor cortex», *The Lancet*, vol. 325, no. 8437, p. 1106–1107. 152

[3] BENABID, A. L., S. CHABARDES, J. MITROFANIS et P. POLLAK. 2009, «Deep brain stimulation of the subthalamic nucleus for the treatment of parkinson's disease», *The Lancet Neurology*, vol. 8, no. 1, p. 67–81. 156

[4] BICKFORD, R. G. 1965, «Neuronal stimulation by pulsed magnetic fields in animals and man», dans *Dig. 6th Int. Conf. Med. Electr. Bio. Eng. 1965*. 152

[5] BLAIR, N. T. et B. P. BEAN. 2002, «Role of tetrodotoxin (ttx)-sensitive na+ current, ttx-resistant na+ current, and ca2+ current in the action potentials of nociceptive sensory neurons», *Journal of Neuroscience*, vol. 22, no. 23, p. 10 277–10 290. 161

[6] BOHNING, D. E., A. SHASTRI, E. M. WASSERMANN, U. ZIEMANN, J. P. LORBERBAUM, Z. NAHAS, M. P. LOMAREV et M. S. GEORGE. 2000, «Bold-f mri response to single-pulse transcranial magnetic stimulation (tms)», *Journal of Magnetic Resonance Imaging*, vol. 11, no. 6, p. 569–574. 152

[7] BONMASSAR, G., M. S. HAMALAINEN et B. ROSEN. 2015, «Deep brain stimulation implant with microcoil array», US Patent 8,944,985. 165

[8] BONMASSAR, G., S. W. LEE, D. K. FREEMAN, M. POLASEK, S. I. FRIED et J. T. GALE. 2012, «Microscopic magnetic stimulation of neural tissue», *Nature Communications*, vol. 3, p. 921. 152, 155, 157, 158, 160, 161

[9] FOX, P., R. INGHAM, M. S. GEORGE, H. MAYBERG, J. INGHAM, J. ROBY, C. MARTIN et P. JERABEK. 1997, «Imaging human intra-cerebral connectivity by pet during tms», *Neuroreport*, vol. 8, no. 12, p. 2787–2791. 152

[10] HABERLER, C., F. ALESCH, P. R. MAZAL, P. PILZ, K. JELLINGER, M. M. PINTER, J. A. HAINFELLNER et H. BUDKA. 2000, «No tissue damage by chronic deep brain stimulation in parkinson's disease», *Annals of neurology*, vol. 48, no. 3, p. 372–376. 156

[11] ILMONIEMI, R. J., J. FUOHONEN et J. KARHU. 1999, «Transcranial magnetic stimulation–a new tool for functional imaging», *Critical Reviews in Biomedical Engineering*, vol. 27, no. 3-5, p. 241–284. 153, 155

[12] ILMONIEMI, R. J., J. VIRTANEN, J. RUOHONEN, J. KARHU, H. J. ARONEN, T. KATILA et collab.. 1997, «Neuronal responses to magnetic stimulation reveal cortical reactivity and connectivity», *Neuroreport*, vol. 8, no. 16, p. 3537–3540. 152

[13] KOLIN, A., N. Q. BRILL et P. J. BROBERG. 1959, «Stimulation of irritable tissues by means of an alternating magnetic field.*», *Proceedings of the Society for Experimental Biology and Medicine*, vol. 102, no. 1, p. 251–253. 152

[14] LEE, S. W., F. FALLEGGER, B. D. CASSE et S. I. FRIED. 2016, «Implantable microcoils for intracortical magnetic stimulation», *Science advances*, vol. 2, no. 12, p. e1600 889. 165

[15] LEE, S. W. et S. I. FRIED. 2013, «Magnetic stimulation of subthalamic nucleus neurons using micro-coils for deep brain stimulation», dans *Neural Engineering (NER), 2013 6th International IEEE/EMBS Conference on*, IEEE, p. 133–135. 165

[16] LEE, S. W. et S. I. FRIED. 2014, «The response of l5 pyramidal neurons of the pfc to magnetic stimulation from a micro-coil», dans *Engineering in Medicine and Biology Society (EMBC), 2014 36th Annual International Conference of the IEEE*, IEEE, p. 6125–6128.

[17] LEE, S. W. et S. I. FRIED. 2015, «Magnetic control of cortical pyramidal neuron activity using a micro-coil», dans *Neural Engineering (NER), 2015 7th International IEEE/EMBS Conference on*, IEEE, p. 268–271.

[18] LEE, S. W. et S. I. FRIED. 2015, «Suppression of subthalamic nucleus activity by micromagnetic stimulation», *IEEE Transactions on Neural Systems and Rehabilitation Engineering*, vol. 23, no. 1, p. 116–127. 165

[19] LOO, C. K. et P. B. MITCHELL. 2005, «A review of the efficacy of transcranial magnetic stimulation (tms) treatment for depression, and current and future strategies to optimize efficacy», *Journal of affective disorders*, vol. 88, no. 3, p. 255–267. 153

[20] MCINTYRE, C. C., M. SAVASTA, L. KERKERIAN-LE GOFF et J. L. VITEK. 2004, «Uncovering the mechanism(s) of action of deep brain stimulation: activation, inhibition, or both», *Clinical neurophysiology*, vol. 115, no. 6, p. 1239–1248. 156

[21] MINIUSSI, C. et G. THUT. 2010, «Combining tms and eeg offers new prospects in cognitive neuroscience», *Brain topography*, vol. 22, no. 4, p. 249. 152

[22] MONTGOMERY, E. B. et J. T. GALE. 2008, «Mechanisms of action of deep brain stimulation (dbs)», *Neuroscience & Biobehavioral Reviews*, vol. 32, no. 3, p. 388–407. 156

[23] NITSCHE, M. A., P. S. BOGGIO, F. FREGNI et A. PASCUAL-LEONE. 2009, «Treatment of depression with transcranial direct current stimulation (tdcs): a review», *Experimental neurology*, vol. 219, no. 1, p. 14–19. 155

[24] PANNETIER-LECOEUR, M., V. TRAUCHESSEC, L. CARUSO, F. CHAVANE, S. ROUX et F. MATONTI. 2016, «Device for prosthetic rehabilitation of the retina», URL `https://www.google.com/patents/WO2016120557A1?cl=en`, wO Patent App. PCT/FR2016/050,156. 165

[25] PARK, H.-J., G. BONMASSAR, J. A. KALTENBACH, A. G. MACHADO, N. F. MANZOOR et J. T. GALE. 2013, «Activation of the central nervous system induced by micromagnetic stimulation», *Nature communications*, vol. 4, p. 2463. 165

[26] PICHT, T., S. SCHMIDT, S. BRANDT, D. FREY, H. HANNULA, T. NEUVONEN, J. KARHU, P. VAJKOCZY et O. SUESS. 2011, «Preoperative functional mapping for rolandic brain tumor surgery: comparison of navigated transcranial magnetic stimulation to direct cortical stimulation», *Neurosurgery*, vol. 69, no. 3, p. 581–589. 153

[27] RAKHYANI, A. K. R. 2014, *Design and optimization of efficient magnetic coils for biomedical applications*, The University of Utah. 158

[28] REZAI, A. R., M. PHILLIPS, K. B. BAKER, A. D. SHARAN, J. NYENHUIS, J. TKACH, J. HENDERSON et F. G. SHELLOCK. 2004, «Neurostimulation system used for deep brain stimulation (dbs): Mr safety issues and implications of failing to follow safety recommendations», *Investigative radiology*, vol. 39, no. 5, p. 300–303. 156

[29] ROTH, B. J. et P. J. BASSER. 1990, «A model of the stimulation of a nerve fiber by electromagnetic induction», *IEEE Transactions on Biomedical Engineering*, vol. 37, no. 6, p. 588–597. 154

[30] RUOHONEN, J. et J. KARHU. 2010, «Navigated transcranial magnetic stimulation», *Neurophysiologie clinique/Clinical neurophysiology*, vol. 40, no. 1, p. 7–17. 155

[31] TEHOVNIK, E., A. TOLIAS, F. SULTAN, S. WM et N. LOGOTHETIS. 2006, «Direct and indirect activation of cortical neurons by electrical microstimulation», *Journal of neurophysiology*, vol. 96, no. 2, p. 512–521. 156

[32] THIELSCHER, A. et T. KAMMER. 2004, «Electric field properties of two commercial figure-8 coils in tms: calculation of focality and efficiency», *Clinical neurophysiology*, vol. 115, no. 7, p. 1697–1708. 155

[33] THUT, G. et C. MINIUSSI. 2009, «New insights into rhythmic brain activity from tms–eeg studies», *Trends in cognitive sciences*, vol. 13, no. 4, p. 182–189. 153

[34] THUT, G. et A. PASCUAL-LEONE. 2010, «A review of combined tms-eeg studies to characterize lasting effects of repetitive tms and assess their usefulness in cognitive and clinical neuroscience», *Brain topography*, vol. 22, no. 4, p. 219. 152

[35] VIRTANEN, J., J. RUOHONEN, R. NÄÄTÄNEN et R. ILMONIEMI. 1999, «Instrumentation for the measurement of electric brain responses to transcranial magnetic stimulation», *Medical and Biological Engineering and Computing*, vol. 37, no. 3, p. 322–326. 152

Conclusion

> *Nous n'héritons pas de la terre de nos parents, nous l'empruntons à nos enfants*
>
> Proverbe africain

The aim of this thesis was to develop a new tool to perform magnetophysiology, a domain that had not been explored much so far. Brain activity is already measured by a wide range of techniques, but there was no such tool able to measure the magnetic field coming from the activity of a small population of cells. Over the past three decades, the domain of spin-electronics devices has kept expanding, and the magnetoresistive sensors have emerged as a powerful solution to detect fields down to 10^{-9} Tesla. Before targeting neurons, the use of GMR-based sensors for magnetic recordings of biological activity has been validated through *in-vitro* experiments on the mouse soleus muscle. This biological system has been chosen because of its simple organization, allowing for a realistic modeling, and for its robustness, in order to get reliable and replicable results. The perfect agreement between the measurements and the theoretical predictions represents a consistent validation of the GMR technology for biological applications. Then a specially adapted needle-shaped probe carrying micron-sized GMR sensors has been developed for *in-vivo* experiment in cat visual cortex. The very first magnetic signature of action potentials inside the neuropil has been measured, paving the way towards magnetophysiology.

Plenty of improvements could be made for future experiments. An ideal design of the probe would consist in several aligned GMR-sensors to record the magnetic laminar amplitude profile along the cortical layers, while recording the local potential through electrodes deposited on either side of each sensors. The meanders can be designed so that the probe can be sensitive to both the radial and the tangential component of the magnetic field. The next microfabrication process will be based on new lithography masks including these features. The development of tunnel magnetoresistive (TMR) sensors is also planned to obtain a better detectivity, especially in the frequency range of spiking activity. Moreover, the sensors could operate in a modulated regime that suppresses most of their low-frequency noise. The theoretical principles have been presented in Chapter 2, and forthcoming work should bring successful results that could be applied broadly to every magnetoresistive sensor. Low-noise electronic chain can also be adapted to perform multi-channels recordings and to be integrated as much as possible on a chip. Data processing should be improved as well, in order to perform efficient spike sorting. It would allow a new kind of mapping of the local configuration of the cells, taking benefits of the vectorial information to determine action potential propagation direction. The potential advances that can be made on every step of this work raise a lot of expectations for the future.

In a very long-term and ambitious view, the ultimate goal of this project would be to perform simultaneously local magnetic recordings and magnetic stimulation, by mounting micro-inductors and GMR-sensors on a single probe. It would provide a microscopic combination of MEG and TMS on an implantable device, a invaluable tool for brain research. Moreover, as soon as any onset of neurodegenerative disorder would be detected, local stimulation could be applied to boost the deficient cells, which could provide major clinical advances. Despite the essential findings of fundamental research, which have led to the discovery of the sensors used along this work, the opportunity to foresee such outstanding applications has been a decisive source of motivation throughout this thesis.

université
PARIS-SACLAY

ÉCOLE DOCTORALE
Physique
en île-de-France
(EDPIF)

Titre : Détection et stimulation magnétique locale de l'activité neuronale

Mots clés : Capteurs GMR, Biomagnétisme, Neurones, In vitro, In vivo

Résumé: L'activité cérébrale se traduit par des courants ioniques circulant dans le réseau neuronal. La compréhension des mécanismes cérébraux implique de sonder ces courants, via des mesures électriques ou magnétiques, couvrant différentes échelles spatiales. A l'échelle cellulaire, les techniques d'électrophysiologie sont maitrisées depuis plusieurs décennies, mais il n'existe pas actuellement d'outils de mesure locale des champs magnétiques engendrés par les courants ioniques au sein du réseau neuronal. La magnéto-encéphalographie (MEG) utilise des SQUIDs (Superconducting QUantum Interference Devices) fonctionnant à très basse température, placés en surface du crâne, qui fournissent une cartographie des champs magnétiques mais dont la résolution spatiale est limitée du fait de la distance séparant les capteurs des cellules actives. Le travail présenté dans cette thèse propose de développer des capteurs magnétiques à la fois suffisamment sensibles pour être capable de détecter le champ magnétique extrêmement faible générés par les courants neuronaux (de l'ordre de 10^{-9} T), et dont la géométrie est adaptable aux dimensions des cellules, tout en fonctionnant à température ambiante. Ces capteurs, basés sur l'effet quantique de magnétorésistance géante (GMR, sont suffisamment miniaturisables pour être déposés à l'extrémité de sondes d'une finesse de l'ordre de 100 µm. L'utilisation de capteurs GMR pour la mesure de signaux biomagnétiques fut d'abord testée lors d'expériences *in-vitro*, réalisées sur le muscle soléaire de souris. Ce système biologique a été choisi pour sa simplicité, rendant la modélisation accessible, ainsi que pour sa robustesse, permettant d'avoir des résultats fiables et reproductibles. Le parfait accord entre les prédictions théoriques et les signaux magnétiques mesurés valide cette technologie. Enfin, des expériences *in-vivo* dans le cortex visuel du chat ont permis de réaliser la toute première mesure de la signature magnétique de potentiels d'action générés par des neurones corticaux, ouvrant la voie à la magnétophysiologie.

Title : Local magnetic detection and stimulation of neuronal activity

Keywords : GMR Sensors, Biomagnetism, Neurons, In vitro, In vivo

Abstract: Information transmission in the brain occurs through ionic currents flowing inside the neuronal network. Understanding how the brain operates requires probing this electrical activity by measuring the associated electric or magnetic field. At the cellular scale, electrophysiology techniques are well mastered, but there is no tool to perform magnetophysiology. Mapping brain activity through the magnetic field generated by neuronal communication is done via magneto-encephalography (MEG). This technique is based on SQUIDs (Superconducting QUantum Interference Devices) that operate at liquid Helium temperature. This parameter implies to avoid any contact with living tissue and a shielding system that increases the distance between the neurons and the sensors, limiting spatial resolution. This thesis work aims at providing a new tool to perform magnetic recordings at the neuronal scale. The sensors developed during this thesis are based on the Giant Magneto-Resistance (GMR) effect. Operating at room temperature, they can be miniaturize and shaped according to the experiment, while exhibiting a sensitivity that allows to measure amplitude of 10^{-9} T. Before targeting neurons, the use of GMR-based sensors for magnetic recordings of biological activity has been validated through *in-vitro* experiments on the mouse soleus muscle. This biological system has been chosen because of its simple organization, allowing for a realistic modelling, and for its robustness, in order to get reliable and replicable results. The perfect agreement between the measurements and the theoretical predictions represents a consistent validation of the GMR technology for biological applications. Then a specially adapted needle-shaped probe carrying micron-sized GMR sensors has been developed for *in-vivo* experiment in cat visual cortex. The very first magnetic signature of action potentials inside the neuropil has been measured, paving the way towards magnetophysiology.

Université Paris-Saclay
Espace Technologique / Immeuble Discovery
Route de l'Orme aux Merisiers RD 128 / 91190 Saint-Aubin, France